FAR INFRARED Ge DETECTORS:

CONDUCTION AND ABSORPTION MECHANISMS

by

SAMIR ABDALLAH EL-ATAWY

Department of Physics

Queen Mary College

A thesis submitted in accordance with the regulations for the degree of Doctor of Philosophy in the University of London

1976

CONTENTS

ABSTRACT

This report describes an experimental study of the conduction and absorption mechanisms of Germanium in the temperature range 4.2 - 1.5^{o}K. The results of these studies were mainly devoted to the developments of very far infrared detectors.

Germanium (Ge) is a well-known semiconductor element used widely, when doped with small concentration of impurities, for detection of far infrared wavelengths up to 100μm. For doping concentrations less than 1.0 x 10^{16} atoms/cm^{3}, the absorption of radiation in the range 100-1000μm is very weak because of the lack of the proper absorption mechanisms, except for some photo-hopping absorption in compensated samples around 1000μm. In the range of doping between 1-8 x 10^{16} cm^{-3}, there exists additional thermal activation energy not present in the lower concentrations. It was thought that this activation energy results from impurity interactions in this doping range, and hence a delocalized energy band is thus formed above the ground state level. However, the electrical conduction, the width of this band and its position, and the relevance of this band to the marked bolometric effect for 100-1000μm wavelength detections are not yet clear.

This thesis presents further study on this band together with its relation to the conduction and absorption mechanisms. Comparative studies were usually made for two samples of Ge differing in doping configuration, one of which does not have this additional activation energy (low concentration).

The first two chapters give a review of the absorption and conduction mechanisms in Ge at low temperatures, and the performance relations and measurements for different types of infrared detectors.

In this report, the conduction mechanism is studied for the two samples, and includes galvanometric properties, thermal properties and energy scattering processes for the carriers in the delocalized band.

The absorption characteristics, in 100-1000μm range of the two samples were investigated.

Germanium elements with absorbing surfaces are also studied using two different techniques, namely, surface ion implantation and metal film deposition. The mutual effects of the implanted surface and the bulk material are discussed and suggestions for the future of this technique are given.

Finally, the design and performance of the constructed high sensitivity far infrared Ge detectors using the higher concentration sample are given. Theoretical noise limitations were reached in these detectors. Measurements and practical astronomical applications are also given.

CHAPTER 1

REVIEW ON THE ELECTRICAL CONDUCTION AND ABSORPTION MECHANISMS OF Ge AT VERY LOW TEMPERATURES

1.1. Electrical conduction

1.1.1. Low concentration range

The conduction mechanism of Ge in the low concentration range of impurities (N_D or $N_A \lesssim 1 \times 10^{16}$ cm^{-3}) is now established to be what is known as impurity conduction first observed by Hung [1] and Hung and Gliessman [2]. These authors observed anomalous behaviour, at very low temperatures, in the Hall constant and the electrical resistivity of Ge doped to the upper limit of this range. Many papers have been published on this topic which have introduced more refinements to our understanding of this new phenomenon of impurity conduction. Much of this work is referenced in a review article in the theory of impurity conduction by Mott and Twose [3]. The best description of the phenomenon was given by the Mott-Conwell model in which, for n-type material, the majority donors are randomly distributed in the coulombic potential of negatively charged acceptors. The charge distribution can respond to an applied electric field, F, by an electron hop associated with an energy increase, ΔE, from an uncharged to an adjacent charged donor. For such hopping to take place there should be some vacant localized states to which electrons hop. The hopping rate is a function of the majority concentration, the energy difference ΔE between two hopping centres, and the absolute temperature T. The hopping time, τ , is the inverse of the transition rate and is given by [4,5]

$$\tau \cong 5 \times 10^{-13} \left(\frac{r}{a}\right)^{-3/2} e^{\frac{2r}{a}} \tanh\left(\frac{\Delta E}{2kT}\right) \qquad .. (1.1)$$

where,

r is the mean majority centre separation,

and a is the ground state Bohr radius of the impurity atom.

The free hopping carrier concentration is given by [3]

$$n \cong (N_D N_A)^{\frac{1}{2}} \exp\left(\frac{-\Delta E}{2kT}\right) \quad .. (1.2)$$

where N_D and N_A are the donor and acceptor concentrations respectively. The average energy separation ΔE is a function only of donor and acceptor concentrations; for n-type material it has been found [20] that

$$\Delta E \cong \frac{e^2}{k} (N_D^{1/3} - 2N_A^{1/3}) \quad .. (1.3)$$

where k is the dielectric constant.

The temperature dependences of τ and n are different. The maximum variation of τ will occur when $T \simeq \frac{\Delta E}{2k}$, but it will be insensitive to T when $kT \ll \frac{\Delta E}{2}$ or $\gg$, which is usually met in practice. The dependence of n on T, through the exponential factor in (1.2), has a maximum variation when $T = \frac{\Delta E}{4k}$; a saturation in carrier concentration should set in when $n = N_A \equiv$ number of vacant centres. Substituting in (1.2), the corresponding temperature T_s can be obtained from,

$$\exp \frac{-\Delta E}{2kT_s} \cong K^{\frac{1}{2}} \quad .. (1.4)$$

K here is the compansation ratio (N_A/N_D)

When a steady electric field is applied across the sample, the situation is altered due to the change in potential energy associated with each hopping centre and an equilibrium polarization has to be established even if the phonon excitation is not sufficient to overcome the coulombic potential around the minority impurity. This relaxation will take a time of the order of the hopping time (1.1). The rate of change of polarization can be detected as a current in an ac experiment [5].

For low concentration of impurities, the wavefunction overlap between adjacent majority impurity centre is small but finite, resulting

in a finite propability of tunnelling of majority carriers from occupied to unoccupied centres. Experimentally, the conduction process in this concentration range at low temperatures is characterized by a single activation energy $\varepsilon_3 = \frac{\Delta E}{2}$, which confirms that the only conduction mechanism in these conditions is due to the activated hopping mechanism. The electrical conductivity at low temperatures will take the form [6]

$$\sigma = \sigma_3 \exp \frac{-\varepsilon_3}{kT} \qquad .. (1.5)$$

where σ_3 represents the conductivity in the limit $\frac{1}{T} \simeq 0$.

Fritzsche and Cuevas [14] found that for p-type Ge, the value of ε_3 was nearly independent on acceptor concentration in the range $1.4 \times 10^{15} \lesssim N_A \lesssim 3.5 \times 10^{16}$ cm^{-3} for constant K = 0.4, a broad maximum occurring for $N_A = 3.2 \times 10^{15}$ cm^{-3}. With increase in N_A above 3.5×10^{16} cm^{-3}, for the same K, the value of ε_3 falls rapidly to zero at $N_A \sim 1.5 \times 10^{17}$ cm^{-3} corresponding to the onset of metallic type of conduction. For K = 0.04, an approximately three-fold larger ε_3 value is obtained at $N_A = 3.7 \times 10^{15}$ cm^{-3}, and an even faster fall to zero occurs for increasing N_A up to the same limiting value.

In spite of the good understanding of the theory of impurity conduction, some uncertainties still remain. The work of Miller and Abrahams [4] based on phonon-induced hopping model for n-type compensated Ge with impurity content up to 6×10^{15} cm^{-3} showed, for all samples, that the calculated resistivity is higher than the measured one. The ratio between the calculated and the measured resistivities reduces with increasing donor concentration. This deviation is explained by the authors as to arise from the uncertainties connected with the treatment of the effective mass anisotropy, the deformation potential constant and the spread in the orbit radius due to zero-point lattice motion. The latter and the uncertainty arising from the choice

of transverse orbit will affect the computed value of resistivity by about 60%. However, from their calculations on a sample having donor concentration of 1.6×10^{15} cm^{-3}, the calculated value is about 3.8 times higher than the measured one.

As we mentioned, in the low concentration range and sufficiently low temperatures the only dominating conduction is the activated hopping mechanism. However, it was shown by Sladek [13] that free carriers in the conduction band exist at low temperatures. N-type samples of Ge with As and Sb doping concentrations of 7.8×10^{15} - 1.7×10^{16} cm^{-3} were investigated in a magnetic field. The author found magneto-resistance for all samples investigated which are of the same order of magnitude as those observed when the current is carried by electrons in the conduction band. This effect being happened in the impurity conduction range, the author mentioned that the mechanism should be entirely different if it is attributed to the impurity conduction carriers. The reason for this, he stated, that the Lorentz current of normal magnitude caused by a magnetic field H will be given by $\frac{\mu_i H}{c}$ times the impurity conduction current; μ_i is the mobility of impurity conduction carriers and c is the velocity of light. This magnitude of current component will be negligibly small (μ_i is several orders of magnitude less than the conduction band mobility). The author explained the observed magneto-resistance by the effect of magnetic field on the wavefunctions spread describing the localized electron motion. The author also found that the conduction band carriers came as a natural extrapolation from its values at high temperatures. As an example for this, the author found that for Sb-doped sample having $N_D = 1.7 \times 10^{16}$ cm^{-3} at $3.54^{o}K$, the number of conduction band carriers has to be $10^{8.29}$ cm^{-3} with mobility of 3420 cm^2 $(V.sec)^{-1}$. The author also attributed the decrease in the Hall coefficient R_H with increasing the magnetic field H to the decrease

in the conduction band conductivity contribution than the impurity contribution, and that the Lorentz current is only caused by conduction band electrons. The Hall coefficient formula that was used in this last speculation is

$$R_H = \frac{S_{12}}{H.S_{11}^2} \qquad .. (1.6)$$

where

S_{12} is the contribution of the conduction band electrons to the overall conductivity.

S_{11} is the purely impurity conduction contribution.

1.1.2. Intermediate and high concentration ranges

The intermediate doping range ($\sim$ 1-8 x 10^{16} cm^{-3}) is generally characterized by the existance of an activation energy ε_2 in the electrical conduction mechanism. The reason for the appearance of this activation energy is not fully understood. The low frequency conductivity at low temperatures, in this range, can be expressed as follows [6]:

$$\sigma = \sigma_2 \exp \frac{-\varepsilon_2}{kT} + \sigma_3 \exp \frac{-\varepsilon_3}{kT} \qquad .. (1.7)$$

σ's represent the limit of the respective conductivity when $\frac{1}{T} = 0$.

The second term in R.H.S. may represent the hopping contribution as before but probably with different nature [13] and dominates at the lowest temperatures. This activation energy only exists for doping concentration up to about 8 x 10^{16} cm^{-3} and disappears for higher concentrations. The doping concentration range between 8 x 10^{16} - 1.3 x 10^{17} cm^{-3} is again characterised by a single activation energy which in its turn disappears at the upper limit mentioned due to the onset of metallic conduction [17]. It was mentioned that this unique activation energy might be associated with the process which gives rise

to ε_2. Further work suggests that this is the actual case. In the last reference, the author studied the effect of uniaxial compression in $\langle 111 \rangle$ direction on n-type Ge. This compression affects greatly the impurity conduction in intermediate and high concentration ranges which depends originally on the wave-function overlap. The maximum stress used was 2×10^9 dynes/cm^2. The main effect of the stress was a change in the activation energy ε_2 of impurity conduction. This effect was similar for both As and P impurities which is a decrease of both resistivity and the activation energy ε_2. However, the opposite effect was observed in the case of Sb impurity, i.e. an increase of both resistivity and ε_2. The author also investigated as a function of stress the critical impurity separation for the transition from non-metallic to metallic conduction in the concentration range $7 \times 10^{16} < N_D < 3 \times 10^{17}$ cm^{-3}. The author's conclusion was

(i) The activation energy ε_2 depends strongly on the wavefunction overlap.

(ii) Shear strains change the donor wavefunctions originating from the individual valleys by an amount proportional to the valley-orbit splitting of the donor element.

The author also indicated that the case of Sb-doped Ge is complicated by the fact that the three-fold 1S-like state lies very close to the ground state and probably overlaps it at the intermediate concentrations. Finally, the author did not expect the strong temperature dependence of $\frac{\rho_x}{\rho_o}$ (the ratio between the resistivity under stress and the zero stress value).

Frood [18] proposed that, at intermediate concentration range, the conduction takes place in the lower tail of the conduction band which includes the delocalized higher laying impurity states. Based on this proposition, the dominating conduction mechanism will be due to the

delocalized carriers having mobility higher than the hopping mobility and smaller than the conduction (or valence) band mobility.

The impurity conduction in this concentration range has also been discussed by James [16,19] from adifferent point of view. The author introduced a theory based on the activationless tunnelling for carriers between atoms having maximum amount of overlap. This preferred path always exists as a result of the random distribution of impurities in the crystal. In this path, the carriers will move with large speeds and dominate any other type of conductivity at very low temperatures. As the concentration increases, the number of these preferred paths increase and/or may broaden to allow more carriers to tunnel through but its contribution to overall conductivity will decrease as the concentration approaches the metallic type of conduction. By this model, the author wanted to speculate the behaviour of the activation energy ε_2 with doping concentration. His theory, as a matter of fact, may be able to speculate some of the uncertainties between theory and experiments especially the overall conductivity and average drift mobility in the low and intermediate concentration ranges. As we mentioned, in Miller and Abrahams work [4], the deviation of the calculated resistivity from the measured one decreases with increasing impurity concentration could well be speculated by James' theory.

The Hall coefficient measurements for Sb-doped Ge in a very wide range of concentration as a function of temperature have been done by Fritzsche [16]. From these measurements, we observe a clear maximum in the Hall curve for low concentration samples which occurs at temperatures at which the free carrier conduction and impurity conduction compete; for higher temperatures the free carrier conduction dominates. On the other hand, for samples in the intermediate concentration range, such a finite clear maximum is not present, which indicates that for the doping level at which this occurs (about 6×10^{16} cm^{-3})

there is no such conduction competition and the free carrier conduction does not disappear completely but still acting as an essential part of the conduction mechanism at the lowest temperatures. The free carriers may transfer to another lower broadened state when reducing temperatures and will behave similar to the carriers in the conduction band.

Within the impurity concentrations in which there are clear maxima of the Hall coefficient, the peak shifts towards the lower temperatures as the impurity content decreases. Therefore, we may say that the temperature of equal conductivities increases with increasing doping level. Since for impurity concentrations $< 10^{16}$ cm^{-3} (low concentration range), the main participation to conductivity comes from the conduction band carriers and the hopping carriers in the vicinity of the Hall maximum, therefore, the effect of incremental increase in the majority impurity on the hopping conductivity is larger than its effect on the free carrier conduction at low temperatures.

The activation energy ε_2, being created by the majority impurity wavefunction overlap, should not be affected by the degree of compensation. However, the density of delocalized carriers may be affected through the change of the hopping activation energy ε_3. It was shown by Fritzsche and Cuevas [14] that ε_3 reduces when the compensation ratio K increases thereby increasing the domination of ε_3 conduction. Moreover, the ε_2 conduction vanishes at K = 0.4. This is also clear from Price's formula given by equation (1.3) for ε_3 and from Miller and Abrahams' [4] work for K up to 0.2 for n-type Ge that is

$$\varepsilon_3 = \left(\frac{e^2}{k}\right)\left(\frac{4\pi N_D}{3}\right)^{1/3}\left(1 - 1.35\, K^{1/3}\right) \qquad .. (1.8)$$

The variation of ε_2 with magnetic field for impurity concentrations $5 \times 10^{16} - 2 \times 10^{17}$ was studied by Sadasiv [21] who concluded that ε_2 increases by an amount proportional to the square of the magnetic induction H, i.e.

$$\varepsilon_2(H) = \varepsilon_2 + \alpha H^2 \qquad .. (1.9)$$

α being the constant of proportionality which depends on the nature and concentration of the impurity, but in general a decreasing function of impurity concentration. As an example, the author found that for Sb-doped sample of 5.9×10^{16} cm^{-3}, the value of α is equal to 4.01×10^{-13} $eV.G^{-2}$. The main concern of Sadasiv's work is to study the transverse magneto-resistance in the intermediate concentration range and showed that the transverse magneto-resistance ratio decreases with decreasing temperature from 4.2 to $\sim 2.1^{o}K$ for a sample having 3.8×10^{16} Sb/cm^3 as a result of increasing the domination of ε_3. While for samples in which ε_3 does not exist (concentrations > 8×10^{16} cm^{-3}), the magneto-resistance keeps increasing with decreasing temperatures down to $1.14^{o}K$. However, the author did not measure the Hall coefficient and its variation with electric or magnetic fields.

The impurity conduction of Ge at specific doping level depends on the nature of impurities, mainly the atomic radius. Antimony atom has the largest atomic number and hence largest atomic radius. The conductivity at low temperatures for specific doping is larger for Sb than, for instance, As or P. The large atomic dimensions of Sb atom in Ge results in a smaller ionization energy from the ground state to the conduction band for isolated atoms. It also has been demonstrated by Sawaki et al.[22] that the density of states in heavily doped Ge with antimony (5×10^{18} and 1.5×10^{19} cm^{-3}) has a little evidence for a dip between the impurity band and the main band, while for As doped sample (the same doping) there was a strong dip, but there existed only a long tail going down continuously below the main band. The fact that Sb atoms have a larger effective potential in the crystal than As, which reduces the concentration at which the metallic conduction sets in, does not explain this behaviour of state density. The conclusion that the author reached for this doping level, is that the complete merging

of the impurity band with the main band in Sb case suggests that the electrons will behave as a free electron, while in As samples, the electrons still have a strong localized nature at the same doping.

1.2. Absorption of radiation

1.2.1. Photon-induced hopping absorption

Research on ac conductivity on compensated n-type Ge were carried out by Pollak and Geballe [5], Golin [7] and Pollak [8] for frequencies up to 10^5 Hz, much lower than the far infrared frequencies ($3 \times 10^{11} - 3 \times 10^{12}$ Hz). The experimental results and theoretical speculations conducted by these authors confirm the existance of an ac conductivity superimposed on the dc value. Higher frequency investigations, up to 9×10^9 Hz, were done by Tanaka and Fan [9], and Tanaka et al. [10] who proposed the inadequacy of the phonon-assisted hopping model at these higher frequencies, and that direct photon absorption, without phonon participation, was involved for hopping to occur.

Further support to the last proposal was published by Blinowski and Mycielski [11] who calculated the absorption of the very far infrared radiation at low temperatures in doped semi-conductors with compensation ratios up to 0.2. The behaviour of n-type Ge with a doping concentration up to 6×10^{16} cm^{-3} was calculated by them for wavelengths 500-2500μm.

For this photon-induced hopping to occur, the quantum energy of the incident photon should be comparable to the energy difference between two hopping centres, $\Delta E = 2\ \varepsilon_3$, where ε_3 is the hopping thermal activation energy. The calculated and measured value of ε_3 makes this tuned absorption occur at the millimetre range of the infrared spectrum. For low doping samples, this is the only significant absorption mechanism for quantum energies less than the energy gap between the ground

state and the continuum conduction (or valence) band at which direct photoionization of neutral impurities will occur.

1.2.2. Excitation to higher excited states

For low doping concentrations, where the impurity atoms are nearly separated, absorption of radiation will occur if the quantum energy is equal to the energy separation between the ground state and higher excited states. Since the excited states for this doping level are not affected by the nearest impurity centres, well defined absorption lines must be observed for excited states below the conduction band in n-type sample. If the quantum energy is equal to or slightly greater than the ionization energy to the conduction (or valence) band, large continuum absorption of radiation will occur due to the existing very large density of states. In doped Ge, the ground state is separated from the continuum band by 10-13 meV, and the radiation wavelengths necessary for transition are about 125-95μm. This photoionization is different from the mentioned photon-induced hopping in a way that it is independent of the compensating centres concentration which is essential in the hopping transitions.

The well defined absorption lines due to single excited states and the energy threshold for the excitation to the continuum band will be affected by increasing doping concentration because of the impurity interactions. The dependence of absorption characteristics of Sb-doped Ge with impurity content in the range $6 \times 10^{14} - 7 \times 10^{16}$ cm^{-3} at $2.3^{o}K$ has been carried out by Nisida et al.[15]. The author observed broadening of the absorption lines of excited states of the donors with increasing donor concentration. The background absorption in the specimens becomes dominant at a concentration of 2×10^{16} cm^{-3} and approximately independent of the frequency of photons in the range 100-1000μm. The author suggested that this is due to the wavefunction

overlap. At 7 x 10^{16} cm^{-3}, the structureless background absorption spreads, with larger value, all over the spectrum of submillimetre region, the origin of which is not due to the free carrier absorption but it is possibly due to donor clusters and/or conduction band tailing. Also, the absorption lines occurring at higher energy side are broadened more than at the lower energy. The broadening of the absorption lines may be due to the life-time of the excited state interacting with phonons. The author also found that an excited state will disappear at specific doping level if the mean impurity separation becomes less than 2.5 times the radius of this state.

Further investigation [12] on Sb-doped Ge has been made for photo-conductivity spectra for concentrations of Sb of 3.1 x 10^{15} - 2.1 x 10^{16} cm^{-3} and for quantum energies of 5 - 13 meV. The authors in this paper refer the photoexcitation at quantum energies less than the ionization energy of electrons in isolated donor atoms to be as photothermal excitation in which the smaller quantum energy can excite the donor electrons to higher excited states which can be promoted further by interaction with phonons. A model was suggested by them in which the impurity atoms assemble to form small clusters together with other isolated atoms. The interaction between impurity atoms in this model reduces the activation energy of donors to values below the value relevant to the isolated atoms. At 4.2°K there was definite photo-excitation by the proper activation energy, in addition to further excitation with less activation energies. These authors also found that the quantum energy necessary for photoexcitation is reduced with increasing donor concentration and the photo spectra become structureless for donor concentration of 1.2 x 10^{16} cm^{-3}. When reducing temperature down to 1.6°K, for a given sample, the structure of the photo response flattens down. At this temperature the ratio of residual photoconductivity to the essential photoconductivity increases. Regarding the

mobility of excited carriers, the authors assumed that electrons excited by the proper quantum energy for isolated atoms have mobilities equal to the conduction band mobility, and they found that electrons excited by less quantum energies have mobilities which do not deviate too much from the conduction band mobility. This small deviation from the conduction band mobility was not expected by the authors because they mentioned that if these electrons are moving in the D^- band or in the conduction band tail, it should have much lower mobilities.

The existence of the thermal activation energy ε_2 in the intermediate doping concentration as shown in equation (1.7) was speculated by Yoshihiro et al.[31] as to arise from the formation of a delocalized energy band as a result of the wavefunction overlap. The centre of this band is separated from the ground state level by an energy equal to ε_2. Hence, phototransition to this band can occur with quantum energies appropriate to the value of ε_2 (smaller than the main ionization energy to the continuum band). The authors used 377μm radiation with variable concentrations of Sb-doped samples in the intermediate range. They found that the absorption cross section

$$\sigma = \frac{\alpha}{N_D - N_A} \quad cm^2,$$

where α is the absorption coefficient, has a maximum value for the sample in which $\varepsilon_2 \simeq$ 377μm quantum energy = 3.7 meV. However, they have not mentioned any relation between the position of this band and any of the higher excited states of the impurity atom. The first excited state being separated by about 5 meV from the ground state, means that the energy band formed lies between this state and the ground state as clear in their paper.

1.3. Scattering mechanisms and mobility of free carriers

The scattering mechanism of free carriers at intermediate and high concentration ranges is mainly caused by impurities (ionized and neutral) at low temperatures. The lattice limited mobility varies as $T^{-3}/2$ where T is the temperature, while the ionized impurity limited mobility varies as $T^{3/2}$. Even in very pure samples of n-type Ge, there are variations from the lattice limitation as the temperature is lowered as shown by Koenig et al.[23]. The minimum temperature at which the lattice contribution still dominant in the purest sample he used was about $7^{o}K$.

The contribution of neutral impurities to overall mobility is however smaller than the ionized centres. From the results of Erginsoy[24], the partial mobility due to $N_n cm^{-3}$ neutral, hydrogen like donors, is

$$\mu_N = 2.2\ N_n^{-1} \times 10^{20}\ cm^2/V.sec \qquad .. (1.10)$$

In the last given example in section 1.1.1 from Sladek's work [13], the extracted conduction band mobility for doping concentration of 1.2×10^{16} Sb atoms/cm^3 is 3420 cm^2/V.sec. at $3.54^{o}K$. Using equation (1.10), the mobility will be about 13,000 cm^2/V.sec which reduced the ionized impurity mobility by about 26% only.

Since scattering by impurity ions causes insignificant energy loss by carriers, the lattice vibrations are still responsible for energy loss. At liquid helium temperatures, only acoustic modes of vibrations are probably important, but, in ionic materials like InSb, there is a piezo electric polarization as well as deformation potentials associated with these modes. Another energy loss mechanism may exist, which is intervalley scattering by ionized impurities mentioned by Koenig et al.[23]. This scattering mechanism becomes more significant as the impurity concentration increases and temperature is lowered. It was first suggested by Weinreich et al.[25] that an

electron can be captured in an excited orbit followed by re-emission in another valley. It was mentioned then by Koenig et al. that if this is correct the re-emitted electrons will have lost any memory of their initial energy and thereby become thermalized in one collision. Such collisions are more frequent than capture (the rate of which increases as T decreases), and below $4^{o}K$ begin to approach within an order of magnitude of the lattice collision frequency. But lattice collisions are not as lossy per collision so that this intervalley mechanism cannot be neglected.

Callaway and Cummings[26] have considered another kind of inelastic scattering of electrons in Ge. In doped compensated samples of Ge at low temperatures, a scattering centre analagous to the hydrogen molecule ion may be formed in which an electron (or hole) is shared between two donors (or acceptors). Mobile carriers can lose energy through excitation of this molecule. This mechanism will also increase with increasing impurity content, but decreases with decreasing temperature. As an example, the authors found at 4.2 and $1.5^{o}K$, an energy loss rate of 1.5×10^{8} eV/sec. and 1.3×10^{8} eV/sec. respectively for sample with 10^{16} N_D/cm^3. However, a maximum value of this energy loss for a given compensation ratio occurs at about 10^{16} cm^{-3} and starts to decrease for larger concentrations at $4.2^{o}K$. The author attributed this to the exponential decrease of the probability that an electron in the conduction band has enough energy to cause excitation. Finally, the authors compared this with the energy loss rate due to collision with phonons using Shockley formula [27] and averaging they get

$$\left\langle \frac{W_{ph}}{\tau} \right\rangle = \frac{3m^{*}S^{2}}{\tau_L} \qquad .. (1.11)$$

where m^* is the electron effective mass,

S is the velocity of sound in the crystal,

τ_L is the relaxation time for lattice scattering.

At 4^oK this loss rate is about 10^5 eV/sec., much less than the previous figures. Therefore, if this mechanism is present it will become indeed the dominating energy loss process. As a result, the authors deduced the electric field strength at breakdown in compensated sample to that in the uncompensated sample as

$$\frac{E_{BC}}{E_B} = \left[\left\langle \frac{W_x}{\tau} \right\rangle \Big/ \left\langle \frac{W_{ph}}{\tau} \right\rangle \right]^{\frac{1}{2}} \qquad .. (1.12)$$

where $\left\langle \frac{W_x}{\tau} \right\rangle$ is the energy loss rate due to molecular excitation.

The conduction band mobility μ_c is related to the averaged momentum relaxation time τ as

$$\mu_c = \frac{e\tau}{m^*} \qquad .. (1.13)$$

where e is the electronic charge.

The mobility variation with impurity content and temperature will arise through the change in τ . However, if these parameters are fixed τ will change with the internal energy of the carriers. This happens when an external electric field is applied across the sample. The combined relaxation time due to lattice scattering τ_L and impurity scattering τ_I is given by

$$\frac{1}{\tau} = \frac{1}{\tau_L} + \frac{1}{\tau_I} \qquad .. (1.14)$$

The variation of τ with an electric field F depends on which scattering mechanism is dominant. But, in general for the presence of both scattering mechanisms, the mobility (and hence τ) for small electric fields will be given by [28]

$$\mu = \mu_o (1 + B F^2) \qquad .. (1.15)$$

where μ_o is the ohmic mobility and related to the lattice-limited mobility μ_{L_o} as

$$\mu_o = \mu_{L_o} \frac{3a + 1}{(a + 1)^2} \qquad .. (1.16)$$

and

$$a = \frac{\tau_{L_o}}{\tau_{I_o}} \quad \text{(the o refers to zero field value)}$$

B is a constant depends on the energy gain and loss rate of carriers and is given by

$$B = \frac{3(9a + 1)\ (a-1)}{16(a+1)^3} \cdot \frac{\mu^2_{L_o}}{S^2} \qquad .. (1.17)$$

S is the phonon phase velocity.

Investigating the last expression of B, it is of particular interest to consider the following two limiting cases.

(i) $a < 1$ (lattice scattering dominant), and B is negative resulting in decreasing the mobility with increasing electric fields. In this condition the loss rate of energy ~~exceeds the energy gain~~ increases when small electric field is applied across the sample.

(ii) $a > 1$ (impurity scattering dominant), and B is positive resulting in an increase in mobility with increasing electric field due to the increase in the energy gain from the external field ~~than the loss rate of carrier energy~~. In relation (1.17), largest B occurs for $a = 3.6$, then

$$\frac{(9a + 1)\ (a-1)}{(a + 1)^3}$$

has its maximum value of 0.89. For very large a, B tends to $\frac{27\mu^2_{L_o}}{16a\ S^2}$ which is a typical situation for intermediate and high concentration ranges at low temperatures. However, for large electric

fields, the situation is different and the mobility is a decreasing function with F as

$$\mu = (\frac{8}{3})^{\frac{1}{4}} \left(\frac{S\mu L_o}{F} \right)^{\frac{1}{2}} \qquad .. (1.18)$$

As we mentioned, scattering by phonons is the responsible mechanism for carriers energy relaxation (assuming that no other energy relaxation mechanisms present). In this case, the energy relaxation time τ_r is related to the phonon relaxation time τ_p as

$$\tau_r = \frac{kT\ \tau_p}{2m^* S^2} \qquad .. (1.19)$$

where

T is the absolute temperature,

m^* is the electron effective mass,

S as before is the phonon velocity.

Apart from the variation of momentum relaxation time given by (1.13) and (1.14) with the carrier energy, it has been shown by Gershenzon et al.[29] that this time should also depend on magnetic field due to the effect on electron motion in different ways. The author showed some experimental results about the dependence of the cyclotron resonance line width ($\frac{1}{\tau}$) on the magnetic field. The conclusion was that the contribution to this line width from scattering by ionized impurities decreases significantly when the cyclotron radius becomes less than the effective impurity radius a. The dependence of phonon scattering frequency ($\frac{1}{\tau_p}$) on magnetic field and temperatures 30 - 100°K were observed by Fink and Braunstein [30] who found an increase in scattering frequency of 1.5 - 5 times. These authors used a superconducting magnet of up to 110 kG, and the measurements were done at 891 GHz.

CHAPTER 1

REFERENCES

(1) Hung, C.S., Phys. Rev. 79, 727 (1950)

(2) Hung, C.S. and J.R. Gliessman, Phys. Rev. 79, 726 (1950)

(3) Mott, N.F. and W.D. Twose, Advances in Phys. 10, 107 (1961)

(4) Miller, A. and E. Abrahams, Phys. Rev. 120, 745 (1960)

(5) Pollak, M. and T.H. Geballe, Phys. Rev. 122, 1742 (1961)

(6) Fritzsche, H., Phys. Rev. 99, 406 (1955)

(7) Golin, S., Phys. Rev. 132, 178 (1963)

(8) Pollak, M., Phys. Rev. 133, A564 (1964)

(9) Tanaka, S. and H.Y. Fan, Phys. Rev. 132, 1516 (1963)

(10) Tanaka, S., M. Kobayashi, E. Hanamura and K. Uchinokura, Phys. Rev. 134, A256 (1964)

(11) Blinowski, J. and J. Mycielski, Phys. Rev. 136, A266 (1964)

(12) Nagazaka, K. and S. Narita, J. Phys. Soc. Japan, 35, 3, 788, 797 (1973)

(13) Sladek, R.J. and R.W. Keyes, Phys. Rev. 122, 437 (1961)

(14) Fritzsche, H. and M. Cuevas, Phys. Rev. 119, 1238 (1960)

(15) Nisida, Y. and K. Horii, J. Phys. Soc. Japan 26 No.2, 388 (1969)

(16) Fritzsche, H., J. Phys. Chem. Solids 6, 69 (1958)

(17) Fritzsche, H., Phys. Rev. 125, 1552 (1962)

(18) Frood, D.G.H., Proc. Phys. Soc. (London), 75, 185 (1960)

(19) James, H.M. and A.S. Ginsbarg, J. Phys. Chem. 57, 840 (1953) (end discussion)

(20) Price, P.J., J. Phys. Chem. Solids 2, 268 (1957) (appendix)

(21) Sadasiv, G., Phys. Rev. 128, 1131 (1962)

(22) Sawaki, N., A. Yashida and T. Arizomi, J. Phys. Soc. Japan 36, 149 (1974)

(23) Koenig, S.H., R.D. Brown and W. Schillinger, Phys. Rev. 128, 1668 (1962)

(24) Erginsoy, C., Phys. Rev. 79, 1013 (1950)

(25) Weinreich, G., T.M. Saunders, Jr., and H.G. White, Phys. Rev. 114, 33 (1959)

(26) Callaway, J. and F.W. Cummings, Phys. Rev. 126, 5 (1962)

(27) Shockley, W., Bell System tech. J. 30, 990 (1951)

(28) Gunn, J.B., Progress in semiconductors Vol.2, pp.213 (1957)

(29) Gershenzon, E.M., Gurvich Yu A., and S.L. Orlava, Soviet Phys.-Solid State, 11, 2743 (1970)

(30) Fink, D. and R. Braunstein, Solid State Communication (USA) vol. 15, No.2, pp.1627-31 (1974)

(31) Yoshihiro, K., M. Tokumoto and C. Yamanouchi, International Conference on Submillimetre Waves and Their Applications, June 5, 6, 7 (1974)

CHAPTER II

FAR INFRARED DETECTORS: REVIEW

2.1. Introduction

The far infrared wavelengths interval (100-2000μm) represents the part of spectrum of particular importance to astronomy as well as far infrared spectroscopy. However, detecting such radiation faces many difficulties for the following reasons:-

(i) The weakness of this radiation compared to the short wavelength part of the spectrum.

(ii) The lack of absorption mechanisms in detectors used, especially in Ge and Si (intrinsic materials are nearly transparent to such wavelengths).

(iii) Because of the weakness of this radiation, proper cooled filters are needed for cutting out short wavelengths especially in broad-band thermal detectors. Otherwise the photon noise can dominate any other kind of noise making the detection of such wavelengths inefficient.

The first point is common for all kinds of detectors, and the only improvements that can be done is to integrate the radiation to be absorbed by the detector element. The second point is the main problem that could be overcome by the proper design of the element (type of element and doping level etc.). In the last point, one has to be very careful about the selection of the cooled filters which have to be efficient enough to stop any high quantum energy leakage reaching the element.

In this chapter, the two main types of far infrared detectors (photoconductive and thermal detectors) will be reviewed in nearly all aspects. Special emphasis will be given to broad-band thermal detectors.

2.2. Photoconductive detectors

This type of detector depends upon the quantum energy $\hbar\omega$ to cause the conductivity change. The conductivity may change either by changing the carrier concentration contributing to conduction or by changing the conduction carrier mobility. The first category depends mainly on the photoexcitation of carriers from non-conducting to conducting states thereby increasing the number of conducting carriers. For this mechanism to occur, the quantum energy $\hbar\omega$ should be equal to or greater than the energy separation between these states. For such photoexcitation to be effective in creating conductivity change, a large number of the carriers has to be originally in the non-conducting states. This necessitates cooling the detector element. For wavelengths of interest, it is important to select special materials in which the energy separation between the two states defines the maximum wavelength of radiation to be detected. In this respect we find, for example, that doped Ge can absorb wavelengths about four times longer than in doped Si. It should be noted here that this is different from intrinsic photoionization due to creation of electron-hole pairs which needs quantum energy corresponding to the intrinsic energy gap in the semiconductor. This subject will not be met here.

The second category of these detectors depend for their photoconductive response upon the change in mobility of the conducting carriers without significant change in carrier concentration. These detectors depend for their operation on the weak electron-lattice coupling at low temperatures. Therefore the electron distribution temperature (it is not actually necessary for pseudo-thermodynamics to exist among the electrons themselves) can rise above the lattice temperature under the dc or radiation fields. The result of this carrier heating is a change in mobility. Therefore these devices are usually called hot-electron detectors. A successful material used in this mode is

n-type indium antimonide.

2.2.1. Photoionization detectors

2.2.1.1. Responsivity

An extrinsic semiconductor doped with a donor concentration N_D will absorb quantum energies equal to or greater than the ionization energy ε_d of electrons in the donor centres. The number of available conduction electrons will therefore increase resulting in a change in conductivity. At low temperature, the number of available centres for ionization is $(N_D - N_A - n)$ cm^{-3}, where N_A is the concentration of the compensating centres, and n is the concentration of conduction electrons thermally excited when the element is not looking to any higher temperature sources. If photons with quantum energy $> \varepsilon_d$ with a rate ΔJ $sec.^{-1}$ are shone on the element and modulated with a frequency w, then

$$\Delta J = \Delta J_o (1 + \exp jwt) \qquad .. (2.1)$$

the rate of generation of free carriers will increase by an amount $\eta \Delta J$ where η is the quantum absorption efficiency of the element. This assumes that each photon can excite one electron (if $\hbar w > 10 \varepsilon_d$, multiple ionization might occur). The relation between ΔJ and ΔN can be expressed by the equation

$$\frac{d(\Delta N)}{dt} = \Delta J_o (1 + \exp jwt) - \frac{\Delta N}{\tau} \qquad .. (2.2)$$

$\frac{\Delta N}{\tau}$ represents the recombination rate of excited carriers,

τ is the life time of free electrons.

Solving (2.2) and considering $w \tau << 1$ we find

$$\Delta N = \eta \tau \Delta J \qquad .. (2.3)$$

The corresponding change in conductivity will be

$$\Delta\sigma = \frac{e\mu\ \eta\ \tau\ \Delta J}{v} \qquad .. (2.4)$$

where μ is the mobility and v is the element volume.

The total energy ΔQ falling on the detector at frequency ν is

$$\Delta Q = h\nu\,\Delta J \qquad .. (2.5)$$

(h is the Planck constant = 6.624×10^{-34} Joules.sec.)

Then

$$\Delta\sigma = \frac{e\ \mu\ \eta\ \tau}{v\ h\nu}\,\Delta Q \qquad .. (2.6)$$

If R is the element resistance, ℓ is its length and A is the cross sectional area through which the current flows, then

$$R = \frac{1}{\sigma} \cdot \frac{\ell}{A} \qquad .. (2.7)$$

If the element obeys Ohm's law, the responsivity defined as $\frac{dV}{dQ}$ (volts/watt) can be expressed as

$$\frac{dV}{dQ} = \frac{dV}{dR} \cdot \frac{dR}{dQ} = I \cdot \frac{dR}{d\sigma} \cdot \frac{d\sigma}{dQ} \qquad .. (2.8)$$

Using (2.6) and (2.7) we get

$$\frac{dV}{dQ} = \frac{V\ \eta\ \tau}{N\ h\ \nu} \qquad .. (2.9)$$

Usually far infrared detectors have non-linearity in their characteristics. In this condition it was shown [1] that the responsivity will take the form

$$\frac{dV}{dQ} = \frac{R_L\ Z\ V_B}{R(Z+R_L)(R+R_L)} \left(\frac{\partial R}{\partial Q}\right)_V \qquad .. (2.10)$$

where Z is the dynamic impedance of the element at the operating point $= \frac{dV}{dI}$,

R_L is the load resistor and $\left(\frac{\partial R}{\partial Q}\right)_v$ is the rate of change of the element resistance w.r.t. the radiation energy Q when the element voltage is held constant,

V_B is the bias battery voltage.

2.2.1.2. Absorption cross section and quantum efficiency

The absorption cross section is defined as

$$\sigma_\nu = \frac{\alpha}{N_I} \qquad .. (2.11)$$

where α is the absorption coefficient and N_I is the concentration of impurity centres.

σ_ν is a function of the type of impurities. Burstein et al.[2] obtained

$$\sigma_\nu = \frac{8.28 \times 10^{-17}}{\varepsilon\sqrt{K}} \left(\frac{m}{m^*}\right) \left(\frac{\varepsilon}{h\nu}\right)^{8/3} \ (cm^2) \qquad .. (2.12)$$

where $h\nu \geq \varepsilon$

ε is the ionization energy of the impurity centre (ev)

K is the dielectric constant (16 for Ge, 12 for Si)

and m* is the carrier effective mass.

This relation is in good agreement with the measured values for group III impurities in Si and Ge, although, some disagreements still remain for some impurities in Ge [3]. However, we can consider relation (2.12) is good enough for impurities whose absorptions cross section has not been measured absolutely. The value of the effective mass in the above relation is that obtained by inserting the ionization energy ε in the Bohr formula

$$\varepsilon = 13.6 \left(\frac{m^*}{m}\right) \cdot \frac{1}{K^2} \ (ev) \qquad .. (2.13)$$

Considering (2.12) and (2.13), we get for Ge (K = 16).

$$\sigma_{\nu} = 1.1 \times 10^{-18} \varepsilon^{-2} \quad (cm^2) \qquad .. (2.14)$$

The relation between the quantum efficiency η and the absorption coefficient α can be derived by considering parallel-faced element with thickness d subjected to a normal surface incidence of infrared radiation. Then the total absorption A for single incidence is given by

$$A = \frac{(1 - r)\ (1 - e^{-\alpha d})}{1 - re^{-\alpha d}} \qquad .. (2.15)$$

where r is the single surface reflectance and is given approximately by

$$r \cong \frac{(n - 1)^2}{(n + 1)^2} \quad , \qquad .. (2.16)$$

n being the refractive index of the element material.

Assuming that each photon ionizes one neutral impurity centre then η will be given by

$$\eta = \frac{(1 - r)\ (1 - e^{-\alpha d})}{1 - re^{-\alpha d}} \qquad .. (2.17)$$

This relation implies that no other absorption mechanisms are involved such as lattice or free carrier absorption. In practice, α will have a spectral distribution because of these absorption mechanisms as well as the absorption caused by sub-band transition in the intermediate doping concentration as shown in Chapter I. Consequently, η deduced from (2.17) will follow the spectral variation of α. Experimental measurements of the external transmission spectrum of the sample will enable the determination of the overall spectral values for α, η and r [4]. The maximum value of η occurs when $\alpha d >> 1$ and will be given by $(1 - r)$. However, η can approach unity in perfectly designed detector; this can be achieved either by blooming

the surface and/or using an integrating system for the incident radiation.

2.2.1.3. Response time

Let us consider the following steady state rate equation [5-7]

$$\frac{dn}{dt} = 0 = A_T (N_D - N_A - n) + A_I\, n(N_D - N_A - n) + A_p (N_D - N_A - n) - B_T\, n(N_A + n) - B_I\, n^2 (N_A + n) - B_p\, n(N_A + n) \quad .. (2.18)$$

where

A_T and B_T are the thermal generation and recombination coefficients,

A_I and B_I are the coefficients representing the impact ionization and its inverse process (Auger recombination) respectively. A_p and B_p are the generation and recombination coefficients representing the external radiation photoionization not in thermal equilibrium with the receiver.

At very low temperatures, the term containing A_T can be neglected w.r.t. the non-equilibrium photoionization rate. Also n (equilibrium value) becomes very small and can be neglected compared to $(N_D - N_A)$ and the terms containing $B_I\, n^2$ and $B_p n$ become negligibly small at such low temperatures. This is also emphasised by the fact that at very low temperatures, the thermal recombination mechanism offers the major contribution to the recombination process [8]. Therefore, equation (2.18) reduces to

$$0 = A_p (N_D - N_A) - n(N_A B_T - A_I (N_D - N_A)) \quad .. (2.19)$$

or

$$n = \frac{A_p (N_D - N_A)}{B_T N_A - A_I (N_D - N_A)} \quad .. (2.20)$$

Equation (2.20) indicates that the equilibrium free carrier concentration n is mainly due to the photoionization process. Comparing (2.20) with (2.3) we find

$$\eta J = A_p (N_D - N_A) . v \qquad .. (2.21)$$

where v is the sample volume

and the time τ will be

$$\tau = \frac{1}{B_T N_A - A_I (N_D - N_A)} \qquad .. (2.22)$$

This expression is valid for low electric fields where $A_I (N_D - N_A) << B_T N_A$. As the electric field increases, τ increases and at breakdown, the denominator approaches zero; but at this condition, the Auger recombination must be involved and the response time passes through maximum and decreases again.

The value of τ can be estimated from (2.22) by measuring the capture cross section σ which is related to B_T as

$$B_T = \sigma v_T \qquad .. (2.23)$$

v_T is the thermal velocity of the carrier $\sim \left(\frac{3kT}{m^*}\right)^{\frac{1}{2}}$

Knowing B_T and an approximate value of N_A and neglecting the impact ionization term a value of τ can be estimated. The value of capture cross section and hence τ varies greatly with temperature. We find that for antimony in Ge, $\sigma = 6 \times 10^{-12}$ cm^2 at 4^oK [7], while Cu impurity gives a value of 6.9×10^{-12} cm^2 at 4^oK [9] and 1.5×10^{-14} cm^2 at 20^oK [10] for a 0.04 eV (≡ 31μm quantum energy) impurity level. Also the time τ depends on the amount of compensating impurities N_A which can either be controlled or accidentally be associated with the majority impurities. In any case it can accurately be measured [7].

2.2.2. Hot electron detectors

2.2.2.1. Responsivity

In the hot electron detectors, the conductivity change will arise from the change in the carrier energy distributions w.r.t. the lattice which is usually held constant. The non-ohmic behaviour which occurs in such materials under static or radiation fields is mainly due to the change in the carrier mobility when increasing its internal energy. A steady state is achieved when the rate of energy supply to the electron gas balances the rate of delivering this energy to the lattice. Since the electron-lattice coupling is weak, the electron gas will have a steady state temperature higher than the lattice temperature. When the crystal is receiving radiation in addition to the dc power, the free carriers will absorb the radiation causing an increase in the effective steady state temperature of the electron gas and hence a mobility and conductivity change will result. It should be noted here that the conduction carrier concentration is unaltered although the hot carriers might occupy a higher energy state when absorbing radiation. This is the main difference between free carrier photoconductivity and photoionization discussed in the previous sections. As we mentioned, the latter is due to transfer of carriers from non-conducting to conducting states which is not the case in free carrier photoconductivity.

It was shown in Chapter I that the non-linearity caused by an electric field F can be written as

$$\mu = \mu_o (1 + B F^2)$$

or

$$\sigma = \sigma_o (1 + B F^2) \qquad .. (2.24)$$

The parameter B as before describes the non-linearity of the element and is defined as

$$B = \frac{1}{\sigma} \frac{d\sigma}{dF^2} \qquad .. (2.25)$$

And the voltage responsivity (volts/watt) will be

$$\mathcal{R} = \frac{BV}{v.\sigma} \qquad .. (2.26)$$

where v and σ are the volume and conductivity of the element respectively.

V is the voltage across the element.

For InSb, which was used successfully in this mode, we find at $4^{o}K$, a typical value of $B = 20\ V^{-2}\ cm^2$, $V = 10$ mV, $v = 5 \times 10^{-3}\ cm^3$, $\sigma = 0.3\ (\Omega.cm)^{-1}$. This gives a value of $\mathcal{R} = 130$ volts/watt.

A similar expression for B was used by Rollin [11] in his investigation of the detection of millimetre and submillimetre waves in semiconductors. The term is the mobility sensitivity S, where

$$S = \frac{1}{\mu} \frac{d\mu}{dW} \qquad .. (2.27)$$

where $\frac{d\mu}{dW}$ represents the rate of change of mobility w.r.t. the dc or ac power input. S has a dimension of $watts^{-1}$, and contributes to the voltage responsivity as

$$\mathcal{R} = -V.S \qquad .. (2.28)$$

It was also shown by Rollin that for polar semiconductors, as in InSb, where the piezo electric scattering is dominant, assuming that the mobility is limited by ionized impurity scattering, we have

$$S \alpha E^{-\frac{1}{2}} (m^*)^{-3/2} \qquad .. (2.29)$$

where E is the mean carrier energy, m* is its effective mass.

For non-polar non-degenerate semiconductor, such as Ge,

$$S \alpha E^{-3/2} (m^*)^{-5/2} \qquad .. (2.30)$$

From this we can see that for Ge, the inverse dependence of S on m* and E is stronger than in InSb (for Ge, m* = 0.11 m_o, and 0.015 m_o for InSb), therefore, for equal constant of proportionality and internal energy E, S for Ge will be much smaller than in InSb. However, the voltage responsivity in Ge may exceed that for InSb for hot electron performance, because the voltage across the element is much greater and the conductivity is much smaller (relation 2.26).

A typical value for S and R was quoted by Rollin for InSb sample of $n = 5 \times 10^{13}$ cm^{-3} at $2^{o}K$ showing a resistance of 140 Ω and a voltage across it of 40 mV. For these values it was found that

$$S = \frac{1}{\mu} \frac{d\mu}{dW} = 6 \times 10^{4} W^{-1}$$

and

$$\frac{dV}{dW} = \frac{V}{\mu} \frac{d\mu}{dW} \simeq 2.4 \times 10^{3} \text{ V/W}$$

2.2.2.2. Free carrier absorption coefficient

The classical formula for the free carrier absorption coefficient is

$$\alpha = \frac{\sigma(w)}{c K_o K^{\frac{1}{2}}} = \frac{ne^2}{m^* c K_o K^{\frac{1}{2}}} \cdot \frac{\tau}{1 + w^2 \tau^2} \quad .. (2.31)$$

where

$\sigma(w)$ is the ac conductivity and is expressed as

$$\sigma(w) = \frac{ne^2}{m^*} \frac{\tau}{1 + w^2 \tau^2} \quad .. (2.32)$$

Here, τ is the momentum relaxation time,

c is the velocity of light, and

K_o is the free space permittivity.

It was pointed out by Rollin [11] that the value of τ used should be appropriate to the excited carriers with energy $E = \hbar w$.

When $w\tau << 1$ the value of α will be independent of frequency while for $w\tau >> 1$ it decays as w^{-2}. There is a turn-over point at $w\tau = 1$ when the decay starts to occur. For a typical sample of InSb [1] with $\tau = 8.5 \times 10^{-13}$ sec., the value of λ, for $w\tau = 1$, is 1.6 mm and, for $n = 5 \times 10^{13}$ cm^{-3} and a mobility of 10^5 $cm^2.(V.sec.)^{-1}$, the corresponding value of α is 22 cm^{-1} for λ = 1 mm falling down to 0.3 cm^{-1} at λ = 100μm.

The short wavelength cut-off of the free carrier absorption is defined by the relaxation time τ. For good conductors as in Cu and Al, τ is very short ~~indeed~~ $\sim 10^{-14}$ sec, so that the value of w given by $\frac{1}{\tau}$ is very large and the absorption coefficient has nearly a uniform distribution throughout the whole infrared spectrum. For Cu with $\sigma_{dc} = 5.8 \times 10^5$ $(\Omega.cm)^{-1}$ and $\tau = 1.5 \times 10^{-14}$ sec, the free carrier absorption is flat down to less than 20 μm wavelength. Therefore, for selecting a material as a thin film broad-band absorber down to 100 μm, say, τ should not be greater ~~than 10 (Ω.cm)~~ 10^{-13} sec.

2.2.2.3. Response time

The radiation absorbed by free carriers is eventually delivered to the lattice via the effective coupling between the free carriers and the lattice. The response time is defined as the rate of increase of the mean carrier energy E w.r.t. the power input W, i.e,

$$\tau_r \cong \frac{dE}{dW} \qquad .. (2.33)$$

If the energy relaxation is caused by interaction with phonons, τ_r is related to the photon scattering time τ_p by

$$\tau_r \cong \frac{k\,T\,\tau_p}{2\,m^*\,u^2} \qquad .. (2.34)$$

where u is the phonon velocity,

k the Boltzmann constant and T is the absolute temperature.

τ_r and τ_p can be estimated from experiments on the change in mobility with applied voltage [12], since

$$\frac{1}{\mu}\frac{d\mu}{dW} = \frac{1}{E}\frac{dE}{dW} = \frac{\tau_r}{n\,v\,k\,T} \qquad .. (2.35)$$

n is the carrier concentration and v is the element volume.

An alternative method to determine τ_r was used by Kinch and Rollin [13] that since at low temperature, the ionized impurity scattering is dominant then

$$\mu \alpha T_e^{3/2} \qquad .. (2.36)$$

where T_e is the electron temperature. Using $S = \frac{1}{\mu}\frac{d\mu}{dW}$ we find

$$S = \frac{3}{2T_e} \cdot \frac{dT_e}{dW}$$

$$= \frac{3}{2T_e.G} \qquad .. (2.37)$$

$\frac{dW}{dT_e} = G$ represents the coefficient of thermal coupling between the carriers and the lattice.

Estimates of the carrier temperature T_e can be made from the Hall mobility measurements vs temperature and for InSb, $T_e \gtrsim 1^oK$. Knowing S and T_e, the coefficient G can be determined. The time response τ_r will then be given by

$$\tau_r = \frac{3\,n\,k\,v}{2.G} \qquad .. (2.38)$$

where $\frac{3}{2}\,n\,k\,v$ represents the classical value for the thermal capacity of the carriers which is very close to the actual value.

An estimated value for G was found to be $\sim 50\mu w.^oK^{-1}$ and $\tau_r \sim 3 \times 10^{-7}$ sec. Where an accurate value of τ_r was measured

directly using pulse techniques and found to be 10^{-7} sec.

2.2.2.4. Effect of magnetic field on hot electron detection

For the materials used for hot electron detectors with low effective mass and high mobility, the presence of magnetic field affects greatly the hot electron detection. For InSb with fields B given by $\mu B > 1$ which corresponds to $B > 1kG$, quantization of electron motion occurs and the conduction band starts to split into a series of sub-bands or Landau levels. The physical meaning of this is that the motion of electrons will be composed of a rotation of electrons in a plane perpendicular to the field direction, while in the field direction the motion unaffected by the magnetic field. The separation between the sub-bands is $h\nu$, where ν is the cyclotron frequency and is given by

$$\nu = \frac{eB}{2\pi m^*} \qquad .. (2.39)$$

e is the electronic charge.

The effect of a magnetic field is to reduce the interaction between impurities. For a field of few kilogauss, the carriers will start to occupy the lowest impurity states at low temperatures. At $1.35^{o}K$, the majority of the carriers will occupy the impurity states, this together with the magneto-resistance effect can increase the resistance of the element by several orders of magnitudes.

The advantages of the magnetic field on the hot electron detection can then be summarized in the following

(i) Increase in responsivity due to the increase in the voltage across the element for the same bias current (relations (2.26) and (2.28)).

(ii) Tuning the detector to any radiation wavelength by varying the magnetic field. The detected radiation frequency will be

defined by (2.39), and the response will be sharp having a line-width of the order of $\frac{1}{2\pi\tau}$, where τ is the momentum time. If the detector is tuned to short wavelengths at which the absorption is very weak, in the absence of the magnetic field, the resonance absorption will be comparable to the low frequency value. Thus, this should improve the hot electron photoconductive effect. Such tuned detectors is useful in line detection especially when the radiation noise is dominant.

Typical values of the responsivity and response time were calculated by Putley [1] from the voltage-current curve under the magnetic field which are

$$\mathcal{R} = 3 \times 10^{4} \text{ V/W} \quad , \quad \tau_r \cong 1.0 \times 10^{-8} \text{ sec.}$$

2.3. Thermal detectors

These types of detectors depend for their operation on the lattice temperature modulation caused by the modulated incident radiation together with the existance of a finite value of temperature coefficient of resistance produced by the activated conduction mechanism involved at the operating temperature. Several materials are successfully used as a thermal bolometer such as Ge, Si, GaAs and Carbon and also we can include the superconducting bolometers as far as the lattice temperature variation is concerned in spite of the dissimilar design and mechanism involved.

For many purposes in modern spectroscopy and astronomical work, a broadband detector (100-2000μm) is needed. Thermal detectors offer the best solution. Many detectors have been constructed in the past. They included the superconducting bolometer of Andrews et al.[14] and of Martin and Bloor [15], the carbon resistor bolometer of Boyle and Rodgers [16] and the cooled Ge bolometer first described by Low [17]. The construction of the superconducting bolometer is complicated and

it needs super control of the bath temperature, in addition to its long response time ($\sim$ 1 sec.). These are considered disadvantages of these bolometers. The measured noise value of the carbon bolometer [16] indicates that there is large noise in excess of the calculated value and was attributed to current noise arising either from the difficulty of producing a good contact or intrinsic noise in the element itself.

Probably the most successful elements for thermal detectors are Ge and Si. The dependence of responsivity upon the spectral distribution of infrared radiation suggests using an absorbing layer coupled efficiently to the element itself and can have a large and uniform absorption throughout the infrared spectrum. However, the absorbing layer will add to the thermal mass of the element and hence a longer time response will result. Apart from that, the Ge itself can have an adequate absorption in a wide band region of the spectrum especially in the millimetre range depending on the doping characteristics and hence the mechanism involved. For instance, singly doped Ge with Ga acceptors was used by Low [17] although no concentration was mentioned. P-type compensated Ge (Ga $\sim 9 \times 10^{15}$, Sb $\sim 1.0 \times 10^{15}$ cm^{-3}) was tested and used by Zwerdling *et al.* [4,18]

2.3.1. Responsivity and response time

In thermal detectors, the temperature coefficient of resistance α is the responsible factor for the detector response. This factor depends on the thermal activation energy ε of the dominating conduction mechanism. For fixed activation energy, α is strongly dependent on lattice temperature (variation as T^{-2}). This illustrates the need of cooling down the element to the lowest temperature possible (usually pumped helium temperatures). The definition for α is

$$\alpha = \frac{d \ln R}{dT} = \frac{1}{R} \frac{dR}{dT} \qquad .. (2.40)$$

where R is the element resistance.

For the dominating electrical conduction at temperature T and activation energy ε , the resistance could be written as [19]

$$R(T) = R_o \exp \frac{\varepsilon}{kT} \quad .. (2.41)$$

where R_o is the resistance when $\frac{1}{T} \sim 0$

It follows from (2.40) and (2.41) that

$$\alpha = - \frac{\varepsilon}{kT^2} \quad .. (2.42)$$

The sign of α depends whether R increases or decreases with temperature. It is negative for semiconductors and usually positive for metal bolometers. α can be determined for any given bolometer by plotting ln R vs $\frac{1}{T}$ for the temperature region of interest. This should give a straight line whose slope is $\frac{\varepsilon}{k}\,^{o}K$ which defines the activation energy ε and hence α.

The actual ac voltage responsivity $\mathcal{R}(w)$ (volts/watt) using the electro-thermal parameters was discussed in detail by Zwerdling et al.[18] and given by

$$\mathcal{R}(w) = \frac{\alpha . V . \epsilon . F}{\mathcal{G}_e (1+w^2 \tau_r^2)^{\frac{1}{2}}} \quad .. (2.43)$$

Here V is the voltage across the element, ϵ is its emissivity.

F is called the "static transfer function" and is given by

$$F = \frac{R_L}{R_L + R} \quad .. (2.44)$$

R_L is the load resistor connected in series with the detector element of resistance R.

$\mathcal{G}_e$ is the effective dynamic thermal conduction to the heat sink and is expressed as

$$\beta_e = \beta_d - \alpha P B \qquad .. (2.45)$$

$\beta_d = \frac{dP}{dT}$ is the dynamic thermal conduction and is obtained from the slope of the curve plotted between the dc power dissipation P and the element temperature T at the operating temperature of the element. The term $\alpha P B$ arises from the electro-thermal interaction in which

$$B = \frac{R_L - R}{R_L + R} \qquad .. (2.46)$$

$\tau_r = \frac{C}{\beta_e}$ is the response time of the bolometer of thermal capacity C. For Ge, the appropriate formula for C is given by (20,17,18)

$$C = 6.8 \times 10^{-6} \cdot T^3 \cdot v \qquad .. (2.47)$$

v is the element volume.

For detectors working at infinite load (constant current) $B = F \simeq 1$ and an ultimate responsivity is obtained. τ_r is the determining factor for the maximum speed ω of the bolometer. The cut-off frequency f_c is defined as

$$f_c = \frac{1}{2\pi \tau_r} \qquad .. (2.48)$$

Equations (2.42) and (2.47) show the great improvements in responsivity and response time one can achieve by cooling the element to the lowest operating temperatures (assuming that the variation in γ_e is small). An improvement in τ_r can also result by reducing the element volume v to the smallest practicable size. On the other hand, reducing v will decrease the total absorbance resulting in a decrease in responsivity so that a compromise must be made.

For optically thick crystals, the emissivity ϵ is simply expressed as

$$\epsilon = (1 - r) \qquad .. (2.49)$$

where r is the single surface reflection coefficient.

If the crystal is not optically thick, (2.49) should be replaced by equation (2.17) given before for the quantum efficiency η.

The responsivity expression (2.43) may take another form depending on how the element resistance is formulated as function of temperature as found by experiments. Low [17] has deduced an empirical relation for his Ga doped Ge detector from measurements between 1.1 - 4.2^{o}K, which is

$$R(T) = R_o \left(\frac{T_o}{T} \right)^A \qquad .. (2.50)$$

where T_o, T are the bath and the element temperatures respectively.

A is a constant depending on the element and doping situation and should be measured for each bolometer.

From (2.50), the temperature coefficient of resistance is then,

$$\alpha = \frac{1}{R} \frac{dR}{dT} = \frac{-A}{T} \qquad .. (2.51)$$

Comparing (2.51) and (2.42) we find that A replaces $\frac{\epsilon}{kT}$.

In equation (2.43), if we consider for simplicity the infinite load, zero frequency and unity emissivity operation, then we have

$$R = \frac{\alpha V}{\mathcal{G} - \alpha P} \qquad .. (2.52)$$

For an element fed by a dc power P and linked to the heat sink bath via a thermal conduction $\mathcal{G}$, resulting in a temperature rise $\Delta T = (T - T_o)$, then

$$P = \mathcal{G} (T - T_o) \qquad .. (2.53)$$

Then at the operating point on the load curve, the voltage V(T) and the current I(T) will be given by

$$V(T) = (\mathcal{G} R(T - T_o))^{\frac{1}{2}} \qquad .. (2.54)$$

$$I(T) = (\mathcal{G} R^{-1} (T - T_o))^{\frac{1}{2}} \qquad .. (2.55)$$

Substituting for α and V in (2.52) and introducing the parameter $\emptyset = \frac{T}{T_o}$, we get for the responsivity

$$\mathcal{R}_{(\emptyset)} = \left\{ \frac{A^2 (\emptyset - 1)}{\left[(A+1)\ \emptyset - A\right]^2 \emptyset^A} \right\}^{\frac{1}{2}} \left[\frac{R_o}{T_o \mathcal{G}(T_o)} \right] \qquad .. (2.56)$$

Excluding the second term in R.H.S. which is constant for constant bath temperature, then for each value of A, the responsivity has a maximum value if it is plotted as function of $\emptyset$. Therefore, the last expression is useful in determining the temperature for maximum responsivity once A is determined.

A third and very useful expression for the responsivity was given by Jones [20]. This depends only on the electrical parameters of the detector. The zero frequency responsivity and unity emissivity is given as

$$\mathcal{R} = \left(\frac{Z - R}{2V} \right) . U. \qquad .. (2.57)$$

Measurements of the V-I characteristics of the mounted bolometer, (2.57) can be evaluated at any operating point, where

$Z = \frac{dV}{dI}$ is the dynamic impedance of the element,

$R = \frac{V}{I}$ is the static element resistance,

U is called the "dynamic transfer function" and is defined as

$$U = \frac{R_L}{R_L + Z} \qquad .. (2.58)$$

Expression (2.57) is very simple and allows rapid evaluation of ℜ for any bias current that permits selecting the bias current for optimum conditions. Furthermore, this expression is more general than (2.43) or (2.56) in a sense that it takes into account the actual non-linearity of the mounted element whatever its cause, i.e., there may be another mechanism that adds to the non-linearity of the detector characteristics and contributes to the actual responsivity. For instance, there may exist a hot carrier effect and subsequent impact ionization when the crystal is biased especially in the singly doped elements. While equations (2.43) and (2.56) only consider the lattice temperature variation through the parameter α which is usually deduced from measurements in the ohmic region. A determination of the identity of Jones' expression with the other two comes through the measurements of the V-I curve under fixed lattice temperature. If the operating point lies in the ohmic region when the lattice temperature is held constant, then the three expressions should be identical.

2.3.1.1. Determination of the operating conditions

After selecting and designing the bolometer element and mounting it for operation, a measurement of the V-I characteristics

allows to plot the responsivity on the same graph as a function of bias current using Jones' formula. A maximum responsivity will be observed which defines the appropriate region for detector biasing.

First, to determine the bias current for maximum responsivity, we draw a vertical line from the peak responsivity to the required operating point "O" on the V-I curve as shown in Figure (2.1) from which a line can be drawn connecting O to the point on the V-axis representing the value of the bias battery. The slope of this line is equal to R_L required to be connected in series with the bolometer. However, in some cases, the peak responsivity does not represent the optimum conditions (min. NEP)[18]. In this case higher and lower values of R_L should be tried until an optimum condition is reached.

Knowing the element resistance $\frac{V}{I}$ at the operating point, the temperature could be obtained from the R-T plot at low temperatures. The temperature coefficient of resistance $\alpha = \frac{-\epsilon}{kT^2}$ can also be known from $\ln R - \frac{1}{T}$ plot and the known operating temperature. The thermal capacity of the element is also obtainable if T is known.

To plot the thermal conduction of the connecting leads as function of temperature, the measured load curve can be used to plot P vs R and hence P vs T using the R-T plot. Then at any operating temperature $\mathcal{G}_d = \frac{dP}{dT}$ and hence $\mathcal{G}_e = \mathcal{G}_d - \alpha PB$ is obtained. P vs R is also useful to determine the amount of background radiation received by the element [18] by plotting P-R with and without radiation (a cooled blank should be used). The difference in P for the same R should give the background radiation power absorbed by the element. Furthermore, if these measurements are done using a calibrated black body source of known power output, an estimate for the element emissivity ϵ can be found.

The load curve data, i.e. R, Z and P are also able to relate the thermal temperature coefficient α and the thermal conduction as

follows

$$\frac{\gamma_d}{\alpha P} = \frac{Z + R}{Z - R} \qquad .. (2.59)$$

so that, knowing either α or γ_d, the other can be obtained.

Equation (2.59) also yields the following useful information; in the part of the V-I curve in which Z is positive, the R.H.S. of (2.59) is always greater than unity, in other words $\gamma_d > |\alpha P|$ in this region. While if Z is negative than $\gamma_d < |\alpha P|$, and the point of maximum voltage is reached when $\gamma_d = |\alpha P|$ [20]. This can give a picture of the degree of non-linearity desired for a given power input to the detector. It is sometimes advantageous to use small power input for biasing associated with certain degree of non-linearity in the V-I curve. In this case smaller thermal conduction should be used. This will improve the responsivity but with some sacrifice on the time response. Equation (2.59) was obtained by equating both responsivity expressions, the load curve data and the electro-thermal data in which case the dynamic impedence Z should represent the lattice temperature effect only as we mentioned.

2.3.1.2. Measurement of responsivity and response time

The zero frequency responsivity can be calculated using either Jones' formula (2.57) or using (2.52) which requires a knowledge of α and γ_d. However, in spite of the simplicity and generality of Jones' formula at zero frequency, it becomes more difficult to calculate at a given frequency w because of the fact that Z(w) becomes complex. A direct way of measuring the ac responsivity by purely electrical means was given also by Jones [20] of what he called the bolometer bridge. This method can be described by considering the bridge shown in Figure (2.2), one arm of which is the mounted bolometer connected in series

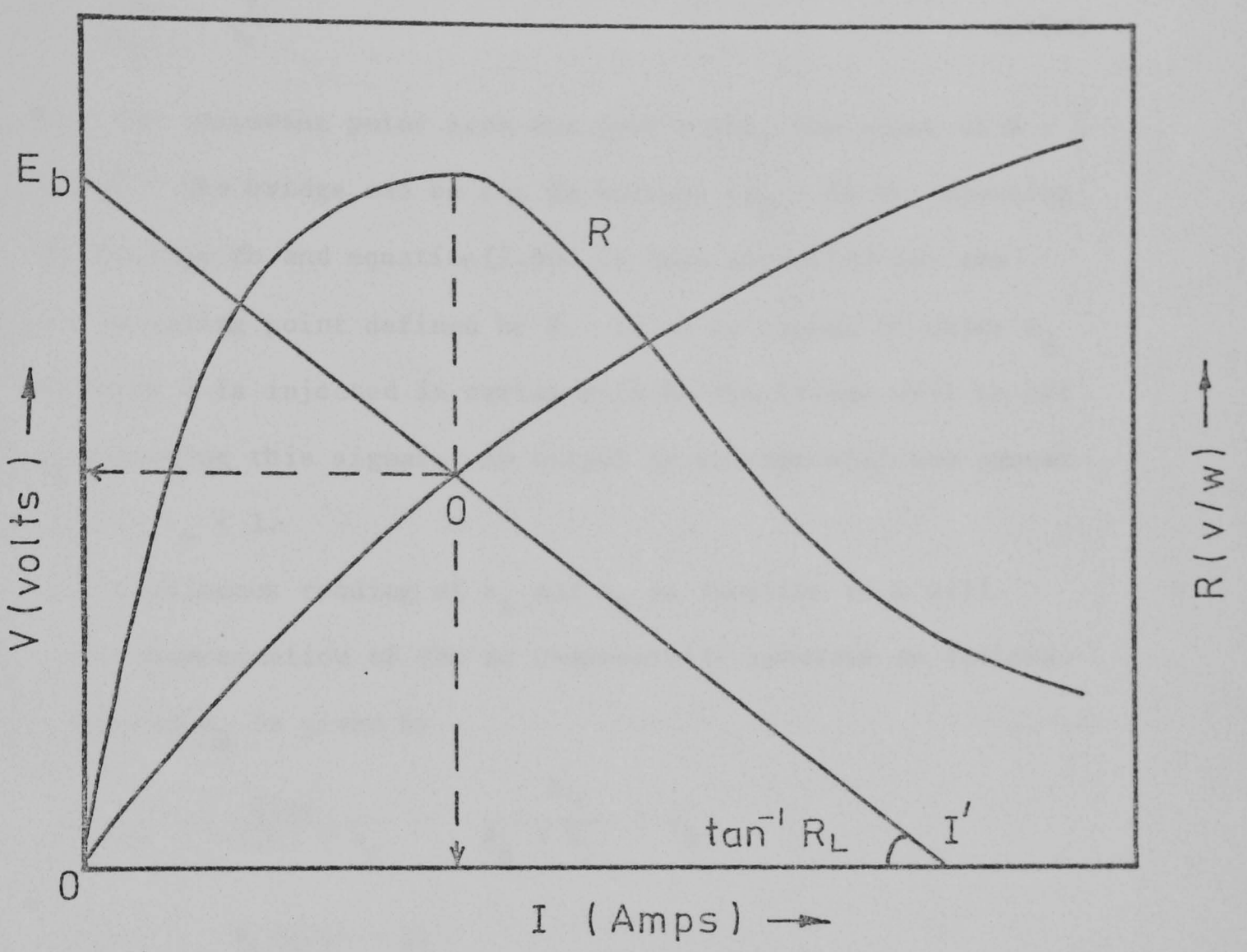

Figure 2.1. Determination of the operating point in thermal bolometers

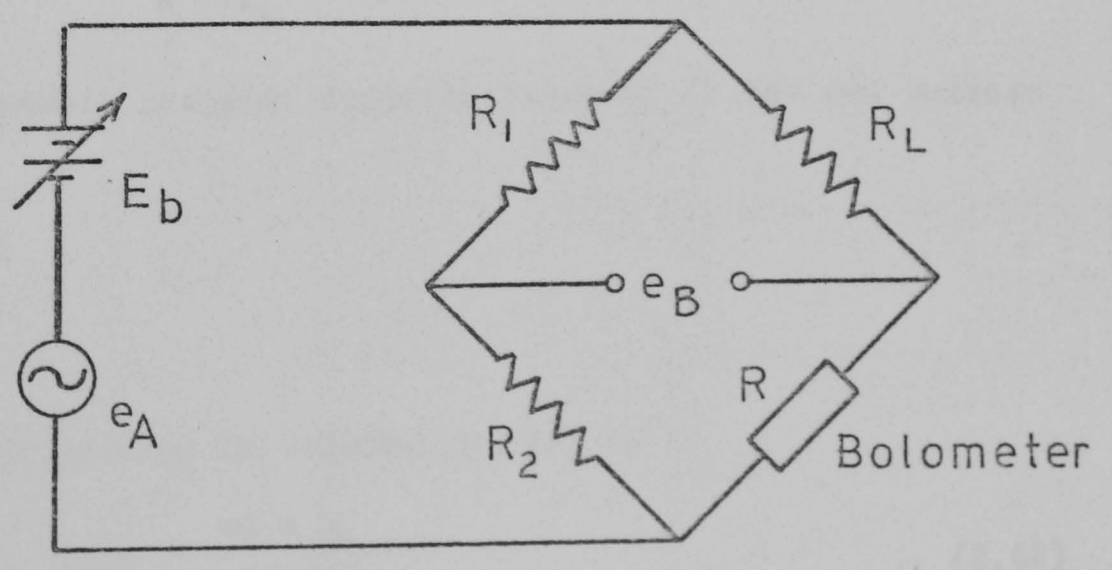

Figure 2.2. Bolometer bridge for determination of the responsivity and its spectrum for a given detector

with R_L. R_1 and R_2 are chosen such that

$$\frac{R_1}{R_2} = \frac{R_L}{R} \qquad .. (2.60)$$

Selecting the operating point from the load curve, the value of $R = \frac{V}{I}$ is obtained. The bridge can be set in balance ($e_B = 0$) by adjusting the bias voltage Eb and equation (2.60) is thus satisfied for the required operating point defined by R. If an ac signal of value e_A and frequency w is injected in series with Eb the bridge will be off balance regarding this signal. An output ac voltage will now appear as e_B if $w \tau_r < 1$.

Continuous reading of e_A and e_B as function of w will enable the determination of the ac responsivity spectrum as follows. The ac voltage e_B is given by

$$e_B = \left(\frac{Z(w)}{Z(w) + R_L} - \frac{R_2}{R_1 + R_2} \right) e_A$$

$$= \frac{R_L (Z(w) - R)}{(Z(w) + R_L)(R + R_L)} \; e_A \qquad .. (2.61)$$

Introducing the transfer function $T(w) = \frac{e_B}{e_A}$ we find

$$T(w) = U. \; \frac{Z(w) - R}{R + R_L}$$

where U is the dynamic transfer function given by (2.58) and defined as

$$\frac{R_L}{R_L + Z(w)}$$

then the responsivity $\mathcal{R}(w)$ is related to T(w) as

$$\mathcal{R}(w) = T(w) \; . \; \frac{R + R_L}{2V} \qquad .. (2.62)$$

Thus knowing $T(w) = \frac{e_B}{e_A}$, we can plot $\mathcal{R}(w)$ vs w and hence

the responsivity and the response time can also be found.

It should be noted here that the responsivity determined using this method does not consider any specific absorption mechanism for i-r radiation, and hence the element emissivity, but only considers the voltage responsivity arising from the modulation of the dc power input (it would not work, of course, for a photoionization detector working in the ohmic region).

Using the above method together with measuring the spectral dependence of the absorption coefficient will enable nearly all the required information about the actual radiation performance and emissivity to be obtained.

An alternative ideal and more general method is to use a calibrated black body source whose radiation power is modulated with a variable speed motor. The output ac voltage of the crystal can be measured and hence the responsivity and time response. Knowing the dc, unity emissivity responsivity from Jones' formula, a value of ϵ can be found. This method, however, requires good knowledge of the emissivity of the "blackbody" and the exact spectral function of the cooled filters used.

2.4. Detector Noise

Apart from the difficulties in detecting far infrared radiation mentioned at the beginning of this chapter, various types of noise are present. Some of these are unavoidable, but optimisable, while the others can be avoided or minimised by the proper design and construction of the detector.

2.4.1. Fluctuations in the background radiation

This is unavoidable noise, which, for ideal receivers, must limit the sensitivity of a given detector, especially for the high

frequency side of the infrared spectrum. Proper design of cooled band pass filters, for the desired frequency band, is essential to minimise this noise.

For photoionization detectors, if the mean rate of arrival of background photons is J, and having an rms fluctuations spectrum ΔJ which is effective in producing corresponding change in the number of free conducting carriers, then[11]

$$\overline{\Delta J}^2 = \frac{4(k\,T_b)^3}{c^2 h^3} \cdot \alpha \cdot \cos\theta \cdot A \cdot \Delta f \cdot \int_0^\infty \frac{x^2\, e^x}{(e^x - 1)^2} \cdot \eta(\nu)\, dx \quad .. (2.63)$$

where

T_b is the background temperature, α is the solid angle through which a detector of area A receives radiation in a direction θ to its normal.

$$x = \frac{h\nu}{kT_b}$$

$\eta(\nu)$ is the quantum efficiency spectrum,

Δf is the bandwidth of the following system,

c and h are the speed of light and the Planck constant respectively. If cooled filters are used, the integration limits must be modified accordingly. This together with the solid angle α and A have to be considered to minimise this noise.

If $h\nu >> k\,T_b$, where ν is the detected radiation frequency, the integral can be easily performed. Otherwise, tabulated functions must be used.

For detectors which respond to energy rather than photons, such as the hot electron and thermal detectors, the corresponding mean

square energy fluctuations of the background radiation can be found by writing

$$\overline{\Delta P}^2 = (h\nu)^2 \cdot \overline{\Delta J}^2 \qquad .. (2.64)$$

This leads to an expression of the form[1]

$$\overline{\Delta P}^2 = \frac{4(kT_b)^5}{c^2 h^3} \cdot \alpha \cos\theta \cdot A \cdot \Delta f \int_0^\infty \frac{x^4 e^x}{(e^x-1)^2} \eta(\nu) \, dx \qquad .. (2.65)$$

Again, if $x >> 1$, the last integral can easily be evaluated. If $x << 1$ tabulated functions have to be used. Also, the integration limits have to be modified by the inserted cooled filters. If the filters have a non-uniform spectral function $f(\nu)$, then this function must be included in the integrals of (2.63) and (2.65). If (2.65) is to be applied to thermal bolometers, the quantum efficiency $\eta(\nu)$ represents, in this case, the emissivity of the detector element.

The above results apply strictly to a detector in thermal equilibrium, however, they have been applied to a detector cooled to a temperature much lower than the background temperature[21,22].

2.4.2. Thermal noise - Johnson and phonon noise

These types of noise are also unavoidable and should dominate, for a blanked detector, all other types of noise if the detector element is perfectly built.

2.4.2.1. Johnson noise

This noise is associated with the static resistance R of the element at a given temperature T. The mean square noise voltage created is given by

$$\overline{e_j^2} = 4k\,TR \cdot \Delta f \quad volts^2 \qquad .. (2.66)$$

where k is Boltzmann constant = 1.38×10^{-23} $J.^{o}K^{-1}$

Δf is the frequency bandwidth of the following stage.

As a unified measurement, we usually consider $\Delta f = 1Hz$. The noise voltage spectrum is independent of frequency from dc up to the frequency given by the reciprocal of the momentum relaxation time ($\sim 10^{12}$ Hz).

2.4.2.2. Phonon noise

Thermal detectors depending mainly on lattice temperature variation are always linked to the heat sink via a finite effective thermal conduction $\mathcal{G}_e$. The power flow through this thermal link due to absorption of radiation as well as the dc field is usually accompanied by the so-called phonon noise. For a crystal temperature T the noise power appears to be

$$p_p = 2T\sqrt{k\,\mathcal{G}_e} \quad \text{watts. Hz}^{-\frac{1}{2}} \qquad .. (2.67)$$

$\mathcal{G}_e$ is given by (2.45).

In a hot electron detector, this type of noise is also present due to the existence of a finite thermal conduction between the electron gas and the lattice as we discussed before. This will take the same form as (2.67) with the proper value of $\mathcal{G}_e$ and replacing T by the average temperature of the hot electron gas.

It is worth noting here, that, in thermal and hot electron detectors, the background fluctuation noise mentioned in section 2.4.1. can be included in the phonon noise formula given by (2.67) such that $\mathcal{G}_e$ will be replaced by $(\mathcal{G}_e + \mathcal{G}_r)$ where $\mathcal{G}_r$ is the coefficient of thermal coupling between the element and the background through the optical system used. This radiation conduction might well exceed the value of $\mathcal{G}_e$ depending on the solid angle and band pass filters used.

2.4.3. Low frequency noise

It is found that in some types of conductors, the resistance shows different sources of fluctuations. These fluctuations transfer to voltage noise when current passes through it. This resistance variation may be due to the surface conditions of the semiconductor and also dislocations in a single crystal [1].

The spectrum of the low frequency noise varies as $f^{-\alpha}$ where α is of the order of unity or may be greater. However, the exact mechanism causing such noise is poorly understood but in photoconductive devices it may be the dominant source of noise at frequencies as high as 1 kHz. The mean square noise current may take the form

$$\overline{i_f^2} = \int_{f_1}^{f_2} \frac{DI^B}{f^\alpha} \cdot df \qquad .. (2.68)$$

where $B \sim 2$, and D is a constant.

2.4.4. Generation-recombination noise

This source of noise arises from the fluctuation accompanying the generation and recombination of carriers in thermal equilibrium. Therefore, the balanced free carrier concentration will accordingly fluctuate thereby creating fluctuations in the conductivity. At low temperatures, this effect is enhanced by the large reduction of the conducting carriers controlling the overall conductivity.

For a semiconductor in thermal equilibrium, the G-R r.m.s. noise voltage can be expressed in the form [1].

$$e_g = 2 I R \left\{ \frac{\tau}{N_{eff}(1+w^2 \tau^2)} \right\}^{\frac{1}{2}} \text{ volts.Hz}^{-\frac{1}{2}} \qquad .. (2.69)$$

where

I is the current through the crystal, R is its resistance,

N_{eff} is the effective total number of carriers in the sample,

τ is the lifetime of the excess carriers produced by the fluctuations.

At very low temperatures such that the carrier concentration n is much smaller than the concentration of impurity centres, we have

$$N_{eff} = N = nv \qquad .. (2.70)$$

where v is the sample volume.

Equation (2.69) includes the fluctuations both in the rates of generation and recombination.

2.4.5. Signal fluctuations

If the fluctuations of the background radiation is eliminated in some circumstances, noise fluctuations can arise from the source signal itself due to fluctuations in the rate of emission of quanta. This can usually be found in detectors working at long wavelengths with narrow band pass filters especially when looking to background of low effective temperatures. Also for detectors used for line observation which respond to a very narrow frequency band.

2.4.6. Amplifier noise

In many cases, the noise of the following amplifier may limit the performance of a detector. In a low impedance detector when properly designed such that background and thermal noise are small, the performance will be limited by the preamplifier if the crystal resistance is less than the noise equivalent resistance of the preamplifier at the same crystal temperature. In practice this condition can be met for crystal resistance of the order of several kΩ for the best amplifiers available.

In the InSb hot electron detectors, the maximum value of the resistance for reasonable absorption would be less than 1 kΩ. Therefore,

a considerable improvement in the detectivity can be obtained by using a cooled step-up transformer [13]. The transformer will increase the element resistance as well as the voltage responsivity, but net improvements will be achieved to the overall system as long as the crystal equivalent resistance is still smaller than the amplifier equivalent noise resistance (provided that the transformer will contribute negligible noise to the system). However, if high frequency performance is required, the transformer will present restrictions to such application.

Considerable improvements could also be achieved by cooling the preamplifier down to liquid He temperature especially the first input stage including the first FET. This stage contributes much to the overall amplifier noise. FET amplifiers represent an advancement over the ordinary dipolar transistors regarding the noise characteristics together with the possiblility of cooling down associated with considerable improvement. Also FET's are superior to valve amplifiers used in the past for the fact that the latter are microphonic and have relatively large input capacitance which limit the ability of designing wide-band amplifiers.

2.5. Figures of merit for infrared detectors

The principal figures of merit for infrared detectors are:

2.5.1. Noise equivalent power(NEP)

This is defined as the r.m.s. value of modulated radiant power falling on the detector required to produce an r.m.s. signal to r.m.s. noise of unity $(\frac{S}{N} = 1)$. The post-detection electrical bandwidth, also called noise bandwidth, should be specified. The NEP varies in proportion to the square root of the electrical bandwidth, the smaller the bandwidth, the lower the NEP, and the better the

detector sensitivity. Usually NEP is given referred to a 1 Hz bandwidth, and expressed in units of watts. $Hz^{-\frac{1}{2}}$.

2.5.2. Detectivity

In most infrared-to- millimetre detectors, the NEP is proportional to the square root of the detector area. The detectivity D is the reciprocal of the NEP normalised to a detector area of 1 cm^2, and a 1 Hz electrical bandwidth. This is usually called normalised detectivity, thus

$$D = \frac{A^{\frac{1}{2}} \cdot B^{\frac{1}{2}}}{NEP} \qquad .. (2.71)$$

where A is the detector area in cm^2, and B is the post-detection bandwidth.

It should be distinguished here between the detectivity of a continuum blackbody source and of a monocromatic radiation of wavelength λ, and in addition, the modulation frequency also should be quoted. As an example, the detectivity, of a bolometer to a blackbody source of $300^{o}K$ at a chopping frequency of 200 Hz followed by a 1Hz bandwidth, is written as $D(300^{o}K, 200, 1)$.

2.5.3. Time Constant

This is the measure of the detector speed of response and is specified in units of seconds. It is always desirable for the time response to be short either in thermal or quantum detectors.

2.6. Sensitivity of an actual infrared detector

The sensitivity of an optical-to-millimetre incoherent detector is determined by summing all of the noise contributions, the most important of which has already been discussed. For example, we have for a thermal detector, $\overline{NEP}^{2}$ value of

$$\frac{}{NEP}^2 = \frac{4k\ T\ R}{\mathcal{R}^2} + \frac{4(k\ T_b)^5}{c^2 h^3} \cdot \alpha \cdot \cos\theta \cdot A \int_0^\infty \frac{x^4 \cdot e^x}{(e^x - 1)^2} \epsilon(\nu) dx$$

$$+ 4k T^2 \epsilon_e + \frac{D\ I^B}{\mathcal{R}^2 f^\alpha} R^2 + \frac{4 k T_o\ Req}{\mathcal{R}^2} \quad .. (2.72)$$

due to the contribution of Johnson, background, phonon, inverse frequency and preamplifier noise respectively,

where Req is the equivalent noise resistance of the preamplifier,

$\mathcal{R}$ is the responsivity of the detector,

$\epsilon(\nu)$ represents the spectral variation of the element emissivity,

the other symbols have the usual meaning as before.

CHAPTER II

REFERENCES

(1) Putley, E.H., Physica Status Solidi 6, 571 (1964)

(2) Burstein, E., G. Picus and N. Sclar, Atlantic City photoconductivity conference P.353 (John Wiley & Sons New York, 1956)

(3) Newman, R. and W.W. Tyler, Solid State Physics 8, 49 (1959)

(4) Zwerdling, S., J.P. Theriault and H.S. Reichard, Infrared Phys. 8, 135 (1968)

(5) Sclar, N. and E. Burstein, J. Phys. Chem. Solids 2 (1957)

(6) Koenig, S.H., Phys. Rev. 110, 986 (1958)

(7) Koenig, S.H., R.D. Brown III and W. Schillinger, Phys. Rev. 128, 1668 (1962)

(8) Lax, M., Phys. Rev. 119, 1502 (1960)

(9) Picus, G.S., J. Phys. Chem. Solids 23, 1753 (1962)

(10) Brown, D.A.H., J. Elect & Control 4, 341 (1958)

(11) Rollin, B.V., Proc. Phys. Soc. 77, 1102 (1961)

(12) Sladek, R.J., Phys. Rev. 120, 1589 (1960)

(13) Kinch, M.A., and B.V. Rollin, Brit. J. Appl. Phys. 14, 672 (1963)

(14) Andrews, D.H., R.M.Milton and W.D. Sorbo, J. Opt. Soc. Am. 36, 518 (1946)

(15) Martin, D.H. and D. Bloor, Cryogenics 1, 159 (1961)

(16) Boyle, W.S., and K.F. Rodgers, Jr., J. Opt. Soc. Am. 49, 66 (1959)

(17) Low, F.J., J. Opt. Soc. Am. 51, 1300 (1961)

(18) Zwerdling, S., R.A. Smith and J.P. Theriault, Infrared Phys. 8, 271 (1968)

(19) Fritzsche, H., Phys. Rev. 99, 406 (1955)

(20) Jones, R.C., J. Opt. Soc. Am. 43, 1 (1953)

(21) Putley, E.H. Infrared Phys. 4, 1 (1964)

(22) Low, F.J. and A.R. Hoffman, Appl. Opt. 2, 649 (1963)

CHAPTER III

CONDUCTION MECHANISMS OF Ge AT LOW TEMPERATURES

In this chapter, various aspects of the conduction mechanisms of Ge at very low temperatures are considered. These include the thermal behaviour of crystal resistivity for temperatures 4.2 - 1.5°K for n- and p-type samples, the galvanometric properties for the n-type sample and the hot electron phenomenon borne out by the dc measurements as well as the behaviour under magnetic field.

3.1. Thermal behaviour

In the two samples of Ge, n-type (Sb $\sim 5.5 \times 10^{16}$ cm^{-3}) and p-type compensated (Ga $\sim 9 \times 10^{15}$, Sb $\sim 1 \times 10^{15}$ cm^{-3}), the resistivity vs temperatures were measured for the temperature region 4.2 - 1.5°K. From this, the values of the activation energies for the two main conduction mechanisms were determined. The two samples differ in a way that the n-type sample, being in the intermediate concentration region, exhibits two different activation energies in this temperature region, as it is clear from the equation

$$\sigma = \sigma_{o2} \exp \frac{-\varepsilon_2}{kT} + \sigma_{o3} \exp \frac{-\varepsilon_3}{kT} \qquad .. (3.1)$$

The term containing ε_2 is not present in the p-type sample. The term containing ε_3 is present in both samples at low temperatures. This term was understood as the contribution from the activated hopping of carriers between localised centres as mentioned in the first chapter. Using (3.1), the values of ε_2 and ε_3 are obtainable from $\ln \sigma$ or $\ln \rho$ vs $\frac{1}{T}$ plot. These are shown in Figures (3.1) and (3.2) for the two samples. The slope of $\ln \rho$ vs $\frac{1}{T}$ for the dominating conduction mechanism is $\frac{\varepsilon}{k}$ from which ε can be evaluated. We found from the measurements that,

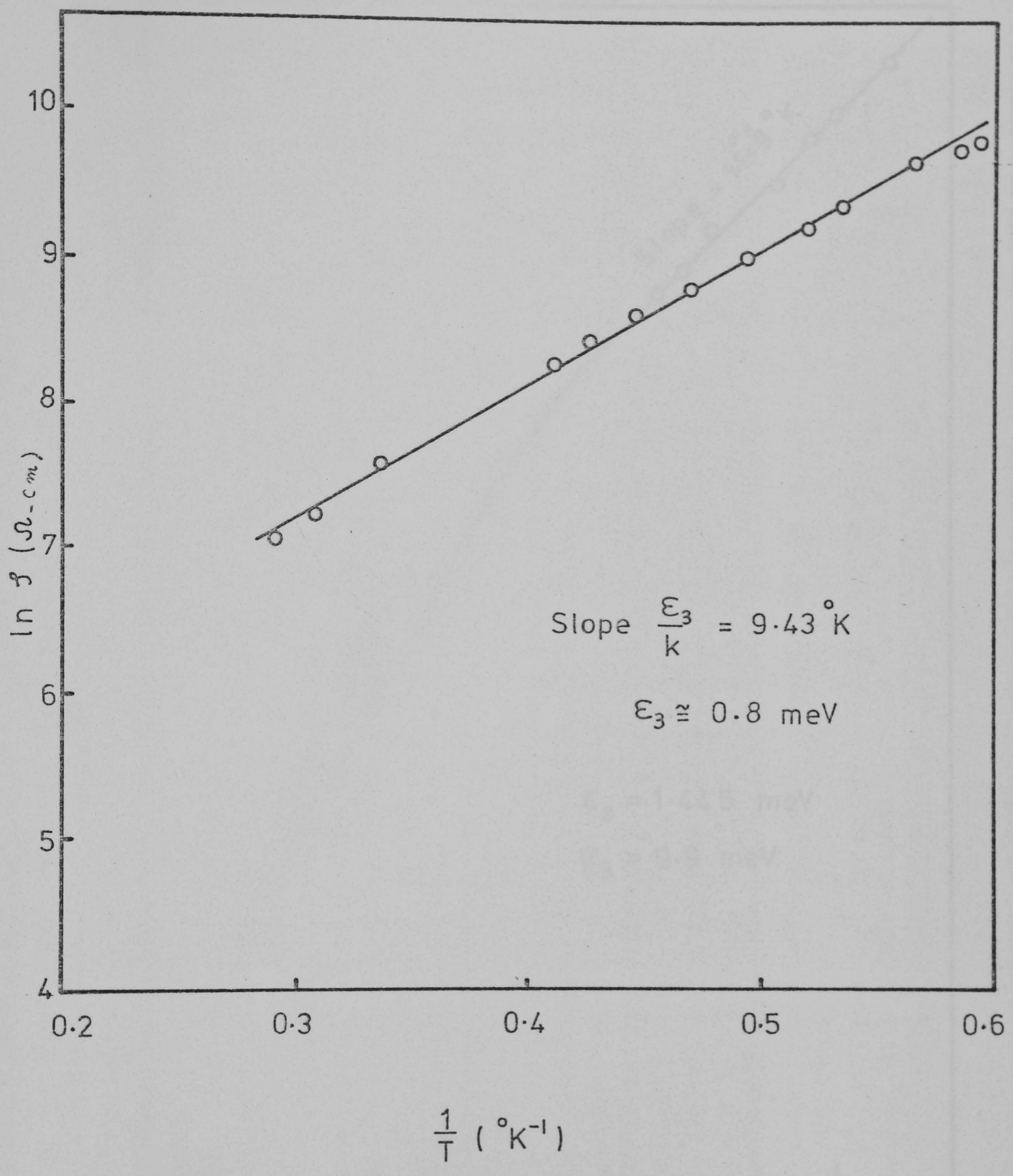

Figure 3.1. Determination of the activation energy ε_3 for p-type compensated Ge

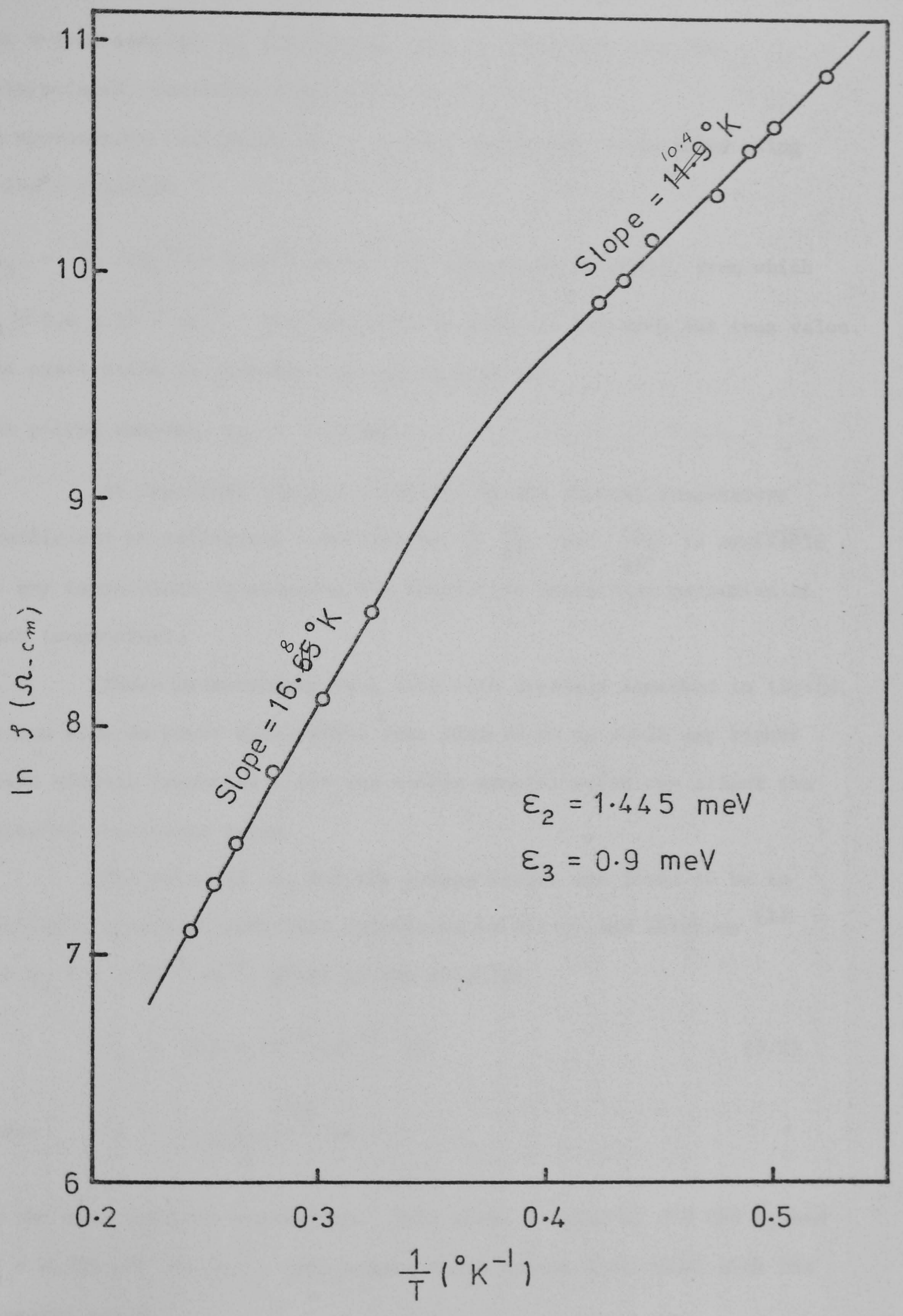

Figure 3.2. Determination of activation energies ε_2 and ε_3 for n-type Ge

for n-type sample: $\varepsilon_2 = 1.445$ meV and $\varepsilon_3 = 0.9$ meV, and the interpolated transition temperature is $2.27^{o}K$.

An approximate evaluation of N_A in this sample can be obtained using Price's relation

$2\varepsilon_3 = \frac{e^2}{\epsilon} (N_D^{1/3} - 2 N_A^{\frac{1}{2}})$ (valid for low concentrations), from which $N_A \cong 6.6 \times 10^{15}$ cm^{-3}. This value is in fact not far from the true value. The exact value is probably less as we will see.

for p-type sample: $\varepsilon_3 = 0.8$ meV

An important thermal parameter is the thermal temperature coefficient of resistance α defined by $\frac{1}{\rho}\frac{d\rho}{dT}$ or $\frac{-\varepsilon}{kT^2}$ is available at any temperature considering the respective conduction mechanism at that temperature.

These measurements were done with crystals immersed in liquid helium with dc power dessipation less than 10 nW to avoid any higher field effects (especially for the n-type sample) which may affect the measured resistance value.

The value of ε_3 for the p-type sample was found to be in excellent agreement with that calculated by Miller and Abrahams [1] for $N_A < 5 \times 10^{15}$ cm^{-3}, given by the relation

$$\varepsilon_3 = 2.5 \times 10^{-9} (d)^{-1} \text{ eV} \qquad .. (3.2)$$

where $d = (\frac{3}{4\pi N_A})^{1/3}$ cm

is the mean impurity separation. This gives a value of d = 298 Å, and $\varepsilon_3 = 0.838$ meV for the p-type sample which agrees quite well with the measured value.

3.2. Galvanometric properties

Galvanometric properties in the impurity conduction temperatures in Ge have been studied theoretically by several authors, for weak fields [2] and strong fields [3,4,5]. Experimental measurements on the Hall coefficient temperature dependence and magneto-resistance for doped semiconductors have been also carried out [6,7,8,9]. Scattering of carriers by impurities in magnetic fields was considered through observing the change in cyclotron resonance line-width [10,11]. In this section we describe measurements of the Hall coefficient for different values of magnetic fields and with a wide range of applied electric fields at 4.2 and 1.7°K. Carrier mobilities and transverse magneto-resistance were also deduced and discussed.

3.2.1. Sample and apparatus

The sample investigated was cut out from an antimony-doped Ge single crystal grown in <110> direction having impurity content of $\sim 6 \times 10^{16}$ cm^{-3}. The dimensions of the sample are $4.5 \times 1.5 \times 0.5$ mm^3, with the current flowing through the 4.5 mm length, and the Hall field was measured across the 1.5 mm width. The sample was polished and etched for about two minutes in CP4A solution before any soldering contacts.

The sample is then mounted in a long brass sample holder at the end of which there is a chamber for the crystal and two grooves for the electrical leads; one for the sample leads and the other for the magneto-resistance probe situated near the crystal. The sample holder considts of three solid faces and moveable one which can block or admit the background radiation to the sample. This movable face is connected to a thin stainless steel tube to outside the cryostat and vacuum sealed by an "O" ring and a nut. This allows the movements from outside

the cryostat when the helium is under pumping conditions. The sample holder is shown in Figure (3-3a).

The cryostat system consists of a superconducting magnet with an upper field limit of 50 kG used with a metal dewar of 30 litres capacity. The sample, when situated in the centre of the magnet near the bottom of the dewar, can face the radiation through two windows aligned with the magnet axis, Figure (3-3-b). (Only one window was used in this experiment). The magnet is suspended from the top plate of the dewar by means of three stainless steel tubes, they are also used to accommodate all the electrical leads including the magnet supply wires. A German silver light pipe of 2 cm diameter was mounted in front of the movable face of the sample holder through the magnet central hole which leads the radiation (through cooled 200μm short wavelength cutting filter) from outside the cryostat to the sample when the movable face is up).

The overall system with 20 litres of helium after fully pumping down to 7.5 torr ($T = 1.67^{o}K$) allows running over at least eight hours which was sufficient for lowest temperature measurements, after the $4.2^{o}K$ measurements were performed.

The measuring instruments used for the normal V-I characteristics are Fluke digital multimeters having voltage and current sensitivities of 0.1 mV and 0.1 μA respectively. The low level electric fields were supplied by a one volt standard supply from which the smallest voltage available is 1 mV. For measuring the Hall voltage a digital voltmeter with 0.01mV sensitivity was used. The magnetic field was measured by a calibrated magneto-resistance probe and checked by the calibrated magnet current supply.

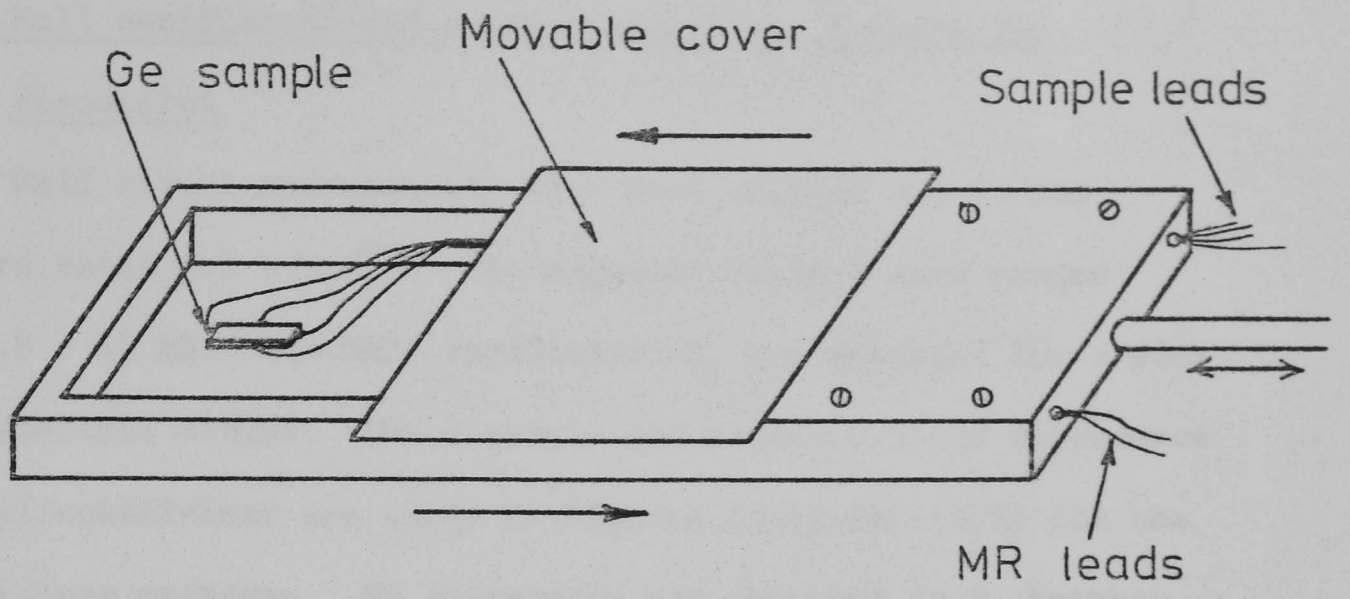

Figure 3.3.a. Sample and sample holder for Hall measurements

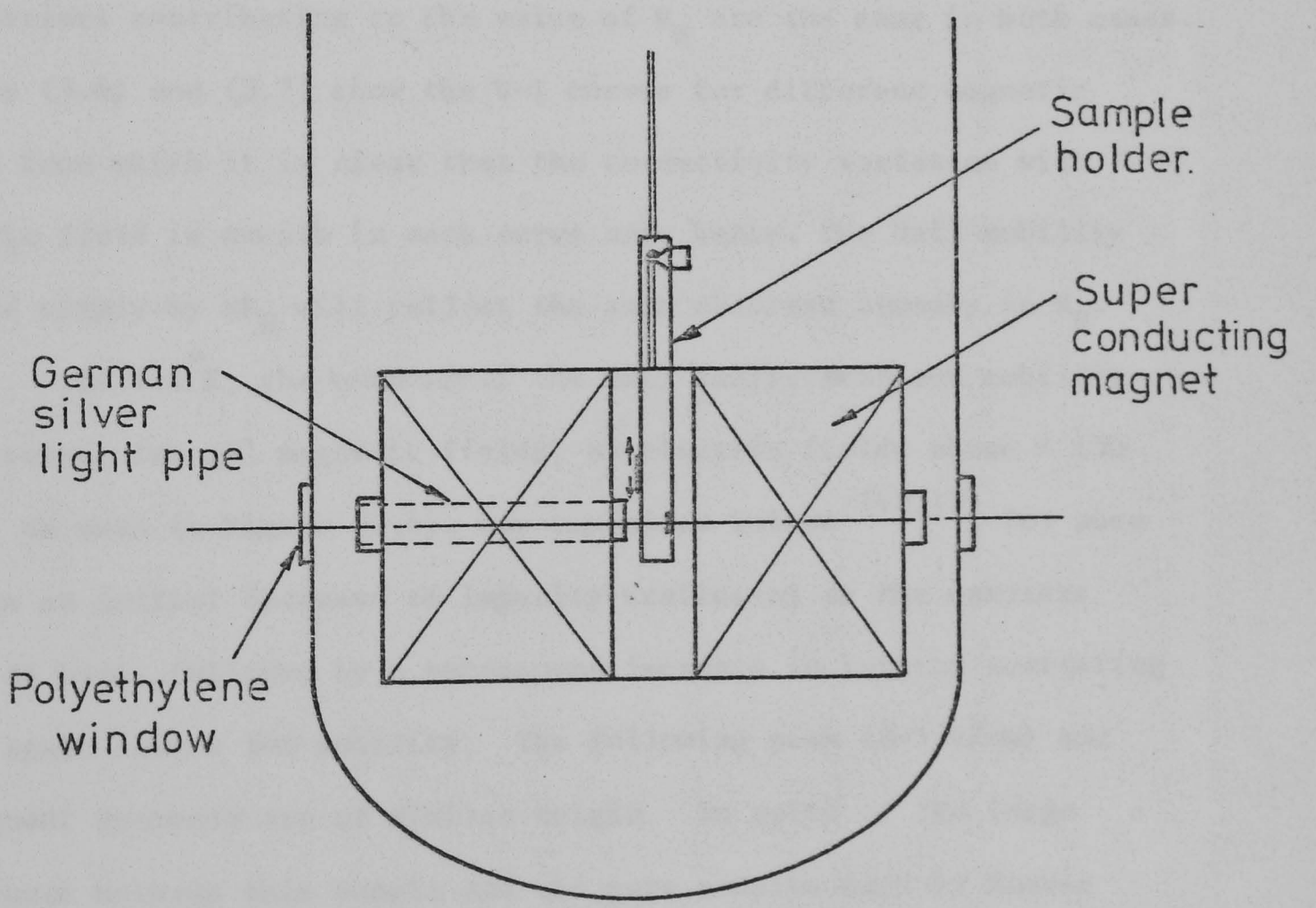

Figure 3.3.b. Superconducting magnet system used for Hall measurements

3.2.2. Hall coefficient and carrier mobility: results and discussion

Hall effect measurements have been carried out in the temperature range 4.2 - 1.7°K. The magnetic field H used ranges between 2.8 - 25 kG. The Hall coefficient R_H was measured for a wide range of electric fields. The electric and magnetic field dependence of the Hall coefficient are shown in Figures (3.4) and (3.5) for the two temperature extremes. No difference was observed in R_H between blanking and admitting radiation. At 1.7°K the ε_3 mechanism dominates, while at 4.2°K, the ε_2 mechanism dominates. However, the increase in R_H with H is about the same for both temperatures. This suggests that the carriers contributing to the value of R_H are the same in both cases. figures (3.6) and (3.7) show the V-I curves for different magnetic fields from which it is clear that the conductivity variation with electric field is smooth in each curve and, hence, the Hall mobility defined simply by σR_H will reflect the same observed anomaly in R_H.

At 4.2°K, the tendency of the Hall coefficient and mobility to increase, for all magnetic fields, at electric fields above ∿ 150 mV/cm, as seen in Figure (3.4), was explained before [12,13] for pure n-Ge as an initial decrease of impurity scattering as the carriers begin to heat, followed by a subsequent increase in lattice scattering which again lowers the mobility. The following peak (3-5 V/cm) and subsequent decrease are of similar origin. In spite of the large difference between this sample and the pure samples used by Koenig et al [13] for temperatures not less than ∿ 7°K, the main features still remain. The carrier concentration in Koenig sample is around 10^{13} cm^{-3} and the main conduction mechanism is that for the free conduction band carriers at the mentioned temperature. The scattering mechanism limiting the carriers mobility is shared between the impurity

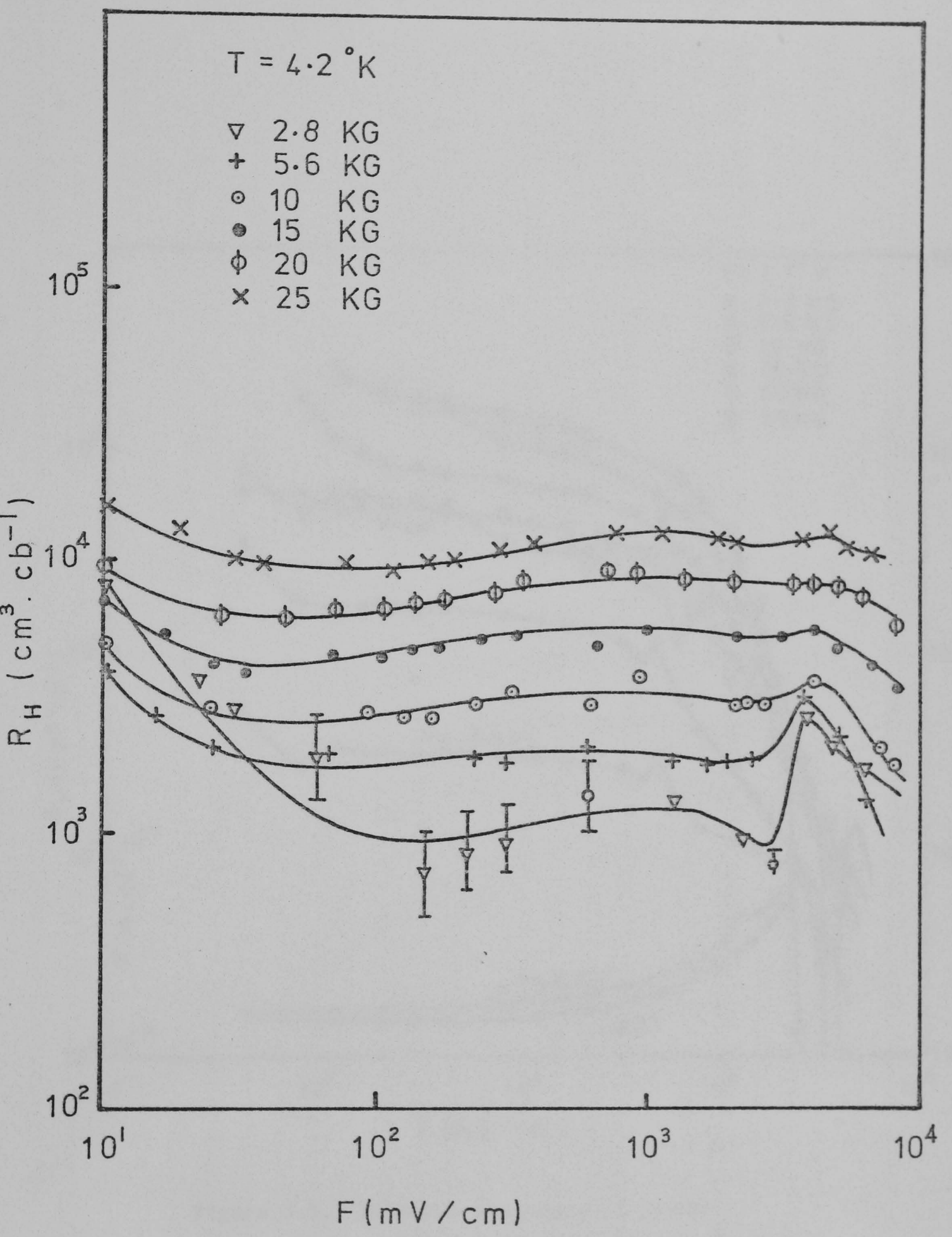

Figure 3.4. Electric and magnetic field dependence of R_H in n-type Ge at 4.2°K

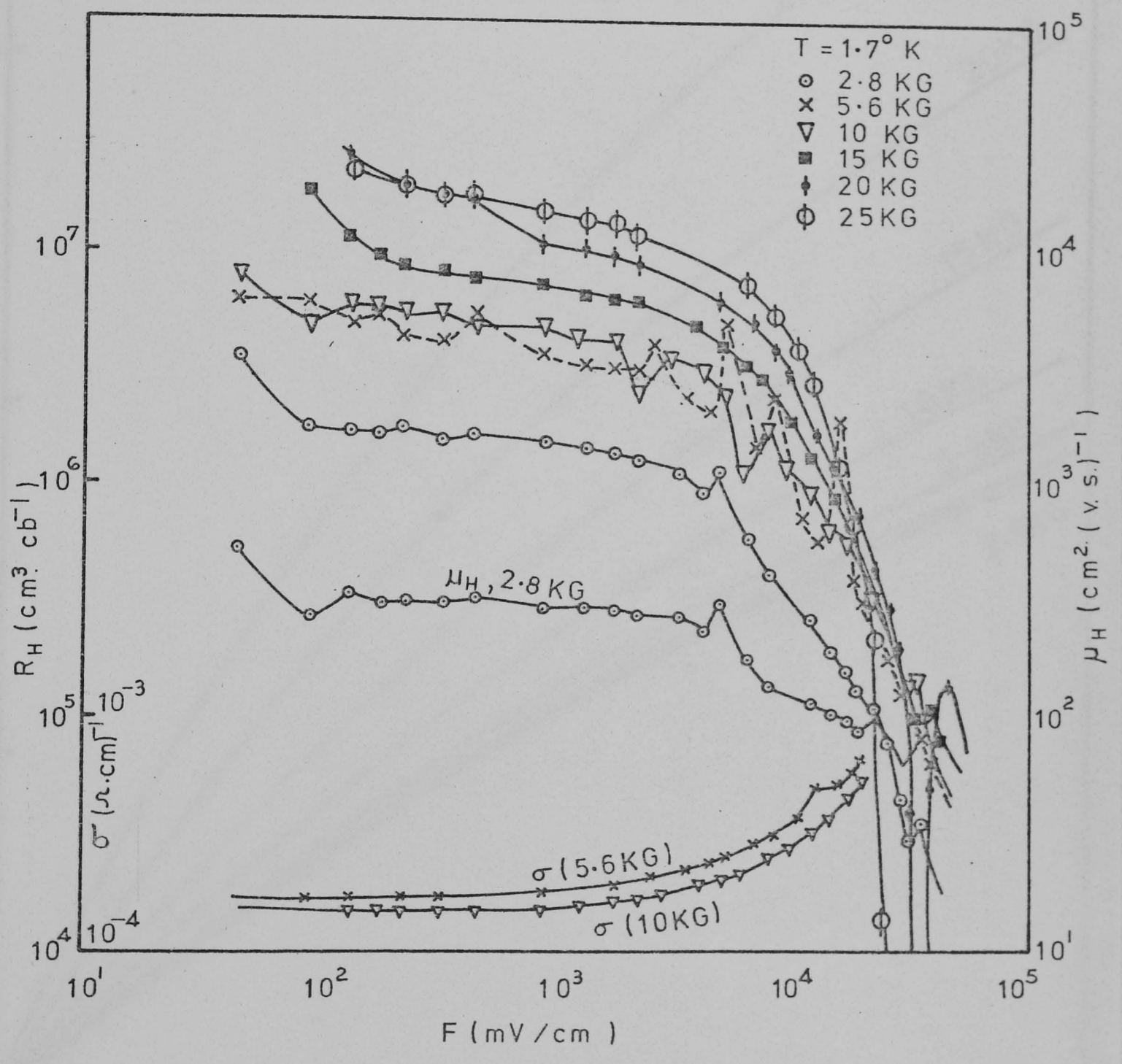

Figure 3.5. Electric and magnetic field dependence of the Hall coefficient R_H of n-type Ge at 1.7°K. The figure also shows the variation of μ_H at 2.8 kG and σ at 5.6 and 10 kG.

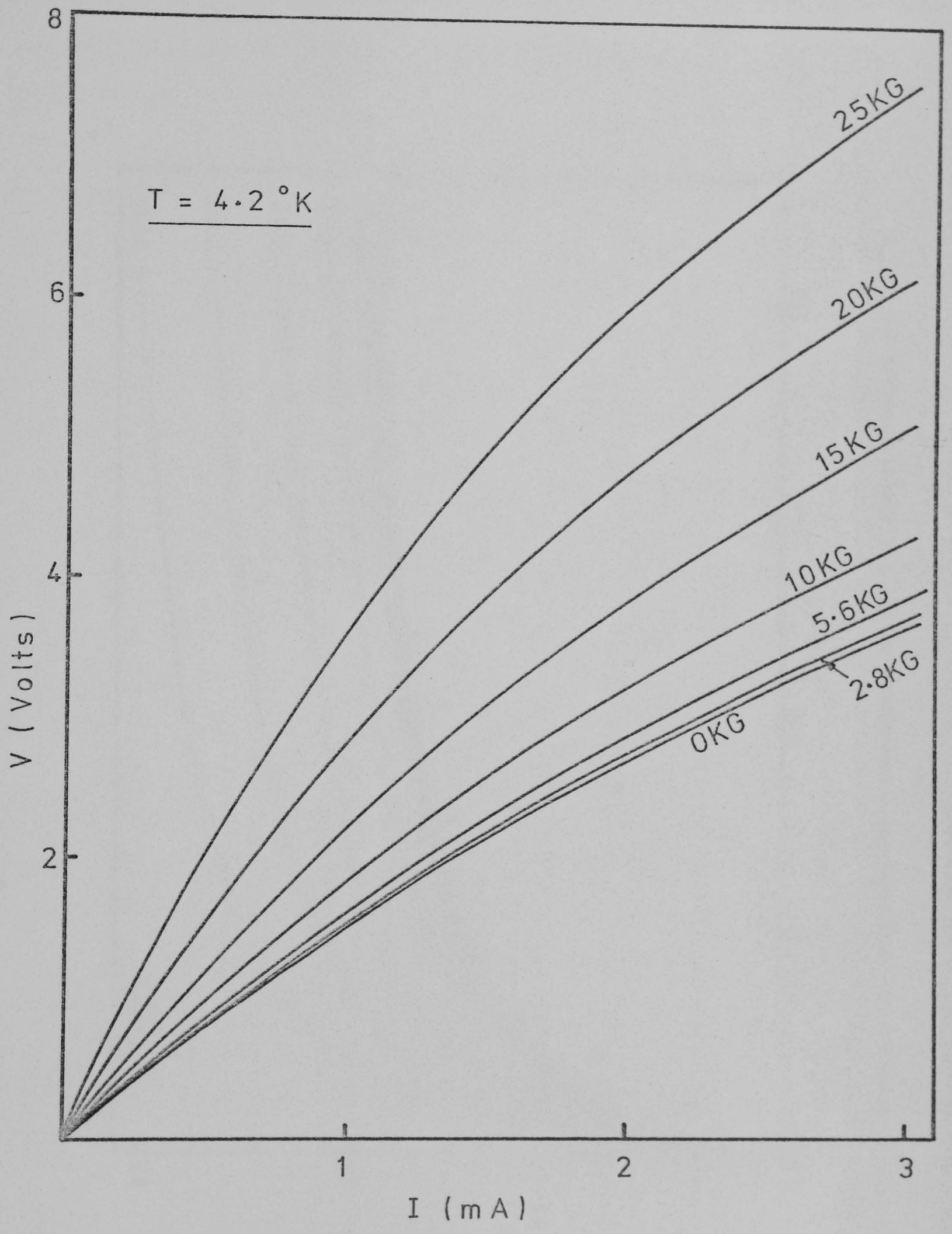

Figure 3.6. Magnetic field dependence of the V-I characteristics at $4.2^{O}K$

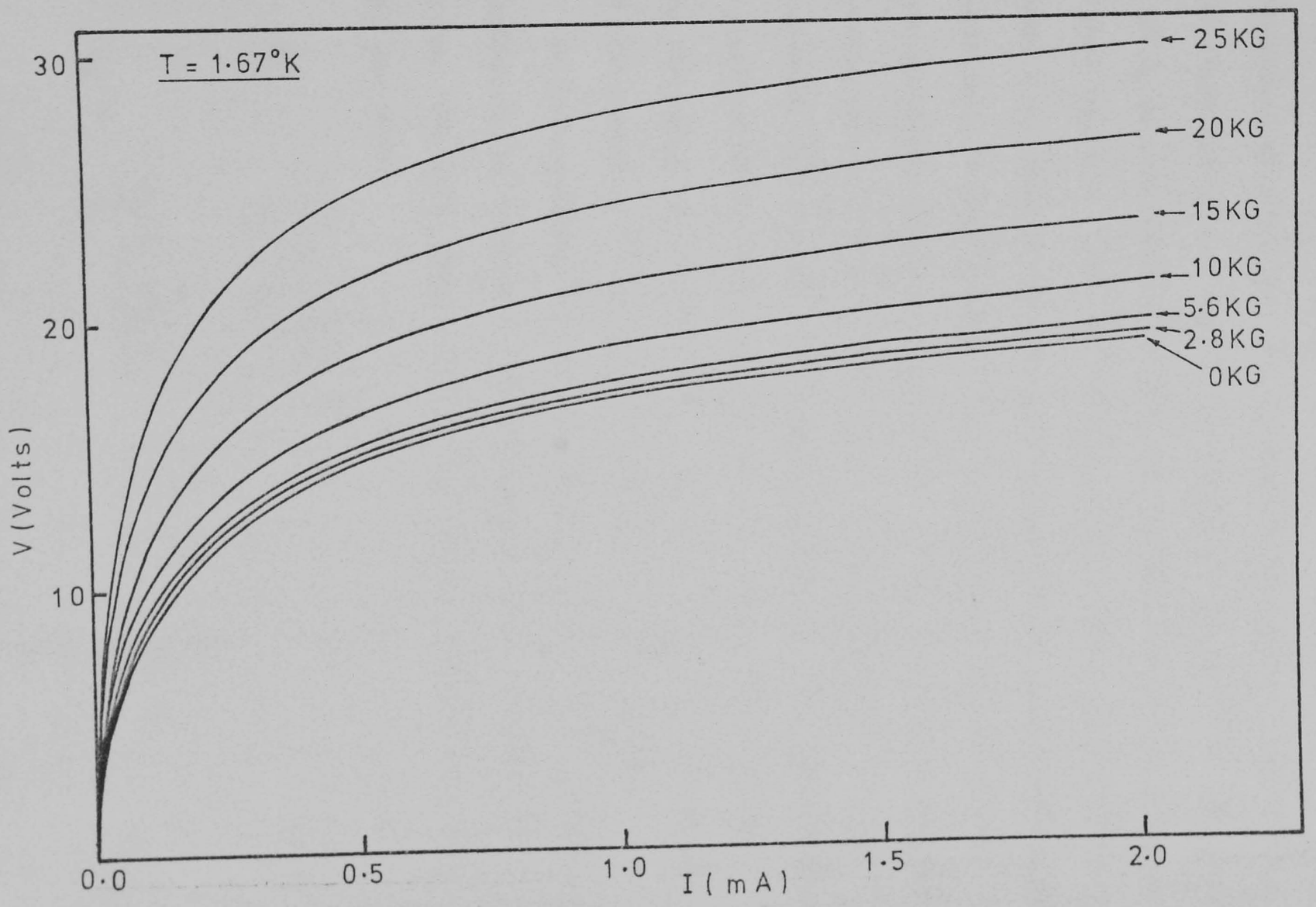

Figure 3.7. Magnetic field dependence of the V-I characteristics at 1.67°K

and phonon scatterings. Further, it was pointed out by Koenig that the last feature should be more apparent at lower temperatures and in more impure samples.

At 4.2°K, in our sample, the electrical conduction is dominated by the motion of electrons in the delocalised band situated above the ground state and gives rise to the existance of ε_2 [14]. The initial decrease in R_H at low electric fields at both temperatures is not apparent in pure samples. This may arise from the initial excitation of the captured electrons in the delocalised band by the mobile electrons. This low energy excitation might occur as an inverse process to the giant trap mechanism in which the carriers can be captured in excited states having energy $\sim$ kT from the conduction band edge and are not able to conduct current. This mechanism accounts for the very large capture cross-section found experimentally for the conduction band electrons and speculated by Lax [15]. We think that this theory may apply to the electrons in the delocalised band in this sample.

At both temperatures, both conduction mechanisms (σ_2 and σ_3) are contributing to conduction with different ratios depending on temperature. The Hall coefficient R_H and the Hall mobility μ_H will then take the form

$$R_H = \frac{\sigma_2 \mu_2 + \sigma_3 \mu_3}{(\sigma_2 + \sigma_3)^2} \qquad .. (3.3)$$

and

$$\mu_H = \frac{\sigma_2 \mu_2 + \sigma_3 \mu_3}{(\sigma_2 + \sigma_3)} \qquad .. (3.4)$$

where μ_2 and μ_3 are the delocalised and hopping Hall mobilities respectively. The value of R_H has increased for both temperatures by about an order of magnitude when increasing H from 2.8 to 25 kG.

The values of σ_2 and σ_3 differ only by about a factor of 2 (Figure 3.1) if $\mu_3 << \mu_2$, then the term $\sigma_3\mu_3$ can be neglected in the above expressions. Since the observed decrease in $\sigma_T = \sigma_2 + \sigma_3$ is about a factor of three at 4.2^oK, as we will see, which if squared will give the observed increase in R_H. This indicates that $\sigma_2\mu_2$ has not changed much i.e. a decrease in σ_2 is associated with an increase in μ_2. This is also clear from equation (3.4) for μ_H. The observed decrease in σ_T at both 4.2 and 1.7^oK, in spite of the different contributions from σ_2 and σ_3, is a factor of 2.8 and 3.7 respectively. This indicates that both σ_2 and σ_3 suffer a decrease with magnetic field.

From the graphs and using equations (3.3) and (3.4) together with $\sigma = ne\mu$, the following values of n_2 and μ_2 were found at 4.2^oK for the two extreme magnetic fields at low electric field values (assuming that $\sigma_2 = {}^2/_3\ \sigma_T$)

2.8 kG : $n_2 \cong 2.8 \times 10^{15}\ cm^{-3}$, $\mu_2 = 44\ cm^2\ (V.sec)^{-1}$

25 kG : $n_2 \cong 2.78 \times 10^{14}\ cm^{-3}$, $\mu_2 = 166\ cm^2\ (V.sec)^{-1}$

These values assume that $\mu_3 << \mu_2$, but since $\sigma_3 = \frac{1}{2}\sigma_2$ at this temperature, and the first value of n_2 is approximately equal to the number of saturated hopping carriers given by the acceptor concentration. Then μ_3 is approximately $\frac{1}{2}\mu_2$, i.e., 22 $cm^2\ (V.sec)^{-1}$ at low field. This value seems very large for the pure localised motion. But if the actual delocalised carrier concentration is less, then the assumption $\mu_3 << \mu_2$ is correct as shown below.

At 1.7^oK, where σ_3 dominates σ_2 by about a factor of two, similar increase in R_H with H is observed. Following the same procedure we found

2.8 kG : $n_2 \cong 4.1 \times 10^{11}\ cm^{-3}$, $\mu_2 = 203\ cm^2\ (V.sec)^{-1}$

25 kG : $n_2 \cong 4 \times 10^{10}\ cm^{-3}$, $\mu_2 = 610\ cm^2\ (V.sec)^{-1}$

These values assume that the ratio of σ_2 to σ_3 has not affected much by magnetic field (i.e. $\sigma_3 = 2\sigma_2$).

The large decrease of n_2 at 2.8 kG when cooling from 4.2 to 1.7°K does not agree with the measured activation energy ε_2 of 1.445 meV for which the value of n_2 should be 1.47×10^{14} cm^{-3} at 4.2°K with corresponding mobility μ_2 of 840 cm^2 $(V.sec)^{-1}$ at 2.8 kG, and 1.4×10^{13} cm^{-3} and 3169 cm^2 $(V.sec)^{-1}$ at 25 kG. This also agrees with $\mu \alpha T_e^{3/2}$ ($\sim$ 3.9) between 4.2 and 1.7°K. The measured values given before at 4.2°K and 2.8 kG do then represent mixed carrier concentration of the two conduction mechanisms with an average mobility. The values at 1.7°K are assumed to be correct to give n_2 and μ_2 for ε_2 carriers because the rate of decrease in n_3 is much smaller than n_2 when cooling down and $\mu_3 << \mu_2$ and therefore, since the conductivity contributions are comparable, the neglect of $\sigma_3\mu_3$ represents the actual case.

The values of mobilities at low H for both temperatures seem to be reasonable for ε_2 delocalised band motion. At 25 kG, the value of 3169 cm^2 $(V.sec)^{-1}$ at 4.2°K is very close to the predicted conduction band mobility of 3810 cm^2 $(V.sec)^{-1}$ for nearly similar sample [9] ($Sb \cong 1.7 \times 10^{16}$ cm^{-3}). However, it could not represent the conduction band mobility because the corresponding carrier concentration n_2 (1.4×10^{13} cm^{-3}) is far higher than the conduction band concentration at this temperature assuming an activation energy of 10 meV or even the reduced value of 6.3 meV measured by Fritzsche [8]. Thus, the carrier concentrations and mobilities given by these measurements do represent the ε_2 band conduction.

The strange behaviour of R_H at 1.7°K at some values of electric fields especially for $H \leqslant 10$ kG is rather striking. At 5.6 kG, there are always peaks at specific electric fields. While at 10 kG, there are some dips. The peaks at 5.6 kG have a relative magnitude which increases with electric field. The value of R_H at any peak does

not exceed the ohmic value. This, coupled with the increased magnitude of the peaks with electric field, suggests that these disturbances only occur among the impactly ionized carriers, and that these peaks represent some types of resonant capture of carriers. We believe, therefore, that this process of capture is a process in which the Auger recombination mechanism (inverse of the impact ionization mechanism) yields a major contribution to it. To describe this in more detail, let us consider the steady state electron concentration n extracted from the rate equation which is given by [13]

$$n = \frac{A_T (N_D - N_A)}{B_T N_A - A_I (N_D - N_A) + n B_I N_A} \qquad .. (3.5)$$

where

A_T , B_T are the thermal generation and recombination parameters respectively.

A_I , B_I are the impact ionization and its inverse process (Auger process) parameters respectively.

N_D , N_A are the donor and acceptor concentrations.

The majority of the peaks occur at large electric fields, near breakdown voltages in which case the thermal and impact ionization terms are nearly equal and the controlling factor for n will be the Auger recombination factor. This is also clear from the n dependence of this factor. The Auger recombination process can simply be described as follows; two electrons collide in the vicinity of an ionized centre, one of them is captured, the other can carry the energy away [13]. This process if it occurs with the presence of magnetic field, can be greatly enhanced if the cyclotron radius is comparable to the capturing orbit radius. For 5.6 kG, assuming an average effective mass m* of $0.11\ m_o$ [11] (m_o is the free electron mass) for electrons having an energy of $\sim \frac{3}{2}$ kT, the cyclotron radius defined by

$$r = \frac{m^* v}{eH} \qquad .. (3.6)$$

is 301.5 Å

here v is the thermal velocity $= \left(\frac{3kT}{m^*}\right)^{\frac{1}{2}}$, e is the electronic charge, and H is the magnetic induction.

This value of r is much larger than the ground state Bohr radius a_o of the impurity atom, given by the relation.

$$a_o = \frac{\hbar^2 K}{m^* e^2} \qquad .. (3.7)$$

For the same value of m*, this is equal to 77Å (K = 16 is the dielectric constant of Ge). The situation now is not clear whether this capture (at the Hall coefficient peaks) is caused by single impurity excited states having a radius comparable to that given by (3.6), or it is due to a capture by positive ion pairs and/or atomic clusters of the Sb atoms which are more likely to occur especially at this doping concentration at which the average impurity separation is 158.5 Å i.e., very close to 2 a_o. In any case, the captured electrons will not be able to carry current. Since this phenomenon does not occur in pure n-type samples [13], therefore we may expect that the multiatomic capture is the responsible mechanism. Also in this case, the capturing radius should be comparable to r in (3.6) at the peaks. In the Auger process mentioned, after collision and capture, the free electron will carry the excess energy causing its mobility to increase. At the strongest peak in R_H occurring around 16 V/cm, the R_H value has increased nearly four times so does the mobility μ_H and μ_2 (σ_2 and σ_3 haye not corresponding change at the peaks). This corresponds to an electron temperature increase of the remaining carriers of $(4)^{2/3}$ or about 2.5 times the unperturbed value. The final value of $\mu_H = \sigma_T R_H$ at that peak, however, is still smaller than

the low electric field value. At the peak occurring between 5-6 V/cm, for which the value of R_H is nearly equal to the ohmic value, the value of μ_H is larger than the ohmic value by about 25%.

Probably all the other peaks tend to have a value of R_H equal to the ohmic value and the electric field intervals were not small enough to resolve these values. In this case, the value of μ_H at these peaks, and not the carrier multiplication, will be responsible for the conductivity increase with electric field.

At 10 kG, on the other hand, there are mainly two smaller dips in the value of R_H. Similarly this is caused by further carrier generation at these dips. We think that this is due to a sudden increase in the impact ionization term in (3.5) with the presence of a magnetic field. The cyclotron radius r for 10 kG is about 169 Å, much larger than the ground state Bohr radius a_o (77 Å), but comparable to the mean impurity separation (158.5Å). On the other hand, the quantum energy associated with the cyclotron frequency ω_c at 10 kG is $\sim$ 1 meV ($\sim$ 0.56 meV for 5.6 kG). This value is comparable to the hopping activation energy ε_3 ($\sim$ 0.9 meV). Probably, these could have some correlation with the observed anomaly at 10 kG.

There are other small peaks in R_H which occur for nearly all values of magnetic fields. These peaks occur at about 35-40 $V.cm^{-1}$ irrespective of the magnetic field, also we can include the very large peak at 20 kG. which nearly occurred after full breakdown. The reason for the small peaks is not known, but we think that the large peak of 20 kG may have similar origin as those discussed for 5.6 kG, i.e. resonant capture.

3.2.3. Magneto-resistance

The transverse magneto-resistance (TMR) observed in this sample is sufficiently high that it could not be explained by the

ordinary magneto-resistance (MR) theory for conduction band electrons. This theory states that the low field condition is satisfied when $\omega_c \tau = \mu H < 1$, where τ is the momentum scattering time. In this case

$$\frac{\Delta\rho}{\rho_o} = \xi \ (\omega_c \tau)^2 = \xi \ (\mu H)^2$$

and ξ is called the MR coefficient and has the value of 0.57 for ionized impurity scattering. From this, the value of $\frac{\Delta\rho}{\rho_o}$ should always be less than unity for $\mu H < 1$. In our case $\mu H < 1$ at any H, and from Figure (3.8), $\frac{\Delta\rho}{\rho_o}$ and $\frac{\Delta\rho}{\rho_o H^2}$ do not agree with the above theory especially at 1.7°K where the localised hopping conduction dominates. Moreover, $\frac{\Delta\rho}{\rho_o H^2}$ is not constant for 1.7°K for H < 15 kG, but has a decreasing value with H. The MR mechanism is, therefore, completely different.

At 4.2°K, we found that the MR is mainly caused by a decrease in σ_{o2} in equation (3.1) for the delocalised motion part, while if the hopping conduction is dominating an increase in both ε_3 and σ_{o3} was observed. This result was obtained from the $\ln R - \frac{1}{T}$ plot with and without magnetic field of 5.6 kG as shown in Figure (3.9).

The TMR observed in this sample at 4.2°K is mainly as a result of carrier depopulation shown before together with partial compensation by mobility increase. At 1.7°K, however, higher MR was observed for a given field. This was believed to arise from the decrease in spacial extent of the ground state wavefunction [9] which accounts for the increase in ε_3 and σ_{o3}. It seemed that this effect is greater than the effect on the delocalised motion of the carriers in the ε_2 band regarding the MR. The individual contribution to the MR ratio $\frac{\rho(H)}{\rho_o}$ for both mechanisms at 25 kG, assuming that the ratio of both contributions remains unchanged by the field, are 2.22 for σ_2 and 5.45 for the hopping. This gives as shown in Figure (3.8) an overall

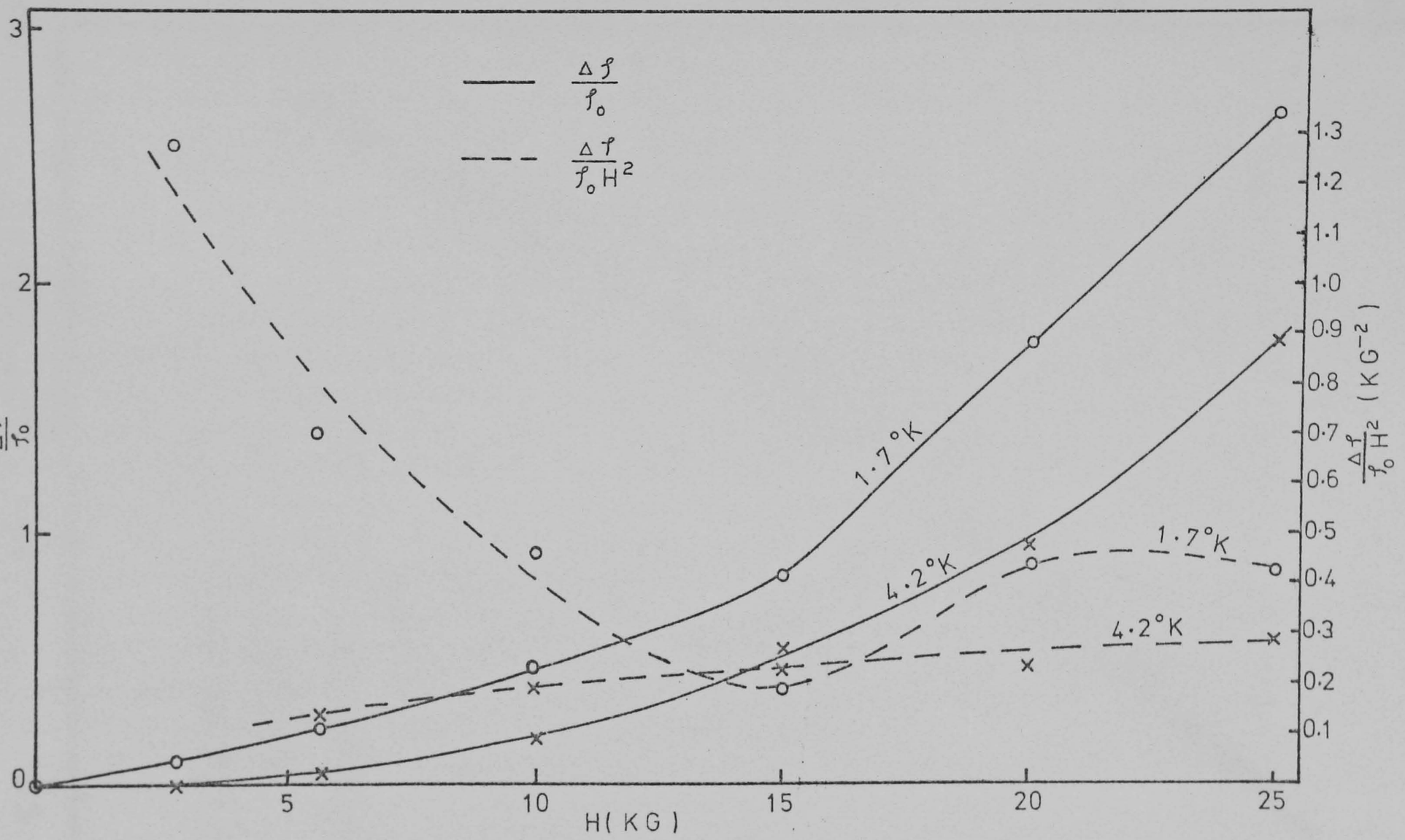
$\frac{\Delta f}{f_0}$
$\frac{\Delta f}{f_0 H^2}$
$\frac{\Delta f}{f_0}$
$\frac{\Delta f}{f_0 H^2}$ (KG^{-2})
1·7°K
4·2°K
1·7°K
4·2°K
H(KG)
0
1
2
3
5
10
15
20
25
0·1
0·2
0·3
0·4
0·5
0·6
0·7
0·8
0·9
1·0
1·1
1·2
1·3

Figure 3.8.

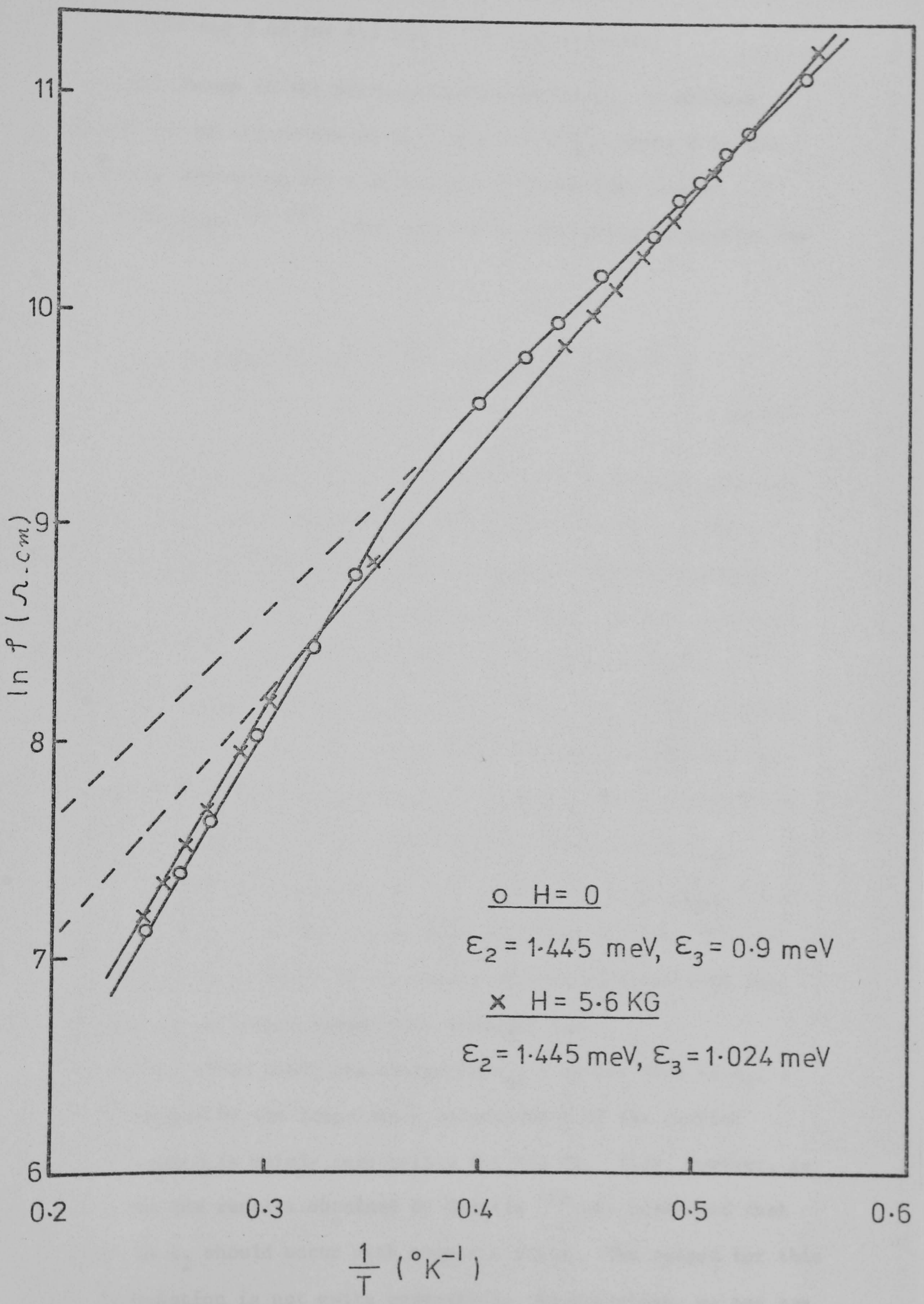

Figure 3.9. Effect of magnetic field on the activation energies ε_2 and ε_3 in n-type Ge

$\frac{\rho(H)}{\rho_o}$ of 2.78 and 3.68 for 4.2 and 1.7°K respectively.

The change in the pre-exponential factor σ_{o3} is obvious through the strong dependence of this term on $(\frac{d}{a})$ where d is the mean impurity separation and a is the ground state Bohr radius. Miller and Abrahams [1, 17] have deduced the following expression for σ_{o3}.

$$\sigma_{o3} = (\text{const.}) \left(\frac{d}{a}\right)^{\frac{-11}{4}} \cdot \exp.\left(1.09 \left(\frac{d}{a}\right)^{\frac{3}{2}}\right) \quad .. (3.8)$$

This relation is valid for large $(\frac{d}{a})$, but it is reasonably good for qualitative description in our case. From this relation σ_{o3} has a positive change with $(\frac{d}{a})$ for doping levels less than that corresponding to $(\frac{d}{a}) \sim 1.4$ ($N_D \sim 1.95 \times 10^{17}$ cm^{-3}) which is well above our doping level. Since the effect of magnetic field is to reduce a [1] which corresponds to an increase in $(\frac{d}{a})$, then, σ_{o3} should increase with H. We found that at 1.7°K and 5.6 kG, the value of $\frac{\rho(H)}{\rho_o}$ due to the activation energy increase alone is ∿2.4 while the measured value for the hopping contribution is only 1.235, so the value of σ_{o3} should have increased by a factor of ∿ 2. This occurs if $\frac{d}{a(H)} = 2.77$ or a(H) = 57.2 Å (a_o = 77 Å), i.e., $\frac{a(H)}{a_o} = 0.74$ at 5.6 kG. This is also clear from Figure (3.9) if we compare the intersection with the vertical axis of the lowest temperature straight line.

On the other hand, the change in σ_{o2}, rather than in ε_2, is also emphasised by the temperature independence of the carrier depopulation which is mainly responsible for the MR. This, however, is different from the results obtained by Sadasiv [6] who concluded that an increase in ε_2 should occur with magnetic field. The reason for this carrier depopulation is not quite understood. Nevertheless, we may say that it is due to the increased effect of recombination parameters

especially B_T in equation (3.5).

3.2.4. Energy scattering and hot electron phenomenon

At low temperatures, the energy coupling between electrons and lattice is generally weak. The main mechanisms by which the carriers can exchange energy with the lattice is electron-phonon and probably ionized impurity scattering. Scattering with ionized impurities at such doping level and at the lowest temperature ($1.7^{o}K$) could represent additional energy relaxation mechanism (the mobility is highly impurity-limited). It is known that impurity scattering is highly elastic because of the small value of mass ratio between the electron and the impurity atom. But the collision frequency $1/\tau$, where τ is the momentum scattering time, is several orders of magnitude greater than the scattering frequency with phonons at such temperatures.

3.2.4.1. Ionized impurity scattering as an energy relaxation mechanism

For the above reasons, we found it is worthy to calculate the energy exchange between carriers and the lattice due to ionized impurity scattering and comparing with that due to scattering with phonons. Using the simple collision theory, the change of the carrier energy was obtained. The mobility as function of electric field was then deduced. The details of these derivations are shown in the appendix at the end of the chapter. We will present here the final results.

An electron energy loss per collision is

$$\Delta E = -\frac{2m^*}{M}(1 - \cos\theta) \qquad .. (3.9)$$

where m^*, M are the electron and the impurity atom masses.

θ is the collision angle; the angle by which an electron deviates from its original trajectory.

The average power loss $\frac{dE}{dt}$ due to this collision per electron was found

to be

$$\left(\frac{dE}{dt}\right)_I = -\frac{Z^2 e^4 N_I \ln B^2}{6\pi^{3/2} \cdot (2m^*)^{\frac{1}{2}} \epsilon^2} \cdot \frac{4m^*}{H} \cdot E^{-\frac{1}{2}} \qquad .. (3.10)$$

and

$$B^2 = \frac{8m^* \epsilon kT E}{\hbar^2 e^2 n} \qquad .. (3.11)$$

where Z is the effective nuclear charge (unity in our case)

N_I is the ionized impurities concentration

ϵ is the permittivity of Ge

n is the free carriers concentration with an effective mass m* and internal energy E and T is the absolute temperature.

If, then, we exclude any other energy relaxation mechanism, the energy gained by an applied electric field F must equal that delivered to the lattice via the ionized impurity scattering. The energy gained by the field is $\mu_I . e . F^2$, where μ_I is the ionized impurity scattering-limited mobility which represent our case. The expression used for μ_I, for conduction band electrons, is (21)

$$\mu_I = \frac{64\pi^{\frac{1}{2}} \epsilon^2 (2kT)^{3/2}}{N_I Z^2 e^3 m^{*\frac{1}{2}}} \cdot \ln\left[\left\{\frac{24m^* k^2 T^2 \epsilon}{e^2 \hbar^2 n}\right\}\right]^{-1} \qquad .. (3.12)$$

In equilibrium we will have

$$\mu_I e F^2 = \left(\frac{dE}{dt}\right)_I \qquad .. (3.13)$$

Neglecting the dependance of the logarithmic terms in both (3.10) and (3.12) upon temperature, relation (3.13) can be written as

$$a \; F^2 \; . \; T_e^{3/2} \; = \; b \; T_e^{-\frac{1}{2}}$$

$$\text{or } T_e \; = \; \frac{b}{a} \; F^{-1}$$

$$\text{and } \mu_I \; \alpha \; T_e^{3/2} \; \alpha \; F^{-3/2} \qquad .. \; (3.14)$$

where a, b are constants defined from the above expressions, i.e., the carriers drift mobility μ_I is inversily proportional to the applied electric field to the power $\frac{3}{2}$ at constant lattice temperature, and the maximum mobility is obtained at zero field (this will be equal to the ohmic value).

Comparing $\left(\frac{dE}{dt} \right)_I$ given by (3.10) with that due to electron-photon scattering which is given by

$$\left(\frac{dE}{dt} \right)_L \; = \; 8 u^2 \; (2\pi m^* \; k \; T_e)^{\frac{1}{2}} \; . \; (T - T_e) / \pi \ell T \qquad .. \; (3.15)$$

where u is the speed of sound in the crystal,

ℓ is the phonon mean free path

T and T_e are the lattice and electron temperatures respectively.

Substituting in (3.10) and (3.15) taking into account that

$T = 1.7^{\circ}K$

N_I is the number of ionized centres = Number of compensators

$\cong 2.8 \times 10^{15} \; cm^{-3}$ (it is not quite known, and this value is that determined from the Hall coefficient at low H and $4.2^{\circ}K$)

$n \cong 4.1 \times 10^{11} \; cm^{-3}$, $m^* = 0.11 \; m_o$ and $\frac{\epsilon}{\epsilon_o} = 16.$

$$\frac{m^*}{M} \; = \; 4.9 \times 10^{-7}$$

$$u \; = \; 4.95 \times 10^5 \text{ cm/sec, and } \ell = u . \tau_p$$

assuming $\tau_p \cong 10^{-9}$ sec at this temperature, then $\ell = 4.95 \times 10^{-4}$ cm.

After substitution we will have,

$$\left(\frac{dE}{dt}\right)_I = -1.0 \times 10^{-14} \text{ watts} \qquad .. (3.16)$$

$$\left(\frac{dE}{dt}\right)_L = -3.6 \times 10^{-14} \text{ watts for } T_e - T = 1^oK \qquad .. (3.17)$$

From this we see that ionized impurity scattering in this sample is competing with that due to electron-phonon scattering. Both values will be equal when $T_e = 2.05^oK$, i.e. $(T_e - T) = 0.35^oK$. Proper comparison can be made by evaluating the coefficient of thermal coupling $K = \frac{-d}{dT_e}\left(\frac{dE}{dt}\right)$ for both cases, where $-\left(\frac{dE}{dt}\right)$ is the power delivered to the lattice. Relations (3.10) and (3.15) can be written as

$$-\left(\frac{dE}{dt}\right)_I = P_I = +A.\ T_e^{-\frac{1}{2}} \qquad .. (3.18)$$

$$-\left(\frac{dE}{dt}\right)_L = P_L = -B\ T_e^{\frac{1}{2}}\ (T - T_e) = B\ T_e^{\frac{1}{2}}\ (T_e - T) \qquad .. (3.19)$$

where

$$A = \frac{Z^2\ e^4\ N_I\ \ln B^2}{6\pi^{3/2}(2m^*)^{\frac{1}{2}}.\ \epsilon^2} \cdot \frac{4m^*}{M} \cdot \frac{2}{3k} \qquad .. (3.20)$$

and

$$B = \frac{8u^2\ (2\pi m^*\ k)^{\frac{1}{2}}}{\pi \ell T} \qquad .. (3.21)$$

Then

$$\frac{dP_I}{dT_e} = K_I = -\frac{A}{2}\ T_e^{-3/2} \qquad .. (3.22)$$

and

$$K_L = \frac{B}{2}\ T_e^{\frac{1}{2}}\ \left(3 - \frac{T}{T_e}\right) \qquad .. (3.23)$$

The negative sign of K_I resulted from the inverse dependence of electron temperature on the applied electric field ($T_e \alpha F^{-1}$ and $\frac{d}{dT_e} \alpha - \frac{d}{dF}$). The magnitude of these coefficients at zero electric field ($T_e = T$) are

$$K_I = -2.94 \times 10^{-15} \text{ watts.} {}^{o}K^{-1} \text{/electron} \quad .. (3.24)$$

$$K_L = 3.6 \times 10^{-14} \text{ watts.} {}^{o}K^{-1} \text{/electron} \quad .. (3.25)$$

From this we see that at low fields, the overall coupling coefficient is controlled by electron-phonon interaction. If an electric field is applied across the sample, both the mobility and T_e will increase resulting in an increase in K_L and further decrease in K_I ($\mu_I = \mu_o (1 + BF^2)$ for electron-phonon scattering, and $\mu_I \alpha T_e^{3/2}$).

All the P's and K's values are given per electron and it should be multiplied by the total number of electrons in the sample to give the total values. For the sample used for the Hall coefficient measurements having a volume of 3.375 mm^3 and carrier concentration of 4.1×10^{11} cm^{-3},

$$K_L = 50\mu \text{ watts.} {}^{o}K^{-1} \quad .. (3.26)$$

This value is close to the experimentally estimated value as we will see.

From these analyses, the value of K_I will increase and may dominate the energy coupling if the sample is more compensated (larger N_I in 3.10) and/or the temperature is further reduced.

3.2.4.2. Electron-phonon coupling and hot electron phenomenon

This hot electron effect can appear as a non-linearity of the element resistivity with electric field. This is caused by the

mobility change of the conducting carriers due to their internal energy change. The sign of the mobility change depends on the momentum scattering mechanism involved. For very pure samples, if the lattice scattering still limiting the mobility at low temperatures, then the mobility should decrease with electric fields. For nearly all practically pure samples at helium temperatures, the ionized and neutral impurities limit the mobility. In this case, the mobility increases with the energy input to the sample. This behaviour is described by the following relation [18]

$$\mu = \mu_o (1 + B F^2) \qquad .. (3.27)$$

where B is the parameter which depends on the energy gain and loss rate of carriers, it is positive for impurity-limited mobility and negative for lattice limited mobility.

μ_o is the zero field mobility.

In our case, the mobility is limited by ionized impurity scattering in which case μ increases with F. For the used doping level, the non-linearity will result from the increased impact ionization caused by the energetic carriers even at very low electric field as shown previously. As we have seen before, the electron-lattice coupling is mainly caused by interaction with phonons. In Figure (3.5) the Hall mobility at 2.8 kG was plotted for comparison with the non-linearity caused by carrier multiplication represented by the Hall coefficient. In fact we may say that the energy gained by the carrier distribution is devoted to generation of new carriers thermally trapped.

As we mentioned, the hot electron phenomenon described is more pronounced in singly doped samples and decreases as the compensation ratio $\frac{N_A}{N_D}$ increases. This is due to the efficient electron-

lattice coupling in the resultant dominant localised motion at low temperatures, as well as the increased ionized scattering centres for free conducting carriers. Figure (3.10) is a comparison between the power dependence resistance for two samples, one is singly Sb-doped sample (similar to that used for the Hall measurements) and the p-type compensated sample at 4.2 and 1.68^{o}K. The small non-linearity in the p-type sample at 1.68^{o}K is believed to be caused by the presence of a small number of conduction band carriers. Both samples show less non-linearity at 4.2^{o}K for the same dc power input, which is what we should expect from electron-phonon interaction together with the fact that the majority of thermally trapped carriers at the bottom of the ε_2 band is highly reduced.

The sensitivity S of the carrier mobility to the dc power P depends on the total number of free carriers that receives the power as well as its mean temperature, i.e., the total internal energy of carriers, E. This can be described as [19]

$$S = \frac{1}{\mu} \frac{d\mu}{dP} \alpha E^{-1} . T_e^{-\frac{1}{2}} \quad .. (3.28)$$

E is defined as

$$E = n v k T_e \quad .. (3.29)$$

n is the carrier concentration with mean temperature T_e in a sample of volume v. As we have seen, at 4.2^{o}K the carrier concentration n_2 is more than two orders of magnitude greater than at 1.7^{o}K, (1.47×10^{14} and 4.1×10^{11} cm^{-3}), the temperature difference of carriers makes the mobility sensitivity at 4.2^{o}K about three orders of magnitudes smaller than at 1.7^{o}K. This strong temperature dependence of S in this sample indicates that the hot electron phenomenon for such doping level will not be observed except for the lowest temperature possible.

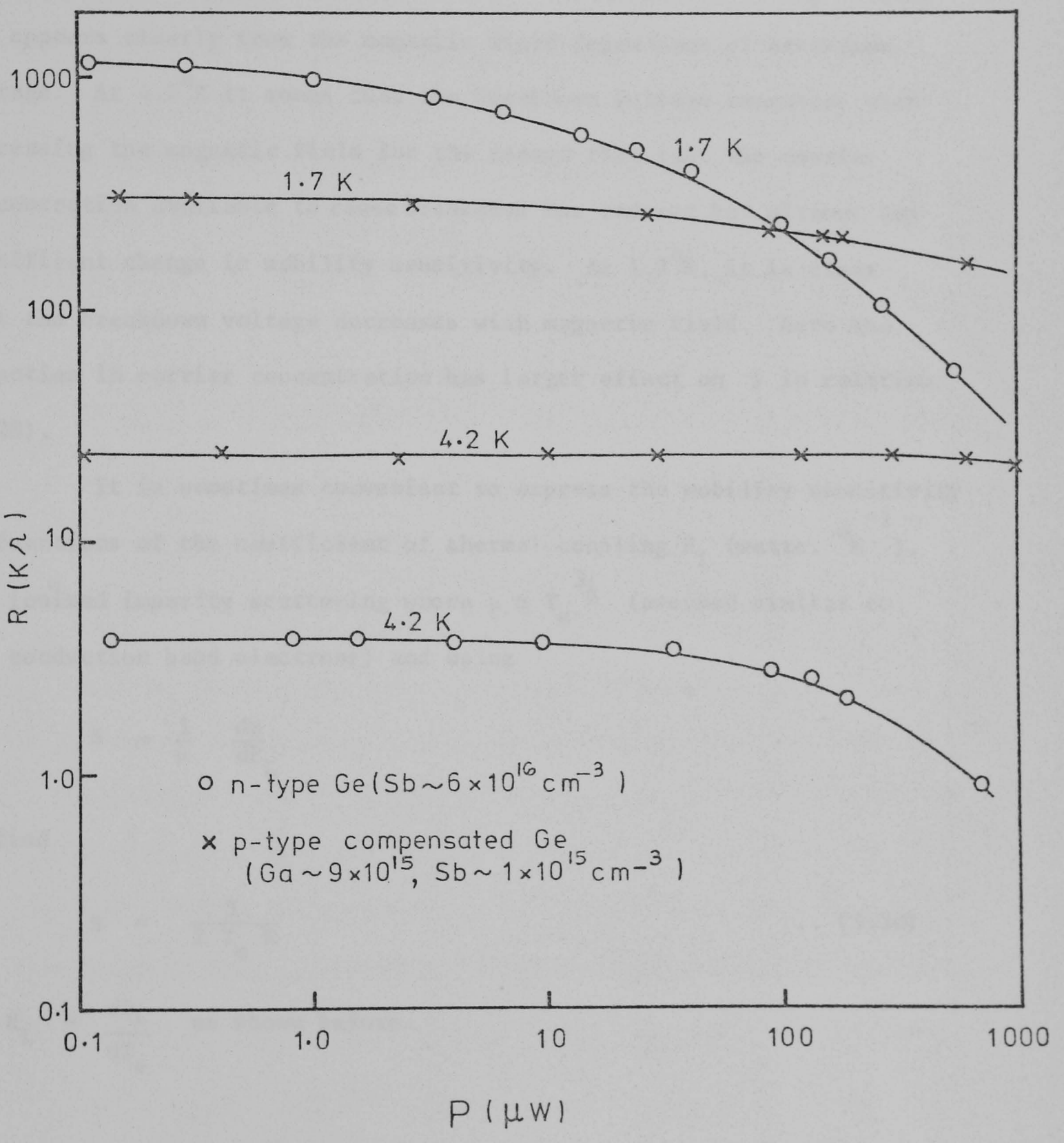

Figure 3.10. Effect of doping conditions and temperature on resistance non-linearity

Regarding the radiation fields, if we take into account the difference in absorption coefficient which goes as the carrier concentration n_2, the related response at 4.2°K will still be more than an order of magnitudes smaller than that at 1.7°K.

In Figures (3.4) and (3.5), the mobility sensitivity comparison appears clearly from the magnetic field dependence of breakdown voltage. At 4.2°K it seems that the breakdown voltage increases with increasing the magnetic field for the reason that just the carrier concentration available to cause breakdown has reduced but without any significant change in mobility sensitivity. At 1.7°K, it is clear that the breakdown voltage decreases with magnetic field. Here the reduction in carrier concentration has larger effect on S in relation (3.28).

It is sometimes convenient to express the mobility sensitivity as functions of the coefficient of thermal coupling K_L (watts. $^{o}K^{-1}$). For ionized impurity scattering where $\mu \alpha T_e^{3/2}$ (assumed similar to the conduction band electrons) and using

$$S = \frac{1}{\mu} \frac{d\mu}{dP_L}$$

we find

$$S = \frac{3}{2\ T_e\ K} \qquad .. (3.30)$$

and $K_L = \frac{dP_L}{dT_e}$ as shown before.

3.2.4.3. Electron-lattice coupling parameter and electron temperature

The non-linearity shown in Figure (3.10) for the n-type sample being caused by electron heating and subsequent generation of trapped carriers is always less than the pure mobility variation

given by (3.27). This can easily be illustrated by a simple calculation as follows; let the conductivity in our sample at any point on the bias curve be σ and that due entirely to mobility variation be σ'. Then, if we consider that the fractional difference of the generated carriers be $x = \frac{\Delta n}{n_o}$ at that point, where n_o is the zero bias carrier concentration, then the total number of carriers will be $(1 + x)n_o$. Since this excess number of carriers $(x\ n_o)$ gained energy from the original free energetic carriers, then the carrier mean energy ε at the mentioned point will decrease by a factor of $(1 + x)$. Taking the mobility variation as $\mu \alpha \varepsilon^{3/2}$ for ionized impurity scattering we can write

$$\sigma \alpha (1 + x)n_o \cdot \left(\frac{\varepsilon}{1 + x}\right)^{3/2} \qquad .. (3.31)$$

$$= \frac{\sigma'}{(1 + x)^2}$$

This assumes that the ionized carriers will have a final mean energy equal to the ionizing one. Therefore in our case it is always better to work at low biasing if we require true hot electron performance. Fortunately, this is the best for Ge regarding S. The value of x could be determined from the Hall coefficient measurements. The plot of $\sigma(1 + x)^{\frac{1}{2}}$ vs F^2 should then give a straight line of slope $\sigma_o B$ from which B could be determined for this sample. Figures (3.11) and (3.12) show this plot for 5.6 kG from which B was calculated to be

$$B = 0.05 \quad cm^2.V^{-2} \qquad \text{for } F = 1\text{-}3.5 \text{ volts.cm}^{-1}$$

and

$$= 0.104 \quad cm^2.V^{-2} \qquad \text{for } F = 0.5\text{-}1.0 \text{ volts.cm}^{-1}$$

and increases more quickly for $F < 0.5$ V.cm^{-1}.

The maximum values available for $B = \frac{\mu^2 L_o}{6u^2}$ $cm^2.V^{-2}$ (18) where

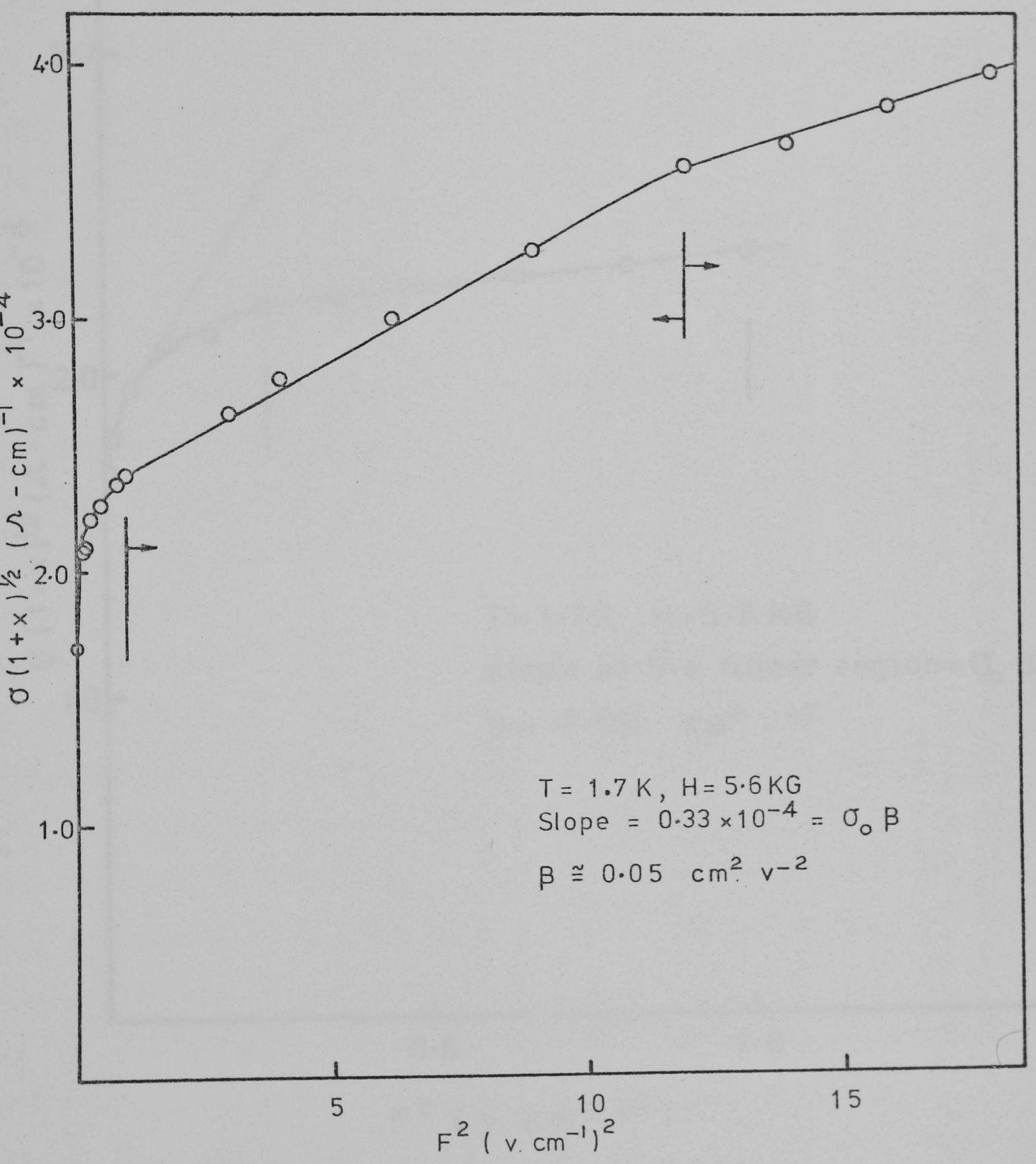

Figure 3.11. $\sigma(1+x)^{\frac{1}{2}}$ vs F^2 for moderate electric fields

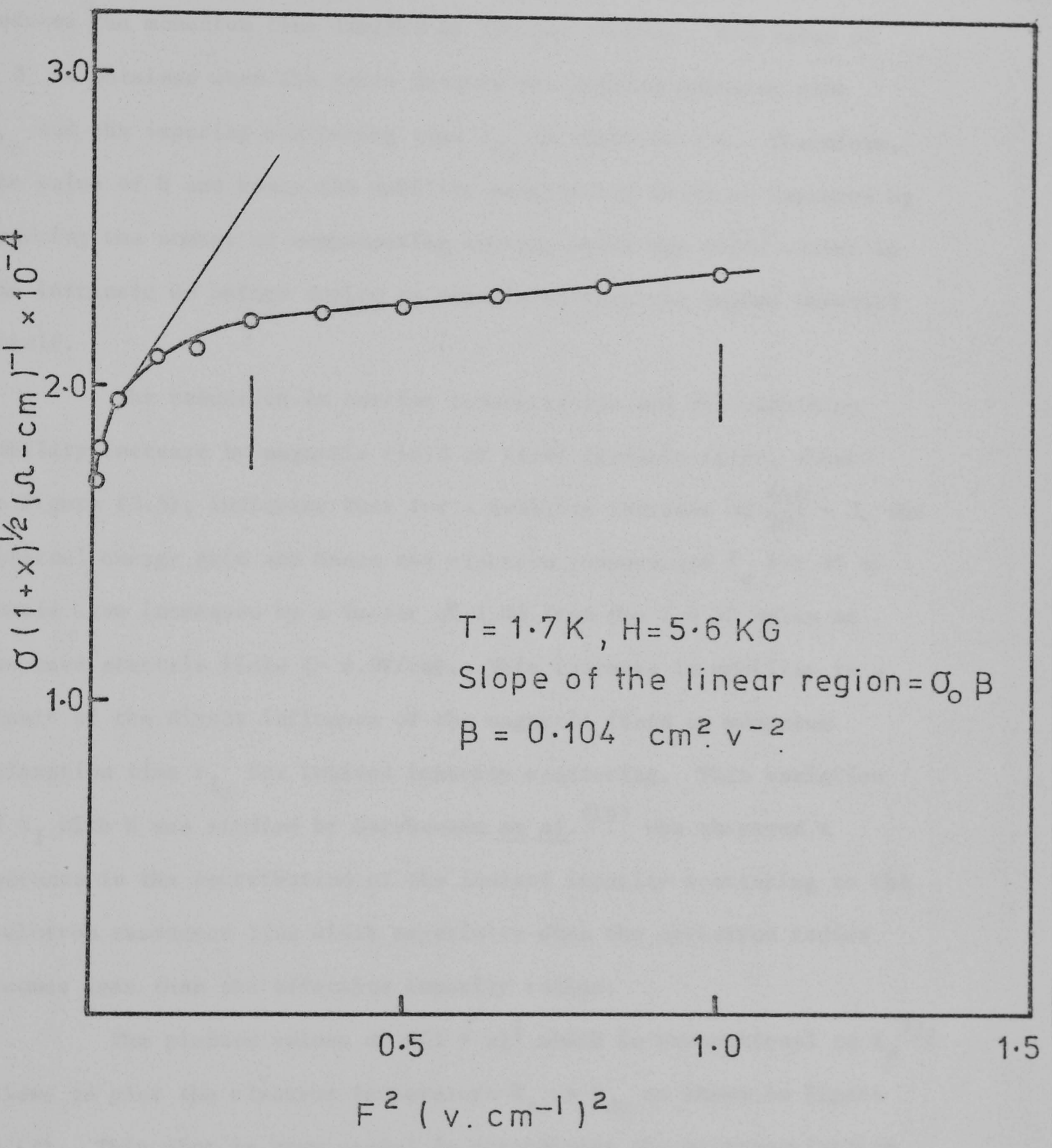

Figure 3.12. $\sigma(1+x)^{\frac{1}{2}}$ vs F^2 for low electric fields

μ_{L_o} is the ohmic lattice mobility and u is the phonon velocity. This value could not be easily achieved for this sample because of the existance of fairly large number of compensating impurities which reduces the momentum time limited by ionized centres. This value of B is obtained when the ratio between the lattice momentum time τ_{L_o} and the impurity scattering time τ_{I_o} is equal to 3.6. Therefore, the value of B and hence the mobility sensitivity could be improved by reducing the number of compensating centres which may exist either in the intrinsic Ge before doping or associated with the dopant material itself.

The reduction in carrier concentration and the resulting mobility increase by magnetic field at fixed electric field, shown in Figure (3.5), indicates that for a mobility increase of $\frac{610}{203} \sim 3$, the internal energy gain and hence the electron temperature T_e for 25 kG should have increased by a factor of 2.08 from the 2.8 kG value at the used electric field ($\sim$ 0.5V/cm). This increase in mobility is a result of the direct influence of the magnetic field on momentum relaxation time τ_{I_o} for ionized impurity scattering. This variation of τ_I with H was studied by Gershenzon *et al.*[10] who observed a decrease in the contribution of the ionized impurity scattering to the cyclotron resonance line width especially when the cyclotron radius becomes less than the effective impurity radius.

The plotted values of $\sigma(1 + x)^{\frac{1}{2}}$ which is proportional to $T_e^{3/2}$ allows to plot the electron temperature T_e vs P_{dc} as shown in Figure (3.13). This plot is very useful in determining the electron-lattice coupling parameter K_L at any given power dessipation as

$$K = \frac{dP}{dT_e} \qquad .. (3.32)$$

Figure (3.14) shows the variation of K with $T_e^{\frac{1}{2}}$. This plot

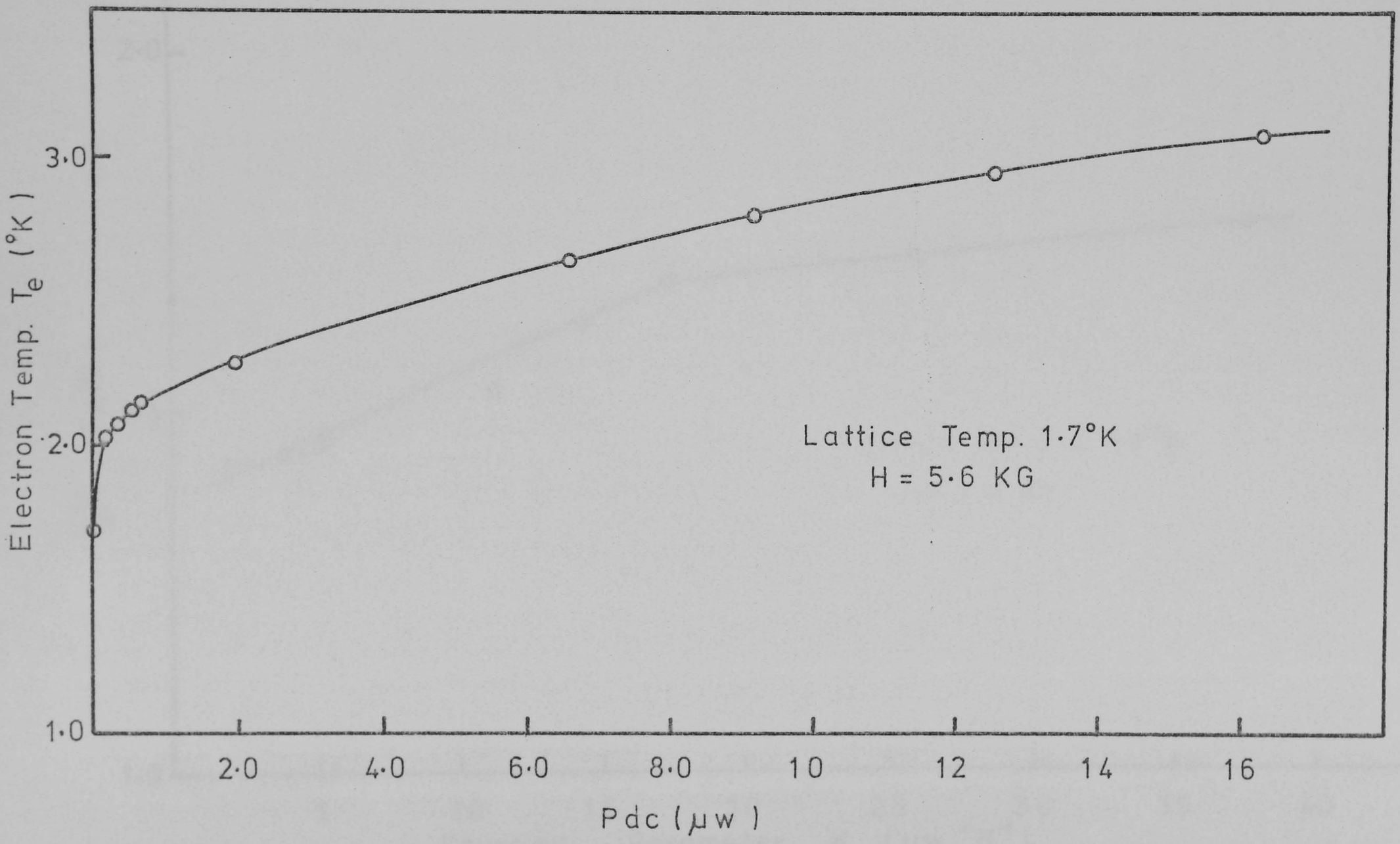

Figure 3.13. Electron temperature as function of the dc power for n-type Ge

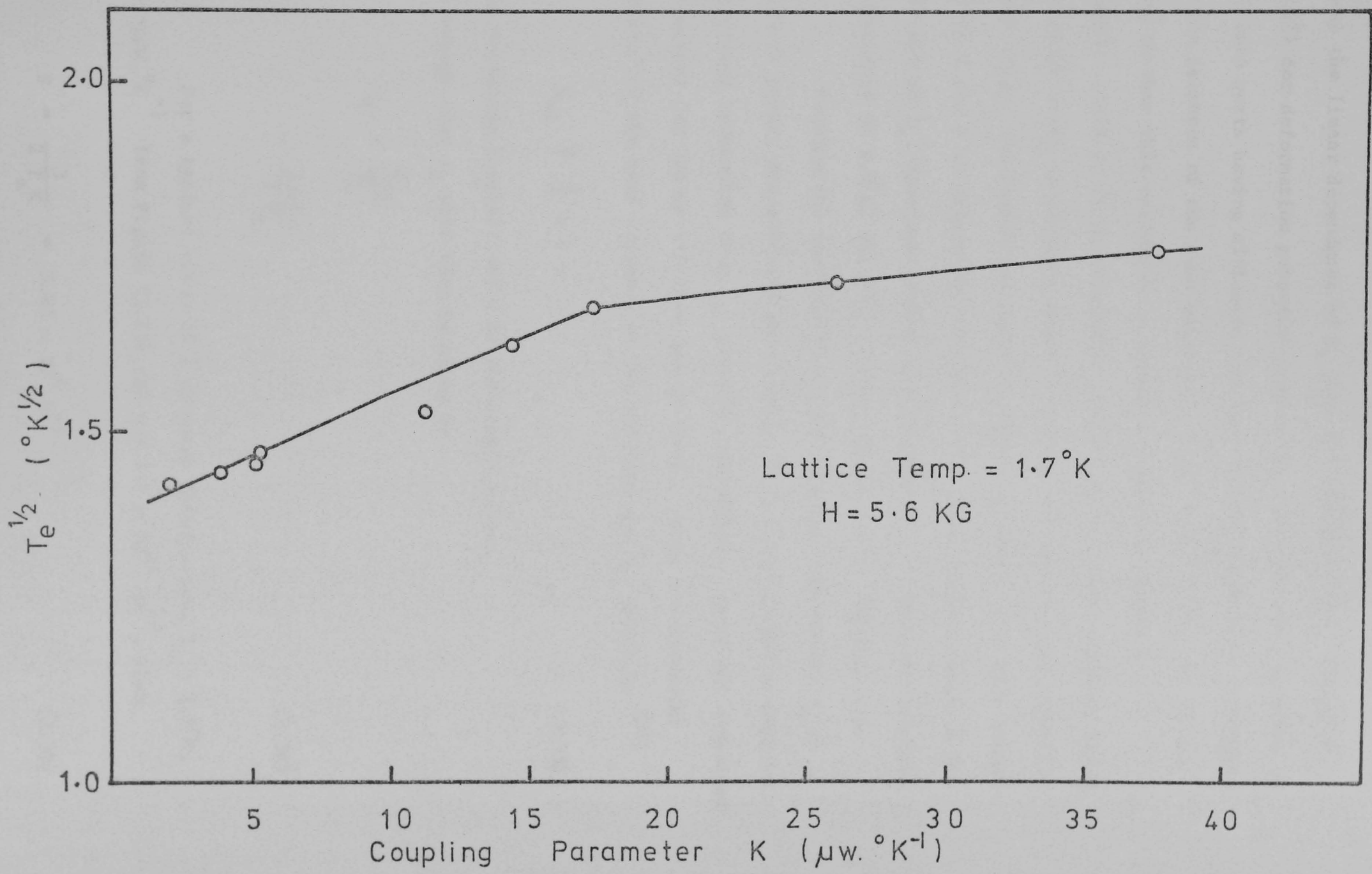
2·0
1·5
1·0
$T_e^{1/2}$ (°K ½)
Lattice Temp. = 1·7°K
H = 5·6 KG
5
10
15
20
25
30
35
40
Coupling Parameter K (μw. °K⁻¹)

Figure 3.14.

shows the linear dependence of K_L upon $T_e^{\frac{1}{2}}$ represented by relation (3.23) for deformation potential scattering. But the plot consists of two main parts having different constant of proportionality (analogous to the presence of the same behaviour of $\sigma(1 + x)^{\frac{1}{2}}$ vs F^2. We do not know whether this variation is associated with the presence of magnetic field or it is originally present in Ge. Nevertheless, since the slope of R_H vs electric field is mainly the same for all magnetic field values (excluding any peaks or dips), we expect that this behaviour of K and B is originally present in Ge. This is speculated as an increase of $T_e^{\frac{1}{2}}$ dependent coupling coefficient K_L at specific electron temperature ($\sim 2.8^{\circ}K$) for some reasons which are not obvious to us.

Knowing the coefficient K_L and electron temperature T_e at a given dc power, the mobility sensitivity S given by (3.30) as well as the energy relaxation time τ_E could be determined. These are essential parameters for the hot electron applications. Using the classical formula for the heat capacity of the electron gas C_{el} given by [20]

$$C_{el} \simeq \frac{3}{2} n k v \qquad .. (3.33)$$

k is Boltzmann constant and v is the sample volume.

The energy time τ_E will then be given by

$$\tau_E = \frac{C_{el}}{K_L}$$

$$= \frac{3 n k v}{2 K_L} \qquad .. (3.34)$$

For a typical value of 2 μW power dessipation, $T_e \sim 2.3^{\circ}K$, $K \doteq 11\mu W.{}^{\circ}K^{-1}$ from Figure (3.13) and $n = 4.1 \times 10^{11}$ cm^{-3}, then

$$S = \frac{3}{2 T_e K} = 5.83 \times 10^4 \ W^{-1} \qquad .. (3.35)$$

This value is very close to that reported for InSb sample at $2^{o}K$ (19).

Also for the investigated sample with $v = 3.4\ mm^3$ we have

$$\tau_E \cong 2.6 \times 10^{-9} \text{ secs.} \qquad .. (3.36)$$

Appendix

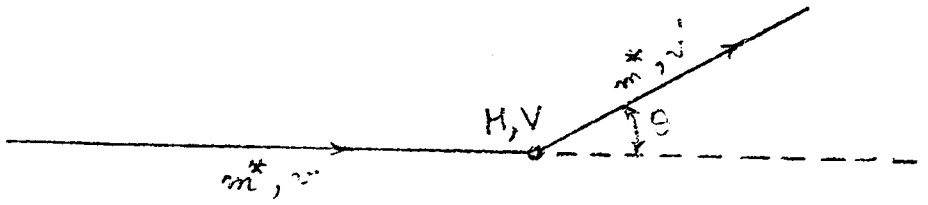

From the shown figure, using the simple collision laws (momentum and energy conservation) it is easy to prove that

$$\left(\frac{v'}{v}\right)^2 - \frac{2m}{M+m}\,\frac{v'}{v}\cos\theta - \frac{M-m}{M+m} = 0 \qquad \ldots (A.1)$$

where m = m* for simplicity

and M is the impurity atom mass.

$$\therefore \left(\frac{v'}{v}\right) = \frac{m}{M+m}\cos\theta \pm \left[\left(\frac{m}{M+m}\right)^2 \cos^2\theta + \frac{(M-m)}{(M+m)}\right]^{\frac{1}{2}}$$

$$= \frac{m}{M+m}\left\{\cos\theta \pm \left[\cos^2\theta + \frac{(M-m)(M+m)}{m^2}\right]^{\frac{1}{2}}\right\}$$

$$= \frac{1}{M+m}\left\{m\cos\theta \pm \left[M^2 - m^2(1-\cos^2\theta)\right]^{\frac{1}{2}}\right\}$$

$$= \frac{1}{M+m}\left\{m\cos\theta \pm \left[M^2 - m^2\sin^2\theta\right]^{\frac{1}{2}}\right\}$$

$$\text{i.e. } \left(\frac{v'}{v}\right) = \frac{M}{M+m}\left[\left(1 - \frac{m^2}{M^2}\sin^2\theta\right)^{\frac{1}{2}} + \frac{m}{M}\cos\theta\right]$$

$$\therefore \left(\frac{v'}{v}\right)^2 = \frac{M^2}{(M+m)^2}\left[1 - \frac{m^2}{M^2}\sin^2\theta + \frac{m^2}{M^2}\cos^2\theta + \frac{2m}{M}\cos\theta \left(1 - \frac{m^2}{M^2}\sin^2\theta\right)^{\frac{1}{2}}\right]$$

$$\left(\frac{v'}{v}\right)^2 - 1 = \frac{M^2}{(M+m)^2}\left[1 - \frac{M^2+2Mm+m^2}{M^2} - \frac{m^2}{M^2}(\sin^2\theta - \cos^2\theta) +\right.$$

$$\frac{2m}{M} \cos\theta \left(1 - \frac{m^2}{M^2} \sin^2\theta\right)^{\frac{1}{2}}\Bigg]$$

$$= -\frac{M^2}{(M+m)^2}\left[\frac{m^2}{M^2}(1 + \sin^2\theta - \cos^2\theta) + \frac{2m}{M}(1 - \cos\theta\right.$$

$$\left.(1 - \frac{m^2}{M^2} \sin^2\theta)^{\frac{1}{2}})\right]$$

$$\simeq -\frac{M^2}{(M+m)^2}\left[\frac{2m}{M}(1 - \cos\theta) + 2\frac{m^2}{M^2}\sin^2\theta\right]$$

$$= -\frac{M^2}{(M+m)^2} \cdot \frac{2m}{M}\left[(1 - \cos\theta) + \frac{m}{M}\sin^2\theta\right]$$

To first order in $\frac{m}{M}$

$$\Delta E = -\frac{2m}{M}(1 - \cos\theta).E \qquad \ldots (A.2)$$

where E is the electron energy.

This value of ΔE has to be averaged overall scattering angles. But if we consider the minimum scattering angle θ_m defined by

$$\tan\frac{\theta_m}{2} = \frac{R}{r_m}$$

where

$$R = \frac{Z e^2}{4\pi\epsilon m v^2}, \quad v \text{ is the electron thermal velocity}$$

and $r_m = \frac{1}{2}\left(\frac{1}{N_I}\right)^{1/3}$, N_I is the ionized impurity concentration

we find that θ_m is so large ($\sim 160^o$), then the value of ΔE will be approximately

$$\overline{\Delta E} \simeq \frac{-4m}{M} \cdot E \qquad \ldots (A.3)$$

Let the ionized impurity scattering time be τ. The mean rate of gain of energy of electrons of energy E due to collision is

$$\frac{\overline{\Delta E}}{\tau} \quad .$$

For ionized impurity scattering,[21]

$$\frac{1}{\tau} = \frac{Z^2 e^4 N_I \ln B^2}{16\pi (2m)^{\frac{1}{2}} E^{3/2} \epsilon^2} \qquad .. (A.4)$$

All the symbols used were defined before.

The logarithmic term varies slowly with electron temperature.

$$\therefore \quad \frac{\Delta E}{\tau} = - \frac{Z^2 e^4 N_I \ln B^2}{16\pi (2m)^{\frac{1}{2}} \cdot \epsilon^2} \cdot 4 \frac{m}{M} \frac{E}{E^{3/2}}$$

$$= -K E^{-\frac{1}{2}}$$

Averaging overall energies, mean rate of gain of energy will be given by

$$\left(\frac{dE}{dt}\right)_I = - \frac{K \int_0^\infty E^{-s} e^{-E/kT} E^{3/2} dE}{\int_0^\infty e^{-E/kT} E^{3/2} dE}$$

$$= -K (kT)^{-s} \Gamma(5/2 - s)/\Gamma(5/2)$$

with $s=\frac{1}{2}$

$$\left(\frac{dE}{dt}\right)_I = - \frac{K}{(kT)^{\frac{1}{2}}} \cdot \frac{\Gamma(2)}{\Gamma(5/2)} = - \frac{2K}{(kT)^{\frac{1}{2}}} \frac{1}{\Gamma(1+\frac{3}{2})}$$

$$= \frac{-2K}{(kT)^{\frac{1}{2}}} \cdot \frac{1}{\frac{3}{2}\Gamma(3/2)}$$

$$= \frac{-2K}{(kT)^{\frac{1}{2}}} \cdot \frac{2}{3} \quad \frac{1}{\frac{1}{2}\pi^{\frac{1}{2}}}$$

$$= \frac{-8K}{3\pi^{\frac{1}{2}}} \quad (k\,T_e)^{-\frac{1}{2}}$$

i.e. $$\left(\frac{dE}{dt}\right)_I = \frac{-8}{3\sqrt{\pi}} \quad \frac{Z^2\, e^4\, N_I \ln B^2}{16\,\pi\sqrt{2m} \quad \epsilon^2} \cdot \frac{4m}{M} \quad E^{-\frac{1}{2}} \qquad \text{.. (A.5)}$$

CHAPTER III

REFERENCES

(1) Miller, A. and E. Abrahams, Phys. Rev. 120, 745 (1960)

(2) Mikoshiba, N. and S. Gonda, Phys. Rev. 127, 1954 (1962)

(3) Mikoshiba, N., Phys. Rev. 127, 1962 (1962)

(4) Yafet, Y., R. Keyes and E. Adams, J. Phys. Chem. Solids 1, 137 (1956)

(5) Landsberg, P.T., Proc. Phys. Soc. (London) 71, 69 (1958)

(6) Sadasiv, G., Phys. Rev. 128, 1131 (1962)

(7) Fritzsche, H., Phys. Rev. 99, 406 (1955)

(8) Fritzsche, H., J. Phys. Chem. Solids 6, 69 (1958)

(9) Sladek, R.J. and R.W. Keyes, Phys. Rev. 122, 437 (1961)

(10) Gershenzon, E.M., Gurvich Yu A. and S.L. Orlava. Sov. Phys. - Solid State 11, 2743 (1970)

(11) Fink, D. and R. Braunstein. Solid State Communication (USA), 15 No.2, 1627 (1974)

(12) Conwell, E.M., Phys. Rev. 90, 769 (1953)

(13) Koenig, S.H., R.D. Brown and W. Schillinger. Phys. Rev. 128, 1668 (1962)

(14) Yoshihiro, K., M. Tokumoto and C. Yamanouchi. International conference on sub-millimetre waves and their applications, June 5, 6, 7 (1974)

(15) Lax, M. Phys. Rev. 119, 1502 (1960)

(16) Mott, N.F. and W.D. Twose, Advances in Phys. 10, 107 (1961)

(17) Zwerdling, S., R.A. Smith and J.P. Theriault, Infrared Phys. 8, 271 (1968)

(18) Gunn, J.B., Progress in semiconductors vol. 2, pp.213 (1957)

(19) Rollin, B.V., Proc. Phys. Soc. 77, 1102 (1961)

(20) Kinch, M.A. and B.V. Rollin, Brit. J. Appl. Phys. 14, 672 (1963)

(21) Smith, R.A. "Semiconductors", published by the syndics of the Cambridge University Press (1964) pp. 151

CHAPTER IV

FAR INFRARED ABSORPTION IN Ge AT LOW TEMPERATURES

4.1. Introduction

General extrinsic photoconductivity (Phototransition and free carrier absorption) in doped Ge represents a major process for far infrared absorption. As we have seen in Chapter I, phototransition is understood as a carrier transition from non-conducting to conducting states by the effect of photons. This occurs when the incident photon energy is equal to or slightly greater than the energy difference between the two states. In lightly doped Ge, the major type of extrinsic photo-transition is the transfer of carriers from the ground states to the conduction or valence bands, thus a change of the sample conductivity will result. This happens for quantum energies of $\sim$ 10-13 meV. However, due to the impurity interactions in practically doped samples, this ionization energy is reduced due to the higher excited states overlap. This effect lowers the bottom of the conduction band or raises the top of the valence band. It was shown by Fritzsche [1] that the ionization energy of isolated antimony atoms in Ge has reduced by more than 3 meV for samples in the intermediate doping concentration ($4.5 , 5 \times 10^{16}$ Sb.cm^{-3}). This was also supported for less doping concentrations by Nagazaka and Narita [2].

The purpose of the present chapter is to study the photo-transition characteristics in singly doped, intermediate concentration Sb-doped Ge and low concentration p-type compensated Ge at low temperatures. From these, the nature of the delocalized band responsible for the appearance of the activation energy ε_2 in the n-type sample is identified. The study includes transmission spectra measurements at 1.5^{o}K in the far infrared region. The hot electron phenomenon and free carrier absorption were also considered through the dc measurements

and actual quantum detection and compared with the phototransition effect mainly in the n-type sample. The absorption behaviour is also given for a biased crystal with identical mount as that used for the best detectors developed.

4.2. Photo-transition; measurements and discussion

These measurements were done using the fourier transform spectrometer and an indium antimonide detector. The sample has a parallel-faced disc shape of 0.25 mm and 0.31 mm thickness for the n-type and p-type samples respectively. Both samples were immersed in liquid helium at 1.5°K. Interference fringes were observed in the fractional external transmission which were geometrically averaged. The absorption coefficient α, extinction coefficient k and reflection coefficient r spectra were then computed using the iteration method used by Zwerdling et al.[3]

The absorption coefficient α is related to the geometrically averaged ratio transmission T and the reflection coefficient r as

$$\alpha = \frac{1}{d} \ln \left[\frac{(1-r)^2}{2T} + \left\{ \left[\frac{(1-r)}{2T} \right]^2 + r^2 \right\}^{\frac{1}{2}} \right] \quad .. (4.1)$$

where d is the sample thickness.

The relation between r and the real part of refractive index n and the imaginary part (extinction coefficient) k is

$$r = \frac{(n-1)^2 + k^2}{(n+1)^2 + k^2} \quad .. (4.2)$$

Also k is related to α at any wavelength λ as

$$k = \frac{\alpha\lambda}{4\pi} \quad .. (4.3)$$

As a first approximation, we neglect k in (4.2) and using $n = 4.1$ [3] for Ge, a value of r is obtained which is substituted in

(4.1) to give a value of α at a selected wavelength λ. The obtained value of α is then substituted in (4.3) to give a value of k from which a better value of r and α can be obtained etc. Twenty iterations have been performed at each wavelength and final values of α, r and k were obtained. Figures (4.1), (4.2), (4.3) and (4.4) show the plots of T, α, k and r spectra respectively.

Measurements with dc fields have also been carried out on the n-type sample with dimensions of 2.2 x 2 x 0.8 mm^3. They include the I.V. characteristics at 1.7^oK at constant lattice temperature. The element is mounted in a detector cryostat system by soldering it to the copper block via an intermediate silver base which was in efficient thermal contact with the liquid helium bath. The measurements were taken with and without exposure to room temperature quantum energies less than 6.2 meV. The short wavelength cutting was obtained by cooled filters at the same low temperature. The spectral response of these filters were tested regarding the high energy leakage and proved to be quite efficient at the high energy end of the spectrum. The composition of these filters and their spectral characteristics will be shown in Chapter VI. The temperature rise of the crystal during the measurements was found to be less than 0.1^oK for electric fields up to 10 $V.cm^{-1}$ (thermal conductivity of Ge at 2^oK is 13 watts $(cm.^oK)^{-1}$). Figure (4.5) shows log R vs log F characteristics in the two cases.

The absorption coefficient α in Figure (4.2) for the n-type sample shows a broad maximum at about 5 meV quantum energy, followed by a minimum at about 6.5 meV from which α starts to increase more rapidly with quantum energy. The broad maximum at $\sim$ 5 meV could be phototransition either from the ground state to the first excited state ($2p, \pm 0$) which lies about 5.3 meV above the ground state or from the first excited state to the continuum conduction band. But the variation of α spectrum with frequency indicates that the transition

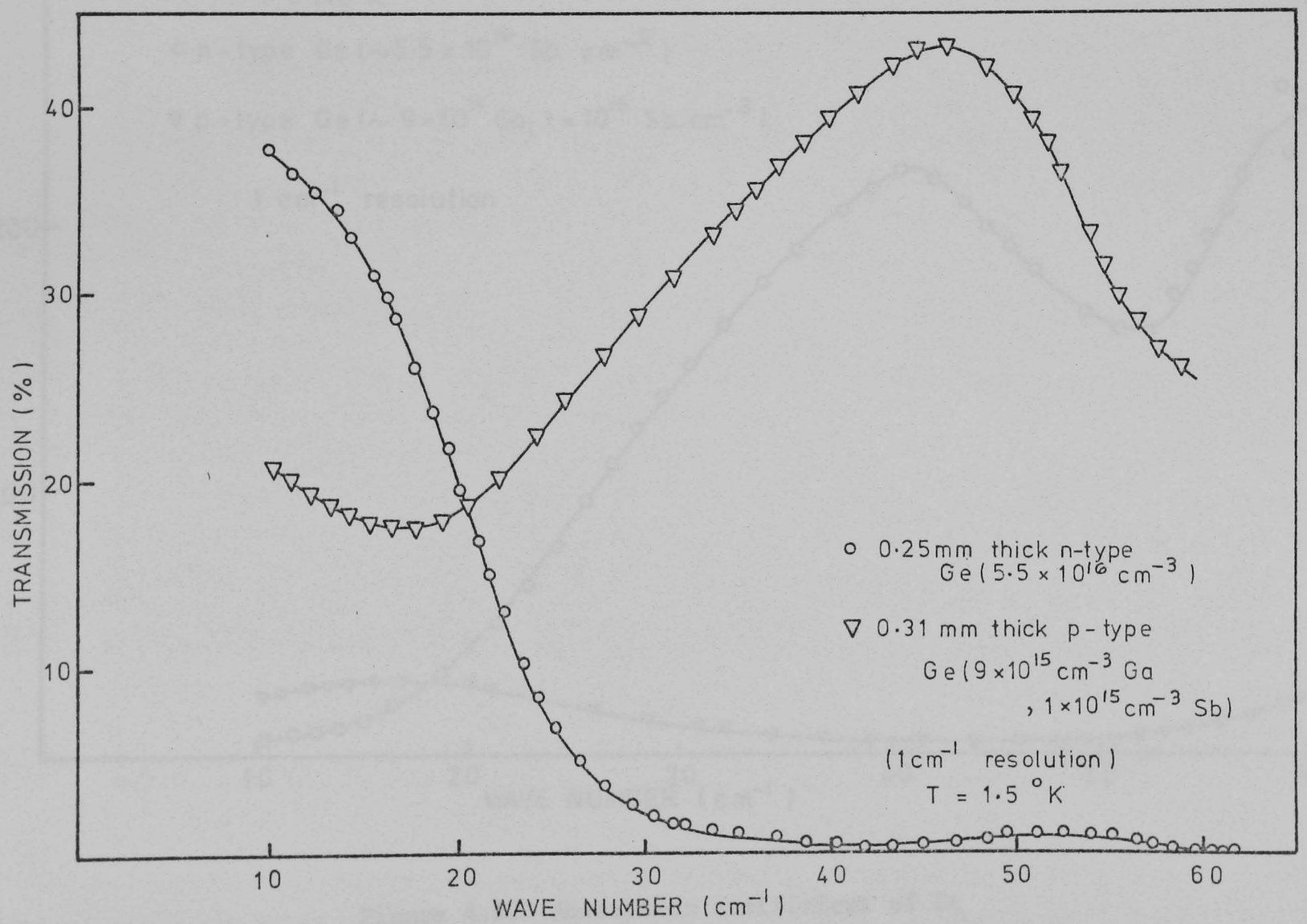

Figure 4.1. Transmission spectra of Ge in far infrared

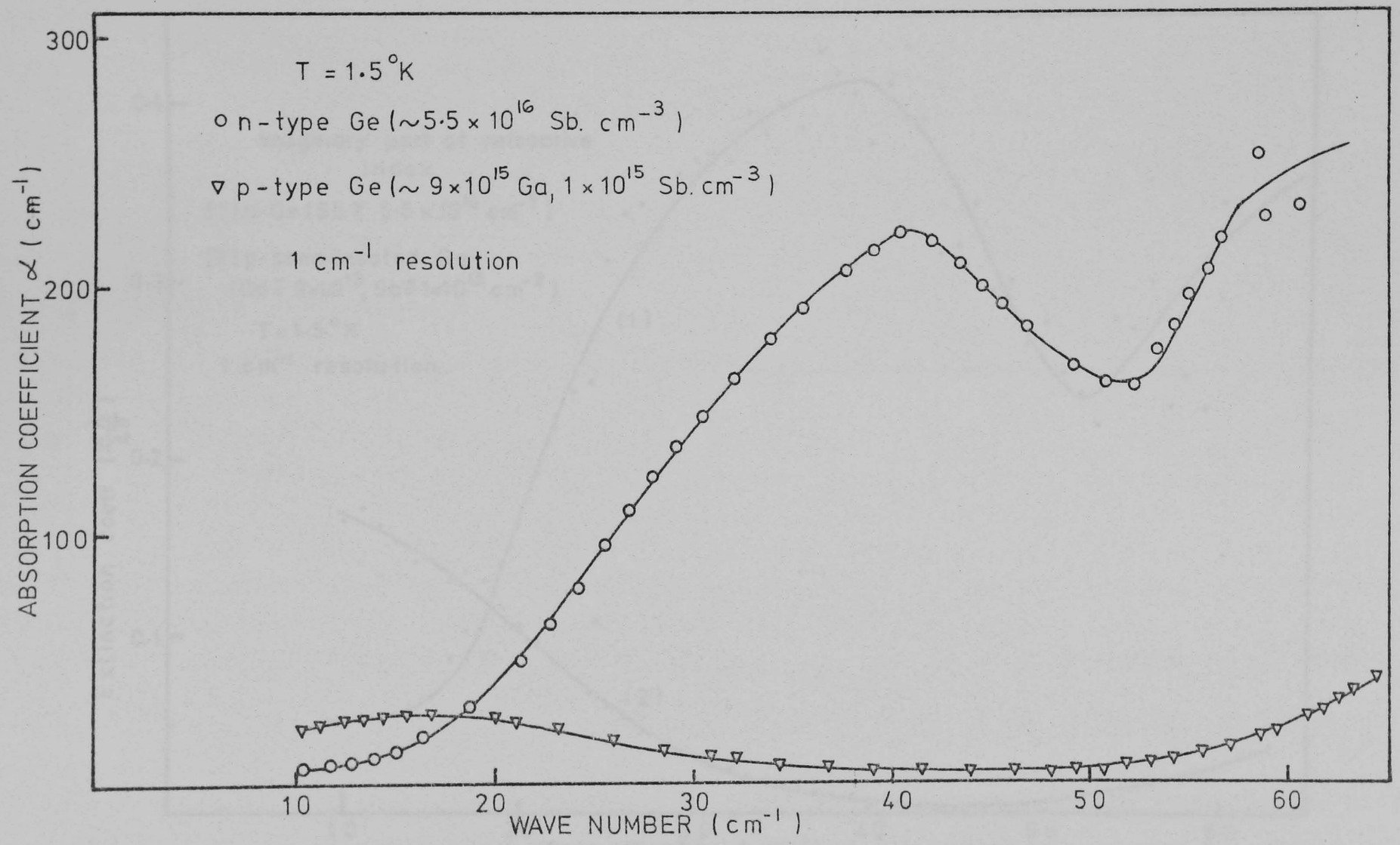

Figure 4.2. Absorption coefficient of Ge

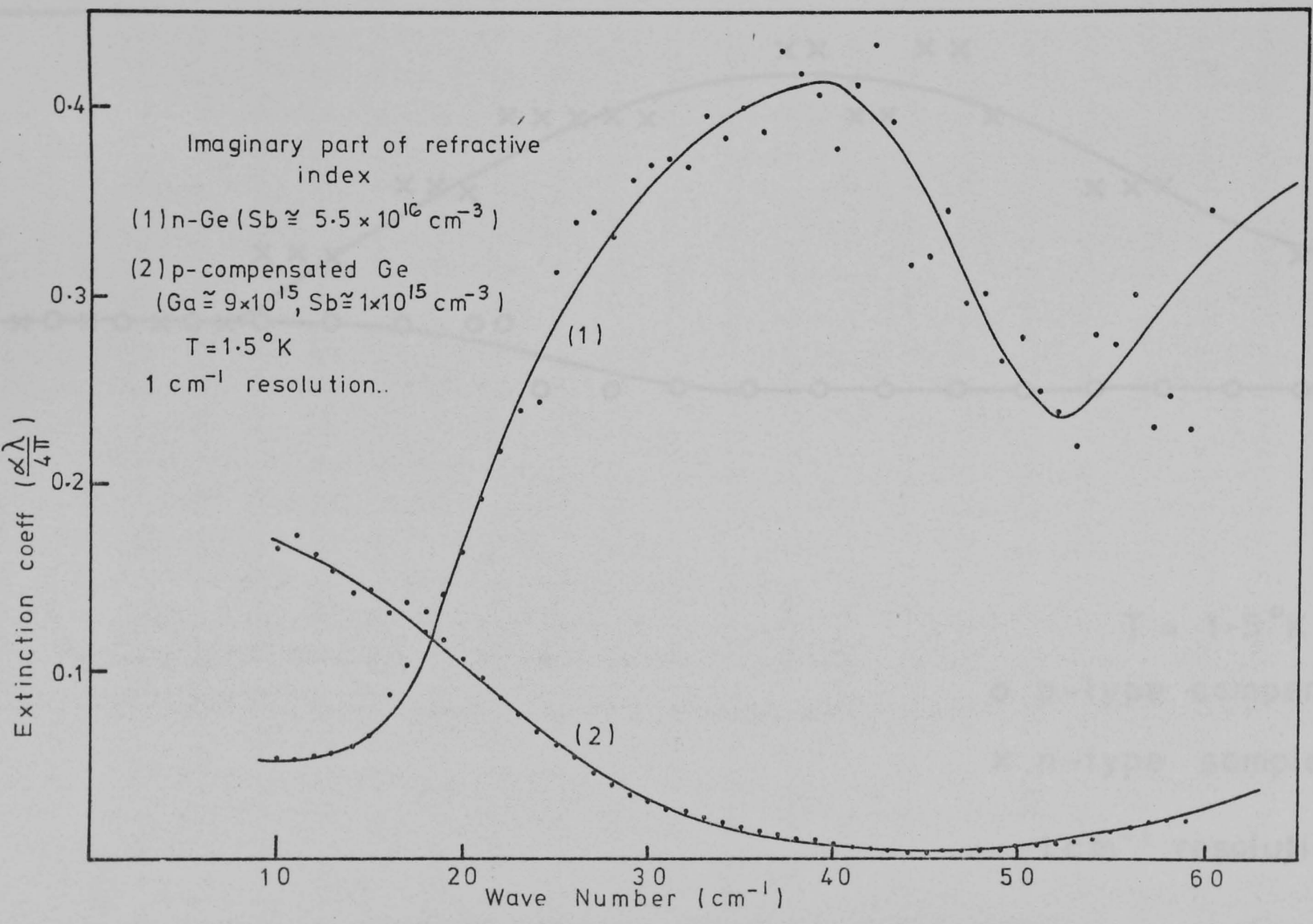

Figure 4.3. Extinction coefficient spectra of two Ge samples

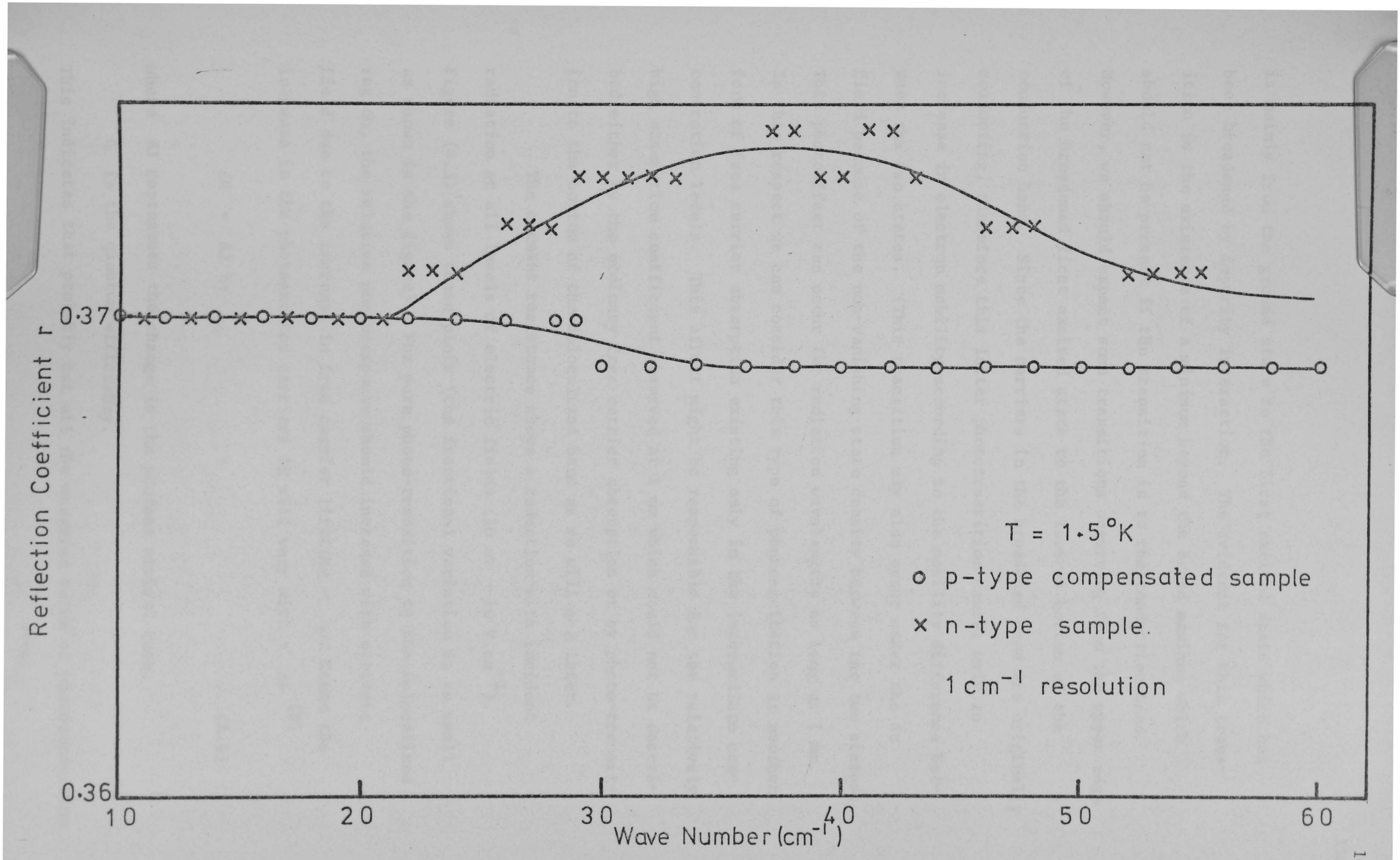

Figure 4.4. Reflection coefficient spectra of two Ge samples

is mainly from the ground state to the first excited state which has been broadened by impurity interaction. The evidence for this transition is the existence of a minimum beyond the broad maximum which should not be present if the transition is to the conduction band. However, we should expect some transitions occurring from the upper edge of the broadened first excited state to the lowered bottom of the conduction band. Since the carriers in the broadened band are originally conducting, therefore this latter phototransition causes only an increase in electron mobility according to the mobility difference between the two states. (This transition may also occur under the dc field because of the non-vanishing state density between the two states). This photoeffect can occur for radiation wavelengths as long as 1 mm. In this respect we can consider this type of photoexcitation as another form of free carrier absorption existing only in the intermediate concentration levels. This effect might be responsible for the relatively high absorption coefficient observed at 1 mm which could not be described either by the ordinary free carrier absorption or by photo-transition to the bottom of the delocalized band as we will see later.

The element resistance shows a reduction with incident radiation at all levels of electric fields (10 mV - 10 $V.cm^{-1}$). Figure (4.5) shows these plots (the fractional variation is so small as shown in the figure). For pure photo-transition to the delocalized region, the relative photoresponse should increase with electric field due to the increase in free carrier lifetime τ and hence the increase in the photoexcited carriers ΔN will vary with τ as [8]

$$\Delta N = \Delta J \, \eta\tau \qquad .. (4.4)$$

where ΔJ represents the change in the photons arrival rate,

η is the quantum efficiency.

This indicates that probably not all the measured value of photoconduction

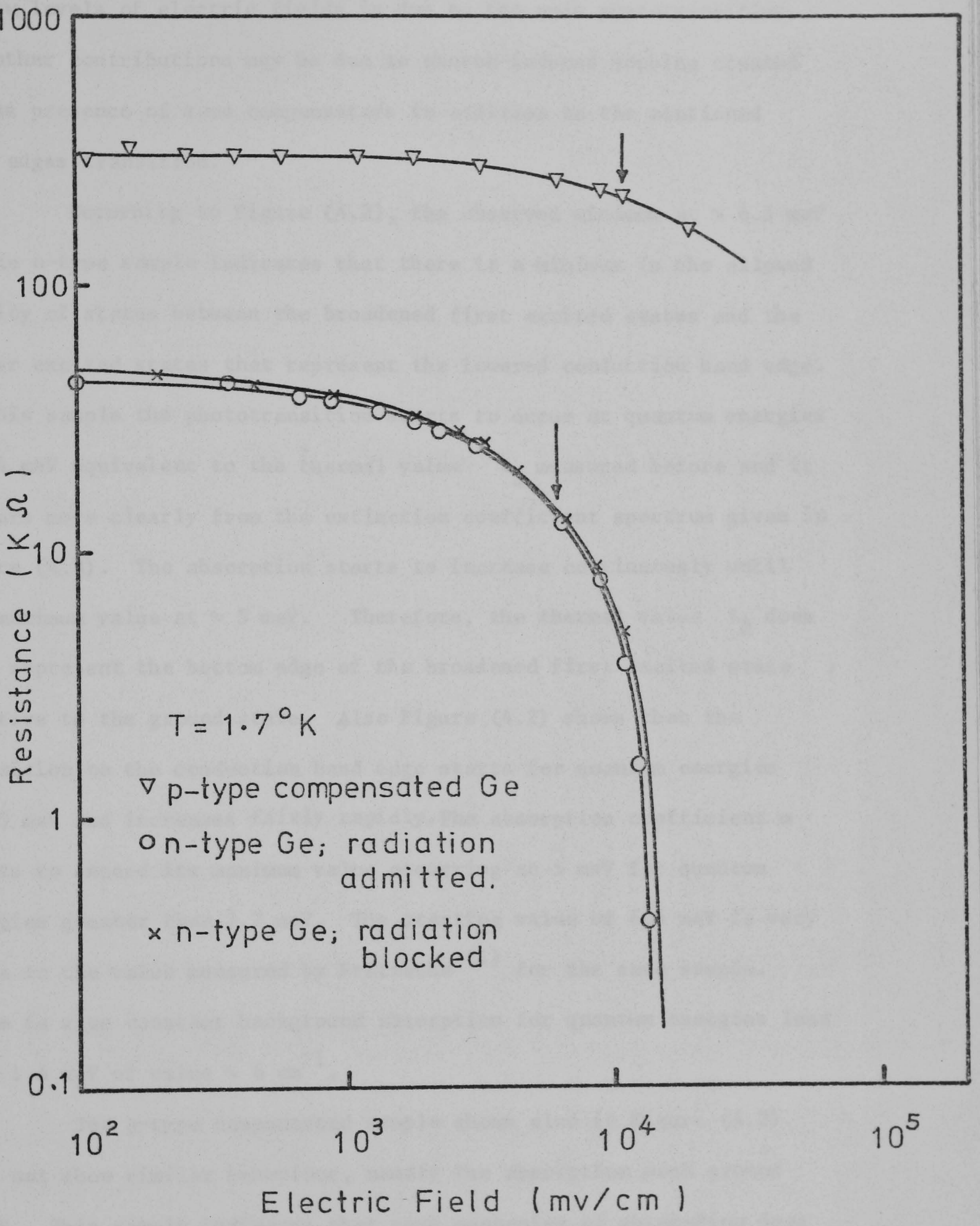

Figure 4.5. Electric field dependence of resistance under Fixed Lattice Temperature

at low levels of electric fields is due to the main phototransition. The other contributions may be due to photon-induced hopping created by the presence of some compensators in addition to the mentioned band edges transition.

Returning to Figure (4.2), the observed minimum at $\sim$ 6.5 meV in the n-type sample indicates that there is a minimum in the allowed density of states between the broadened first excited states and the higher excited states that represent the lowered conduction band edge. In this sample the phototransition starts to occur at quantum energies $\sim$ 1.4 meV equivalent to the thermal value ε_2 measured before and it appears more clearly from the extinction coefficient spectrum given in Figure (4.3). The absorption starts to increase continuously until its maximum value at $\sim$ 5 meV. Therefore, the thermal value ε_2 does then represent the bottom edge of the broadened first excited state relative to the ground state. Also Figure (4.2) shows that the transition to the conduction band edge starts for quantum energies $\sim$ 6.5 meV and increases fairly rapidly. The absorption coefficient α starts to exceed its maximum value occurring at 5 meV for quantum energies greater than 7.2 meV. The starting value of 6.5 meV is very close to the value measured by Fritzsche [1] for the same sample. There is also constant background absorption for quantum energies less than 1.4 meV of value $\sim$ 6 cm^{-1}.

The p-type compensated sample shown also in Figure (4.2) does not show similar behaviour, namely the absorption peak around 5 meV. This simply indicates that such mechanism of absorption does not exist, i.e. phototransition of carriers to any intermediate band between the ground state and the ~~conduction~~ valence band. But rather there exists a broad maximum around 16 cm^{-1} which is attributed to photon-induced hopping transitions without phonon assistance [4,5].

4.3. Free carrier absorption

The classical formula used for free carrier absorption coefficient α_F is

$$\alpha_F = \frac{\sigma_o}{c\, K_o\, K^{\frac{1}{2}}} \cdot \frac{1}{1+(w\tau)^2} \qquad .. (4.5)$$

where

σ_o is the zero frequency conductivity of the element,

K is the dielectric constant,

τ is the momentum relaxation time and w is the frequency of incident radiation, c is the velocity of light.

For n-type sample when $w\tau << 1$:

At 4.2^oK, $\sigma_o = 5 \times 10^{-2}\ (\Omega\text{-cm})^{-1}$ and $\alpha_F = 4.7\ cm^{-1}$.

At 1.7^oK, $\sigma_o = 10^{-4}\ (\Omega\text{-cm})^{-1}$ and $\alpha_F = 0.01\ cm^{-1}$.

(this is due to the delocalised band contribution only).

The value at 1.7^oK is much smaller than the measured value of background absorption at 1 mm wavelength of 6 cm^{-1}. Therefore, other mechanisms should be involved at these wavelengths. The mentioned band edges transition, photon-induced hopping and molecular excitation[10] might be responsible for this absorption.

The value of α was taken under zero bias conditions, in which case, the conductivity and α_F is minimum. The value of σ and α_F increases with increasing electric field due to electron heating and carriers multiplication but at the expense of mobility sensitivity because it depends inversily on the carrier concentration (equation 3.28). The essential photoionization part also increases with electric field due to the decrease in recombination parameters. This field enhanced ionization was understood by Picus [11] as to reduce the sticking

probability of the thermally trapped carriers, i.e. reduce the probability that a trapped electron will fall eventually to the ground state than to be re-excited. It should also be noted here that any free carrier absorption and band edge transitions with subsequent mobility change does not imply similar conductivity change in the unbiased crystal at 1.7°K. The reason for that is the domination of localized (hopping) motion. The free carrier conduction must dominate the overall conductivity and hence a change in the carrier mobility and concentration change ΔN (equation 4.4) of the delocalized carriers will then produce similar change in the overall conductivity. As we have seen before, the hopping conduction will dominate at a temperature below $\sim$ 2.3°K, in which case the corresponding conductivity change will not be adequate if the lattice temperature is held constant. On the other hand, the absorption mechanism of any kind will become more useful at lowest temperature if the lattice temperature follows the absorbed energy (weak link between the crystal and the heat sink) in such a case the detector will be a thermal bolometer rather than a quantum detector. At 1.7°K for the tested n-type sample, the contributions from the delocalized band motion to the overall conductivity is about 30%. Therefore, the mentioned photoeffect will be reduced by nearly the same ratio.

4.4. Sb-doped Ge as a quantum detector; Responsivity and time response

The element used for Figure (4.5) was tested as a detector under fixed lattice temperature conditions for frequencies up to 1 kHz. The photo-responsivity as a function of electric field across the sample is shown in Figure (4.6). The noise characteristics nearly follow the same change in photo-response resulting in much less variation in signal-to-noise (S/N) ratio. The mechanism of this behaviour is not

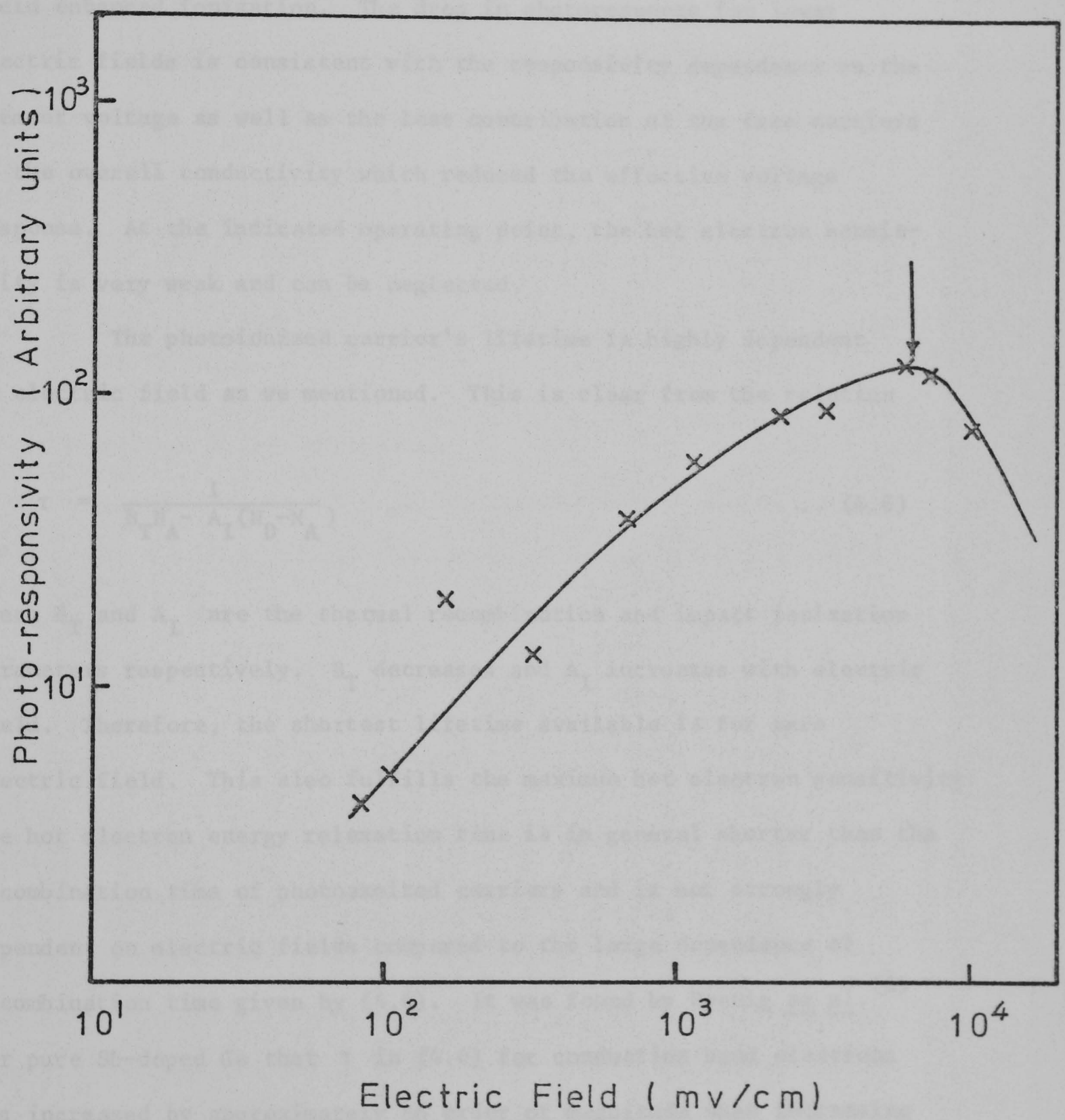

Figure 4.6. Electric Field dependence of photo-response in the n-type sample

understood.

The admitted radiation has a maximum quantum energy of $\sim$ 6.2 meV, higher than the absorption peak energy but lower than the conduction band edge observed (6.5 meV). The relatively high electric field for optimum performance emphasises the last argument about the field enhanced ionization. The drop in photoresponse for lower electric fields is consistent with the responsivity dependence on the element voltage as well as the less contribution of the free carriers to the overall conductivity which reduced the effective voltage response. At the indicated operating point, the hot electron sensitivity is very weak and can be neglected.

The photoionized carrier's lifetime is highly dependent on electric field as we mentioned. This is clear from the relation

$$\tau = \frac{1}{B_T N_A - A_I (N_D - N_A)} \qquad .. (4.6)$$

where B_T and A_I are the thermal recombination and impact ionization parameters respectively. B_T decreases and A_I increases with electric field. Therefore, the shortest lifetime available is for zero electric field. This also fulfills the maximum hot electron sensitivity. The hot electron energy relaxation time is in general shorter than the recombination time of photoaxcited carriers and is not strongly dependent on electric fields compared to the large dependence of recombination time given by (4.6). It was found by Koenig et al.[6] for pure Sb-doped Ge that τ in (4.6) for conduction band electrons has increased by approximately an order of magnitude when increasing electric field from 1 to 4 v/cm and increases more rapidly beyond that. The lowest value reported by the author is slightly less than 10^{-7} sec. Therefore, since τ depends inversily on N_A (neglecting

the A_I term for low electric fields), then the expected value of τ in the ohmic region in our sample should be very short by nearly the same amount of N_A difference. In this sample N_A is expected to be two or three orders of magnitude higher than in the Koenig samples.

4.4.1. Hot electron responsivity and response time

At very low electric fields where the hot electron phenomenon has some effect in producing conductivity change, the responsivity is expressed as

$$\mathcal{R} = \frac{BV}{\sigma v} \qquad .. (4.7)$$

$B = \frac{1}{\sigma} \frac{d\sigma}{d(F^2)}$ is the hot electron parameter,

V is the voltage across the crystal,

v is the crystal volume and σ is the conductivity at the operating point. For V = 19 mV across the sample of volume 2.2 x 2 x 0.8 mm^3, the value of B from figure (3.12) is $\sim 0.1\ cm^2 \cdot v^{-2}$ and σ is $3.2 \times 10^{-4}\ (\Omega.cm)^{-1}$ then,

$$\mathcal{R} = 1.68\ kv/w \qquad .. (4.8)$$

This is a dc value and does not take into account the actual free carrier absorption ~~emissivity~~ efficiency. If the measured value of background absorption coefficient of 6 cm^{-1} does generally represent the free carrier absorption including the other mentioned mechanisms at the longest wavelength of the IR spectrum where the phototransition is absent, then the quantum efficiency η given by

$$\eta = (1 - r)(1 - e^{-\alpha d}) \qquad .. (4.9)$$

will be ~ 0.24

where r is the reflection coefficient ∿ 0.37 and d is the crystal thickness (0.8 mm) and the radiation responsivity will be

$$\mathcal{R}(w) = 405\ v/w \qquad .. (4.10)$$

The calculated value of η assuming the classical free carrier absorption coefficient α_F (0.01 cm^{-1}) is extremely small and does not agree with the measured value of responsivity at very low electric fields and for wavelengths longer than 500μm. This was achieved by operating the detector with additional low frequency pass filter consisting of 3 mm thick high density black polyethylene blocking the external window at room temperature. This filter has a maximum transmission of about 60% starting at about 600μm falling to about 10% at 250μm. This together with the low electric field, makes the dominant response is for the free carrier and the background absorption. The phototransition responsivity at low electric fields is given by

$$\mathcal{R} = -I\left(\frac{\partial R}{\partial Q}\right)_v \qquad .. (4.11)$$

where I is the dc bias current and $\left(\frac{\partial R}{\partial Q}\right)_v$ is the change in the element resistance with the actual incident radiation at constant bias voltage. From the measured value of $\left(\frac{\partial R}{\partial Q}\right)_v$ this will give a value for $\mathcal{R} \simeq 100$ v/w which is less than 25% of the background response. Further, the detector was checked by an additional very narrow band pass filter (∿ 3 cm^{-1} width) with maximum transmission of about 40% centred at about 1.3 mm wavelength and the response was quite consistent with the above measurements. From the photoresponse ratio with and without the additional 3 mm filter assuming Rayleigh-Jeans approximation to hold, the hot electron responsivity is about 200 v/w giving an average value of α_F for the free carrier absorption of ∿ 1.64 cm^{-1}.

(We assumed here that the optical thickness in the absence of the filter is very large and hence the value of emissivity η is $\sim (1-r)$.).

Comparison with InSb hot electron detectors [8] regarding the performance data and operating conditions are

Parameter	InSb	Ge
B $(cm^2.v^{-2})$	20	0.1
V (mV)	10	19
Rdc (v/w)	130	1680
v (cm^3)	5×10^{-3}	3.52×10^{-3}
σ $(\Omega.cm)^{-1}$	0.3	$\sim 3.2 \times 10^{-4}$
η	~ 0.6	~ 0.11

$$\frac{(\frac{S}{N}) \text{ in InSb}}{(\frac{S}{N}) \text{ in Ge}} = 1.14$$

In Ge case, the cooled 200μm filter should be present in all tests to prevent the photon noise which is not the case for InSb. These filters present about 30% loss of the incoming radiation resulting in a reduction in signal response.

As the electric field across the Ge element increases beyond 1 v/cm, the value of B changes to 0.05 $cm^2.v^{-2}$ which would decrease the hot electron effect. However, the increase in the field enhances the domination of photoionization response.

The energy relaxation time in Ge is much shorter than in InSb due to the lower concentration and hence the thermal capacity of the hot carriers in Ge. The value given for τ_E in the last chapter of $\sim$ 3 n sec. makes Ge superior to InSb for the combined response and time constant requirements. These requirements are essential for line

detection (mixers) applications. We attempted to measure the response time at low electric fields by purely electrical means using the bolometer bridge described by Jones [9] as shown in Chapter II. This method uses the dynamical properties of the crystal under ac fields. The crystal responds to an ac signal at a given frequency if the impedence to such a signal is equal to the dynamic value $\frac{dV}{dI}$ at the operating point. The off-balance potential difference in the bridge output gives the value of responsivity at a given frequency. For signal time duration shorter than the response time, the impedance will rise to the original static value $\frac{V}{I}$ at which the bridge was originally balanced, therefore giving zero responsivity at this frequency. Because the responsivity deduced by this method uses the modulation of the dc field with very low electric field operating point, then the time measured by this method will be the hot electron relaxation time. Due to the high frequency effects, these measurements are considered correct up to frequencies of about 1 MHz. But we found that the measurements extended satisfactorily up to 10 MHz after which the responsivity drops gradually to zero followed by other disturbances in the bridge output. The bridge elements were shielded by metallic box and the bolometer element was connected to the bridge via high frequency coaxial cable from outside the cryostat. This can give a rough estimation that the hot electron time response is less than 10^{-7} sec ($\sim$ 1 MHz). For more accurate measurements (fast pulse techniques), we expect the value of 3 n sec can be obtained.

Another attempt to measure the crystal time response was made using a practical mixer system. Heavier doped sample ($\sim 7.5 \times 10^{16}$ cm^{-3}) was required to reduce the crystal resistance for matching requirements. The crystal resistance had about 300 Ω resistance at 20 torr helium pressure and was mounted in a waveguide suitable for 115 GHz (2.6 mm) klystron frequency. The klystron power was modulated by a signal

generator, so that a crystal response to such a modulation frequency could be detected. A detected frequency up to 250 kHz was observed ($\sim 6 \times 10^{-7}$ seconds). This time response is longer than what was expected. But, the tested crystal and the radiation wavelength used were mainly different from the spectrally tested samples such that the exact absorption mechanism involved at such wavelength is not known.

4.4.2. Photoionization responsivity and response time

Photoionization response in this crystal is very high due to the large absorption coefficient α as shown in Figure (4.2). This makes such material very efficient as a photoionization detector for wavelengths up to 500μm at which the smallest value of α is about 40 cm^{-1}. This will require an optimum crystal thickness of 0.25 mm. The peak value of $\alpha \sim 220$ cm^{-1} occurring at about 250μm wavelength allows an optimum thickness as small as 50μm. Reducing the element volume will increase the quantum responsivity by nearly the inverse ratio.

For the same tested element, the point indicated by an arrow in Figure (4.5) represents the optimum performance (maximum $\frac{S}{N}$ ratio) as a photoionization detector, whereas the hot electron and the background responses should be nearly absent. The photoionization responsivity in this case is given by (8)

$$\mathcal{R} = \frac{-R_L Z \cdot V_B}{(Z+R_L)(R+R_L)} \cdot \frac{\eta \tau}{N h\nu} \qquad .. (4.12)$$

where N represents the total number of the delocalized band carriers

R and Z are the static and dynamic impedances respectively at the operating point.

R_L is the load resistor and V_B is the bias battery voltage.

For responsivity measurements, we usually use a human hand as a constant

temperature source, the input power was calculated assuming Rayleigh-Jeans approximation where $kT >> h\nu$, from which

$$Q = \frac{2kT}{c^2} A.\Omega \int_{\nu_1}^{\nu^2} \nu^2 f(\nu)\, d\nu \qquad .. (4.13)$$

where c is the velocity of light and T is the temperature difference between the source and the background.

A is the detector input aperture and Ω is the source solid angle at the detector aperture. ν is the radiation frequency. Calculating the value of Q for a hand temperature of $37^{o}C$ ($19^{o}C$ above the background) assuming blackbody emission, with $A = \frac{\pi}{4}\ cm^2$ and $\Omega = 2\pi$ and taking $\nu = 1.2 \times 10^{12}$ Hz ($\equiv$ 250μm wavelength), if we allowed for the spectral characteristics of the cooled filters and for $\eta = 0.6$, we get

$$Q = 0.33 \times 10^{-6} \text{ watts}$$

The measured crystal output voltage was 8.5×10^{-5} volts. Then the responsivity is

$$\mathcal{R} = 260 \text{ v/w}$$

Other allowance has to be made for the actual radiation hitting the crystal surface because the crystal does not cover the whole exit cone aperture. The area ratio between the exit aperture (5 mm diameter) and the crystal surface is ~ 4.5, and since the bottom of the cylindrical cavity was flat in this mount (this was avoided later by making the bottom part hemispherical), then the actual value of Q should be divided by this factor and we have,

$$Q = 0.073 \times 10^{-6} \text{ watts} \qquad .. (4.14)$$

and

$$\mathcal{R} = 1.17 \text{ kv/w} \qquad .. (4.15)$$

Substituting this value of $\mathcal{R}$ in (4.12) and using the measured values of Z and R at the operating point (6 and 13 kΩ respectively) a value of τ/N was found to be

$$\frac{\tau}{N} = 3.24 \times 10^{-18} \text{ seconds} \qquad .. (4.16)$$

From the Hall coefficient measurements, the value of carrier concentration n at the operating electric field is $\sim 1.2 \times 10^{12}$ cm^{-3}. This will give a total number of carriers in the sample of 4.22×10^{9}, then

$$\tau \simeq 1.4 \times 10^{-8} \text{ seconds} \qquad .. (4.17)$$

The value of $\frac{\tau}{N}$ is also related to the change of element resistance R with the absorbed radiation Q at constant voltage $(\frac{\partial R}{\partial Q})_V$ as

$$\frac{1}{R}\left(\frac{\partial R}{\partial Q}\right)_V = \frac{-\eta\tau}{Nh\nu} \qquad .. (4.18)$$

From the measurements of R vs electric field with and without radiation, the change of the element resistance was found to be about 100 Ω. The estimated value of Q by the last method is 1.15 μ watts. Substituting in (4.18) we find

$$\frac{\tau}{N} = 7.9 \times 10^{-18} \qquad .. (4.19)$$

For the mentioned value of N we get

$$\tau \simeq 3.3 \times 10^{-8} \text{ seconds} \qquad .. (4.20)$$

Those values of τ in (4.17) and (4.20) are consistent within the experimental accuracy. The difference is probably because the measured value of $(\frac{\partial R}{\partial Q})_V$ was deduced from large signal condition by blanking the whole background radiation while the responsivity measurements was made under small signal conditions. Other source of error may arise

from the assumption of blackbody characteristics of the human hand from which the value of ℝ and hence τ are under estimation.

4.5. Photoconduction in p-type compensated Ge

A p-type compensated Ge sample (9×10^{15} Ga, 1×10^{15} Sb/cm^3), having dimensions of $5 \times 2 \times 1$ mm^3, was polished, etched and mounted in an identical way as the n-type sample. For the same filters setting, admitting maximum quantum energy of 6.2 meV, the photoresponse is much smaller than the n-type sample. The electric field for optimum performance was found to be 11.5 v/cm. The fact that this sample does not show any conduction contribution from a delocalized band similar to that existing in the n-type sample, leads to that large reduction in photoresponse. The main photoresponse mechanism existing is the photon-assisted hopping which has its maximum absorption at ~ 16 cm^{-1} (2 meV). The maximum absorption coefficient α is ~ 27 cm^{-1}. Although the crystal is optically thick for this value of α, the photoresponse is much weaker than for the n-type sample taking into account the power dependence on ν^2 at both absorption peaks. Also it seems clear from this operating voltage that the photon-assisting hopping is also enhanced by electric field. Both n-type and p-type samples showed some similarity regarding the positions of the operating point w.r.t. the end of the ohmic region.

For photon induced hopping, the exciting quantum energy should not be less than the energy difference between two hopping centres. In this sample, the energy difference $\Delta E \simeq 2\ \varepsilon_3$ is equal to 1.7 meV which is close to 2 meV for maximum absorption. The small concentration of valence band holes may exhibit some absorption and hence hot carrier effect. These free carriers might also take part in the observed non-linearity in Figure (4.5) at relatively high fields. We expect that the main reason for the observed non-linearity in this sample is the

change in recombination parameters with electric field which results in a change of the hopping distance and time.

The mobility sensitivity $S \alpha n^{-1}$ in the p-type sample should be much higher for the same number of minority ionized centres as in the n-type sample due to the smaller number of free carriers. But the small absorption by such carriers together with the higher effective mass of holes inhibits the observation of such phenomenon. However, this p-type sample works in optimum conditions when mounted as a thermal detector at much lower bias voltage ($\sim$ 2 v/cm) and the response drops appreciably when increasing the bias as we will see later. This, we think does not contradict the observed high electric field performance ($\sim$ 11.5 $v.cm^{-1}$) at constant lattice temperature conditions because the enhancement of hopping transitions could be achieved either by electric field or by lattice temperature increase. The thermal element is always at a temperature higher than the bath temperature when biased. Therefore we think that the combined effect of lattice temperature rise caused by the 2 $v.cm^{-1}$ on the phototransition is equivalent to the effect of electric field (11.5 v/cm) on the same transition.

4.6. Bias dependent spectral transmission of the n-type detector element

It is of great importance to study the spectral properties of the detector element used to develop our best detectors in the best mounting configuration. For this purpose, the spectral transmission was measured for different values of crystal biasing in a wide range of radiation wavelengths (50-2000μm) using Ge detector. The element used is identical to that used in one of the best detectors in doping concentration and cut out from the same grown cyrstal. The crystal has dimensions of 3 x 3 x 0.1 mm^3 and has a resistance at pumped helium temperatures very similar to that used in the good detector

(∿ 1.5 MΩ at 1μ watt power dissipation). After polishing and etching, the crystal was mounted in a secondary copper block similar to the main detector block. The detector mounting and wiring system will be explained in Chapter VI. The tested crystal is identical in mounting to the main detector cyrstal and having the same thermal conductions to the helium bath such that at a given bias power both elements have the same temperature rise above the heat sink temperature. The secondary block was designed to restrict gradually the incident radiation aperture from 5 mm to 2.5 mm in diameter, beyond which the tested element was completely covering this limited aperture. The transmitted radiation was then detected by the main element. Figure (4.7) shows the secondary block with the crystal position as well as the location of the secondary block in the optical arrangement. Changing the bias power for the tested crystal was done by changing the load resistor connected in series with the element at constant bias battery (apart from that used for the detector).

The spectral transmitted power at each bias was ratioed against background spectrum (taken in the absence of the tested element) Six spectra of ratio transmission were performed including the no bias case. The average of two spectra were taken in each case including the background. The series load resistors connected were 5, 2, 1, 0.5 and 0.25 MΩ in addition to the open circuit condition (the bias battery has the value of 8.1 volts). These values of loads give the operating points shown on the load curve, Figure 4.8, and marked as 1, 2, 3, 4 and 5 respectively.

In these measurements, we have not seen any noticeable difference of the spectral ratio transmission for all the biasing conditions even when the element is biased to the negative differential impedance region (point 5). The crystal resistance at point 5 is 222 kΩ (= 1.85 MΩ at zero bias) and hence the free carrier concentration

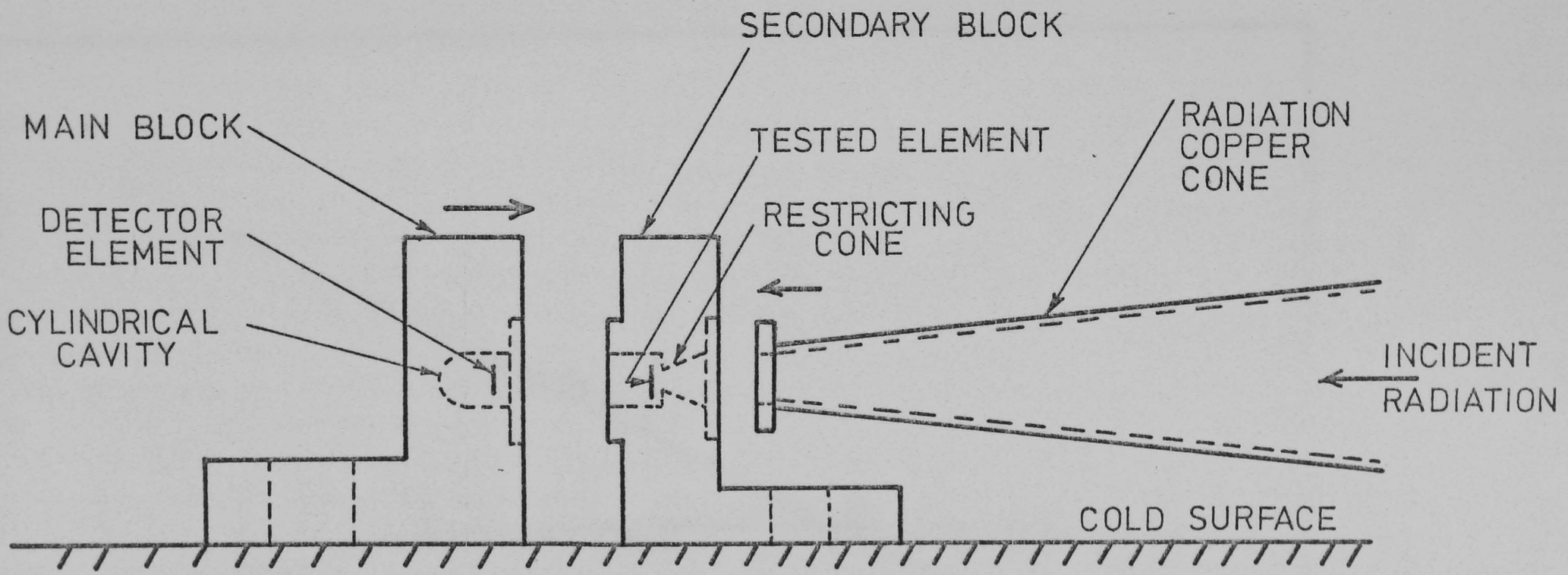

Figure 4.7, Element mount for bias dependent transmission measurements

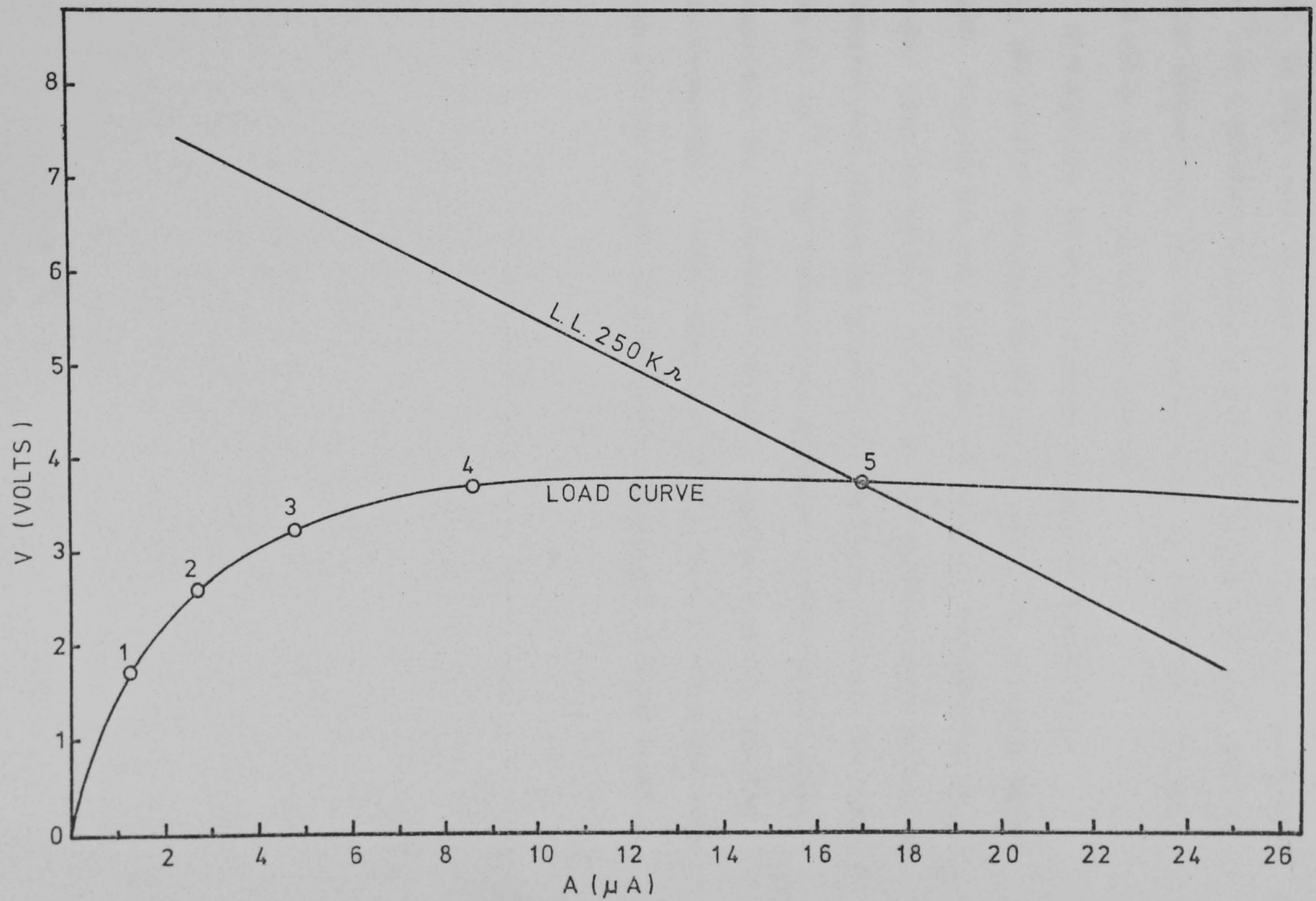

Figure 4.8. Operating points at which transmission spectra were taken

should have increased by more than eight folds. However, no decrease in the ratio transmission was observed even in the millimetre wavelengths part of the spectrum at which the free carrier absorption should be effective. In this case, the previously measured absorption coefficient of $\sim$ 6 cm^{-1} at 1 millimetre has a very small contribution from the free carrier absorption. But this observation is consistent with the calculated value of α at no bias of 0.01 cm^{-1}.

Although the detectors voltage response is highly bias dependent, the overall spectral absorption of radiation is nearly bias independent. Figures 4.9 and 4.10 show the spectral transmission in the frequency range 15-100 cm^{-1} only in the two extreme cases of no bias and the largest bias indicated by point 5. In these figures, the resolution was 0.1 cm^{-1}. The fluctuations in these spectra are not noise, but it represents the interference fringes together with the detailed absorption mechanisms. Reproduceability of all these fluctuations were observed in all the spectra as also clear from Figures 4.9 and 4.10.

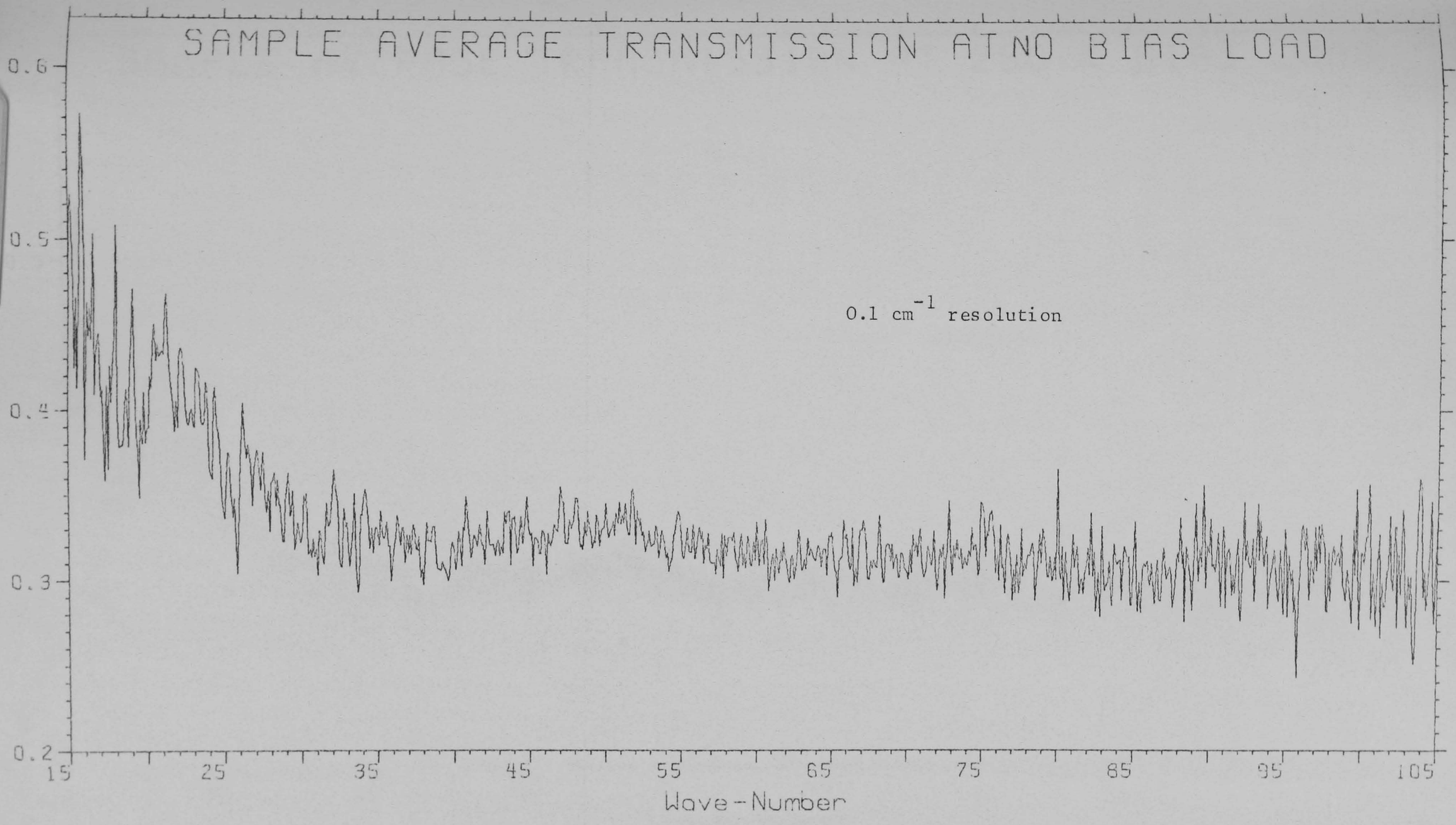
SAMPLE AVERAGE TRANSMISSION AT NO BIAS LOAD
0.1 cm-1 resolution
Transmission
0.6
0.5
0.4
0.3
0.2
15
25
35
45
55
65
75
85
95
105
Wave-Number

Figure (4.9)

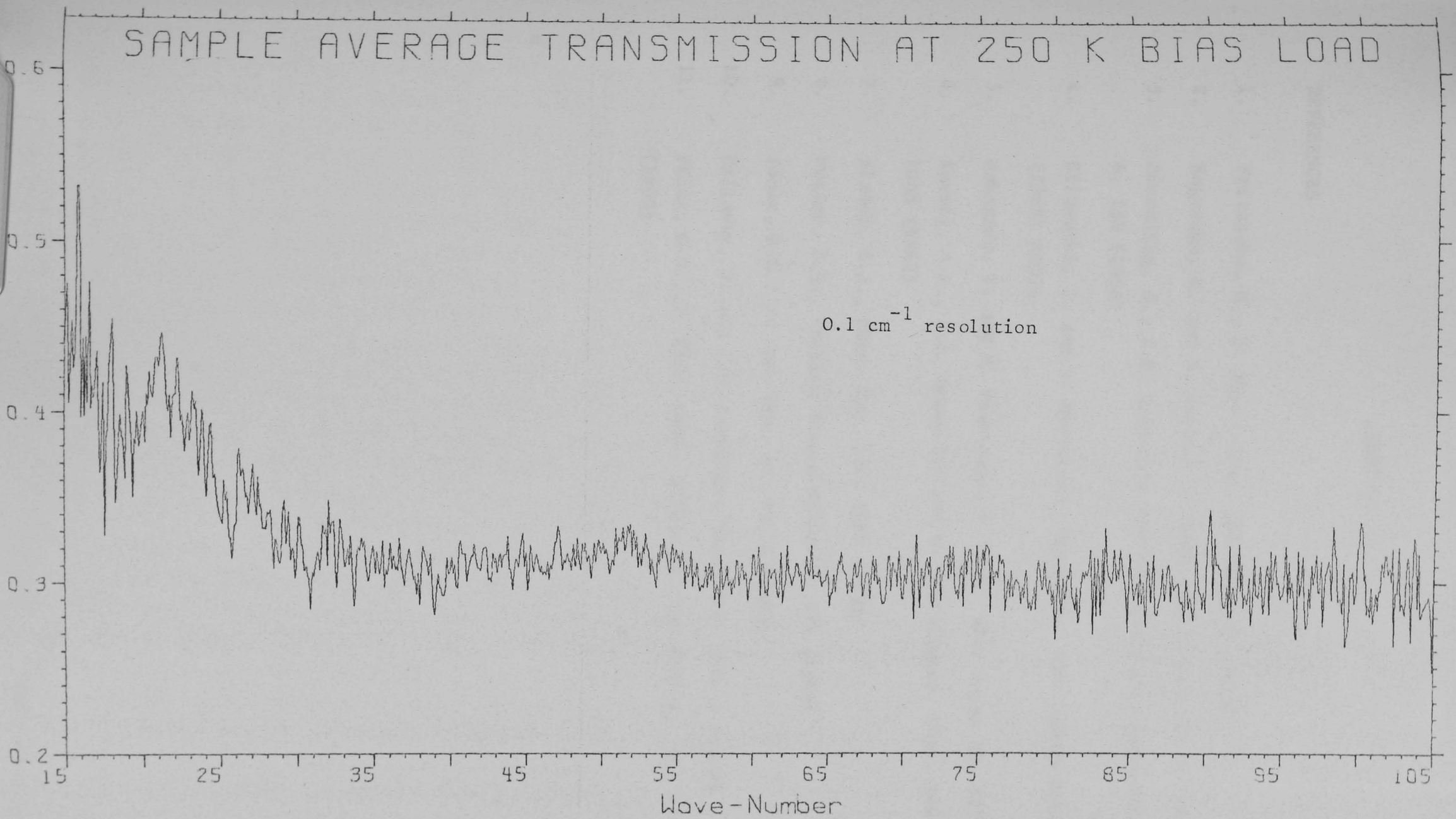
SAMPLE AVERAGE TRANSMISSION AT 250 K BIAS LOAD
0.1 cm-1 resolution
Transmission
0.6
0.5
0.4
0.3
0.2
15
25
35
45
55
65
75
85
95
105
Wave-Number

Figure (4.10)

CHAPTER IV

REFERENCES

1. Fritzsche, H., J. Phys. Chem. Solids 6, 69 (1958)

2. Nagazaka, K. and S. Narita, J. Phys. Soc. Japan 35, 3, 788 (1973)

3. Zwerdling, S., J.P. Theriault and H.S. Reichard, Infrared Phys. 8, 135 (1958)

4. Blinowski, J. and J. Mycielski, Phys. Rev. 136 (1964) A266; 140 (1965) A1024

5. Nakagawa, Y. and H. Yoshinaga, J. Phys. Soc. Japan 30, 1212 (1971)

6. Koenig, S.H., R.D. Brown III and W. Schillinger, Phys. Rev. 128, 1668 (1962)

7. Sladek, R.J., Phys. Rev. 120, 1589 (1960)

8. Putley, E.H., Physica Status Solidi 6, 571 (1964)

9. Jones, R.C., J. Opt. Soc. Am. 43, 1 (1963)

10. Callaway, J. and F.W. Cummings, Phys. Rev. 126, 5 (1962)

11. Picus, G.S., J. Phys. Chem. Solids 22, 159 (1961); 23, 1753 (1962)

CHAPTER V

Ge ELEMENTS WITH ABSORBING SURFACES

5.1. Introduction

The work in this chapter describes an earlier attempt to form an absorbing layer on a Ge element to increase the absorption in Ge detectors especially in the long wavelength of the infrared spectrum. The study includes spectral measurements of power transmission through Ge discs with an absorbing surface having typical detector elements thickness. Comparisons have been made with the uncoated samples. Measurements and discussions of the dc properties of one of these samples have been given. The studied absorbing films include

(i) Ion implantation for Sb-doped Ge ($\sim 5 \times 10^{16}$ cm^{-3}) to form p-type layer with a dc surface resistance appropriate to match the free space incoming radiation.

(ii) Nickel-chrome layer insulated from the Ge element by a thin SiO insulating layer. Both the metal and insulator are vacuum deposited on p-type compensated Ge (Ga $\simeq 9 \times 10^{15}$ cm^{-3}, Sb $\simeq 1 \times 10^{15}$ cm^{-3}).

(iii) The same technique as in (ii) was used but with n-type Ge described in (i).

Detector elements have been designed and constructed using each material described above. The main characteristics of these detectors are discussed. Operating conditions and performance data are given for a detector using an implanted sample. Future developments are suggested to use the ion implantation technique as a useful tool to improve both the N.E.P. and the absorption characteristics.

5.2. Essential requirements of the absorbing layer

The main requirements for the absorbing layer are the surface

resistance and the intimate thermal contact between the layer and the responding element. The absorbing layer is also required to have a uniform absorption spectrum in the interesting part of the infrared spectrum.

5.2.1. Resistance requirements

The surface resistance of the absorbing layer should be such that maximum absorption of the incoming radiation is fulfilled. The required resistance could be calculated from the transmission line theory [2].

Let us assume the case of lossless transmission line (TL) shown in Figure 5.1 with infinite extension on both sides of a load Z_L representing the absorbing film, where $Z_o' \neq Z_o$ represents the characteristic impedance to the electromagnetic waves in Ge assumed infinitely long, and Z_o is the free space impedance. Then

The reflected power intensity at A-A, $r_z = \left| \frac{Z - Z_o}{Z + Z_o} \right|^2$ .. (5.1)

where Z is the parallel combination of Z_L and the rest of the line with Z_o' . Z will then represent the total load affecting the transmission and reflection intensities at A-A.

$$Z = \frac{Z_L Z_o'}{Z_L + Z_o'} \qquad .. (5.2)$$

Substituting in (5.1) we get,

$$r_Z = \left| \frac{Z_L \left(1 - \frac{Z_o}{Z_o'}\right) - Z_o}{Z_L \left(1 + \frac{Z_o}{Z_o'}\right) + Z_o} \right|^2 \qquad .. (5.3)$$

The absorbed intensity in the total load Z, A_Z will be given by

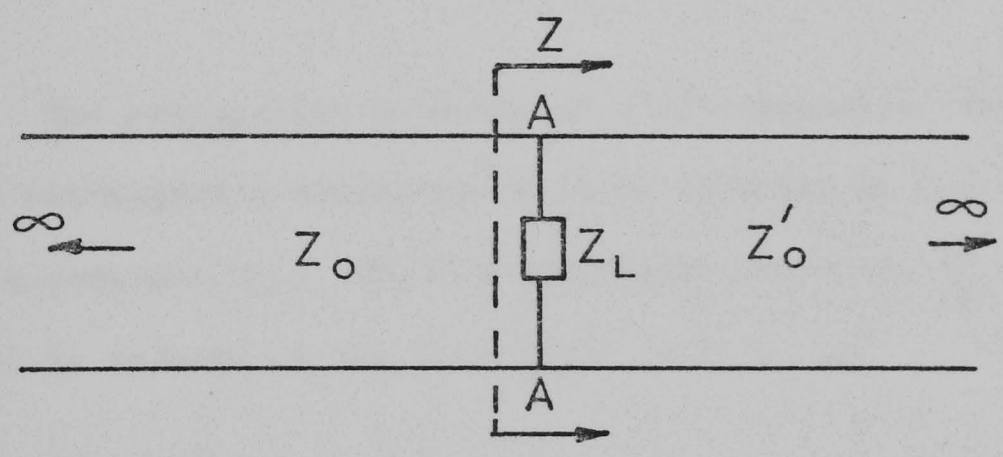

Figure 5.1

$$A_Z = 1 - r_Z$$

$$= \frac{4\left(\frac{Z_L}{Z_o'} + 1\right) Z_L Z_o}{\left[Z_L\left(1 + \frac{Z_o}{Z_o'}\right) + Z_o\right]^2} \qquad .. (5.4)$$

And hence the power absorbed by Z_L alone will be

$$A_{Z_L} = A_Z \cdot \frac{Z_o'}{Z_o' + Z_o}$$

$$= \frac{4 Z_L Z_o}{\left[Z_L\left(1 + \frac{Z_o}{Z_o'}\right) + Z_o\right]^2} \qquad .. (5.5)$$

The propagation velocity of electromagnetic radiation through a non-magnetic dielectric will be affected by its complex dielectric constant ϵ . The characteristic impedance Z_o' of the dielectric is related to the free space value Z_o and ϵ as

$$Z_o' = \frac{Z_o}{\sqrt{\epsilon}} \qquad .. (5.6)$$

Also due to the velocity reduction in the dielectric by the same ratio, the wavelength inside the medium λ_m will be

$$\lambda_m = \frac{\lambda_o}{\sqrt{\epsilon}} \qquad .. (5.7)$$

In Ge, $\sqrt{\epsilon}$ is nearly equal to the real part of refractive index n (the imaginary part is small as we have seen in Chapter IV), therefore

$$Z_o' \simeq \frac{Z_o}{n} \qquad .. (5.8)$$

and $\lambda_m = \frac{\lambda_o}{n}$ .. (5.9)

Substituting for Z_o' in (5.5) we get

$$A_{Z_L} = \frac{4 Z_L Z_o}{\left[Z_L (1+n) + Z_o\right]^2} \qquad .. (5.10)$$

from (5.3) we also get

$$r_Z = \left| \frac{Z_L (1-n) - Z_o}{Z_L (1+n) + Z_o} \right|^2 \qquad .. (5.11)$$

Maximising A_{Z_L} w.r.t. Z_L in (5.10) we get

$$Z_L = \frac{Z_o}{1 + n} \qquad .. (5.12)$$

and the maximum absorption will be

$$A_{Z_L} (\max) = \frac{1}{1 + n} \qquad .. (5.13)$$

From (5.11) the corresponding reflection coefficient is

$$r_Z = \frac{n^2}{(1 + n)^2} \qquad .. (5.14)$$

These values are correct only if the sample thickness with refractive index n is infinitely long. Since the wavelength of propagation inside the Ge will appear reduced by the refractive index factor, then a crystal of 0.25 mm thickness can be considered electrically long for wavelengths much less than 1 mm. However, this limit is dependent on the medium attenuation constant as we will see in the actual case. For Ge, n = 4, then Z_L for maximum absorption is

$$Z_L = \frac{120\pi}{5} \cong 75 \ \Omega/\square \qquad .. (5.15)$$

and the maximum available absorption is

$$A_{Z_L}\ (\max) = 20\% \qquad .. (5.16)$$

$$\text{and} \quad r_Z = 64\% \qquad .. (5.17)$$

this will leave a transmitted intensity of 16% through the bulk Ge.

These values of absorption and reflection are not satisfactory, the reason being that the electromagnetic radiation has to see the following substrate with high refractive index. In this case, as Z_L increases, both A_{Z_L} and r_Z decrease until the limiting case of infinite Z_L, r_Z will have a value appropriate for Ge alone of ∿37%. Therefore, considerable improvements can be obtained if the bulk thickness is made very thin and/or the dimensions of the responding element is much smaller than the absorbing area. In these conditions, the value of n is nearly equal unity and we will have

$$A_{Z_L}\ (\max) = 50\%$$

$$r_Z = 25\%$$

These values are quite satisfactory especially when the reflection coefficient r_Z is smaller than for uncoated Ge. All the measurements done here, are for the absorbing film and the bulk crystal have the same area and with thickness of ∿ 0.25 mm for the n-type Ge and of 0.31 for the p-type compensated one. Transmission line treatment for this finite thickness will be given when discussing the transmission measurements.

5.2.2. Thermal matching requirements

Other essential requirement is that the absorbing layer should be in intimate thermal contact with the responding element. If an absorbing film of different nature than the following substrates has to be used, the thermal impedance for all the materials used

should be selected to be very similar at each interface at the required operating temperature. The transmission coefficient T_T of the heat flow for normal incidence at any interface between two dissimilar solids having densities of ρ_1 and ρ_2 and acoustic velocities U_1 and U_2 is given by [4]

$$T_T = \frac{4\ \rho_1 U_1 \cdot \rho_2 U_2}{(\rho_1 U_1 + \rho_2 U_2)^2} \qquad .. (5.18)$$

This has a maximum value of unity when $\rho_1 U_1 = \rho_2 U_2$ (the specific acoustic impedances are similar for both media). However, it has been shown by the author[4] that the integrated value of (5.18) for all angles of incidence from first medium to the second shows that the last condition is not sufficient for maximum energy transfer if $U_2 > U_1$, and the condition $U_1 = U_2$ and $\rho_1 = \rho_2$ must be satisfied to give a maximum integrated transmission coefficient of 50%. One of our techniques does not fulfill these requirements because it contains metal-insulator-semiconductor interfaces. The thermal mismatch was quite severe although the metal layer absorption seemed quite adequate and hence the element failed to give any improvements as a detector element. The other samples tested were surface implanted in which case these requirements, we believe, were fully achieved, but other considerations should be taken into account as we will see later.

5.3. The absorbing surfaces

5.3.1. Ion implanted surface

A circular disc 12 mm diameter and of 0.25 mm thick was cut out from the crystal grown in <110> direction containing $\sim 5.5 \times 10^{16}$ Sb. cm^{-3}. The disc was finely polished and etched for about 1 minute using the same mixture (CP4A). The disc was then implanted* by 60 keV

* This was carried out at Sussex University, Brighton, by Dr. D. Palmer.

boron ions B^+ to a dose of 3×10^{14} ions/square centimetre to form a p-type layer with thickness of about 2μm such that the surface resistance is $209 \pm 10\ \Omega/\square$. The doping level of this p-type layer ($\sim 1.5 \times 10^{18}$ cm^{-3}) lies in the metallic region of conduction where the resistance should not vary with temperature. The surface resistance was measured at pumped helium temperatures and no change was observed between 300 and 1.5°K. The barrier created due to the p-n junction prevents shortening out the bias current through the Ge sample by the low resistivity layer.

5.3.2. Metallic surface

Two discs similar to those used for ion implantation were used for this purpose, one of them was n-type Ge, as that described above and the other was p-type compensated Ge ($\sim 9 \times 10^{15}$ Ga, 1×10^{15} Sb. cm^{-3}) having thicknesses of 0.25 and 0.31 mm respectively. The discs were coated with thin silicon monoxide layer, sufficient to be pinhole free, by vacuum evaporation, and then coated by nickel-chrome layer to a surface resistance of $\sim 80\ \Omega/\square$ at room temperature. Both samples were polished and etched before vacuum deposition. Other detector elements have been prepared by this method for detector construction. The NiCr layer thickness $\cong 125$ Å, and the resistance of which was measured separately at pumped helium temperatures. An increase by a factor of ~ 2.5 was observed in the sheet resistance. This makes a resistance of $\sim 200\ \Omega/\square$ at the operating temperature. The insulating layer SiO separating the evaporated metal from the Ge sample was thick enough to prevent any electrical contacts between them. This was achieved by evaporating various thicknesses of the insulator on copper discs followed by the metal layer deposition. The electrical resistance was measured in each case until the minimum thickness for good insulation was found.

5.4. Transmission measurements and discussion

Transmission spectra for the three samples have been carried out at 1.5°K using the fourier transform spectrometer and an indium antimonide detector used before. At least three interferograms were performed for each spectrum including the background. The average of each spectrum is ratioed against the average background energy spectrum. The average ratio transmission spectra with and without treatments for the three samples are shown in figures (5.2), (5.3) and (5.4).

5.4.1. Ion implantation

In the ion implanted sample, Figure (5.2), we expected a decrease in the ratio transmission at any radiation frequency w.r.t. the unimplanted sample because of the additional absorption of the low resistivity layer. But rather we observed an increase in ratio transmission for frequencies lower than 30 cm^{-1} and a decrease for higher frequencies (this increased transmission was not observed in the metal-insulator coated sample). This we think is due to the junction formation and the resulting depletion of carriers as we will discuss below.

5.4.1.1. The effect of the p-n junction on the absorption spectrum in the implanted sample

Due to the formation of the p-n junction in the implanted sample, a depletion layer is created. At such low temperatures, the total ~~delocalised~~ *free* carrier concentration is highly reduced relative to the exhaustion value. This will increase greatly the depletion region inside the bulk Ge sample. Because the p-type layer is degenerate, its carrier concentration and the depletion depth are unaffected by cooling. This layer is extremely small compared to the bulk n-Ge even at room temperature and is determined by the charge balance on both sides of the

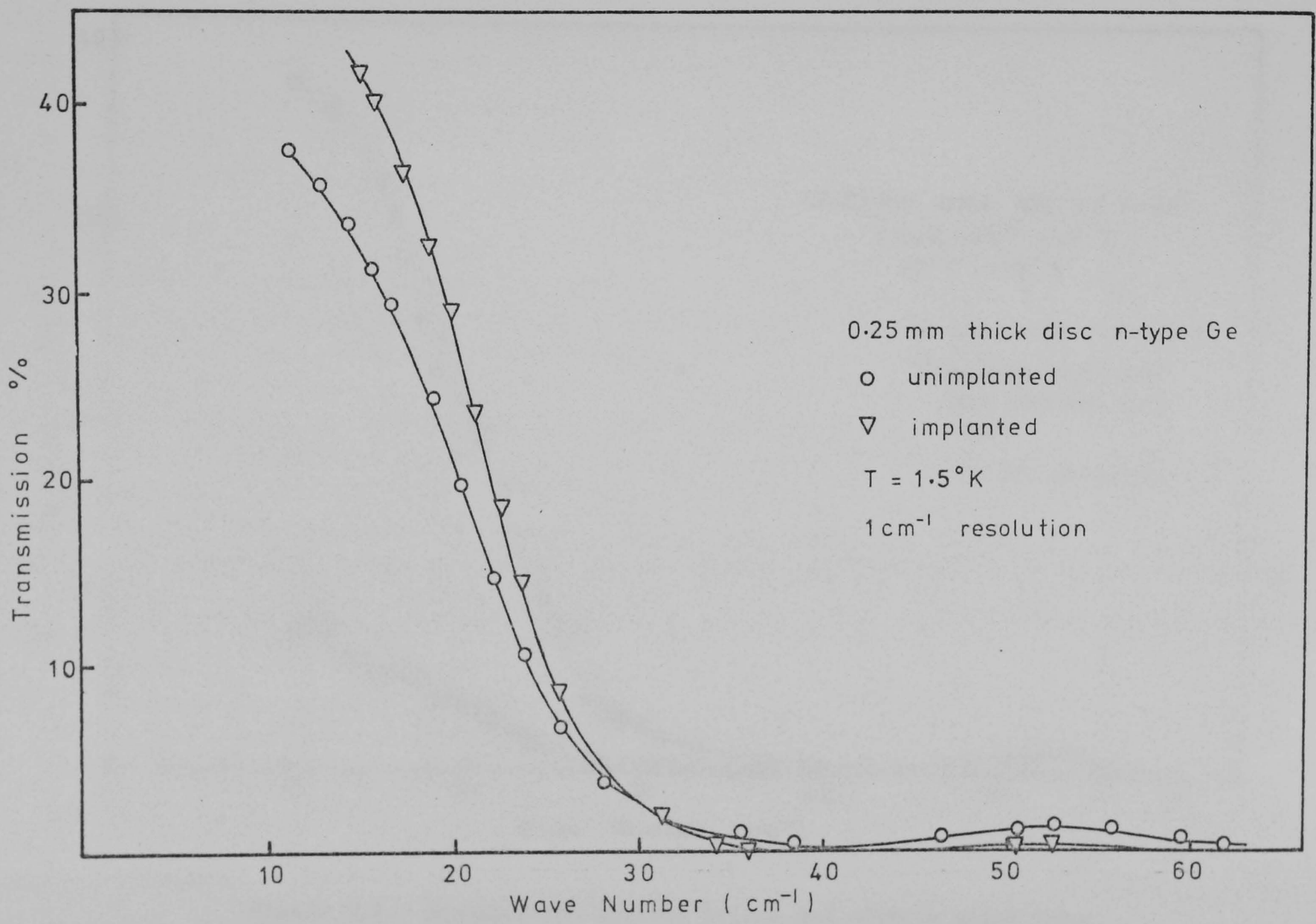

Figure 5.2. Transmission spectra before and after surface implantation

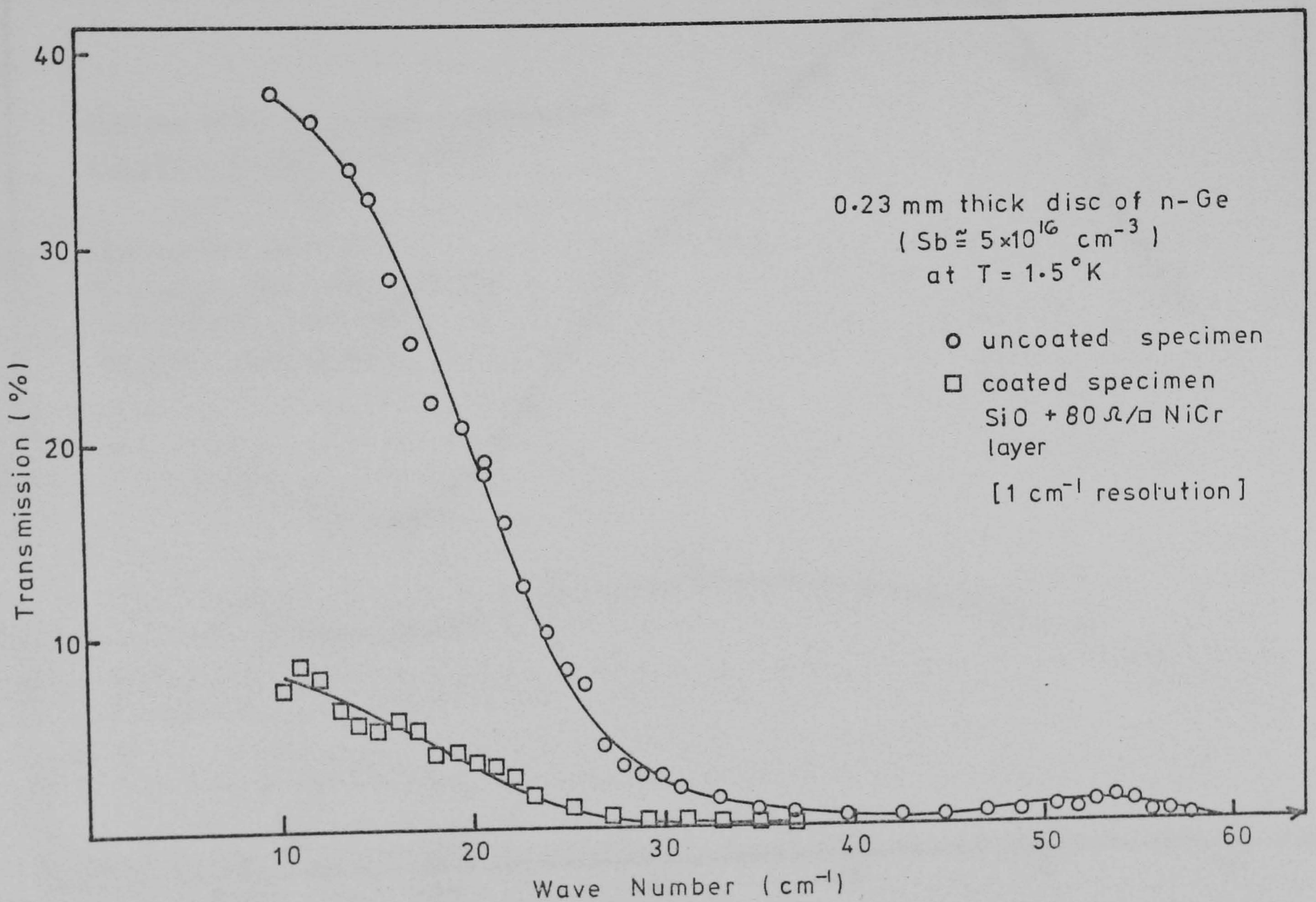

Figure 5.3. Transmission spectra before and after a metal layer

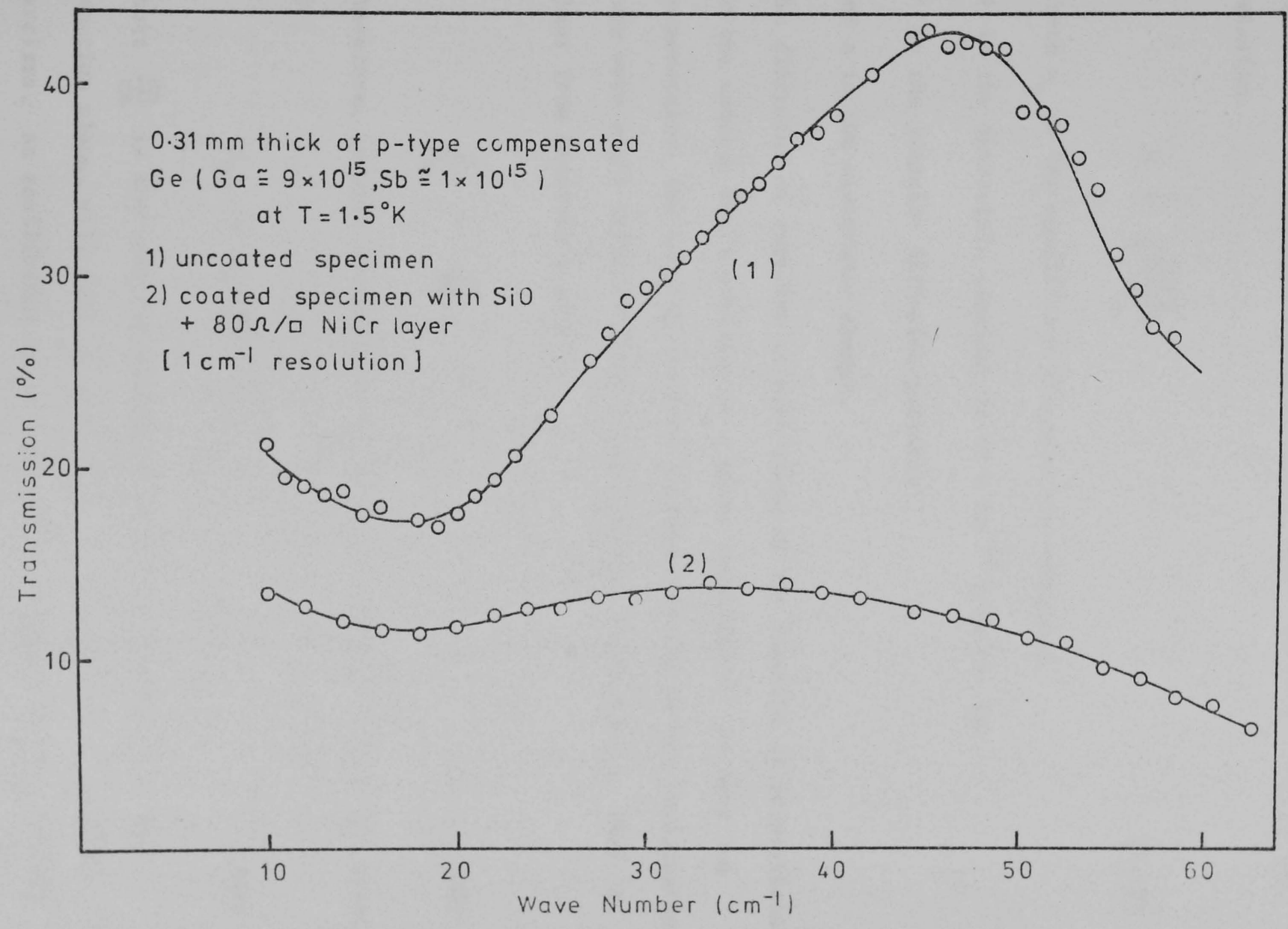

Figure 5.4. Transmission spectra before and after a metal layer

junction. The result of this effect at low temperatures is that the majority of the bulk material is depleted of the free carriers. The depletion depth, H, into the bulk Ge is inversily proportional to the square root of the free carrier concentration, as is clear from the relation.

$$H = \sqrt{\frac{2 \epsilon \phi}{e n_o}} \qquad .. (5.19)$$

where n_o is the equilibrium electron concentration,

ϵ is the dielectric constant (1.42×10^{-12} F/cm for Ge)

ϕ is the junction diffusion potential,

and e is the electronic charge.

The diffusion of carriers to both sides of the junction is proportional to the carrier drift mobility at a given temperature. At very low temperatures, the hopping carriers already existing before implantation have very small drift mobility μ and diffusion constant D_e. This is clear from Einstein's relation

$$\frac{\mu}{D_e} = \frac{e}{kT} \qquad .. (5.20)$$

Therefore, we will assume that the diffision current density J_D, given by

$$J_D = D_e \frac{dn}{dx} \qquad .. (5.21)$$

where $\frac{dn}{dx}$ is the carriers density gradient perpendicular to the junction plane, will only be carried by the highest mobility free carriers. An equilibrium is set up when the current given by (5.21) is equal and opposite to the drift current density created by the built-in electric field F, i.e.

$$D_e \frac{dn}{dx} = n_1 e \mu_1 F \qquad .. (5.22)$$

where n_1 and μ_1 are the carrier concentration and mobility of the dominant conduction mechanism. At 4.2°K, we found by measuring the field effect pinch-off voltage that the created depletion depth H is such that the undepleted carrier concentration causing it should be about 1.7×10^{10} cm^{-3}. This value is much smaller than the delocalised carriers deduced from the Hall measurements (1.47×10^{14} cm^{-3}). But, it does represent the conduction band carrier concentration at that temperature [1]. Also at this temperature, the depletion depth occupies nearly the whole sample thickness (H ≈ 228μm). Since the crystal thickness and contact potential are fixed, at lower temperature almost all the conduction band carriers are depleted, and for further cooling and depletion, the delocalised band carriers must be included. The required carrier concentration for depletion is still less than the ε_2 band carriers determined from the Hall measurements at low magnetic fields but close to the high magnetic field value of 4×10^{10} cm^{-3}. We believe that the participated carriers in depletion are those of highest mobility in the delocalised region.

Now the depletion region is free from the highest mobility carriers. These carriers as we mentioned are responsible for the observed background absorption including the band edge transition which probably no longer exists especially since the depleted carriers are those moving in the top of the delocalised band. Since this absorption mechanism is effective at long wavelengths, this could be a reason for the increased transmission for frequencies lower than 30 cm^{-1} w.r.t. the unimplanted sample. On the other hand, the photo-transition absorption should include phototransition from the ground state in the whole bulk material. This will contribute to the observed decrease in transmission for higher frequencies. The performance of a

detector element in the long wavelengths, will therefore be mainly due to the degenerate layer absorption.

5.4.1.2. (TL) simulation representing the actual case

In the last derived equations for absorption and reflection coefficients, the assumption of infinite length of dielectric behind the absorbing layer is not quite applicable to our case. The crystal has a finite length w.r.t. the radiation wavelengths used. The more general treatment in this case is to assume a finite length transmission line representing the propagation of waves through the crystal followed by an infinite free space transmission. In Figure (5.5), Z_s will replace Z'_o in the last formulae, where Z_s is the input impedance beyond the absorbing load Z_L. Z_s is related to the crystal electrical length ℓ and both Z_o and Z'_o as [2]

$$Z_s = Z'_o \left\{ (Z_o + j\, Z'_o \tan \beta\ell)/(Z'_o + j\, Z_o \tan \beta\ell) \right\} \quad .. (5.23)$$

where β is the imaginary part of the complex propagation constant. It is assumed here that the crystal medium is lossless which represents our case for only long wavelengths. Then relations (5.3) and (5.5) are altered to be

$$r_Z = \left| \frac{Z_L \left(1 - \frac{Z_o}{Z_s}\right) - Z_o}{Z_L \left(1 + \frac{Z_o}{Z_s}\right) + Z_o} \right|^2 \quad .. (5.24)$$

and

$$A_{Z_L} = \frac{4\, Z_L\, Z_o}{\left[Z_L \left(1 + \frac{Z_o}{Z_s}\right) + Z_o \right]^2} \quad .. (5.25)$$

For specific values of $\beta\ell$ in relation (5.23), Z_s is purely resistive and equal to Z_o (the free space value), these values are given

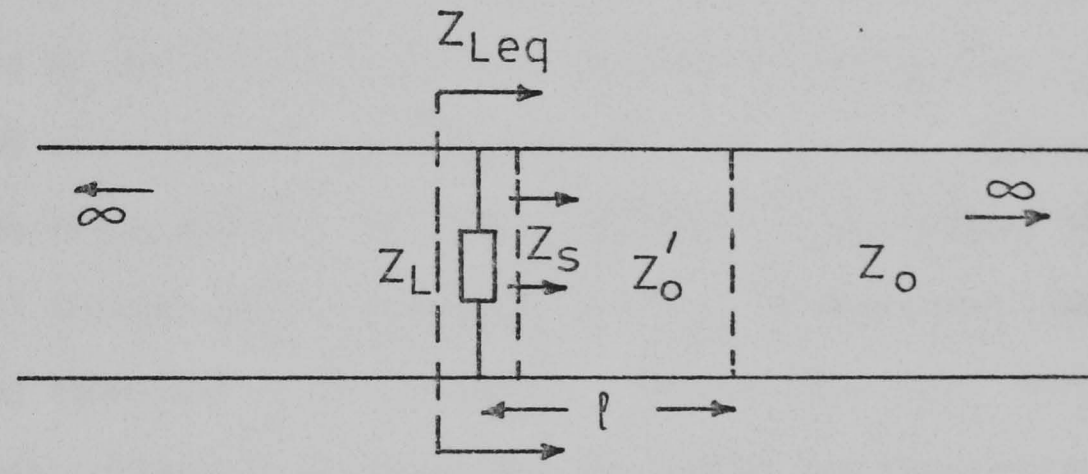

Figure 5.5

by

$$\beta\ell = a\pi \qquad a = 0, 1, 2, 3, \ldots \qquad .. (5.26)$$

and occurs for wavelengths

$$\lambda_m = \frac{2\ell}{a} \qquad .. (5.27)$$

λ_m here is the radiation wavelength inside the crystal ($\sim \frac{\lambda_o}{4}$ for Ge). At these wavelengths given by (5.26), the incoming radiation will not be affected by the substrate, and the maximum absorption (for $Z_L = \frac{Z_o}{2}$) will be 50% while 25% will be reflected as shown before. Therefore, for 0.25 mm thick element, the 2 mm wavelength, 1 mm, 670μm, 500μm etc... will satisfy these conditions, but only at these wavelengths if the crystal faces are exactly parallel. On the other hand, there will be very high reflection and much less absorption for wavelengths satisfying the following conditions

$$\beta\ell = b \cdot \frac{\pi}{2} \qquad b = 1, 3, 5, 7, \ldots \qquad .. (5.28)$$

or

$$\lambda_m = \frac{4\ell}{b} \qquad .. (5.29)$$

Under these conditions, the impedance Z_s is approximately equal to $\frac{Z_o'^2}{Z_o}$ and also nearly purely resistive. The reflection coefficient will be as high as 79% while only $\sim$ 7.9% is absorbed for $Z_L = 210\ \Omega/\square$. As the value of tan $\beta\ell$ increases from zero, the value of Z_s becomes complex and decreases from Z_o (the magnitude and the real part decreases). At tan $\beta\ell = 1$, $|Z_s| \cong Z_o' = \frac{Z_o}{4}$ but the real part drops to about $\frac{Z_o'}{2}$. Therefore, the upper limit of Z_s is Z_o giving maximum layer absorption, and the lower limit is $\sim \frac{Z_o'^2}{Z_o} = \frac{Z_o}{16}$ for Ge for the worst conditions.

Equation (5.28) will be satisfied for space radiation wavelengths of 4, 1.33, 0.8, 0.57 mm ... etc. for the same crystal thickness. Therefore, the required wavelength to be detected will be specified by the sample thickness to give the best conditions.

The successive occurrence of the last conditions w.r.t. the radiation wavelengths appears in the transmission spectrum as maxima and minima corresponding to the fulfillment of the best and worst conditions respectively. The curve shown in Figure (5.2) represents the geometrical average transmission. However, the observed value of transmission in Figure (5.2) is higher than that estimated for $Z_L = 210\Omega$. The value of Z_L required by fitting the measurements of 41.5% transmission at 750μm where still the bulk material is assumed lossless is about 1.5 k Ω/□ . The reason for this change, we think, is the effect of the radiation frequency on the dc resistance of the degenerate layer. The ac conductivity $\sigma(\omega)$ of the implanted layer will change with ω as

$$\sigma(\omega) = \frac{\sigma_o}{1 + (\omega\tau)^2} \qquad .. (5.30)$$

where τ is the momentum scattering time.

For $f = 4.5 \times 10^{11}$ Hz (750μm wavelength), the quoted value of 1.5 kΩ/□ will give

$$\tau \cong 6.1 \times 10^{-13} \text{ seconds} \qquad .. (5.31)$$

For $Z_s = Z_o$ (best condition), $A_Z \cong 20\%$ and $r_Z = 1.25\%$

For $Z_s = \frac{Z_o}{16}$ (the worst), $A_Z \cong 0.3\%$ and $r_Z \cong 78\%$

When the radiation frequency increases, the lossless TL treatments given by (5.22) will not be valid. The absorption coefficient α of the phototransition should be included in the propagation constant. The value of Z_s beyond the absorbing layer will be modified to be

$$Z_s = Z'_o \left\{ (Z_o + Z'_o \tanh \gamma\ell)/(Z'_o + Z_o \tanh \gamma\ell) \right\} \quad .. \quad (5.32)$$

where $\gamma = \alpha + j\beta$ is the complex propagation constant.

For frequencies such that $\alpha >> \frac{1}{\ell}$, $|\gamma\ell|$ will be large and $\tanh \gamma\ell$ tends to unity, then

$$Z_s \simeq Z'_o = \frac{Z_o}{4}$$

and the TL will act as an infinite lossless TL discussed before and equations (5.3) and (5.5) will be valid. In our case, the ac surface resistance at 250μm (where bulk material has maximum α) will be 5.8 k Ω/□ assuming the last value of τ to be correct. This gives a reflection coefficient r_Z of 36.6% and A_{Z_L} of only 1.0% from (5.3) and (5.5). We should note again that the value of r_Z for Ge alone is 36% which will be reached if $Z_L = \infty$ and of course no absorption will be offered by the degenerate layer. Therefore, the behaviour of the implanted samples at high frequencies ($w\tau > 1$, and $\alpha >> \frac{1}{\ell}$) will be approaching the unimplanted sample but slightly reduced depending on frequency as it is clear from Figure (5.2). Nevertheless, this layer could only be used for radiation frequency $f < \frac{1}{2\pi\tau}$, i.e. $f < 2.6 \times 10^{11}$ Hz (∿ 1.15 mm wavelength) after which the value of σ and hence the free carrier absorption of the degenerate layer decreases rapidly as w^{-2}. This is probably the main disadvantage of this layer. However, this could be overcome by decreasing the momentum time τ. This could probably be achieved by increasing the ionized centres, i.e., increasing the surface dose of the degenerate layer. This also implies that the layer thickness should be reduced for specific layer resistance.

5.4.2. Metal coated samples

This includes both the n-type and the p-type compensated Ge.

Nearly constant reduction in the average transmissions were observed. No depletion region was formed in such a case. The bulk material at any wavelength still absorbs the same percentage of the internal incident radiation after the metal layer. The conditions of best and worst fulfillment discussed before still apply and the geometrically average transmission is performed using the successive maxima and minima. The main difference between this and the implanted sample is the identity of the bulk properties before and after treatment. The calculated value of average transmission for 200 $\Omega/\square$ layer is $\sim$ 22% for lossless crystal. However, the average percentage transmission should be less than 22% at any wavelength due to the finite absorption by the crystal. This is clear from Figures (5.3) and (5.4). Moreover, the fractional absorption of the bulk material to the internal incident radiation before and after the layer is nearly the same. For wavelengths of maximum bulk absorption, the calculated reflection coefficient is 50% and the layer will absorb 16% and of course the transmission should be well below 34% as the figures show. In the uncoated p-type sample, for example, the transmission is 17.5% while the internal incident energy is (1-r) i.e., 64% giving a fractional absorption of $\sim$ 73%. After the metal layer, the internal incident energy is only 34% which after the bulk absorption of 73% will leave $\sim$ 9.2% for transmission. This value is very close to the measured value of $\sim$ 11% as shown in Figure (5.4).

Throughout the useful infrared spectrum, the layer resistance will not vary much from the dc value due to the small value of τ. But the thermal mismatch as mentioned will present a great problem to be solved.

5.5. D-C measurements and discussion

These measurements include the bulk crystal of the implanted sample at 4.2 and 1.6°K. An element of area 4 x 2 mm^2 was cut out from the implanted disc. The element edges were then etched for 1 minute in CP4A solution by covering the front and back surfaces of the element fully by black wax dissolved in toluene. The purpose of this etch is to remove any edge direct contact between the degenerate layer and the bulk material. After soldering the crystal from the unimplanted surface near the edges, the crystal is immersed in liquid helium and the V-I characteristics were measured at 4.2 and 1.6°K. Figures (5.6) and (5.7) show the V-I plots and log R - log V for the two temperatures. From these figures, we observe firstly that, for low voltages, the degenerate layer did not shorten out the bulk crystal current because of the junction formation, and secondly, that the observed high resistance of the element, w.r.t. similar unimplanted sample, indicates that the current is confined in very thin conducting channel due to the large spread of the depletion region at these temperatures. At 4.2°K we can see a sudden increase in resistance around 0.1 volts potential difference which is not present at 1.5°K. We think that this phenomenon is associated with the conducting channel pinching-off at the positive end of the contacts which assists the junction built-in potential. Assuming a typical value of $\phi \cong 0.5$ volts, an excess 0.05 volts caused pinching-off, this will indicate that the unbiased conducting channel depth at 4.2°K is 22.7μm (the total thickness is 250μm). The associated increase in the element resistance w.r.t. similar unimplanted sample is in agreement with this scaling factor. At the pinch-off voltage, the resistance, however, is not infinite because a finite current should pass through the pinched-off part of the channel. The channel resistance at the pinch-off is 830 kΩ giving a pinch-off saturation current of about 0.12μA. Beyond 100 mV, the

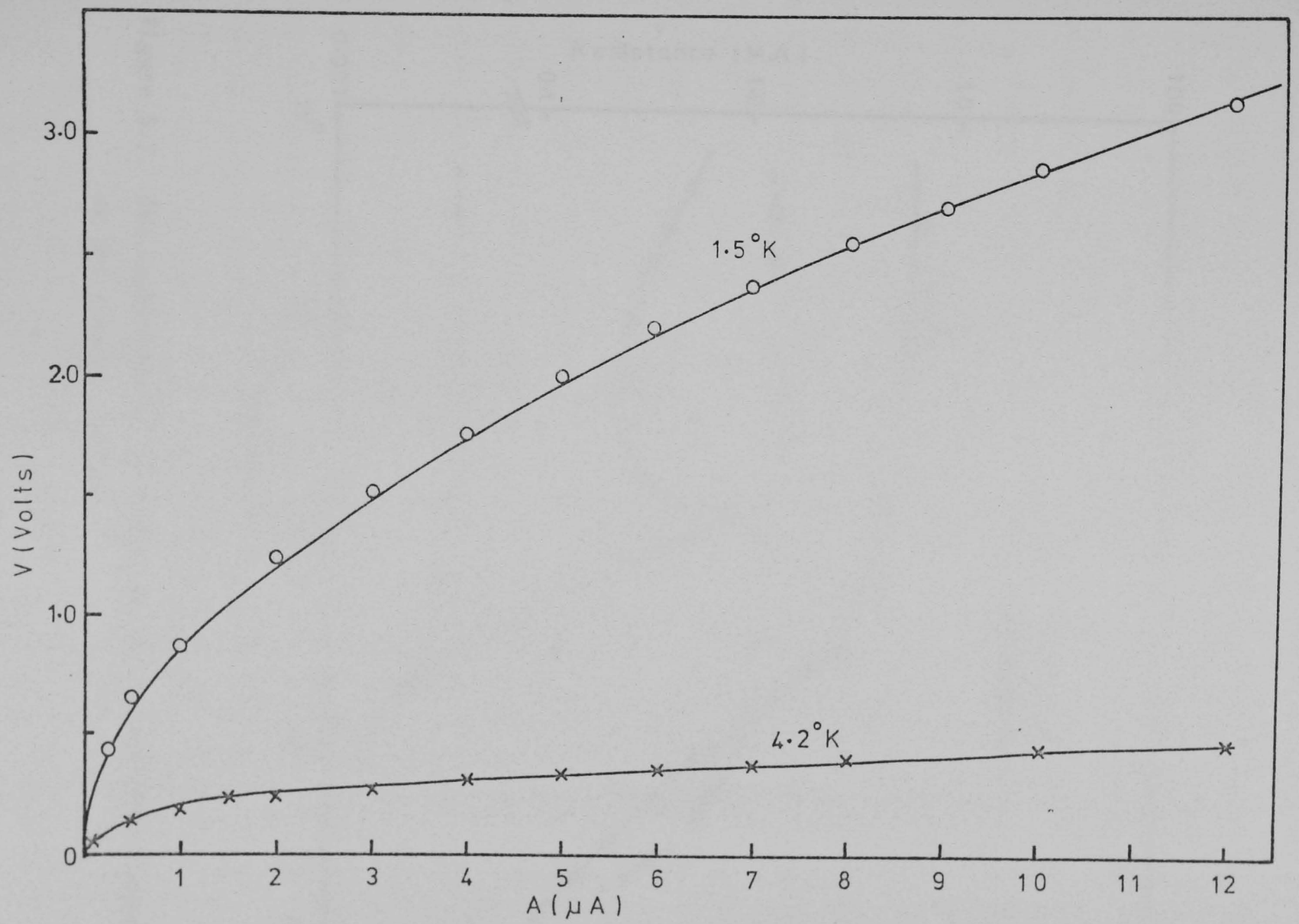

Figure 5.6. The characteristics of implanted Ge at high levels

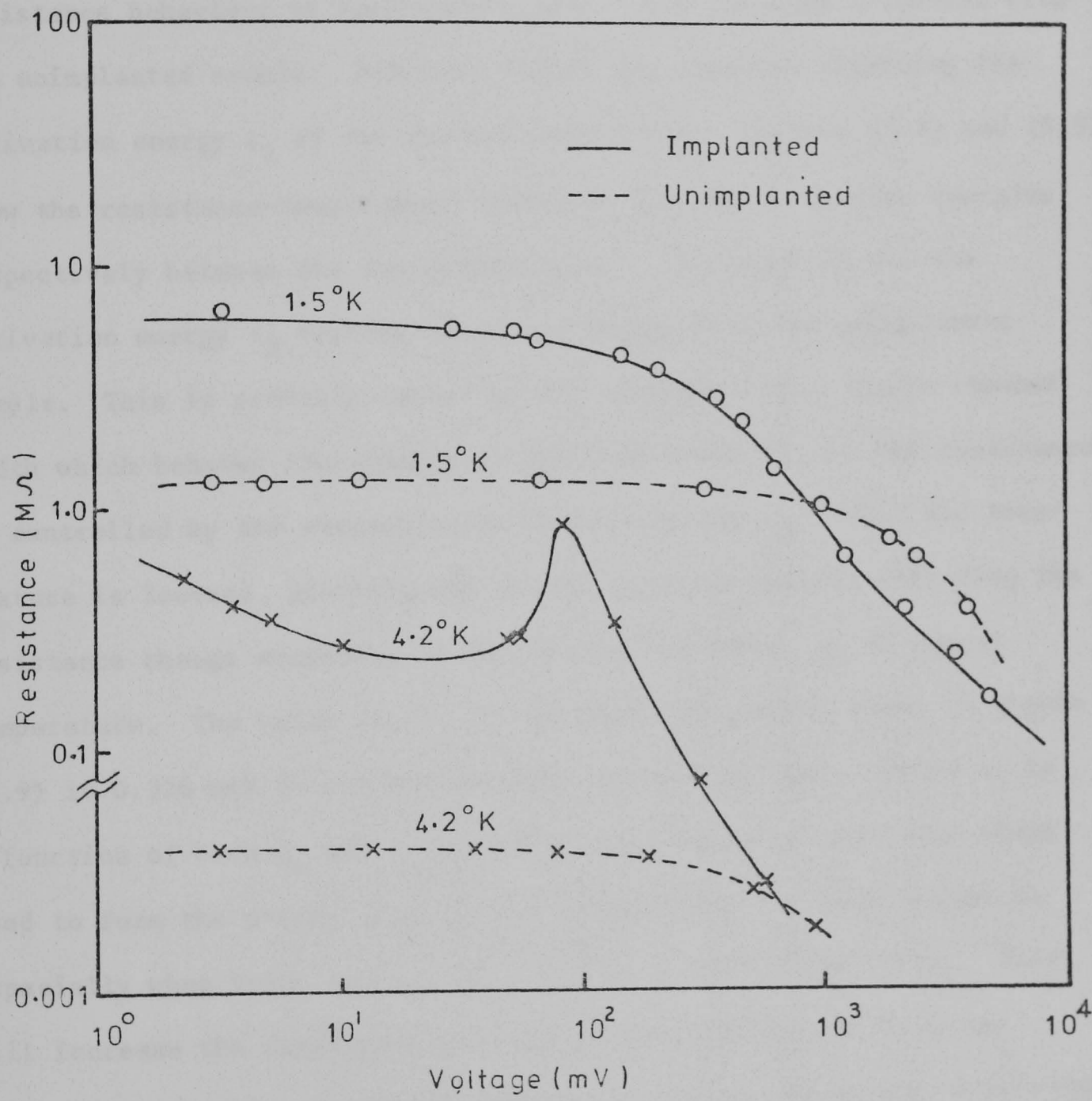

Figure 5.7. The resistance of an n-type Ge before and after implantation vs the element voltage

resistance starts to drop rapidly with larger rate than the unimplanted sample.

At 1.5°K, the element should be self pinched-off and no resistance peak was observed at this temperature which indicates that there was not finite channel width before biasing. Moreover, we found that the resistance behaviour of such sample near 1.5°K was much different from the unimplanted sample. Not much change was observed regarding the activation energy ε_2 of the channel near 4.2°K. Figures (5.8) and (5.9) show the resistance-temperature behaviour and the activation energies respectively between the two temperatures. In Figure (5.9), the activation energy ε_2 suffers nearly no change from the unimplanted sample. This is probably caused by the existance of a finite channel width which behaves identically to the bulk material, so the resistance is controlled by the respective activation energy ε_2. When the temperature is lowered, pinching-off starts to occur thereby affecting the resistance change according to the activation energy ε_3 at lowest temperature. The value of ε_3 in the implanted sample shown in Figure (5.9) is 0.326 meV ($\sim$ 0.9 meV for the unimplanted one). Since ε_3 is a function of both N_D and N_A, we expect that some of the boron atoms used to form the p-type layer have diffused into the bulk n-type Ge especially when boron has a large diffusion coefficient in Ge. This will increase the compensation ratio and reduces ε_3. This is an important factor in thermal bolometers as far as the thermal temperature coefficient of resistance $\alpha = \frac{-\varepsilon_3}{kT^2}$ must be kept as large as possible.

The self pinching off at 1.5°K in this sample could also be a reason of reducing the value of ε_3. This pinch-off is equivalent to applying reverse bias voltage with a certain value at 4.2°K. Therefore we should expect a partial shortening out of the bulk current by the degenerate layer as a result of partial breakdown. This would cause a decrease in the overall value of the activation energy ε_3. Further

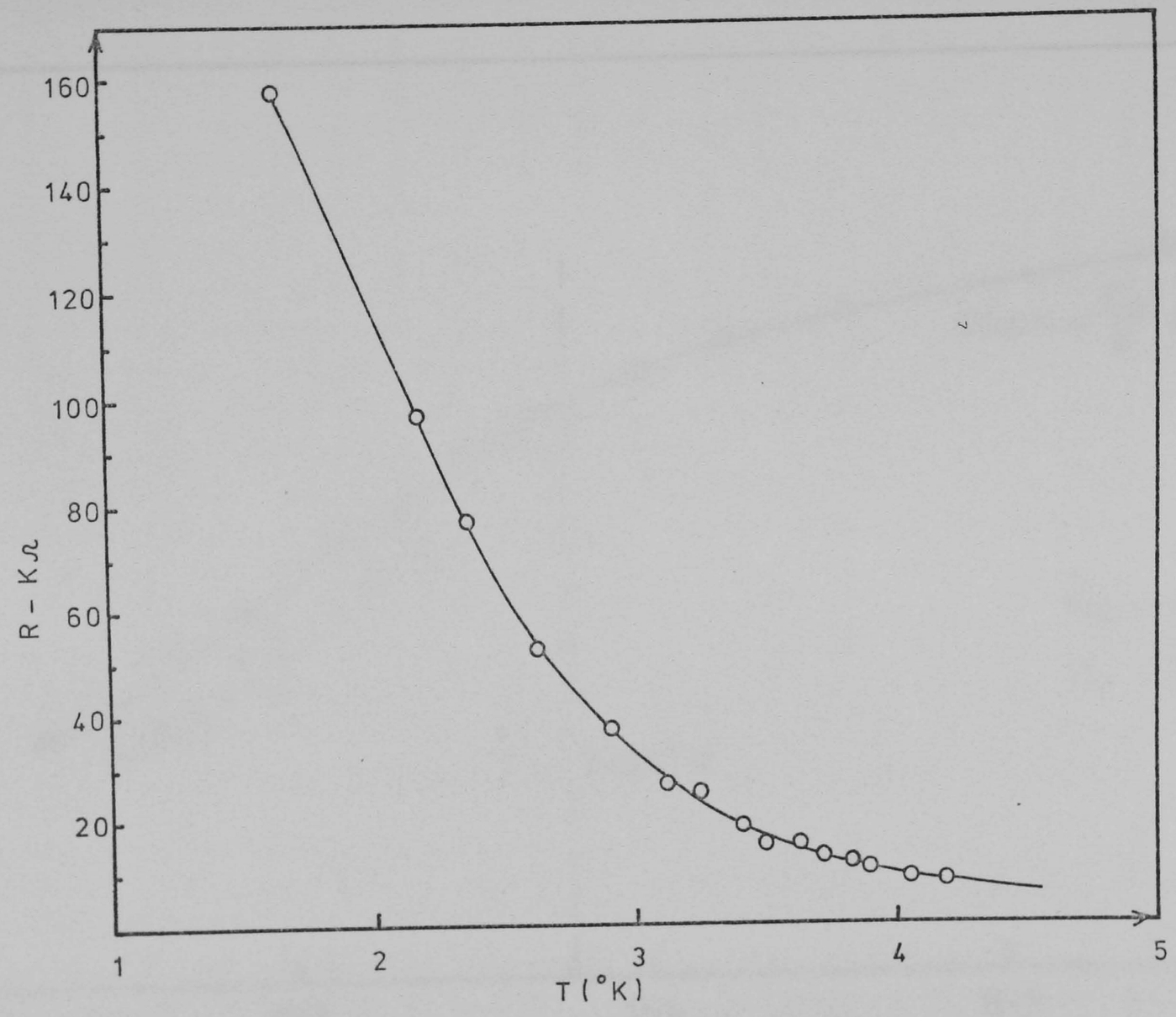

Figure 5.8. R-T curve for implanted Ge

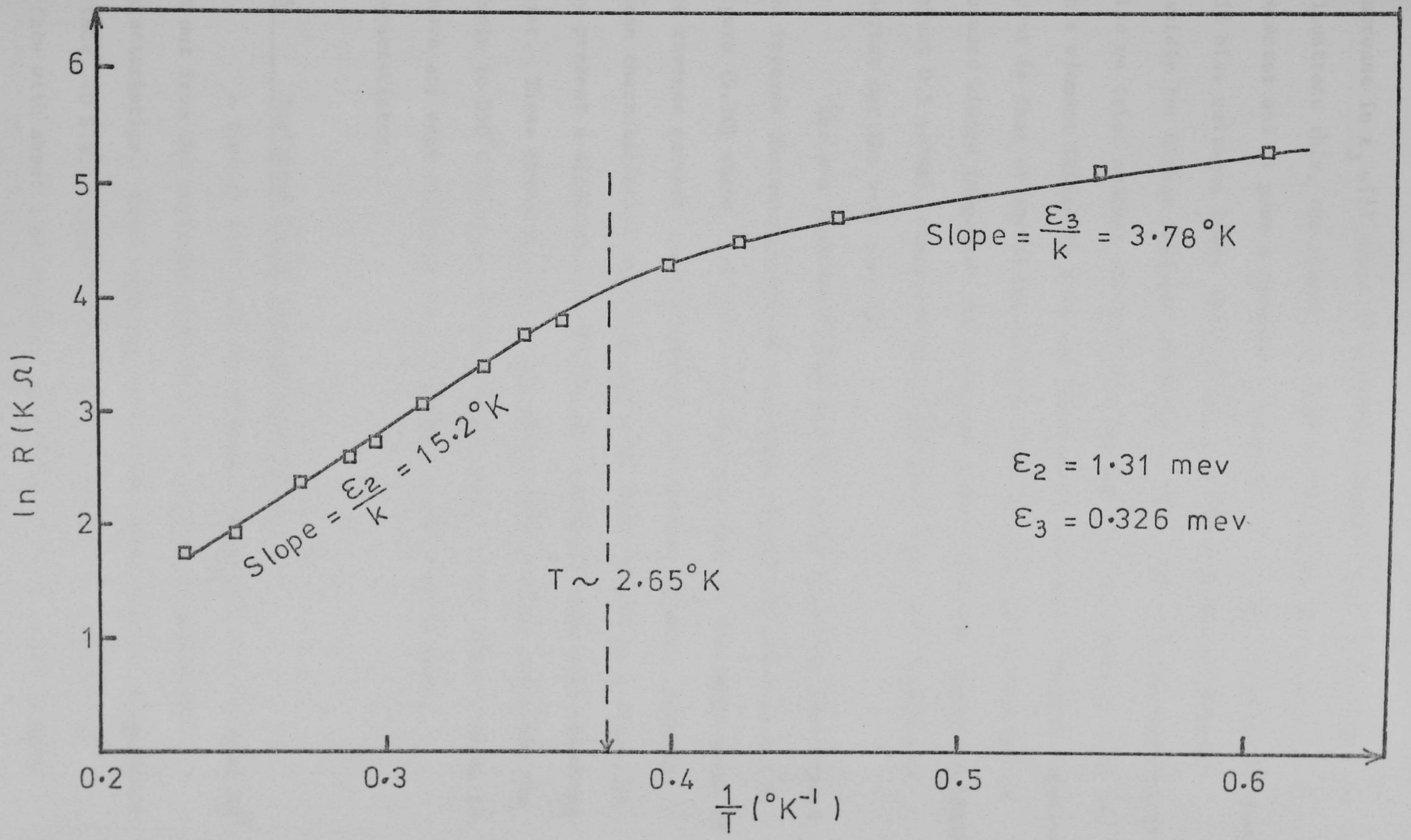

Figure 5.9. Activation energies of implanted Ge

decrease in ε_3 will occur if a reverse bias voltage is applied. To illustrate this, the element of 0.25 mm thickness was mounted as a detector and it gave a reasonable response to the far infrared at nearly all bias voltages lower than $\sim$50 mV, and the response drops very rapidly for higher voltages which is not the case in unimplanted samples. Also we tried another element with reduced thickness down to 0.11 mm. This element failed to give any response at any bias. Another important point is that at any of the two contacts, the junction should not be forward biased (negative) by a voltage higher than the junction potential (about 0.5 volts), otherwise the degenerate layer will completely shorten out the bulk current.

The p-n junction formed was tested by measuring the forward and reverse characteristics of an element of 0.25 mm thick at 4.2^{o}K. Figure (5.10) shows this plot from which we observe the large value of the reverse current associated with the reverse voltage. Although these characteristics seem reasonable at these levels as a diode, it may present a difficulty in obtaining a perfectly insulated absorbing layer. These characteristics have been repeated after annealing the sample to 550^{o}C in argon atmosphere for about 1 hour after etching to remove any edge effects, and no change was observed in these characteristcs.

5.6. Implanted Ge as a detector element

A typical size used for detector element is 4 x 2 x 0.25 mm^3 cut out from the implanted disc with the previously mentioned characteristics. After etching the element edges and the unimplanted surface, 40 S.W.G. copper wires are attached to the unimplanted surface with about 1 mm distance apart to get a reasonable element resistance for the preamplifier best matching. The solder used was lead-tin-antimony alloy solder. The element was rigidly fixed in a

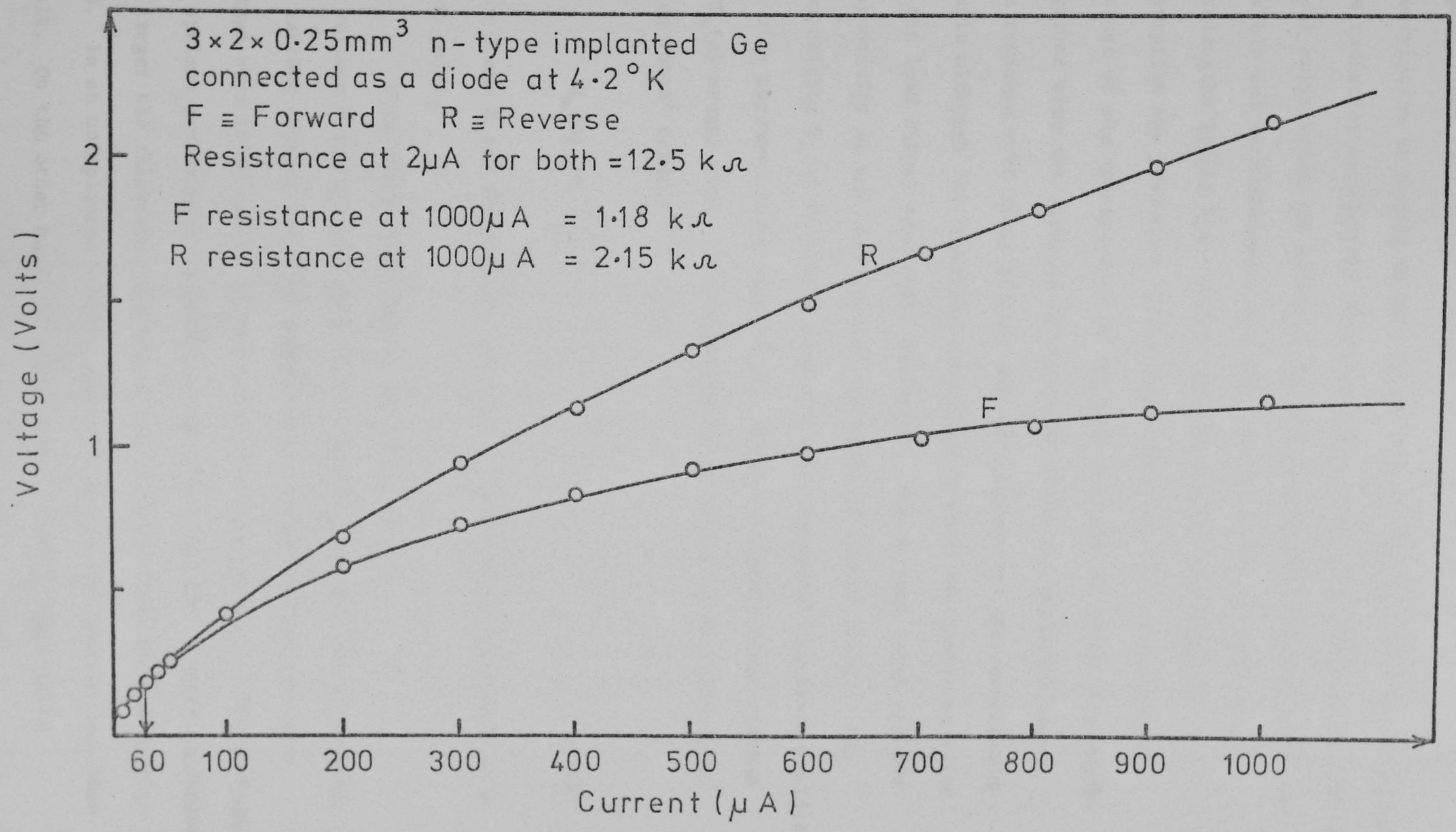

Figure 5.10. Rectification characteristics of implanted Ge

copper block cylindrical cavity by the aid of a thin nylon support (description in detail of this mount will be given in the next chapter). The radiation wavelengths were limited by using 3 mm thick high density black polyethylene in addition to cooled black photographic paper for visible and near frequency cut off. The polyethylene only admits wavelengths longer than 300μm. In this sample, the majority of absorption was presented by the degenerate layer as we mentioned because of the transparency of the bulk material at these wavelengths together with the weakness of radiation after the implanted layer. The response with these filters was very similar to the unimplanted sample although the operating conditions (mainly the operating point on the load curve) were quite different. The dc load curve and the responsivity at any bias current are shown in Figure (5.11). The responsivity $\mathcal{R}_\infty(o)$ (infinite load and zero frequency) increases rapidly for bias currents lower than $\sim 6\,\mu A$. There is another broad maximum in $\mathcal{R}_\infty(o)$ around 10μA. The responsivity in this plot was calculated using Jones' formula [3] i.e.,

$$\mathcal{R}_\infty(o) = \frac{Z - R}{2V} \qquad .. (5.33)$$

where Z and R are the dynamic and static impedances respectively at a given point.

V is the voltage across the element.

The voltage V for optimum conditions (maximum $\frac{S}{N}$ ratio) was 47 mV with one earthed crystal terminal leads. Both forward and reverse bias voltage were tried and no change in response was observed. The voltage for optimum performance is probably dependent upon the element thickness. The larger the thickness, the higher the voltage V for optimum conditions. In an unimplanted sample, this voltage is not usually less than 1 volt. On the other hand, if the sample is made thinner which

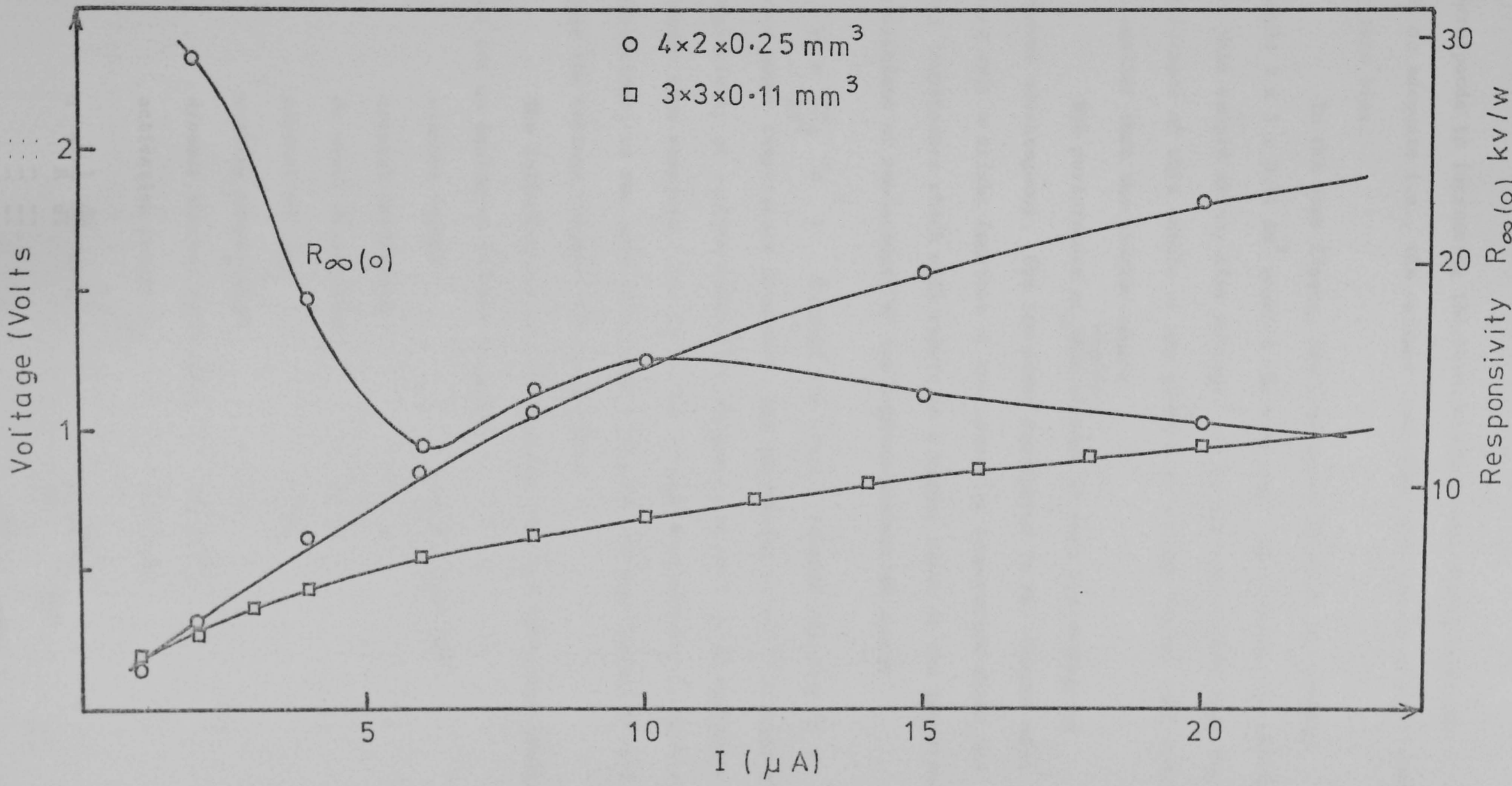

Figure 5.11. Load curves for implanted Ge and the responsivity

corresponds to increasing the reverse bias, the crystal response will not be adequate i.e., the optimum conditions will not be reached even at zero bias.

In the same figure, the load curve is shown for another sample 3 x 3 x 0.11 mm^3 mounted the same way. No response was observed for this sample at any bias voltage. It is also observable that the resistance of this sample at any given bias current larger than 1.3μA is smaller than the thicker sample.

The performance of ~~this~~ *the former* element at very low voltage is however advantageous. The low power dessipated in the element will cause only a slight increase of the operating temperature above the bath temperature which will result in a higher value of the temperature coefficient of resistance "α" for a given activation energy

ε ($\alpha = \frac{-\varepsilon}{kT^2}$ $^oK^{-1}$). Further, the element thermal capacity is a third power temperature dependent, and decreasing it will increase the responsivity at a given modulation frequency as well as it decreases the thermal time response. But since the voltage responsivity is directly proportional to the applied voltage V, the low voltage operation will cause the voltage responsivity to decrease.

The following are the performance data and operating conditions for an implanted element detector.

element volume	=	4 x 2 x 0.25 mm^3
crystal resistance	=	155 kΩ
dc power dissipation	=	14 nW
crystal voltage	=	47 mV
working temperature	=	2^oK
dynamic thermal conduction	=	100 μW. $^oK^{-1}$
activation energy ε_3	=	0.326 meV
$\alpha = \frac{1}{R}\frac{dR}{dT}$ at 2^oK	=	0.94 $^oK^{-1}$

dc responsivity at $R_L = \infty$	=	444 V/W
Cut-off frequency	=	110 Hz
N.E.P. (calculated)	=	9.3×10^{-12} W/Hz$^{\frac{1}{2}}$
Total calculated noise voltage	=	4 nV
Total measured noise voltage	=	120 nV

The element resistance is reduced to match the preamplifier minimum noise figure by decreasing the distance between the two electrical contacts. The high value of the calculated N.E.P. in this bolometer is a result of

(i) The very low bias voltage operation and the reduced value of activation energy ε_3 result in a very low value of responsivity.

(ii) The existance of an absorbing layer prohibits the quantum phototransition and hence the conductivity change especially when the maximum theoretical absorption of the layer was not fulfilled due to the substrate effect.

5.7. Proposed future developments

A great deal of improvement in the implanted Ge detectors could be achieved. An implanted element with well estimated channel width at 1.5°K and of surface area and implantation dose appropriate for good absorption can be prepared. The element will be etched down from the unimplanted surface except only a tiny part with the full thickness which will represent the responding element as shown in Figure (5.12).

The thickness of the absorbing surface could he made as thin as possible. The electrical leads are connected as shown. Reaching to this shape could easily be achieved in practice. The main advantages of such designs are as follows:

(i) The fulfillment of the optimum design of the implanted layer resistance to give maximum absorption at any frequency because of the elimination of substrate effects as discussed before. 50% absorption could be easily fulfilled for single incidence.

(ii) The very large reduction of the element thermal capacity.

(iii) The intimate thermal contact between the absorbing surface and the responding element.

(iv) The expected reduction in N.E.P. due to the element size reduction.

The main consideration which has to be taken into account is the frequency dependence of the free carrier absorption of the degenerate layer. Then the required implantation dose should be designed to cover the interested part of the spectrum. The remaining thickness after etching of the major surface should not necessarily be as small as the implanted layer. But it can be reduced as much as it becomes mechanically reasonable.

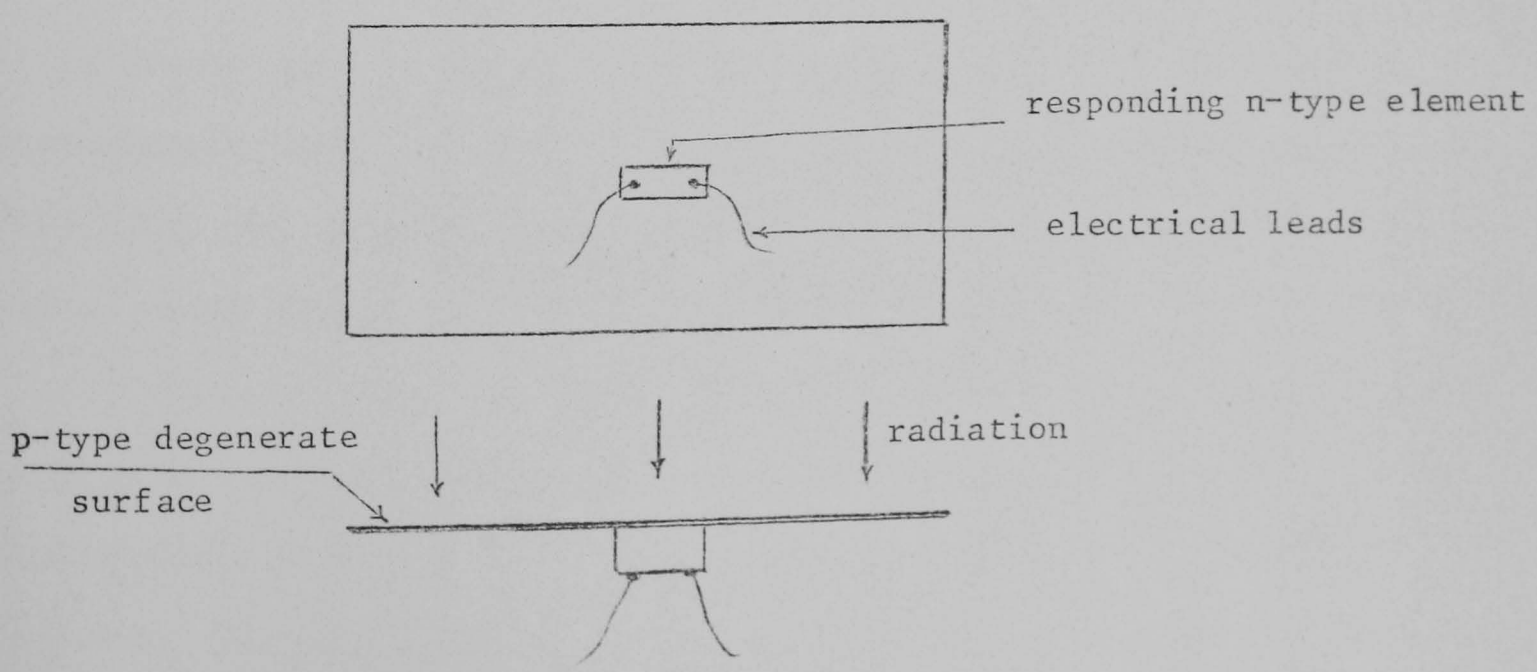

Figure 5.12

CHAPTER V

REFERENCES

(1) Sladek, R.J. and R.W. Keyes, Phys. Rev. 122, 437 (1961)

(2) Harvey, A.F. "Microwave Engineering" Academic Press, London and New York (1963) pp.40

(3) Jones, R.C., J. Opt. Soc. Am. 43, 1 (1953)

(4) Little, W.A., Can. J. Phys. Vol. 37, 334 (1959)

CHAPTER VI

FAR INFRARED Ge DETECTORS

6.1. Introduction

The work in this chapter describes the construction of high sensitivity far infrared Ge detectors; design and performance characteristics are considered. All the dc measurements and calibration tests are also given. The detectors utilise the previous tested Ge samples. The n-type intermediate doping Ge was found to be the most suitable element for this purpose. The majority of the detector measurements and calibrations were done using this sample. However, some comparison with the p-type compensated Ge are also given. Two n-type high sensitivity detectors differing in the operating conditions are compared regarding the various response mechanisms. Both detectors are Johnson noise limited at long wavelengths and background radiation limited for $\lambda > 200\mu m$. An actual N.E.P. of about 2×10^{-13} $W.Hz^{-\frac{1}{2}}$ was fulfilled. Spectral characteristics and astronomical applications at long wavelengths are shown.

We classify both detectors as a semi-quantum detector in which the majority of absorption is due to the quantum transitions while the response is due to both lattice temperature variation and photoconductivity. These two mechanisms are not available together for either pure quantum detectors as in InSb and low doping Ge detectors or purely thermal detectors using absorbing layers.

One of these detectors, which we will refer to as No. 1, is working in the negative dynamic impedance region of the load curve with absolute stability and it has an enhanced millimetre wavelength response. The other (No. 2) is working in the positive region of the load curve and it has an enhanced response at 250μm, although both of them have nearly equal millimetre sensitivity.

6.2. Design and construction

The Ge elements used for these detectors are Sb-doped to an intermediate doping level of $\sim 5.5 \times 10^{16}$ and $\sim 5 \times 10^{16}$ cm^{-3} for No. 1 and No. 2 respectively. As we have seen, this concentration level is distinguished by the existance of an activation energy ε_2 which has now been identified as a broadening of the first excited state of the impurity atoms. The crystal is singly doped with Sb with unintended compensation. The antimony atom has the largest atomic radius among the other known impurities in Ge. Therefore, it has a large effective coulombic potential spread in the Ge lattice. Since the overlap energy band ε_2 is responsible for the majority of far infrared absorption, then Sb atoms present the best choice as a dopant material.

6.2.1. Crystal and filters mounts

The elements were cut out from the same grown crystal in <110> direction tested before. The crystal dimensions are $3 \times 2 \times 0.25$ mm^3 and $4 \times 2 \times 0.12$ mm^3 for No. 1 and No. 2 detectors respectively. The electrical leads were attached to the crystal using lead-tin-antimony alloy solder after the crystals have been freshly etched for about 1.5 minutes in CP4A solution. The connecting leads consist of 7 mm long 46 S.W.G. copper wire attached to another long 40 S.W.G. copper wire, and the final total length from the crystal to the heat sink was limited to $\sim$ 12 mm long. About 2.5 inches of the thick wire was accommodated in grooves milled in the bottom of a copper block and the heat sink was provided by pressing the copper block to the cold surface of the liquid helium flask using silicon heat sink paste. Using this method, the wires coming out of the crystal to the heat sink are completely shielded against any stray warm radiation in the vacuum chamber.

The crystal itself is situated in a cylindrical cavity in the

copper block having 5 mm diameter and depth with semi-spherical bottom. The crystal is supported in the cavity using a thin mylar bridge by the aid of a tiny spot of low temperature sticky varnish, this support was very essential to prevent mechanical vibrations which may dominate any other sources of noise. Besides, the mylar is transparent to the far infrared radiation so that the transmitted power through the crystal is reflected back to the crystal without significant loss. A little groove was milled at the edge of the cylindrical cavity nearest to the cold surface and accommodates the crystal wires fully before the heat sink grooves at the bottom surface of the copper block. The copper block and the radiation copper cone are heavily coated with gold to minimise the reflection losses. Figure (6.1) shows this mount and the crystal position.

All the room temperature ends of the connnecting leads are constantan wires to minimise the boil-off rate of the liquid helium and to decrease the minimum possible temperature after fully pumping. The mentioned crystal sizes are chosen to fulfil the resistance requirements for the preamplifier matching. The load resistors used are all wire wound and cooled down to the helium bath temperature by enclosing them in a copper housing firmly connected to the cold bottom plate. All the leads in the vacuum chamber are firmly attached to the cold surface using sticky varnish. One of the crystal leads after passing through the liquid helium using pin seals is earthed to the copper block. The other signal lead is lead to outside to the preamplifier input.

All the filters used for admitting radiation wavelengths longer than 200μm are cooled to the same temperature, except a thin sheet (100μm) of black polyethylene which is connected to the radiation shield situated between the helium flask and the room temperature body of the cryostat. These filters consist of a double layer of thalium halide absorption filters of 0.5 mm thick each, wedged quartz of 1 mm mean

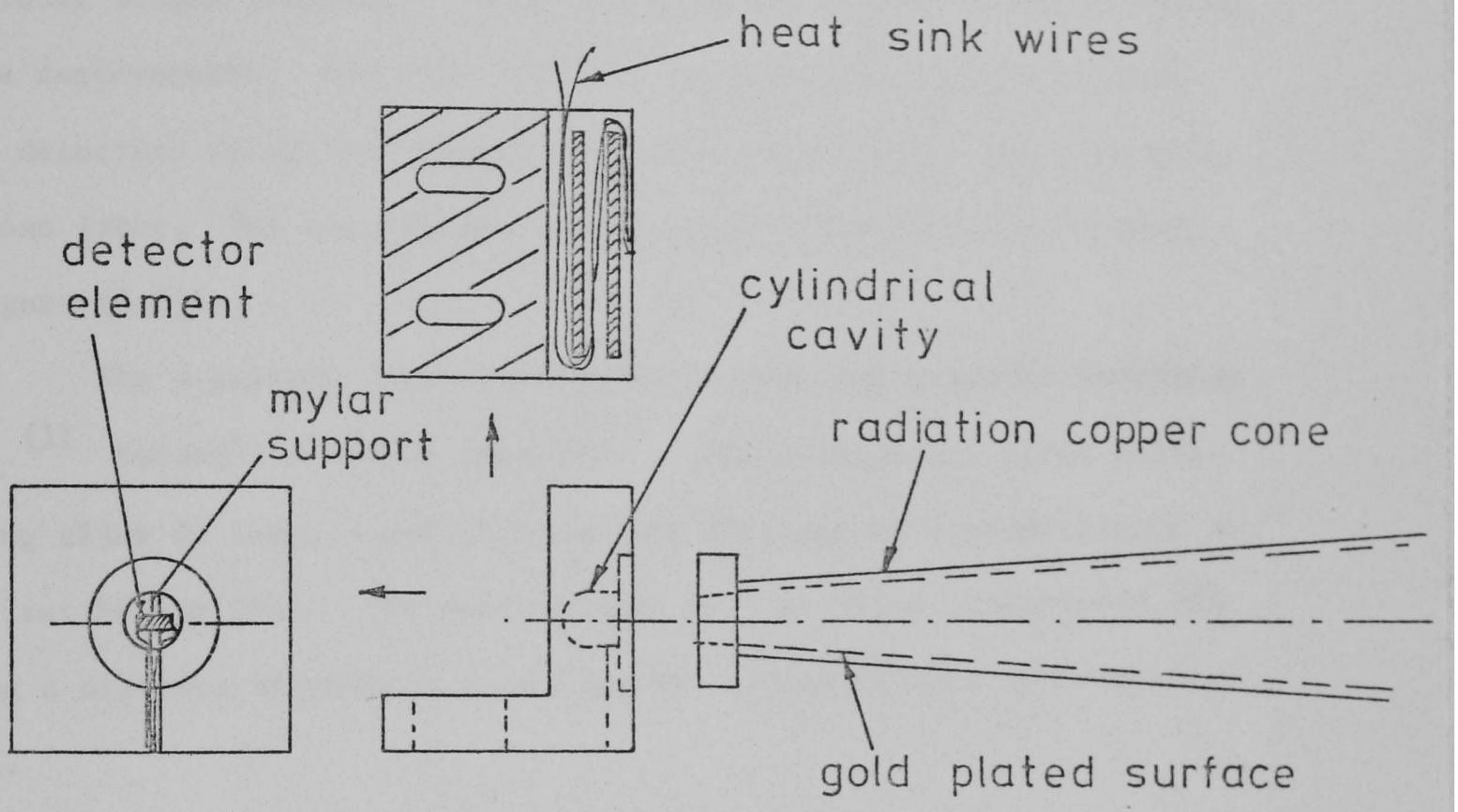

Figure 6.1. Crystal mount

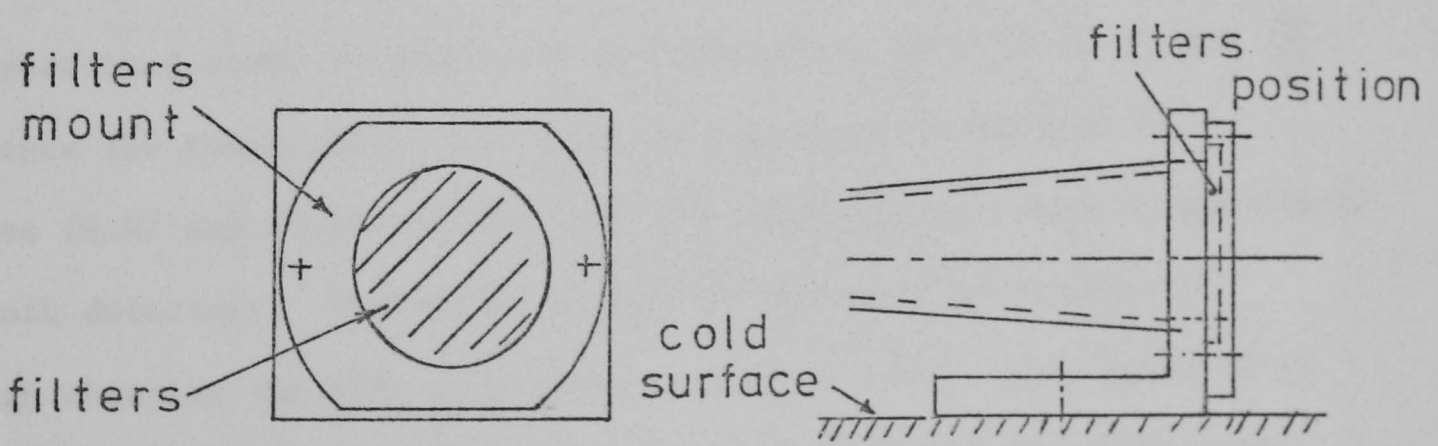

Figure 6.2. Filters mount

thickness and 100μm thick black photographic paper. These filters are accommodated in a special mount at the large end of the copper cone as shown in Figure (6.2). All detectors calibration, testing and practical applications were performed with these permanent filters, additional longer wavelength filters may or may not be added according to the requirements. All these filters are spectrally measured with these detectors using the fourier transform spectrometer and this will be shown later. The overall detector system in the cryostat is shown in Figure (6.3).

The cryostats used are similar to that described by Zwerdling et al.[1] having 1.2 litres capacity.* These cryostats after fully pumping allow at least 8 and 12 hours for HD-1 and HD-3 respectively for the first helium fill. The outer window is 3 mm thick transparent TPX having a distance of about 2.5 cm from the cooled filters and the cone input.

6.3. DC measurements

Continuous measurements of the V-I characteristics of the mounted crystal is of great importance. The dc responsivity and the exact operating point of the bolometer can be determined. The operating point is determined by the intersection of the dc load line with the bolometer load curve at which all the electrical data (V, I, R and $\frac{dV}{dI}$) and hence the responsivity are known as explained in Chapter II. Figures (6.4) and (6.5) are the load and responsivity curves respectively for both detectors. The indicated operating points were selected through changing the bias conditions. Minimum N.E.P. were achieved at these points. The dc responsivity was calculated from the electrical data using Jones'[2] relation

*Supplied by Infrared Laboratories, INC., Tucson, Arizona (U.S.A.)

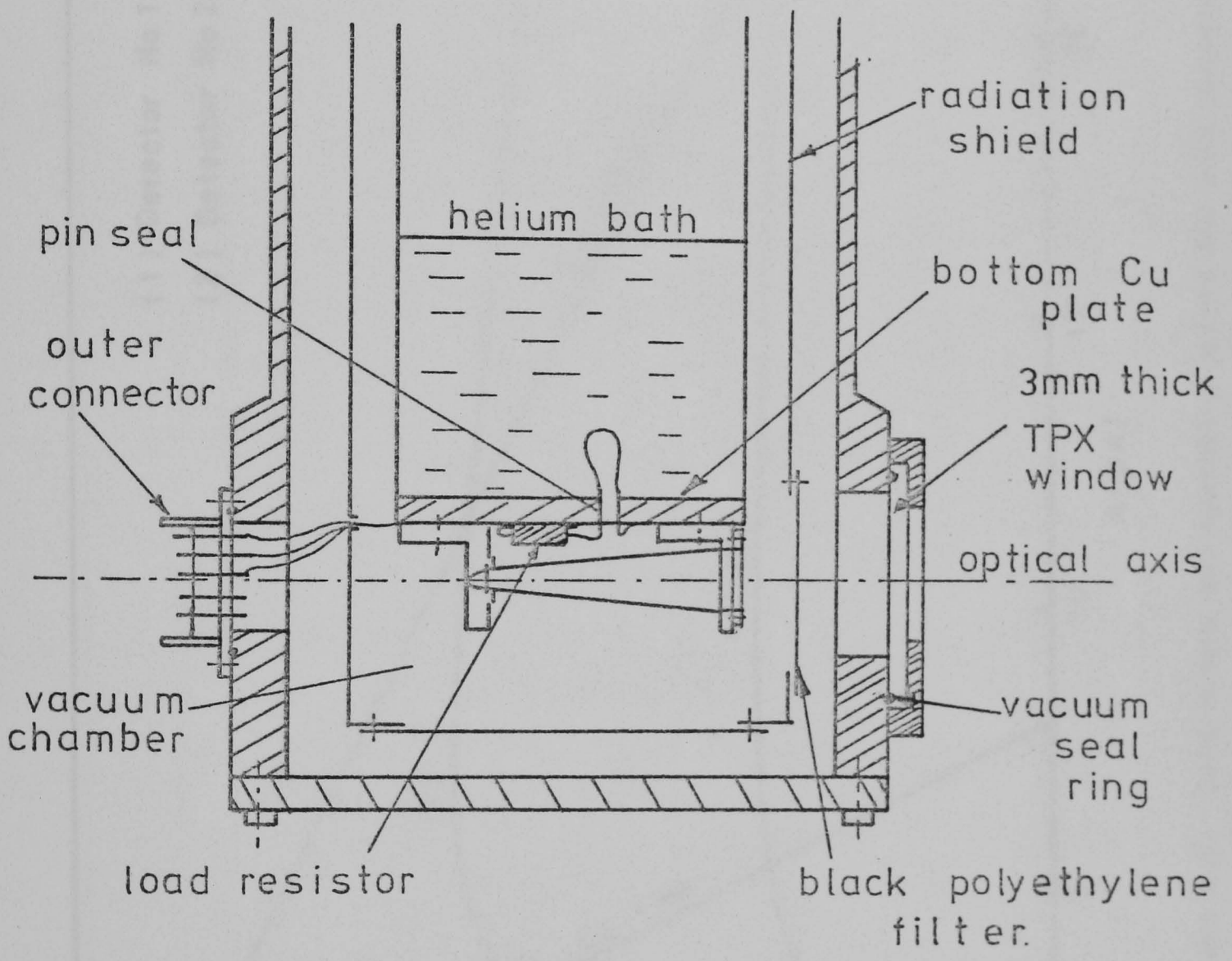

Figure 6.3. Detector assembly

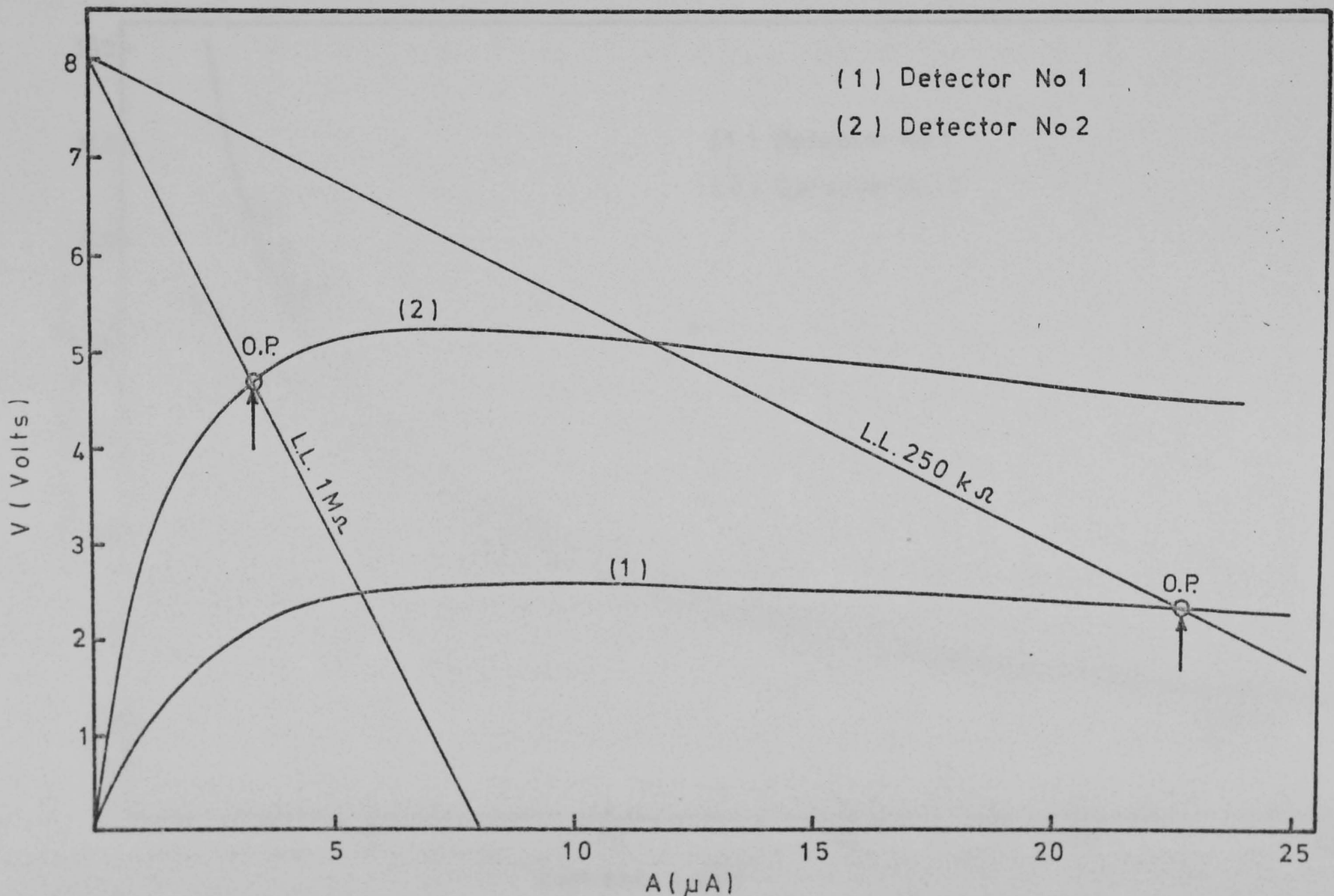

Figure 6.4. Load curves and operating points for both detectors

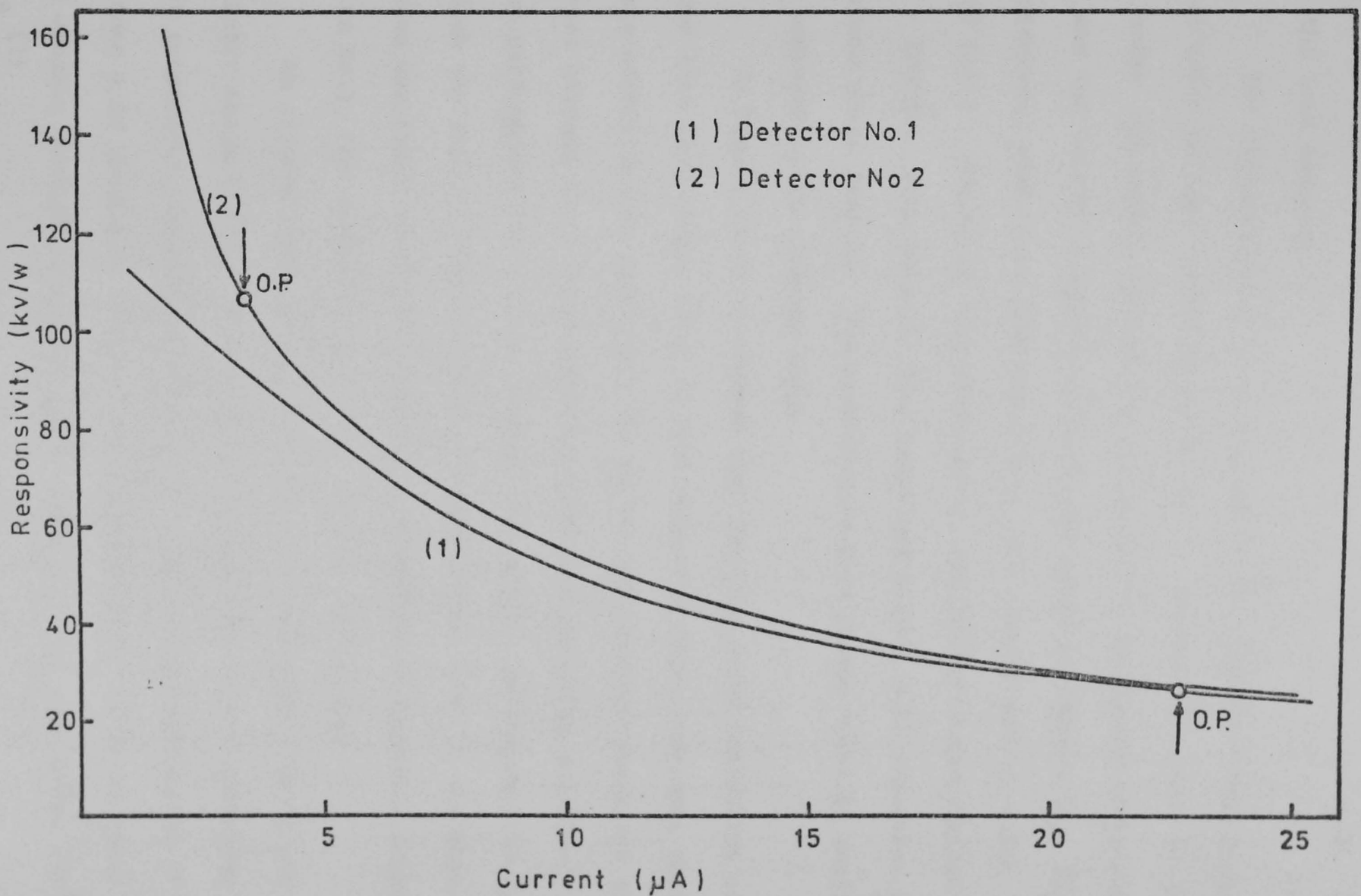

Figure 6.5, Voltage responsivity for both detectors vs I

$$\mathcal{R}_{dc} = \frac{Z - R}{2V} \cdot \frac{R_L}{R_L + Z} \quad v/w \qquad .. (6.1)$$

R and Z are the crystal static and dynamic impedances respectively. R_L is the load resistor.

The calculated N.E.P. is derived by dividing the total theoretical noise voltage contributions by the dc responsivity given by (6.1). These noise are mainly Johnson and phonon noise, background radiation noise and the inverse frequency noise as discussed in Chapter II. These two detectors, under operating conditions, are Johnson and $\frac{1}{f}$ noise limited for f < 200 Hz at long wavelengths, and Johnson noise limited only for f > 200 Hz. With 200μm filters mentioned before, both detectors are background noise limited. The contribution from phonon noise is negligibly small compared to the Johnson noise.

In Figure (6.4) we observe that the load curve intersects with the load line in a single point in both detectors which indicates that absolute stability was fulfilled. We do not know whether there are any relations between the element impurity level and operating point for optimum performance for a given thermal conduction. In detector No.2, for which the doping level is slightly smaller than in No.1, the best operation was found to be in the positive differential impedance region, while in No.1, the negative region was found to be the best.

An alternative expression for the dc responsivity is to use the electro-thermal data. This requires a knowledge of the operating element temperature from which the thermal temperature coefficient of resistance α is obtained. Also at the temperature T, the exact value of the dynamic thermal conduction $\mathcal{G}_d$ is required. The expression for $\mathcal{R}$ is then [1]

$$\mathcal{R} = \frac{\alpha V}{\mathcal{G}_d - \alpha P B} \cdot \frac{R_L}{R_L + R} \qquad .. (6.2)$$

where $\alpha = \frac{-\varepsilon}{kT^2}$ and ε is the respective activation energy of the conduction mechanism involved at the temperature T.

$P = VI$ is the power dissipation at the operating point

$B = \frac{R_L - R}{R_L + R}$ is the electrothermal interaction factor

and $\mathcal{G}_d = \frac{dP}{dT}$ is the slope of the dc power curve vs T at the operating temperature.

Expression (6.1) of $\mathcal{R}$ is more reliable and easy to use as well as it takes into account the total non-linearity of the detector element through the value of Z. This expression was always used in connection with the load curve in our work. However, a comparison of (6.1) and (6.2) is sometimes required as we will see.

The dc measurements done here on another sample of n-type and p-type compensated materials enabled us to plot the variations of the dc responsivities vs the bias currents for various bath temperatures. The thermal conduction $\mathcal{G}_d$ vs T was also plotted for two recommended wiring methods. An estimation of the dc continuum background power absorbed by the typical element at certain filter setting was also performed.

6.3.1. Responsivity variation with temperature

The peak responsivities and the corresponding bias currents vary with bath temperatures in various ways. The peak responsivity for a given crystal mount decreases and broadens with increasing bath temperature. This variation is shown in Figure (6.6) for the p-type compensated Ge and using the same mount but with 40 S.W.G. copper wire. This behaviour can easily be explained if we express the responsivity as a function of the temperature using the simple expression

$$\mathcal{R} = \frac{\alpha V}{\mathcal{G}_d} \quad \text{(dc with infinite load and unity emissivity)}$$

substituting for $\alpha = \frac{-\varepsilon}{kT^2}$

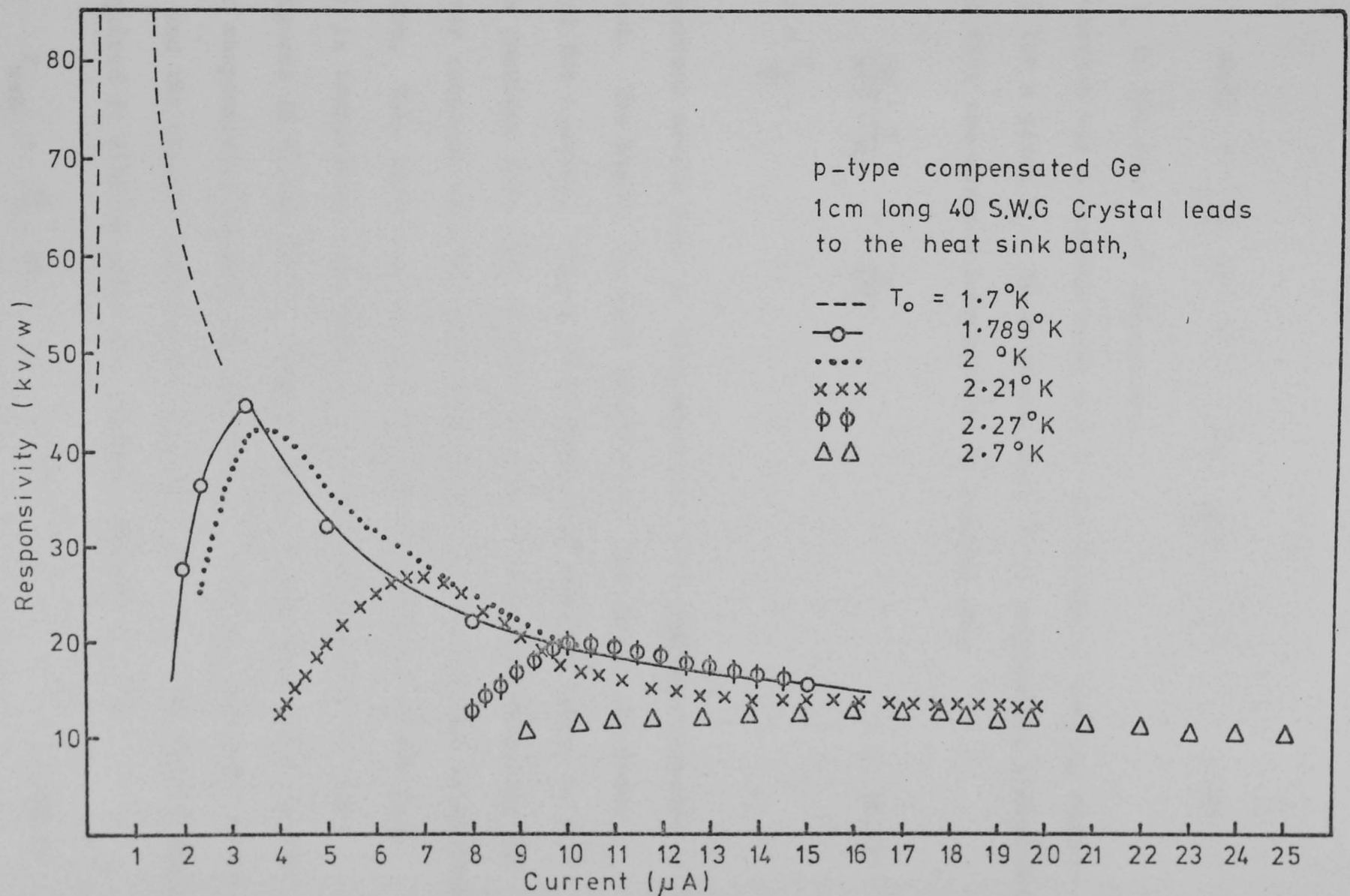

Figure 6.6. Responsivity variation with heat sink temperature and bias current

$$V(T) = \left[\varrho R (T - T_o) \right]^{\frac{1}{2}}$$

and R $\quad R = R_o \exp \frac{\varepsilon}{kT}$

we find

$$\mathcal{R}(T) = \frac{-\varepsilon}{kT^2} (T - T_o)^{\frac{1}{2}} \cdot \exp \frac{\varepsilon}{2kT} \cdot \left[\frac{R_o}{\varrho}\right]^{\frac{1}{2}} \quad .. (6.3)$$

where T_o is the heat sink temperature.

This function has a maximum value w.r.t. the bolometer working temperature T for a given T_o. If we assume that ϱ is temperature independent, we find that the maximum responsivity is reached when

$$\frac{4x - 3}{x(1 - x)} = \frac{\varepsilon}{kT_o} \quad .. (6.4)$$

where $x = \frac{T_o}{T}$.

The important notice here is that the ratio x for maximum response is T_o dependent. The higher the bath temperature, the larger the power required for biasing. Figure (6.7) shows the computed values of x vs T_o. We consider this plot is very important curve for optimising the bolometer response once the bath temperature and the thermal conduction are known. This curve is, however, approximate because of the fact that ϱ is temperature dependent at very low temperatures as clear from Figures (6.8) and (6.9). Nevertheless, a very near value to the maximum responsivity biasing is obtained if we extract the exact value of ϱ_s and the element temperature rise $\Delta T = (T - T_o)$ from Figure (6.7). The required dc biasing power for maximum response P_{max} is

$$P_{max} = \varrho_s . \Delta T \quad .. (6.5)$$

The mentioned variation of peak responsivity with x and T_o explains the decrease of bias currents for $\mathcal{R}_{max}$ with reducing T_o.

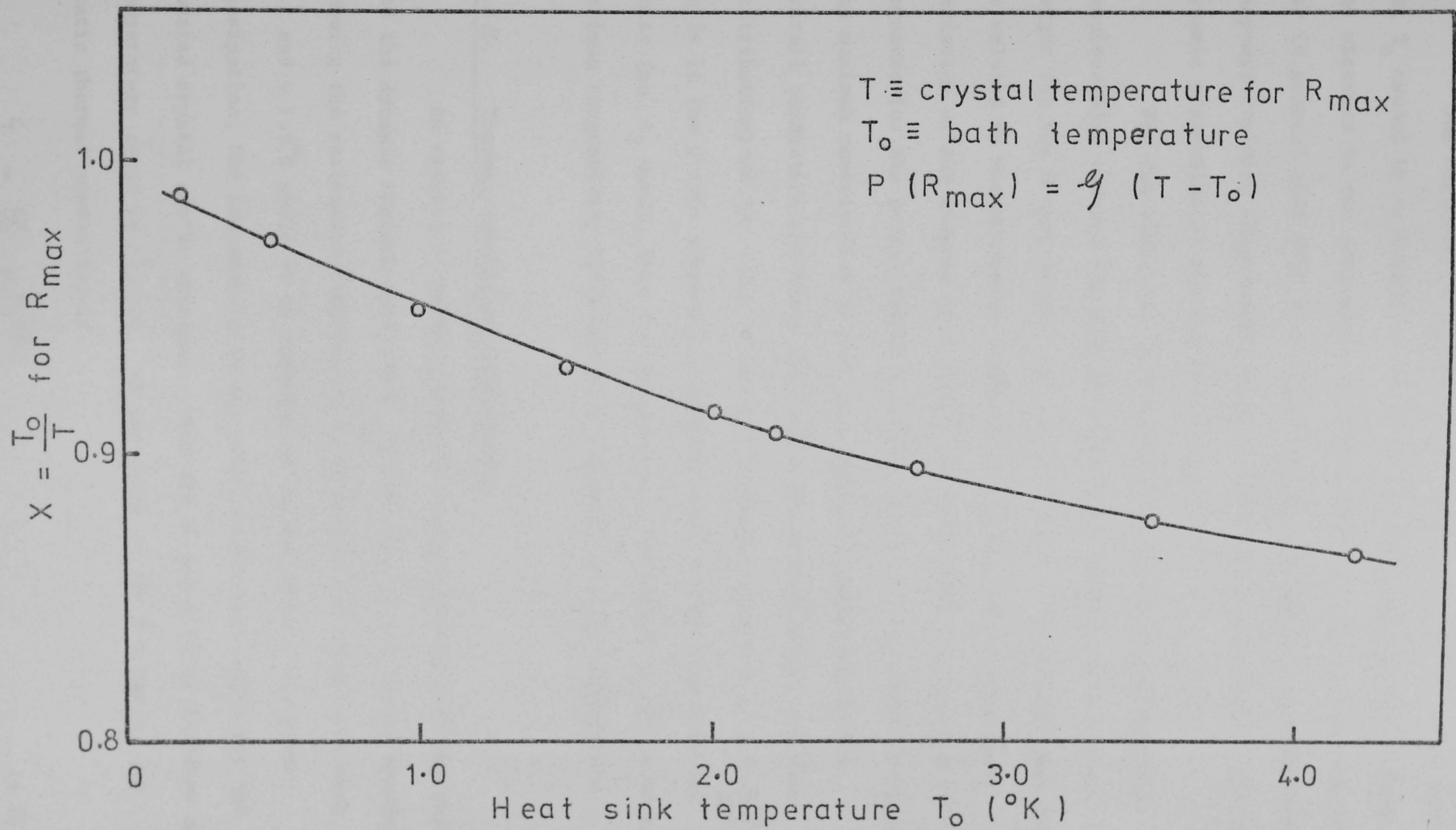

Figure 6.7. Dependence of maximum responsivity point on crystal and bath temperatures

The observed broadening of the peak responsivity with increasing T_o cannot be explained in terms of the doping conditions because it was observed in two completely different samples. But rather, we can say in general that this is a result of the exponential dependence of responsivity with temperature for a given activation energy ε and the dynamic properties of the mounted element.

For the radiation characteristics, it was found that the required bias current for optimum performance (minimum N.E.P.) is larger for the n-type sample than in the p-type. We believe that this is related to the absorption characteristics and the corresponding variation of the element resistance. We think that the optimum performance for the n-type sample is achieved when a compromise is reached for the maximum contribution of the ε_2 conduction mechanism to the overall conduction (and hence the larger photoconductivity response contribution) and the value of thermal response described by $\alpha = \frac{-\varepsilon_3}{kT^2}$. While in the p-type compensated samples, such competition does not exist (no ε_2 band), then the detector must be biased to the point of maximum responsivity fulfilled at the minimum possible temperature.

6.3.2. Thermal conduction measurements

An essential thermal parameter to be determined is the static and the dynamic thermal conduction $\mathcal{G}_s$ and $\mathcal{G}_d$ of the wiring system. Knowing the resistance-temperature variation of the element between 4.2 and $\sim 1.5^{o}K$ while it is immersed in helium at very low power dissipation, the temperature at any point on the load curve for the mounted crystal can be obtained. Then the dc power VI as function of temperature could be plotted. At any point of the P-T curve, the static thermal conduction is

$$\mathcal{G}_s = \frac{\Delta P}{\Delta T} \quad W.^{o}K^{-1} \qquad .. (6.6)$$

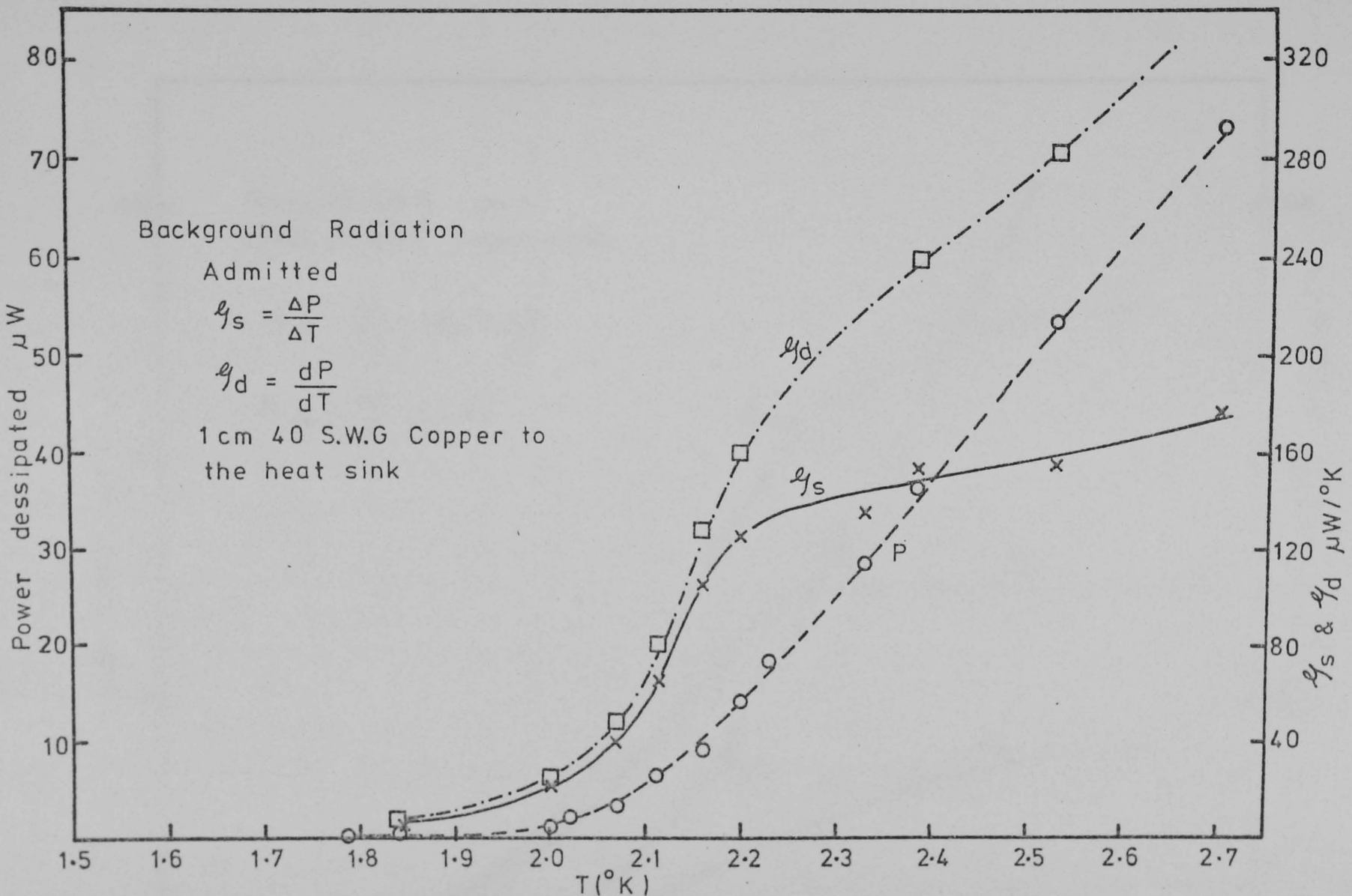

Figure 6.8. Dynamic and static thermal conduction

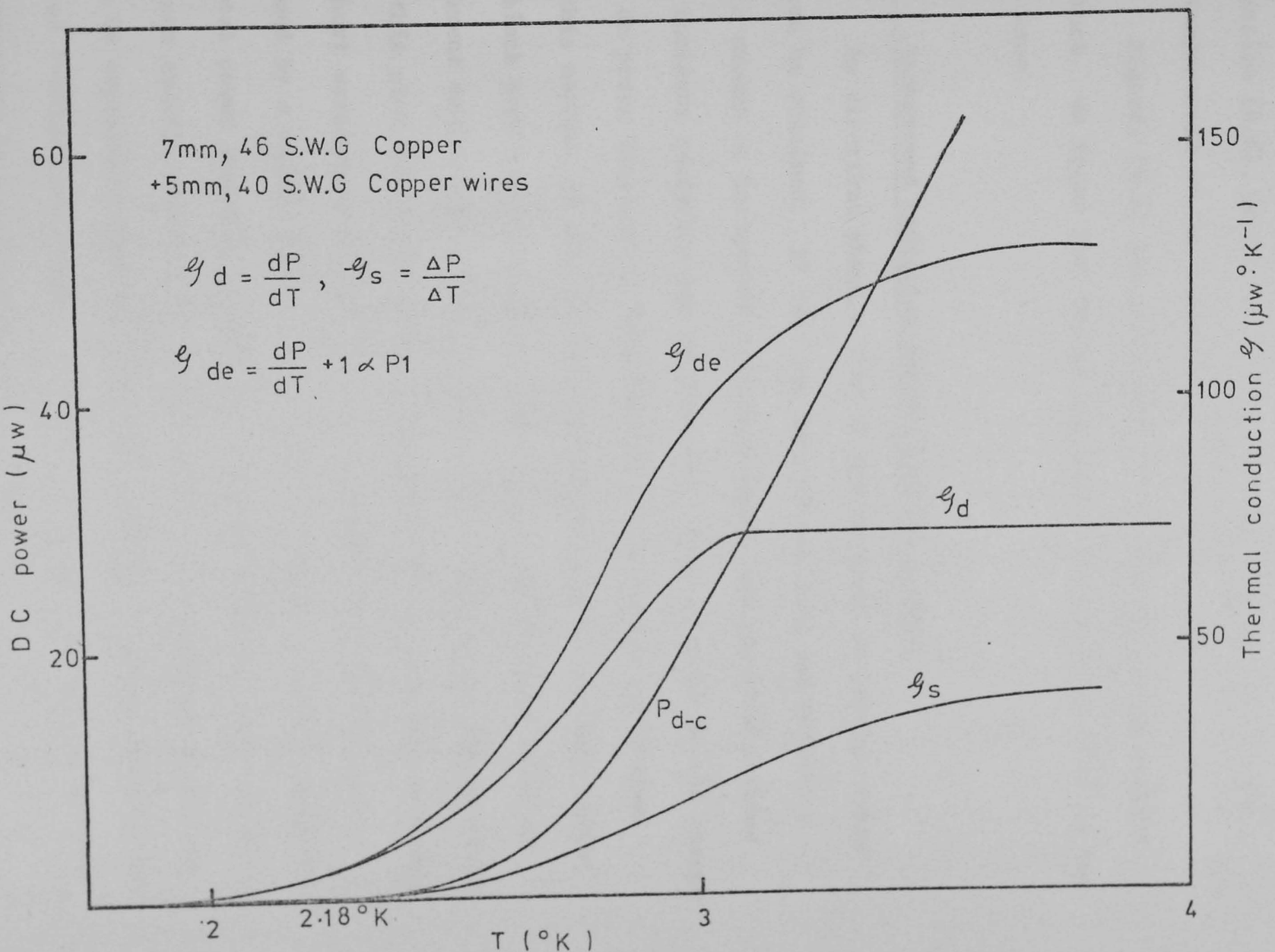

Figure 6.9. Thermal conduction for both detectors

and the dynamic value $\mathcal{G}_d$ will be

$$\mathcal{G}_d = \frac{dP}{dT} \quad W.^{o}K^{-1} \qquad .. (6.7)$$

In expression (6.6), ΔP is the dc power dissipation and ΔT is the excess temperature of the element above the helium bath.

Figures (6.8) and (6.9) show P, $\mathcal{G}_s$ and $\mathcal{G}_d$ vs the element temperature. We found that the wiring system described by (6.9) is the optimum case.

6.3.3. Background radiation absorbed by the element

As described above a plot of the dc power vs crystal resistance can be obtained. If this was carried out with and without a specific amount of background radiation input, the absorbed portion of the incident radiation can be obtained. This is given by the change of the dc power dissipation required for fixed element resistance. Using this method, if the incident radiation is delivered by a calibrated black body source of known power output, an accurate value of the element emissivity can be derived. For illustration, Figure (6.10) shows this plot for p-type compensated material and with system cooled 50μm short wavelength cutting filters. Cutting of radiation was performed by a copper disc in front of the crystal. From the figure, the total power absorbed is about 4μW at the indicated arrow. It is not known exactly whether the absorption is bias dependent or not in p-type Ge especially when the radiation for direct phototransition is involved (∿100μm wavelength). However, it seems from the figure that the absorption is increased by more biasing.

6.3.4. Thermal temperature coefficient of resistance $\alpha = \frac{-\varepsilon}{kT^2}$.

This parameter is the essential part for thermometric

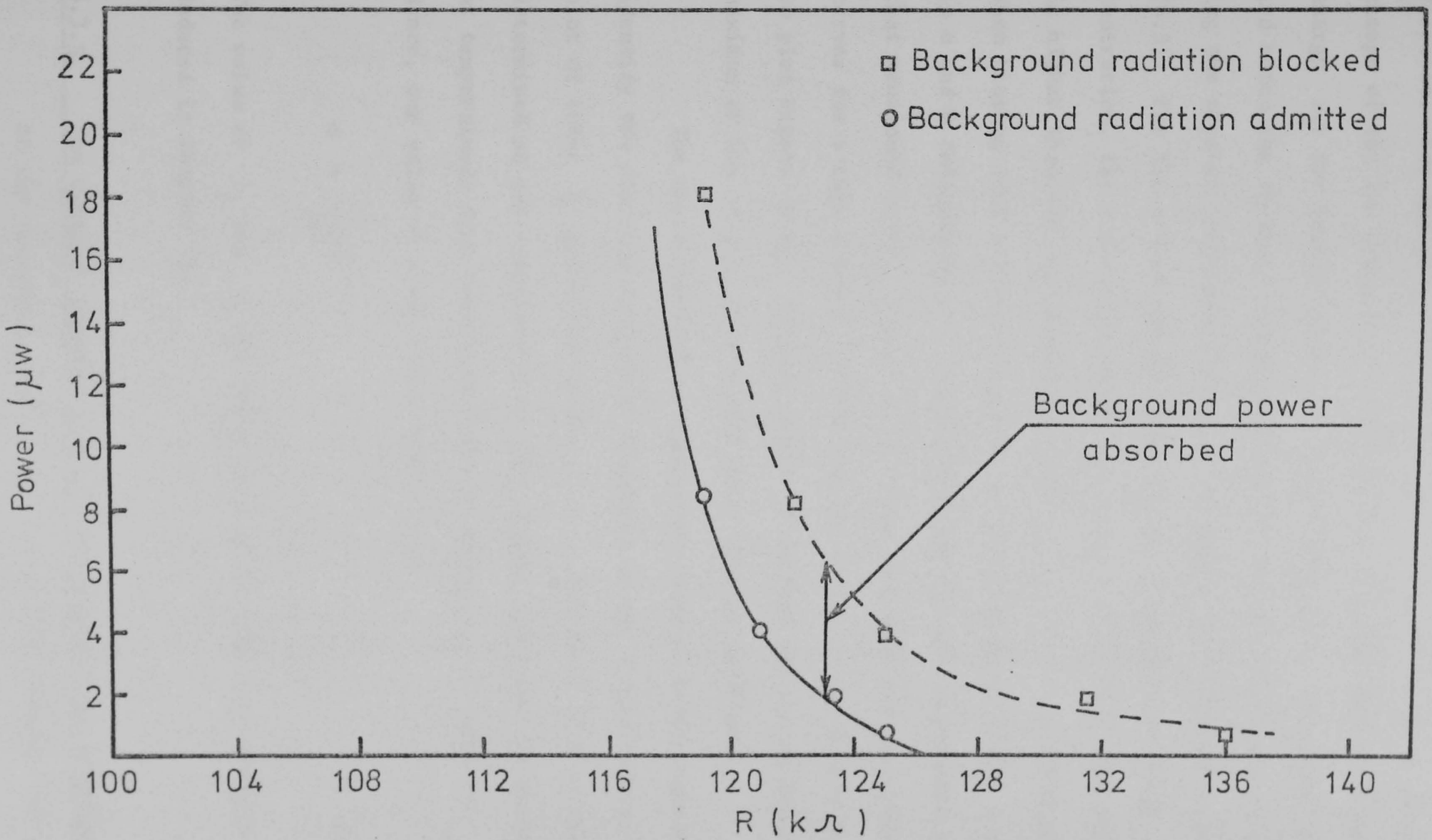

Figure 6.10. Determination of the absorbed power by the bolometer

response. For the p-type compensated material, where there is no change of the low temperature activation energy (hopping activation energy ε_3) for temperatures even higher than 4.2°K, the value of α and hence the thermal responsivity should decrease rapidly with increasing the crystal temperature as shown in Figure (6.6) and expressed by (6.3). For the n-type sample, being in the intermediate doping concentration, the activation energy ε_2, appears at about 2.3°K, which is higher than the low temperature value ($\varepsilon_2 \simeq 1.4$, $\varepsilon_3 \simeq 0.9$ meV). When biasing such a mounted crystal, we should expect firstly a decrease in α and $\mathcal{R}$ followed by an increase when the crystal temperature reaches that mentioned above. Figure (6.11) shows the load and responsivity curves for n-type samples mounted similar to the p-type sample used to plot Figure (6.6). In this figure we observe the second broad maximum of the responsivity around about 10μA as explained.

The operating crystal temperature must be known exactly to identify the involved conduction mechanism in the n-type sample. The plot of lnRvs $\frac{1}{T}$ gives the values of ε. The value of α is then determined at the temperature T. Both n-type detectors are working at temperatures such that the activation energy ε_2 is involved. Hence, our value of α for these detectors is

$$\alpha = \frac{-\varepsilon_2}{kT^2} \qquad .. (6.8)$$

The value of ε_2 and ε_3 for these samples are identical to that deduced in Chapter III.

6.3.5. The element's thermal capacity and thermal time response

At the operating point on the load curve, knowing the crystal temperature T, the volume v and the dynamic thermal conduction $\mathcal{G}_d$, an accurate value of the element thermal capacity C and the response time τ_r can be obtained from

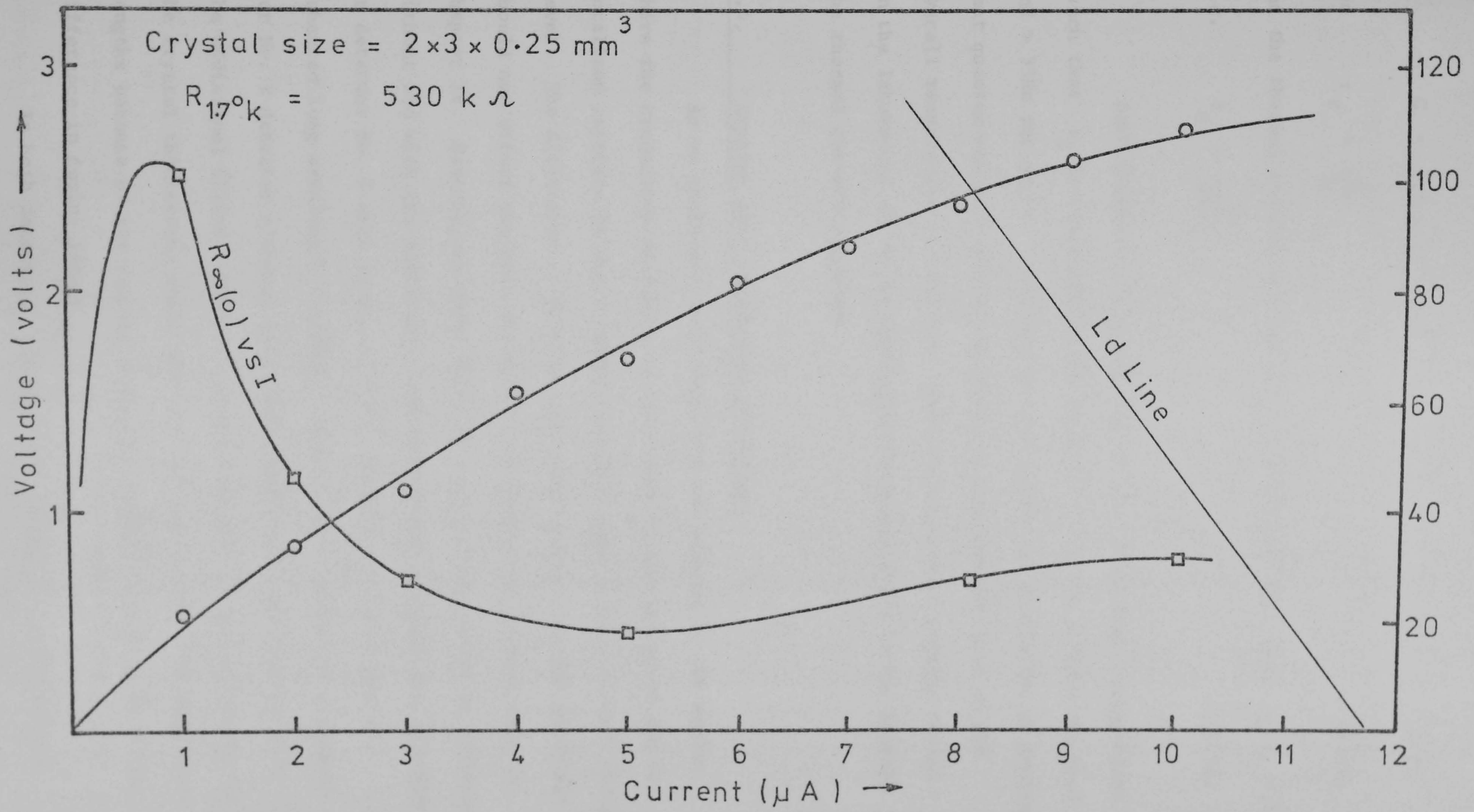

Figure 6.11. DC responsivity for n-type detector (note the second broad maximum)

$$C = 6.8 \times 10^{-6} \; T^3 . \; v \quad J.{}^{o}K^{-1} \qquad .. (6.9)$$

and $$\tau_r = \frac{C}{\varrho_d} \qquad .. (6.10)$$

and the thermal cut-off frequency f_c is determined such that $\omega_c \tau_r = 1$

i.e. $$f_c = \frac{1}{2\pi \tau_r} \qquad .. (6.11)$$

Both detectors being working at relatively high temperatures (such that ε_2 is dominating), the value of f_c is low ($\sim$ 50Hz for No.2 and $\sim$ 33Hz for No.1). This was compensated by the domination of another fast quantum response which contributes a considerable part of the overall response as we will see. Both detectors were usually tested in the laboratory at 200 Hz modulation frequency which is far beyond the thermal cut-off frequency.

6.4. Crystal data and working conditions

As we mentioned, both detectors are working in the region where the conduction mechanism is controlled by the motion of the delocalized carriers in the overlapping energy band created at such doping level. The difference in biasing conditions between the two detectors should not affect the bulk absorption coefficient as we have seen in Chapter IV. However, we found that the ratio of the detectors response without and with the additional 3 mm thick black polyethylene is higher in detector No. 2 than in No. 1, i.e., the No. 1 detector has an enhanced long wavelength response. This ratio is about twice larger for No. 2 detector although both have nearly equal sensitivity with the additional filter. This is probably because of the difference in the crystal thicknesses which was not optimum in No. 2 at long wavelengths because of the smaller absorption coefficient as well as the difference in doping levels.

In both detectors, the conductivity change and hence the

responsivity are due to

(i) Lattice temperature modulation creating purely thermal response, the existance of which is coupled with the existance of the thermal temperature coefficient

$$\alpha = \frac{1}{R}\frac{dR}{dT} = \frac{-\varepsilon_2}{kT^2}$$

(ii) Change in the number and probably the mobility of the dominating delocalized carriers by incident radiation at fixed lattice temperature as discussed in Chapter IV. This quantum effect has a considerable contribution to the bolometer response and dominates at higher frequencies.

The quantum response contribution to the overall response can be estimated by comparing the bolometer performance at very low and very high frequencies compared to the thermal frequency f_c. This was done by using 1kHz chopper blade. It was found that the responsivity dropped to about 35% and 40% for No. 2 and No. 1 respectively with both 200μm and the additional B.P. filters. These percentages do thus represent the photoconductivity contributions for these detectors.

The difference in doping levels in both elements is mainly responsible for the enhanced millimetre response in detector No. 1. This is caused by the further shift of the bottom of the delocalized energy band towards the ground state level and, hence, smaller quantum energy can cause phototransition to this band (we shall see below that ε_2 is smaller in No. 1 than in No. 2). This fact was further emphasised by designing a third detector with doping concentration as high as 6.5×10^{16} cm^{-3}. The unbiased crystal resistance in this detector is only 100 kΩ and the value of ε_2 is about 0.8 meV. Although the thermal response is reduced, the photoconductive part is highly increased and shifted to wavelengths longer than 1.5 mm. This

detector is at least a factor of two better in N.E.P. than these two detectors with much better response at higher modulation frequency. Therefore, these types of materials used can be controlled. The controlling parameter is the spread of the formed delocalised band by choosing the proper doping concentration and hence the desired longest detectable wavelength can be optimized.

The following are the crystals data and operating conditions for both detectors.

Parameter	No. 1	No. 2
Crystal dimensions (mm)	3 x 2 x 0.25	4 x 2 x 0.12
Doping level (Sb atoms.cm^{-3})	5.5×10^{16}	5×10^{16}
Unbiased crystal resistance at 1.5°K (MΩ)	1.19	7.3
Resistance at the operating point (kΩ)	100	1550
Load resistor (kΩ)	250	1000
Bias battery voltage (volts)	8.1	8.1
Heat sink temperature (°K)	1.55	1.55
Operating temperature (°K)	3.44	2.85
Dynamic thermal conduction $\frac{dP}{dT}$ at the operating point ($\mu W.^{o}K^{-1}$)	73	54
Dynamic impedance (kΩ)	-20	420
Thermal capacity ($J.^{o}K^{-1}$)	5×10^{-7}	1.5×10^{-7}
Response time constant $\frac{C}{\ell_d - \alpha PB}$ (ms)	4.8	3.2
Thermal cut-off frequency $\frac{1}{2\pi\tau_r}$ (Hz)	33.2	50
Activation energy ε_2 (meV)	1.46	1.5
$\alpha = \frac{-\varepsilon_2}{kT^2}$ ($^{o}K^{-1}$)	1.43	2.14

DC responsivity from (6.1) kv/w	28.35	85.57
DC responsivity from (6.2) kv/w	21.8	78.83
quantum to overall response ratio	0.4	0.35

In these materials expression (6.1) always gives a higher value of ℜ than that given by (6.2). This is because expression (6.2) does not consider the nature or the level of the dopant material, but rather it considers the value of the activation energy and the operating temperature which is merely controlled by the power input to the crystal and the leads thermal conduction. For example, excess non-linearity caused by carriers multiplication at a given electric field cannot appear in expression (6.2), but it is well taken into account in expression (6.1). In crystals where the electric field at the operating point has insignificant effect on dc conductivity at constant lattice temperature as in the tested p-type compensated material (see Chapter III), both (6.1) and (6.2) should give the same value of responsivity.

6.5. Noise measurements

Both detectors are background noise limited for 200μm filters setting at any modulating frequency. At longer wavelengths which is usually obtained for practical applications by using a cooled 120 lines per inch capacitative mesh filter (equivalent in the integrated energy transmission to the 3 mm high density black polyethylene filter), both detectors are just crystal noise limited. The intrinsic crystal noises are mainly the thermal noise $e_j = \sqrt{4kTR}$ and the inverse frequency noise for frequencies less than 200 Hz. The thermal noise domination is usually checked under no modulations by blanking off the incident radiation by a polished metal plate. We found that for both detectors, the noise voltage on the chart recorder is smaller

when the bias is on than when the crystal is unbiased. The ratio being the same as the square root of the corresponding resistances (taking into account the temperature differences) indicates the fulfillment of this theoretical limit. This condition is not easy to achieve in practice unless great care is taken during the soldering and mounting processes. Types of solder, cleaning the surface by etching and the proper temperature and flux used are of great importance. So many attempts were tried to reach this limit by changing these parameters until they became quite known. However, this was still, together with the wiring and doping conditions, the major field for further study in the design of far infrared Ge detectors.

Noise measurements were done for No. 1 detector*, this is shows in Figure (6.12). From the figure, we observe the domination of $\frac{1}{f}$ noise for $f < 200$ Hz. The horizontal line represents the Johnson and the phonon noise contributions and is reached nearly at 300 Hz. Figure (6.13) shows the circuit block diagram used for these measurements. The phase sensitive detector is used here as a narrow band pass filter with central frequency delivered by a harmonic generator connected to the P.S.D. input. The noise spectrum for a given band width (1 Hz) can then be obtained by varying the harmonic generator frequency. The selected noise sample is rectified by the P.S.D. and then squared and can be recorded as a dc level on a chart recorder.

From Figure (6.12), the noise mean square voltage varies as $f^{-0.73}$. This noise contribution includes the crystal and the preamplifier. From this spectral variation, increasing the chopping speed beyond 300 Hz will reduce the overall response to about 40%, while the total voltage noise contributions will decrease by a factor of 3.75 from the 10 Hz value. Therefore, a decrease in the detector N.E.P. of about

---

* These measurements were done by J. Sollner, Physics Department, Queen Mary College.

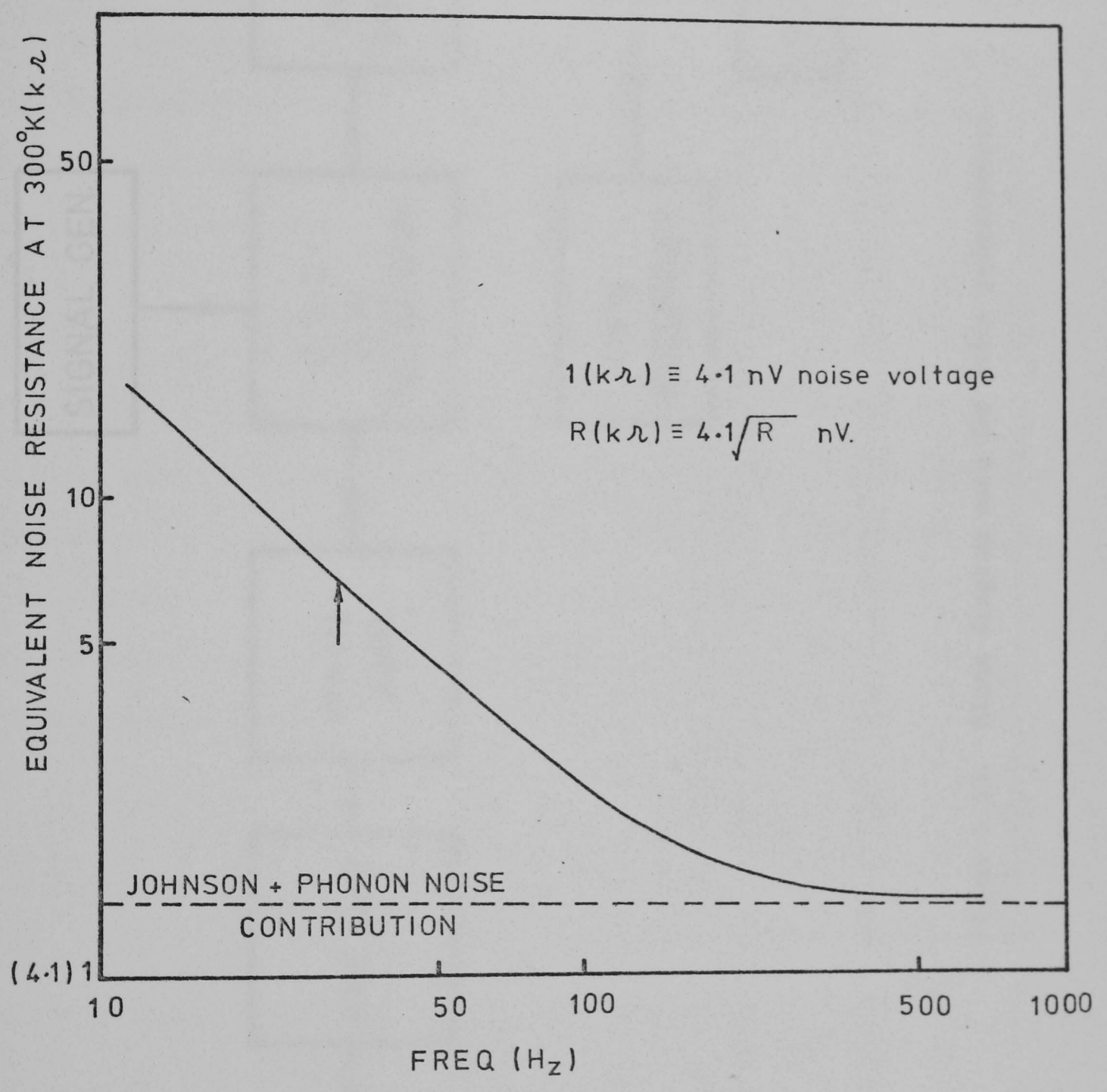

Figure 6.12. Detector No.1 and preamplifier $\frac{1}{f}$ noise spectrum

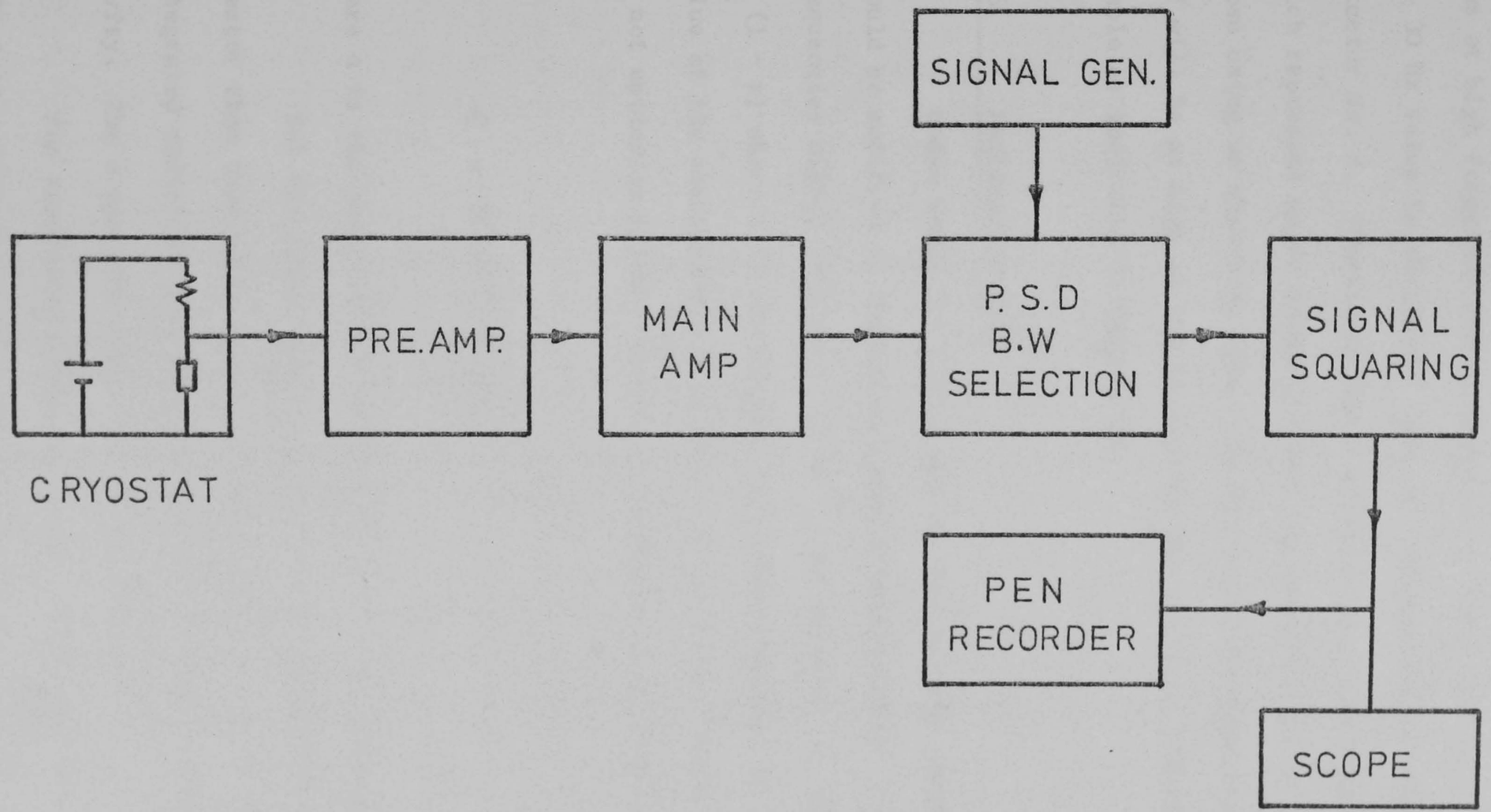

Figure 6.13. Block diagram used for noise measurements

1.5 times the 10 Hz value is obtained. For 30 Hz modulation (thermal cut-off frequency), the overall noise voltage is 2.15 times higher than at high frequency and an increase of the N.E.P. of only 1.16 times the 30 Hz value is obtained. Similar characteristics were observed in detector No. 2. Therefore, these detectors are high frequency detectors which represent major advantages over any thermal detector, especially those using an absorbing film. In this case, the high frequency cut-off will be as high as the inverse of the electrons lifetime in the sample as indicated in Chapter IV.

6.6. Performance data

Under radiation field, the dc responsivity given by (6.1) should be modified by the crystal actual emissivity ϵ . For radiation frequencies higher than about 25 cm^{-1}, the value of ϵ is nearly given by (1 - r) where r is the surface reflectance because of the high value of the absorption coefficient. Below 25 cm^{-1} where the crystal is not optically thick, the single incidence emissivity will be given by

$$\epsilon = \frac{(1 - r)(1 - e^{-\alpha d})}{1 - r\, e^{-\alpha d}} \qquad .. (6.12)$$

where α is the absorption coefficient and d is the crystal thickness.

But the actual value of ϵ at long wavelengths will be greater than that given by (6.12) due to the back reflection of the integrated radiation from the semispherical bottom of the cylindrical cavity. The α spectrum was given in Chapter IV.

For convenience, the N.E.P.'s will be given for unity emissivity, from which the radiation N.E.P. will be obtained by dividing the given value by the actual emissivity. The following are the performance data for both detectors measured at 95 Hz modulation

frequency.

Data	No. 1	No. 2
Noise voltage calculated (Johnson + phonon noises) nV. $Hz^{-\frac{1}{2}}$	4.88	15.6
Noise voltage measured nV. $H^{-\frac{1}{2}}$	6.86	16
Measured N.E.P. (unity emissivity) W. $Hz^{-\frac{1}{2}}$	2.4×10^{-13}	1.87×10^{-13}

These detectors are an order of magnitude more sensitive than the Rollin type InSb hot electron bolometers at long wavelengths although these detectors have the highest free carriers absorption at the millimetre range of the spectrum.

6.7. Black body calibration

Both detectors are calibrated against variable temperature black body* for temperatures between room temperature and 200°C. The response was found to be linear within this temperature range. The black body has an aperture of 6 cm diameter and located at 44 cm distance from the detector window which was limited to only 5 mm diameter. The solid angle of the black body source in this setting is 0.015 steradian. The filters used are the permanent 200μm filters in addition to the cooled mesh filters for further cutting of short wavelengths. The black body energy spectrum modified by the long wavelength filter for 1°K above the background temperature was computed** taking into account 50 cm length of water vapour attenuation. This spectrum is shown in Figure (6.14). The general formula used for computation is

---

*Designed by B. Carli, Physics Department, Queen Mary College.

**P.A.R. Ade, Physics Department, Queen Mary College.

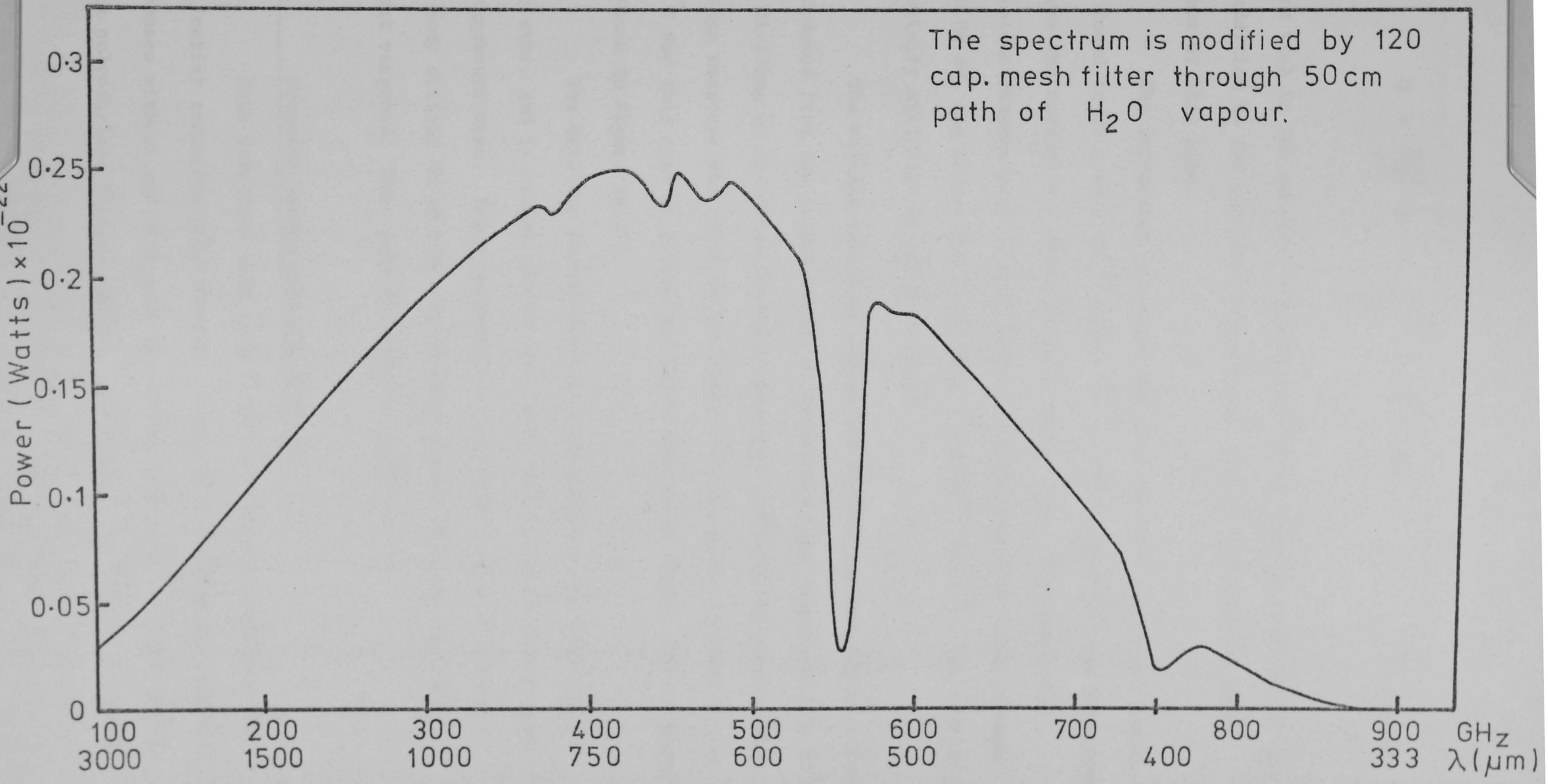

Figure 6.14. Black body energy spectrum /^{o}K

$$Q = \frac{2kT}{c^2} A \cdot \Omega \int_0^{\nu} \nu^2 \, f(\nu) \, d\nu \qquad .. (6.13)$$

where $f(\nu)$ is the spectral transmission of the capacitative mesh filter in addition to the spectral transmission of the 50 cm path of water vapour at that time.

The integrated power per $1^{o}K$ reaching the cylindrical cavity was found to be 7.43×10^{-13} watts. $^{o}K^{-1}$. The output voltage developed across the crystal was measured to be about 7 nV. Therefore, the radiation responsivity is 9.42 kv/w. From the measured noise voltage of 6.86 nV, the actual N.E.P. is then 7.3×10^{-13} $W.Hz^{-\frac{1}{2}}$. The crystal emissivity will also be $\frac{9.42}{28.35} = 0.33$.

The voltage developed across the crystal per one degree Kelvin is deduced from the output signal at relatively high temperature ($\sim 35^{o}C$) and dividing by the total excess temperature ($17^{o}K$ in our case). The voltage response was found to be linear with the power incident up to $200^{o}C$ for this type of filter and black body solid angle. This response is shown in Figure (6.15).

The detector acceptance angle was measured and found to be 1.26 ster. and is nearly similar for both detectors with the optical arrangements used. These measurements were done simply by moving a hot body distant 40 cm from the detector window and observing the output response. This plot is shown in Figure (6.16).

6.8. Detector system spectral response

Both detectors with each filter setting were tested using the fourier transform spectrometer. Figure (6.17) shows the spectral responses without and with each the cooled 200μm and the high density black polyethylene filters for No. 1 detector. The filters used for

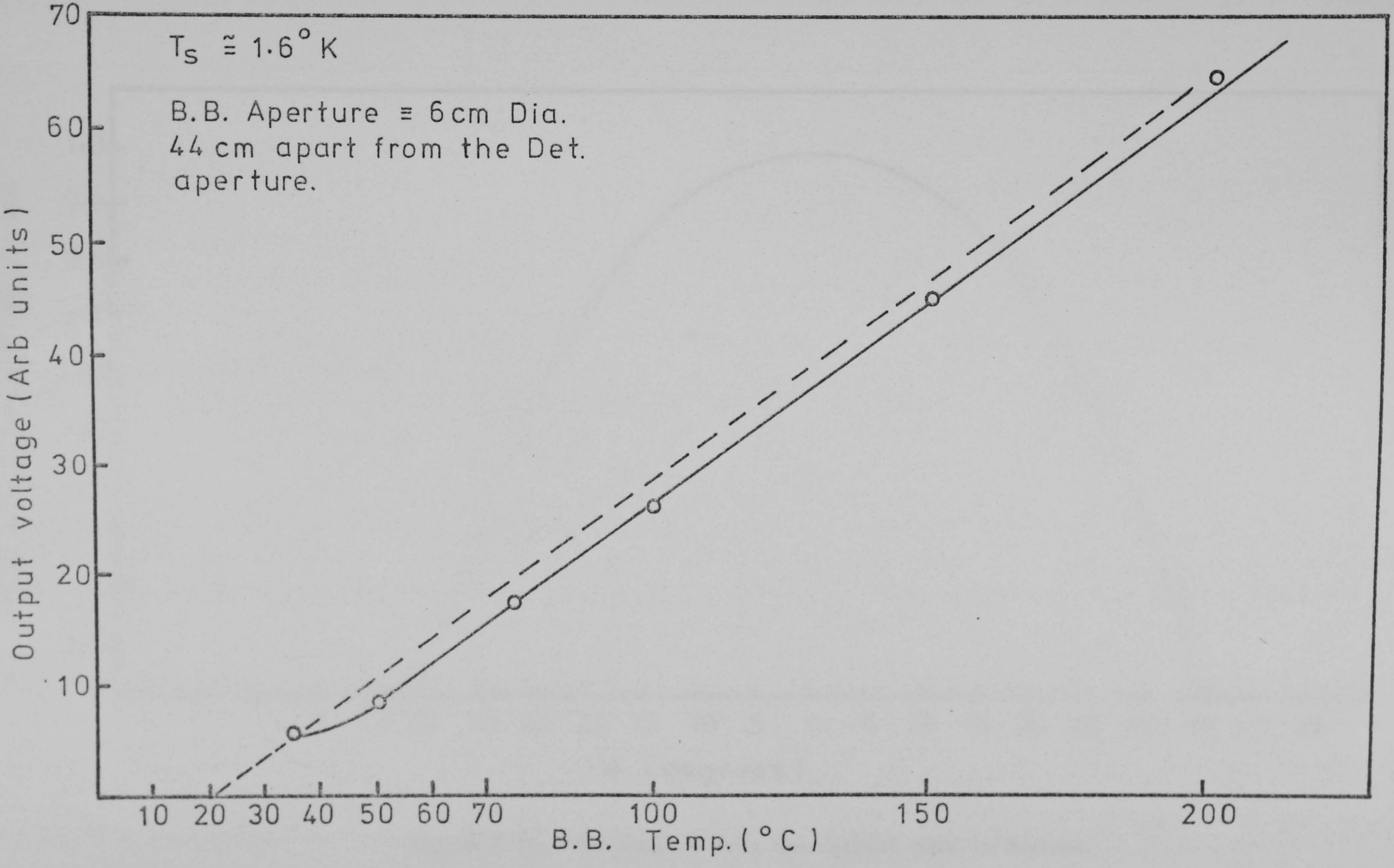

Figure 6.15. Black body detector response vs temperature

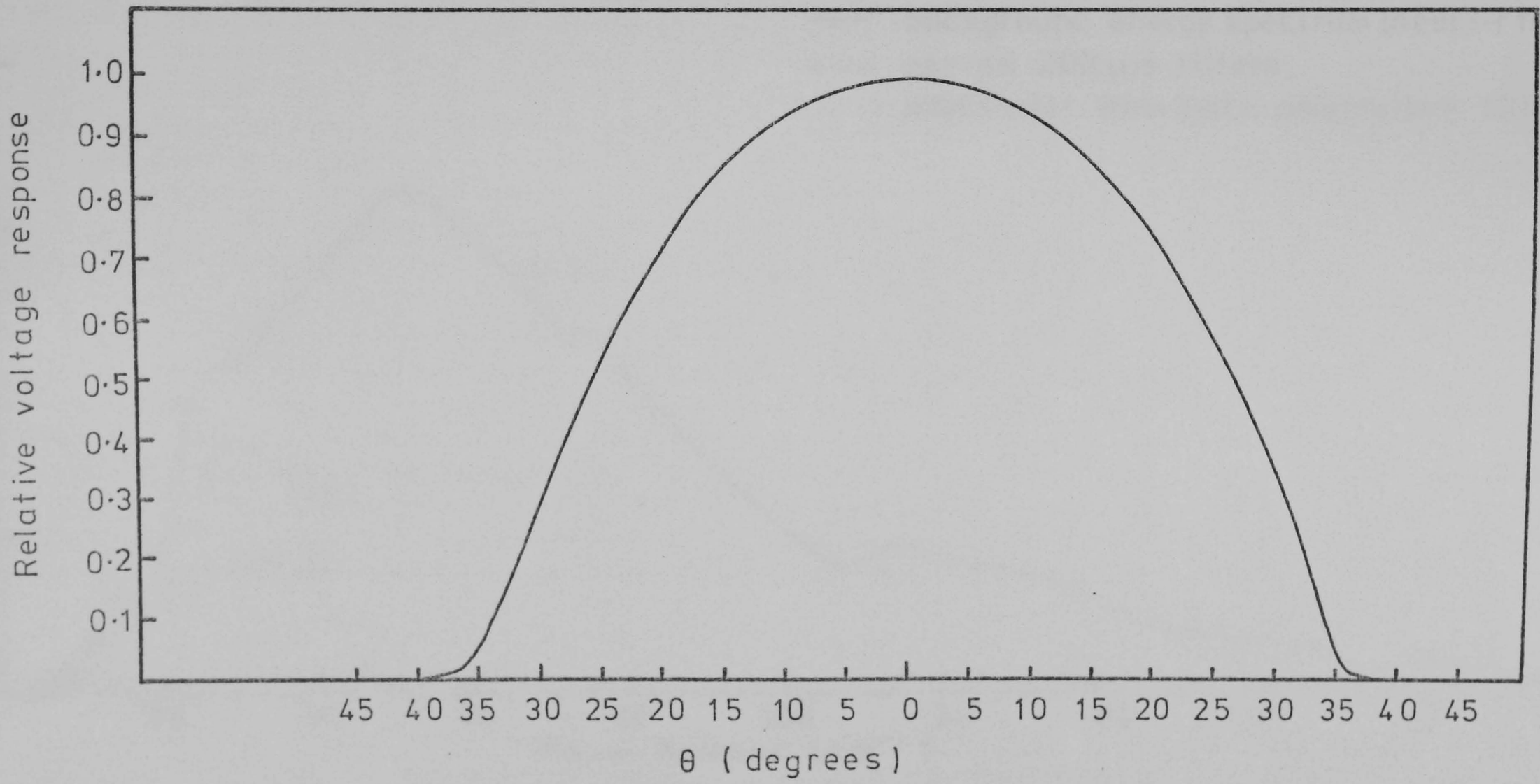

Figure 6.16. The angle θ from the optical axis in degrees

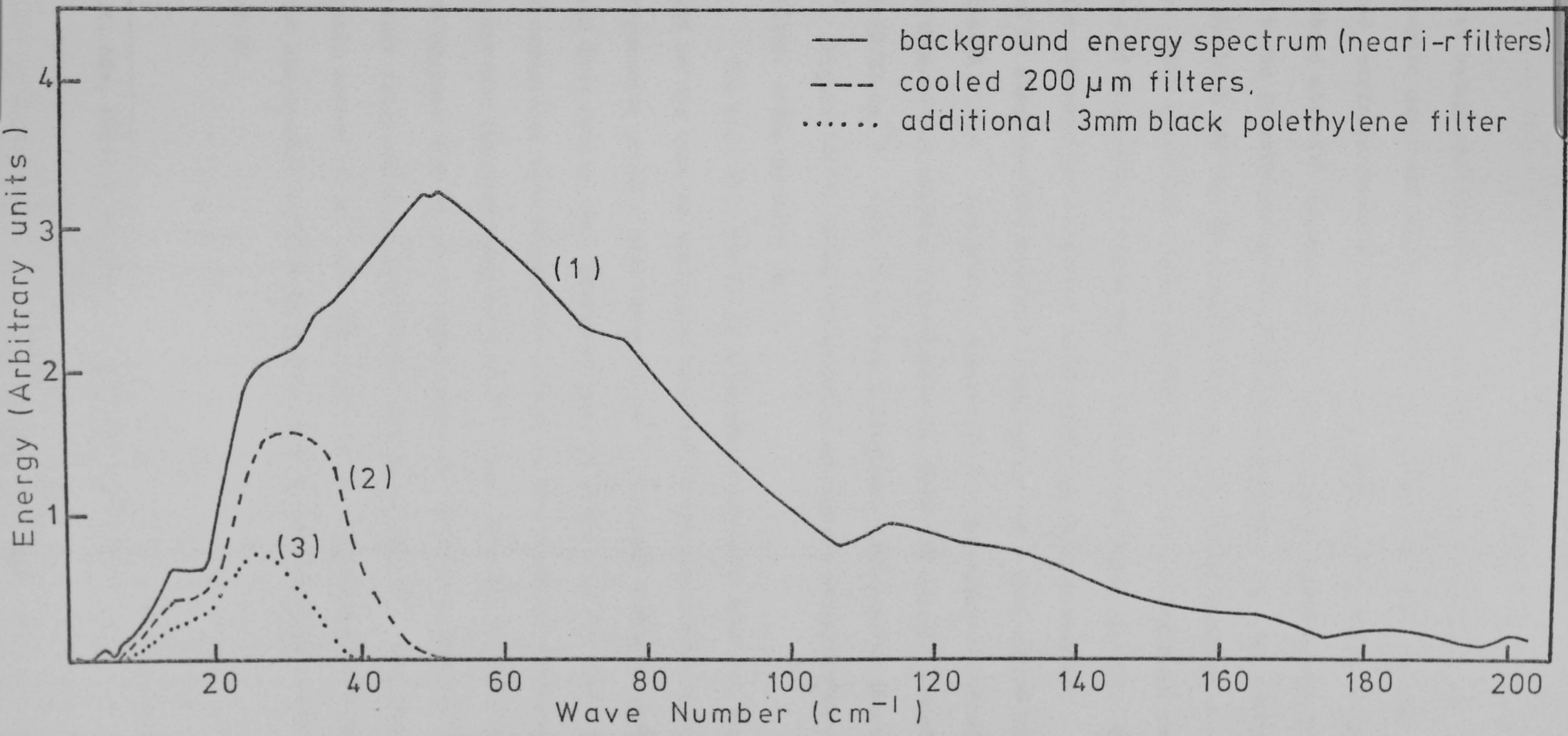

Figure 6.17. Energy spectra for the bolometer and filters

the first background spectrum is only cooled 100μm thick of black photographic paper and black polyethylene sheet to prevent the near infrared intrinsic photoionization. The response bandwidth of Ge as a broadband material appears clearly from the last figure (curve 1), in which the interferometer function and the mercury arc lamp energy limit the high and the low frequencies response of the detector respectively. From curve (2), Figure (6.17), we can see the efficient performance of the cooled thalium halide filters for 200μm cut-off. The detector response for radiation wavelengths longer than 1 mm was checked by measuring the spectral transmission for a very narrow band 3-part mesh filter* constructed especially for astronomical purposes having theoretical maximum transmission of about 40% centred around 1.2 mm (8.33 cm^{-1}). This filter has a frequency band pass of about 3 cm^{-1}. Figure (6.18) shows the measured percentage transmission of this filter using detector No. 1.

The fact that the Ge is a broadband material does not depend strongly on the type of the dopant material or the concentration level for frequencies greater than about 60 cm^{-1}. The only difference appears at lower frequencies, the interested part in these studies, where the doping conditions have the greatest effect on the bolometer response. The background spectral response for the n-type material detector was ratioed against that of the p-type compensated detector. Figure (6.19) shows this ratio which is nearly constant beyond 60 cm^{-1}. The peak of this ratio around 40 cm^{-1} and the reduction at lower frequencies agree with the absorption coefficient spectra for the two materials shown in Chapter IV.

---

* P.A.R. Ade, Physics Department, Queen Mary College.

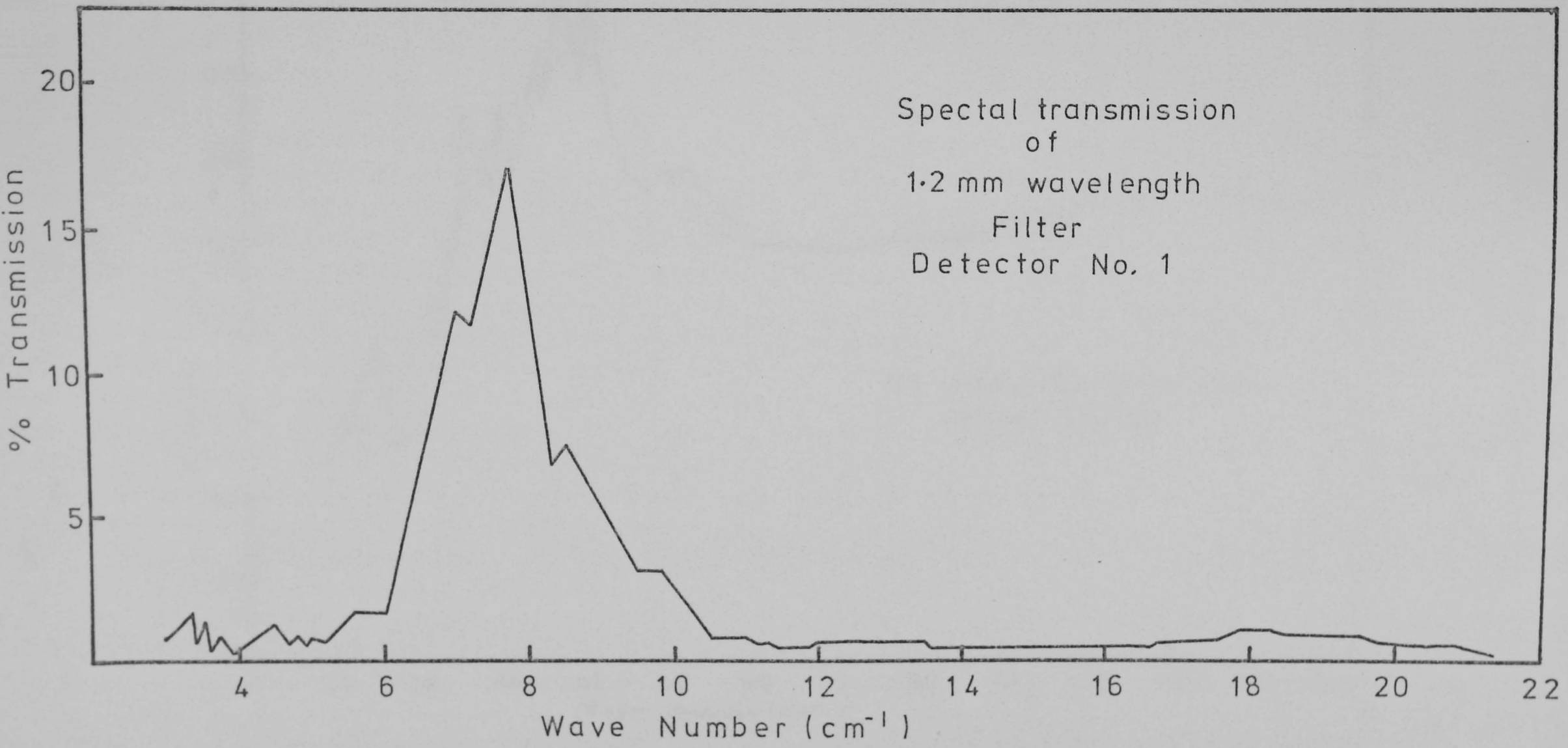

Figure 6.18. Percentage transmission of a narrow band filter

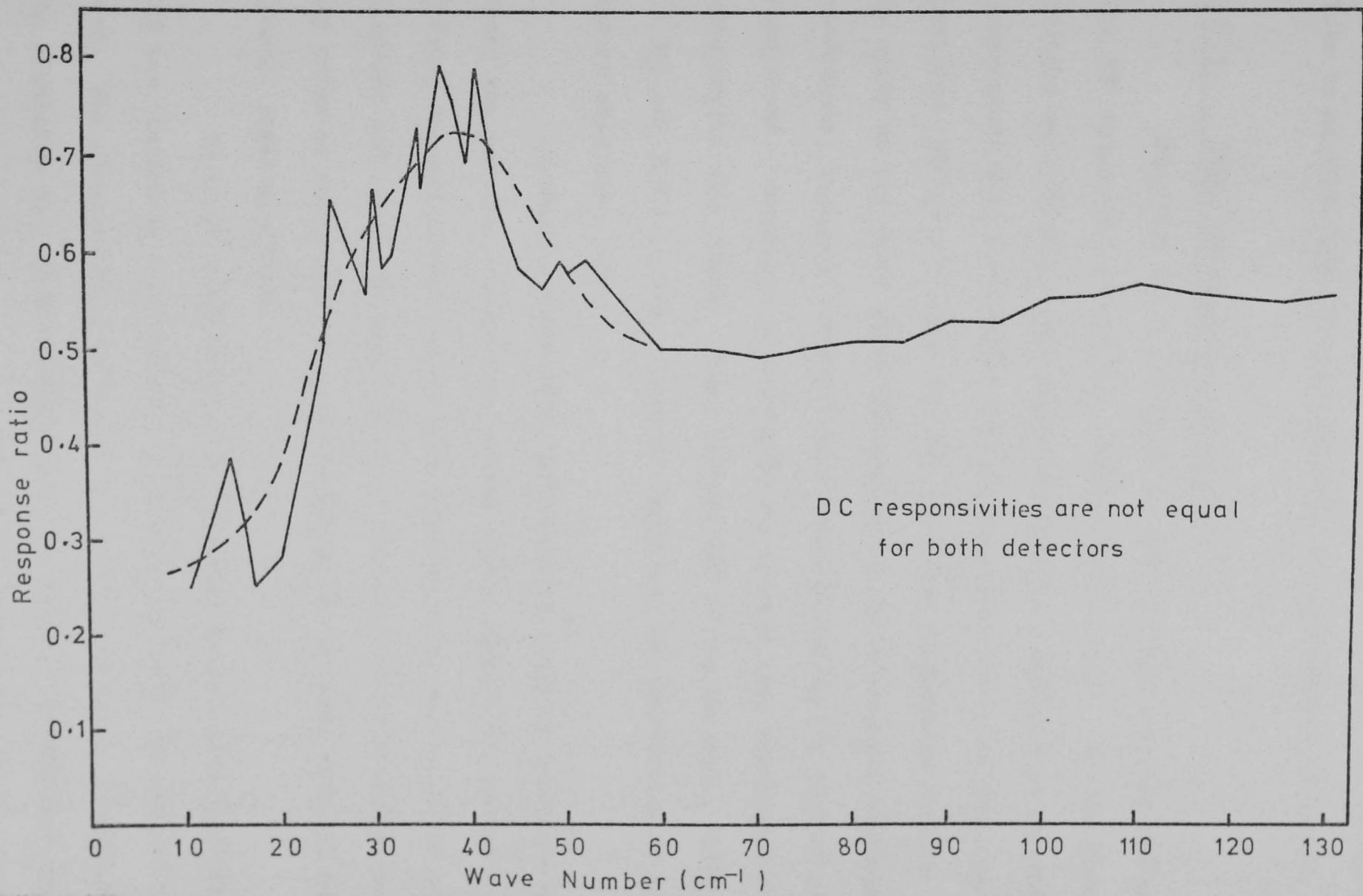

Figure 6.19. Spectral variation of the response ratio of Sb-Ge and Ga-Sb compensated Ge detectors

6.9. Detectors practical applications

Both detectors are used successfully for astronomical applications (apart from many spectrometric measurements), and we would like to mention some of these measurements and results obtained.

6.9.1. 350μm observations at Hawaii[3]

Detector No. 2 was used for astronomical observations using the 88" telescope at Mona Kea, University of Hawaii. The detector filters were 200μm filters described before in addition to an ambient temperature long wavelengths cutting inductive filter to limit the detected radiation to only the 350 and 450μm atmospheric windows. In spite of the short observing period and the inadequate atmospheric conditions, reasonable results were obtained during two days of good conditions. Detection of extragalactic sources were emphasised at wavelengths near 350μm. These include M82 at the 4σ level, 3C345 (3.4σ) and 3C273 (2.2σ). Complete lunar map and observation of planet Saturn were also taken.

In these observations, differential chopping technique was used, the detector window was covered with a copper disc having two irises, located around the detector optical axis, each of 5' of arc in diameter and separated by 6' of arc. This allowed to minimise the sky noise by subtracting the source signal in one beam from the background reference beam.

In these applications, the detector worked quite satisfactorily and was limited by sky fluctuation noise in spite of the limited window used. The chopping frequency used was 95 Hz supplied by a small vibrating aluminium disc of 8 mm diameter. The chopper assembly was attached completely to the cryostat and the window and the chopper disc were protected against the wind streams by enclosing them in a small housing having a thin sheet of transparent melinex window. The cryostat, HD-3,

after fully pumping down to 4 torr helium pressure allowed running over at least 12 hours which was sufficient for each nights observations,

6.9.2. Cosmic background spectrum - QMC/NPL Experiment for NASA/ ESRO Assess Project (Pre-space shuttle experiment) [4]

Detector No. 1 with the 200μm cooled filters was used to measure the cosmic background spectrum and to monitor atmospheric constituents at a height of up to 39,000 feet. The detector was used with an absolute spectrometric radiometer for spectral range 3-40 cm^{-1}. The purpose of the mission is to explore the spectral assignments and concentrations of ozone and minor constituents of the atmosphere, meanwhile to test developments of technique. Resolution as high as 0.01 cm^{-1} unapodized was necessary to resolve the overlapped emission lines from different constituents. This would allow an interferogram to be recorded in a few minutes because significant change can occur in atmospheric conditions in such a time interval. Such improvements were introduced by using fast data aquisition system, the adoption of the polarized interferometric method both to suppress the effects of signal fluctuations and to allow continuous reference to a cooled black body calibration source [5,6], and the incorporation of this high sensitivity and fast detector.

The spectra was taken at an altitude of about 33,000 feet with a controlled elevation angle of 14^{o} to allow minor constituents to be recorded. The atmospheric emission was continuously compared with that from a black body cavity. The primary results show that these newly developed techniques were successful. Figure (6.20) shows a small portion of two interferograms taken successively and ratioed against $0^{o}C$ black body. Each was recorded in eight minutes and the total spectrum obtained covers the range 3-40 cm^{-1}, of which only the part from 20.5 to 22.5 cm^{-1} is shown in the figure. The final

resolution after apodization was 0.02 cm^{-1}. One of the spectra is displaced upwards to avoid overlapping. It can be seen that most features are reproduced in the two spectra. The positions of the lines of possible constituents of the atmosphere are marked at the top of the figure.

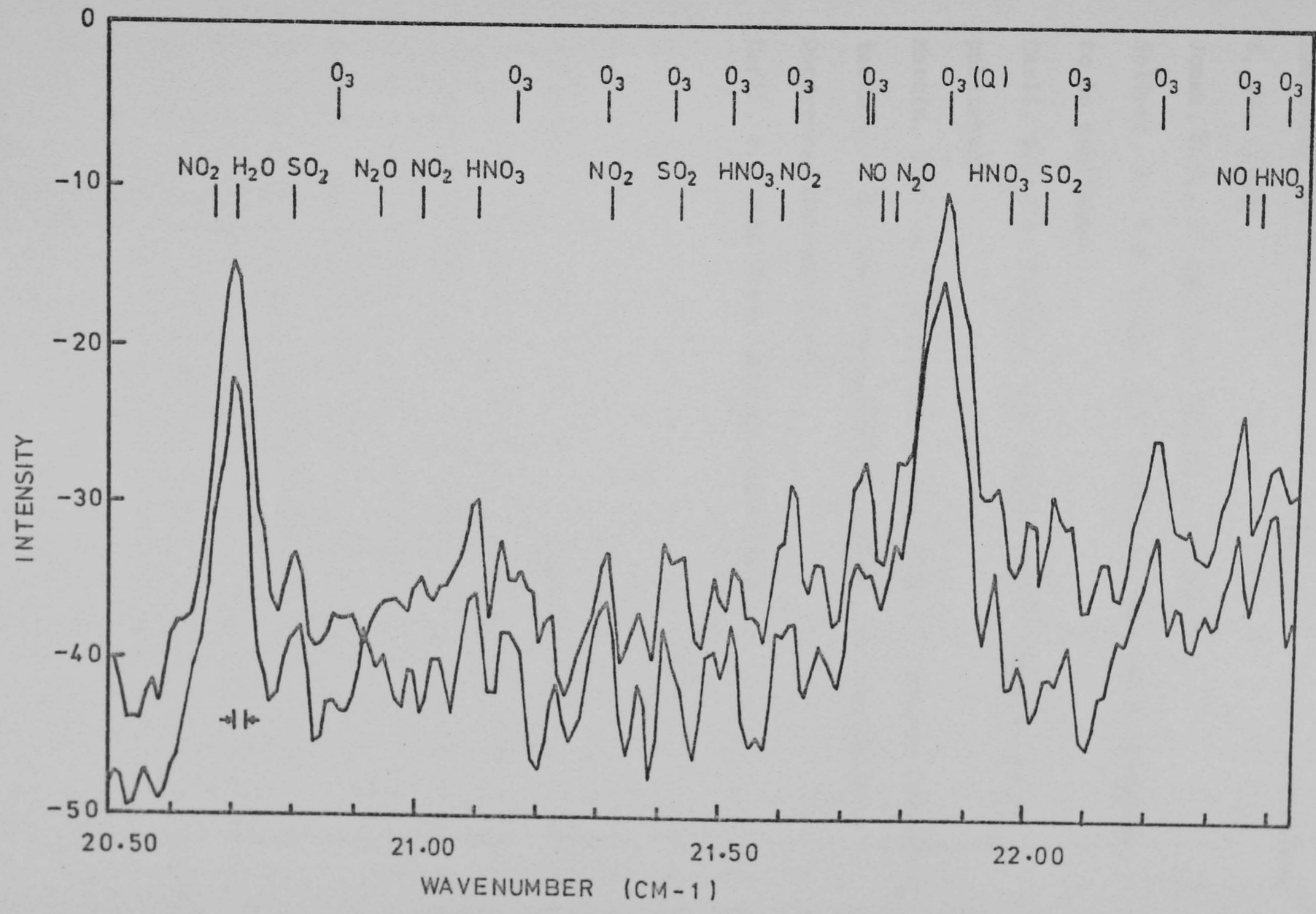

Figure 6.20. Cosmic background spectrum (After ref. 4)

CHAPTER VI

REFERENCES

(1) Zwerdling, S., R.A. Smith and J.P. Theriault, Infrared Physics, 8, 271 (1968)

(2) Jones, R.C., J. Opt. Soc. Am. 43, 1 (1953)

(3) Sollner, J., P.E. Clegg, E.I. Robson, D. Eve and S. El-Atawy, to be published

(4) Carli, B., J.E. Harries, D.H. Martin and E. Puplett, to be published

(5) Martin, D.H. in V. Manno and J. Ring (Eds.) "Infrared detection techniques for space research", D. Reidel, Publishing Co., Dordrecht, Holland (1972)

(6) Carli, B., IEEE Trans. MTT 22, 1094 (1974)

CONCLUSION

The thermal activation energy ε_2 existing in the intermediate doping concentration (1 - 8 x 10^{16} cm^{-3}) in n-type Ge at low temperatures represents thermal ionization of neutral donors from the ground state energy level to the bottom of an intermediate energy band formed between the ground state level and the continuum conduction band as a result of impurity interactions. The delocalized band thus formed results from the broadening of the first excited state of the isolated impurity atoms. The bottom and the top of this band lie about 1.4 and 6.5 meV above the ground state for 5.5 x 10^{16} $Sb.cm^{-3}$ doping level with maximum state density at $\sim$ 5 meV (the first excited state level). The value of the thermal activation energy ε_2 is not affected by the presence of a magnetic field (5.6 kG was used).

The mobility of the delocalized carriers at 1.7 and 4.2°K and hence the momentum scattering time are smaller than the conduction band values at low magnetic fields, but become nearly equal at the highest magnetic field used (25 kG) assuming equal effective masses.

The observed very large absorption coefficient in this sample for the infrared wavelengths 100-1000μm is a direct result of the existance of this delocalized band which is not present in low concentration samples. Absorption of radiation, which is bias independent, occurs as a result of photo-transition from the ground state to the delocalized energy band. The minimum photon energy to be absorbed by this mechanism is equal to the thermal value ε_2 (the bottom of the band) which is dependent on doping concentration. Therefore, the minimum detected photon energy is controllable.

For far infrared detectors, this material is very useful, especially in the wavelengths mentioned, for astronomical applications (350, 450 and 1200μm observations). This material with the proper design

and construction (including the cooled filters) is capable of producing very fast, high sensitivity far infrared receivers.

The lowest temperature activation energy ε_3 was found to be increased by magnetic field (5.6 kG). For this magnetic field, a reduction of the ground state Bohr radius of about 26% was found based on the observed magneto-resistance and the increase in ε_3.

The population of free carriers in the delocalized band is magnetic field dependent. The observed dependence is such that the carrier density is nearly inversly proportional to the magnetic field. The relative change of carrier density with magnetic field is temperature independent between 4.2 - 1.7^{o}K which confirms the ε_2 independence on magnetic field. The observed large anomaly in the Hall coefficient for this sample confirms the existance of the Auger recombination process which seems to be enhanced for specific values of electric and magnetic fields.

Ion implantation of this sample to form a degenerate absorbing film seems promising regarding absorption of infrared radiation especially if the substrate effect is eliminated or reduced and if the implanting ions and dose are properly selected.

The optimum performance of the constructed detectors using this material was such that the chosen thermal conduction should give the proper temperature rise for a reasonable element voltage (usually > 1 volt) such that the two main conduction mechanisms, distinguished by ε_2 and ε_3, compete. This would give the best compromise between the thermal effect and direct photoconductivity.

ACKNOWLEDGEMENTS

I wish to acknowledge my indebtedness to all the academic and technical staff in the Department of Physics, Queen Mary College, particularly Dr. P.E. Clegg, my supervisor, for his encouragement and advice throughout this work and also for many invaluable periods of discussion. Thanks also go to the Ministry of Higher Education in Egypt for financial support.

I should also like to thank Professor D.H. Martin and Professor J.A. Bastin for their useful discussions and advice and also for enabling me to use the excellent facilities in the Physics Department; Dr. P.A.R. Ade for his continuous assistance in many experiments during this work, together with my colleagues in the Astrophysics group for their encouragement and friendship; Miss Mary Pilgrim for preparing the detector elements and filters; Mr. D.G. Vickers and Mr. A. Marston for their excellent technical assistance, the low temperature service department; Dr. D. Palmer, Sussex University, Brighton, for preparing the ion implanted samples; Mrs. Christine Ando for her elegant typing of this thesis and Miss A. Boswell and Mr. S. Adams for their efforts in preparing all the figures in this form.

I am particularly grateful to my wife, Sekina, for her indispensable assistance and encouragement and also for her useful scientific arguments in many aspects of this work.

Infrared Physics, 1976, Vol. 16, pp. 409–410. Pergamon Press. Printed in Great Britain.

LETTER TO THE EDITOR

FAR INFRARED PHOTO-TRANSITION IN SB-DOPED GERMANIUM AT LOW TEMPERATURES*

It is well established that, at low temperatures, at least three conduction mechanisms exist in compensated n-type Ge in intermediate doping levels. In this temperature region, the conductivity may be written in the form[1]

$$\sigma = \sigma_1 \exp -(\epsilon_1/kT) + \sigma_2 \exp -(\epsilon_2/kT) + \sigma_3 \exp -(\epsilon_3/kT) \quad (1)$$

The first term in equation (1) represents direct activation from the ground state of the donor atom to the conduction band while the third term represents thermally activated 'hopping' conduction.[1–3] The second term is not well understood but it has been proposed that this term represents excitation of an electron

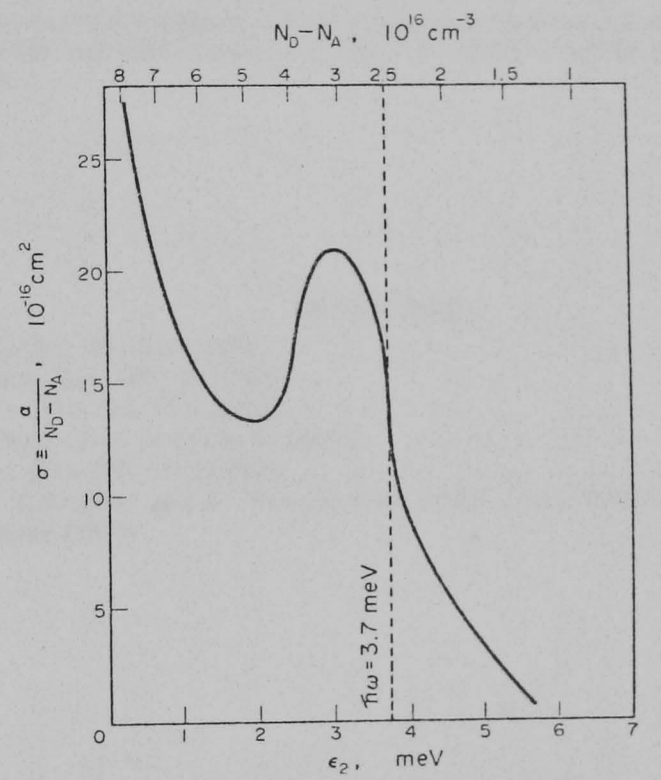

Fig. 1. Absorption cross-section vs ϵ_2. The upper scale gives excess donor concentration (after Yoshihiro *et al.*[6]).

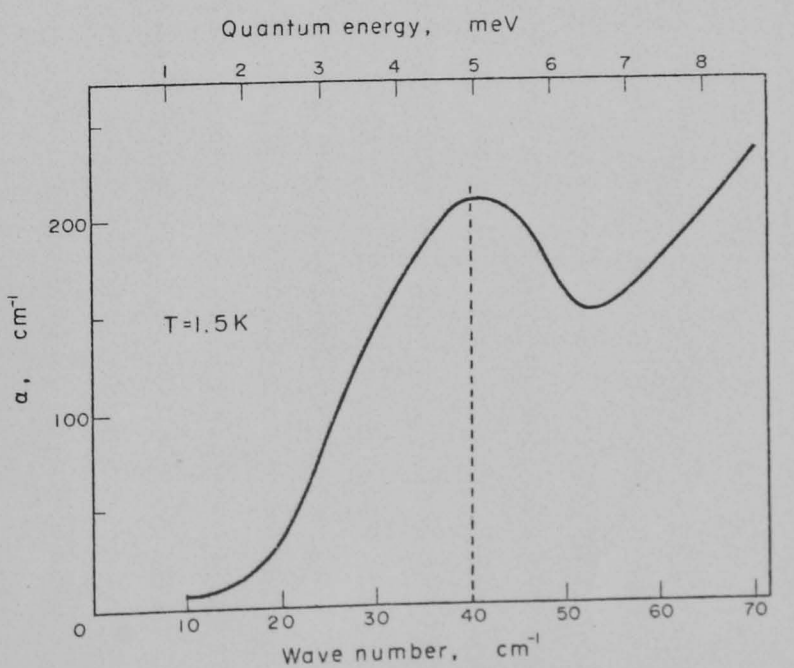

Fig. 2. Absorption coefficient spectrum for a Ge sample containing ~ 5·5 × 10^{16} Sb/cm^3.

* *Received* 5 *May* 1975.

QUEEN MARY COLLEGE LIBRARY

from the ground state into a delocalized state below the conduction band.[4,5] The value of ϵ_2, and therefore the position of this state relative to the ground state, is a strong and unique function of the donor concentration N_D. (It is not a strong function of the degree of compensation for low compensation ratios.)

Recently, Yoshihiro *et al.*[6] claimed to have detected resonant photo-excitation of electrons from the ground state to this delocalized state. They observed a 'resonance' in the relation between the absorption cross-section for 337 μm monochromatic radiation, and the value of N_D (and hence of ϵ_2); this 'resonance' occurs at $\epsilon_2 \sim 3$ meV, corresponding closely to the 3·7 meV of the radiation (Fig. 1).

A more direct way of observing resonant absorption is to vary the frequency of the radiation while keeping the donor concentration (and hence ϵ_2) constant; ideally this should be done for a range of donor concentrations. We have made absorption measurements on a specimen of Ge containing $5{\cdot}5 \times 10^{16}\,cm^{-3}$ Sb donors with no intentional compensations. The measured thermal activation energy, ϵ_2, of this sample was 1·4 meV which is in very good agreement with the activation energy/donor concentration relation of Yoshihiro *et al.* (Fig. 1). If their hypothesis of resonant absorption to the ϵ_2 state were correct, we would expect an absorption peak to occur around 940 μm, i.e., at an energy of 1·4 meV. In fact, the measured volume absorption coefficient shows a very broad maximum at ~ 5 meV (Fig. 2), corresponding very closely to the energy of the first excited state of Sb at 5·3 meV.[6]

It is difficult to reconcile this result with the conclusions drawn by Yoshihiro *et al.* and it is clearly desirable to obtain spectral data for different doping levels. It does, however, seem clear to us that the 'resonance' shown in Fig. 1 lends only fortuitous support to the hypothesis of direct photo-excitation to the ϵ_2 level, and we believe that excitation is to the broadened first excited state of Sb. In support of this, it should be noted that the supposed resonance in Fig. 1 is actually removed from the energy of the exciting radiation by $\sim 0{\cdot}7$ meV.

Queen Mary College,
Physics Department,
Mile End Road,
London, E1 4NS.

S. A. El-Atawy
P. E. Clegg

REFERENCES

1. Fritzsche, H., *Phys. Rev.* **99**, 406 (1955).
2. Conwell, E. M., *Phys. Rev.* **103**, 51 (1956).
3. Mott, N. F., *Can. J. Phys.* **34**, 1356 (1956).
4. Fritzsche, H., *J. Phys. Chem. Solids* **6**, 69 (1958).
5. Fritzsche, H., *Phys. Rev.* **125**, 1552 (1962).
6. Yoshihiro, K., M. Tokumoto and C. Yamanouche, *IEEE Trans. Microwave Theory and Techniques*, **MTT-22** (12) December (1974).